DESIGN AND SIMULATIONS OF SiC BASED REAR CONTACT Si AND SiGe SOLAR CELLS FOR STANDALONE AND TANDEM APPLICATIONS

Thesis submitted by

RAHUL PANDEY

In Partial Fulfillment of the Requirements for the Degree of

DOCTOR OF PHILOSOPHY

Under the Supervision of

Dr. RISHU CHAUJAR

Department of Applied Physics, Delhi Technological University
Bawana Road, Delhi-110042, India

December-2017

DEDICATED TO….

My Family

Delhi Technological University

(Govt. of National Capital Territory of Delhi)
Bawana Road, Delhi-110042

CERTIFICATE

This is to certify that the thesis titled "***Design and Simulations of SiC Based Rear Contact Si and SiGe Solar Cells for Standalone and Tandem Applications***" is being submitted by **Mr. RAHUL PANDEY** with registration number ***2K13/PHDAP/04*** to the Delhi Technological University for the award of the degree of Doctor of Philosophy in Applied Physics. The work embodied in this thesis is a record of bonafide research work carried out by me in the Microelectronics Research Lab, Applied Physics Department, Delhi Technological University (Formerly Delhi College of Engineering), New Delhi under the guidance of ***Dr. RISHU CHAUJAR***. It is further certified that this work is original and has not been submitted in part or fully to any other University or Institute for the award of any degree or diploma.

Rahul Pandey
Candidate
Roll No. 2K13/PHDAP/04

This is to certify that the above statement made by the candidate is correct to the best of our knowledge.

Dr. Rishu Chaujar
Supervisor (Asst. Professor)
Department of Applied Physics
Delhi Technological University
Delhi, India

Prof. S. C. Sharma
Head,
Department of Applied Physics
Delhi Technological University
Delhi, India

ACKNOWLEDGEMENTS

The time spent during the doctoral program was overwhelmed with novel ideas; discussions, research activities and pool exchange of invaluable knowledge; which couldn't have happened without legitimate support, guidance and heed of foremost my supervisor, thereafter my university, department, colleagues, friends, and family members. Hence, I would like to take few moments of the readers to pay this little tribute and express my gratefulness towards my research life gurus and companions.

At the onset, I want to offer my benevolent and courteous gratitude to my guide ***Dr. Rishu Chaujar****, Assistant Professor, Department of Applied Physics, for her enthusiastic assistance and supervision in successfully finishing my research work within time. She brought out the superlative research potential within me by providing incessant counsel and navigation. I would like to thank* ***Dr. Rishu Chaujar*** *for her credence in me and my research vision. Her optimism inspired me to think out of the box and motivated me to work uninterruptedly even after encountering some failures through the path. I have a lot of nostalgic memories working in the research group under her supervision and would even wish for an opportunity to collaborate further.*

Finest research wouldn't have taken place without the constant help and support provided by the department along with the university. Thus, I want to sincerely thank ***Hon'ble Prof. Yogesh Singh****, Vice Chancellor, Delhi Technological University, and* ***Prof. S.C. Sharma****, Head of Department, Department of Applied Physics for providing copious assistance and research productive environment throughout the duration of my doctorate. I wish to acknowledge faculty members for their continuous support as well as departmental and administrative staff members for providing their precious service to ensure smooth functioning of the process which aided my research atmosphere. I further thanks to SRC and DRC members* ***Prof. S.C. Sharma*** *(chairman DRC),* ***Prof. Anurag Sharma*** *(External Expert),* ***Prof. V.D. Vankar*** *(External Expert)****, Dr. Ajay Sharma*** *(External Expert) for taking their momentous time serving in my committee and giving their priceless endorsement on my thesis.*

I wish to explicit my gratitude to ***Ms. Jaya Madan*** *(Research Fellow) and* ***Mr. Kamal Arora*** *(Research Fellow) for their important prospect, suggestions, and support which reinforce the value of my research work. Their continuous moral support made this research work possible. And last, but not the least, I wholeheartedly offer my benign regards to my research group mates* ***Mr. Ajay Kumar*** *and* ***Neha Gupta****, who were beside me through the best and worst of my research days. I would like to explicitly thanks my colleagues and friends* ***Vipin Dahiya, Nisha Deopa, Nishant Shankhwar, Abhishek Bhardwaj, Harpreet Kaur, Kaushal Jha, Deepika Sandil, Ritika Khatri, Kanika Sharma, Lucky Krishnia, Reetu Singh, Vinay Yadav, Neha Gupta, Ardhman Kaur, Swati Aggarwal , Dr. Kamal Kishor, Aman Prasad, Jyotsna Panwar, Ravi Gupta and Sumandeep Kaur****, who filled me with lots of enthusiasm, optimism and vigor which helped me accomplish my research objectives efficiently.*

I would like to earnestly thank **University Grant Commission** *(UGC) for their financial support in the form of fellowships during my Ph.D.*

*In the end, I courteously credit my family members, my father (****Bateshwar Nath Pandey****), my mother (****Sushila Pandey****), my loving brothers (****Arun Pandey and Kaushal Pandey****) and my sister-in-laws (****Jyoti Pandey and Roshani Pandey****) for selflessly caring and backing me psychologically and financially throughout my research work and especially in my life. Their love, affection and constant motivation helped me in concluding my research work successfully in due time.*

(Rahul Pandey)
New Delhi,
December 2017

ABSTRACT

DESIGN AND SIMULATIONS OF SiC BASED REAR CONTACT Si AND SiGe SOLAR CELLS FOR STANDALONE AND TANDEM APPLICATIONS

The most abundant renewable source of energy on the earth is solar energy, yet its potential has not been exploited efficiently by solar cells present in the market. Affordability of solar energy can be enhanced, either by increasing the efficiency of a solar cell or by reducing its cost. In this thesis, several approaches for improving solar efficiency with careful design have been proposed using Technology Computer Aided Design (TCAD). These approaches attempt to improve the solar cell current, solar cell voltage, light absorption, surface recombination, and ultraviolet (UV) stability. Finally, the mechanically stacked tandem architecture addresses thermalization and lack of absorption losses for improved efficiency.

The initial focus is to minimize the issues associated with thin devices such as low absorption and high surface recombination. These issues have been resolved using novel front surface design which consists of Zirconia (ZrO_2) based texturing along with Silicon Carbide (SiC) based front surface passivation. Design principle balances out photonic and electronic effects together and resulted in 15.7% efficient rear contact silicon (Si) solar cell, in the sub-10 µm-thick regime. The next focus is to minimize the thermalisation losses. 300 microns and 10 microns thick SiC passivated rear-contact solar cell has been placed in four terminal (mechanically stacked) tandem configuration with 20.9% efficient perovskite top subcell. Realistic TCAD analysis has been done for both top and bottom subcell; which resulted in 27.6% and 22.4% efficient tandem devices under single air mass 1.5 (AM 1.5) irradiance. Further, SiC passivated interdigitated back contact silicon heterojunction solar cell (IBC-SiHJ) has also been discussed for bottom subcell application under perovskite top subcell since IBC-SiHJ solar cell uses low-temperature fabrication processes and has excellent photovoltaic (PV) performance. The efforts resulted in 29.5% and 23.7% efficient tandem devices which contain 250 µm and 25 µm thick IBC-SiHJ bottom subcells, respectively.

Si as an active material for most of the PV devices, whose absorption coefficient is small at higher wavelengths; therefore, thick silicon wafers are required to obtain greater efficiencies in both standalone as well as tandem configuration. Thicker silicon wafer eventually increases the module cost, and hence, modification in the bandgap (Eg< 1.1 eV) of the Si is required to increase the absorption of sunlight at higher wavelengths while keeping the thickness low. Therefore, Silicon-Germanium (SiGe) material has been introduced to rear contact solar cell designs and investigation is done for both standalone and tandem configuration. The thickness of SiGe based devices reported in this thesis is 10 microns, which is projected to enhance the efficiencies keeping the thickness low. The device exhibits improved higher wavelength absorption without the need of complex texturing schemes and suggested its potential use as a bottom subcell under tandem configuration. 15.4% power conversion efficiency (PCE) is reflected in convention rear contact SiGe solar cell, whereas in interdigitated back contact SiGe heterojunction solar cell (IBC-SiGeHJ) architecture, 15.5% PCE is achieved in a stand-alone configuration, and in combination with perovskite top subcell, further 25.7% PCE is demonstrated.

LIST OF FIGURES

LIST OF TABLES

LIST OF PUBLICATIONS

ARTICLES IN INTERNATIONAL REFEREED JOURNALS (8)

[1] **R. Pandey** and R. Chaujar, "Numerical simulations of novel SiGe-based IBC-HJ solar cell for standalone and mechanically stacked tandem applications," *Materials Research Bulletin,* vol. 93, pp. 282-289, 2017. **(IF=2.446)**

[2] **R. Pandey** and R. Chaujar, "Technology computer aided design of 29.5% efficient perovskite/interdigitated back contact silicon heterojunction mechanically stacked tandem solar cell for energy-efficient applications," *Journal of Photonics for Energy,* vol. 7, pp. 022503-022503, 2017.**(IF=2.287)**

[3] **R. Pandey** and R. Chaujar, "Rear contact SiGe solar cell with SiC passivated front surface for> 90-percent external quantum efficiency and improved power conversion efficiency," *Solar Energy,* vol. 135, pp. 242-252, 2016. **(IF=4.018)**

[4] **R. Pandey** and R. Chaujar, "Numerical simulations: Toward the design of 27.6% efficient four-terminal semi-transparent perovskite/SiC passivated rear contact silicon tandem solar cell," *Superlattices and Microstructures*, vol. 100, pp. 656-666, 2016. **(IF=2.123)**

[5] **R. Pandey** and R. Chaujar, "Numerical simulation of rear contact silicon solar cell with a novel front surface design for the suppression of interface recombination and improved absorption," *Current Applied Physics,* vol. 16, pp. 1581-1587, 2016. **(IF=1.971)**

[6] **R. Pande**y and R. Chaujar, "Novel back-contact back-junction SiGe (BC-BJ SiGe) solar cell for improved power conversion efficiency," *Microsystem Technologies,* vol. 22, pp. 2673-2680, 2016.**(IF=1.195)**

[7] **R. Pandey** and R. Chaujar, "Front surface passivation scheme for back-contact back-junction (BC-BJ) silicon solar cell," *Advanced Science Letters,* vol. 22, pp. 815-820, 2016.**(IF=1.253 @2010)**

[8] **R. Pandey** and R. Chaujar, "Enhanced back-contact back-junction Crystalline silicon solar cell Performance with a silicon-carbide (SiC) Based front surface passivation," *International Journal of Advanced Technology in Engineering and Science,* vol. 2, p. 5, 2014.**(IF=2.870)**

ARTICLES COMMUNICATED IN INTERNATIONAL REFEREED JOURNALS (1)

[1] **R. Pandey** and R. Chaujar, “Rear Contact Silicon Solar Cells with SiC Based Front Surface Passivation for Ultraviolet Radiation Stability, ” *Applied Surface Science* (Elsevier). **(IF=3.387)**

ARTICLES IN INTERNATIONAL CONFERENCES (10)

[1] **R. Pandey**, A. Saini, and R. Chaujar, "Numerical simulation of Reduced Cerium Oxide with polaron transport mobility based ETL for stable and efficient Perovskite Solar Cells," presented at the *17th International Conference On Thin Film*s, CSIR- National Physical Laboratory, New Delhi, India, Nov. 13th -17th , 2017.

[2] **R. Pandey** and R. Chaujar, "Rear Contact Silicon Solar Cell with SiC Based Front Surface Passivation for Ultraviolet Radiation Stability " presented at the *9th International conference on Advanced Nanomaterials*, University of Aveiro, Portugal July 19th - 21st ,2017.

[3] **R. Pandey**, J. Madan, and R. Chaujar, "Gate Drain Underlapping: A Performance Enhancer for HD-GAA-TFET, presented at the *9th International conference on Advanced Nanomaterials*, University of Aveiro, Portugal July 19th - 21st ,2017.

[4] **R. Pandey**, S. Gupta, T. Khatri, and R. Chaujar, "Interdigitated Back Contact SiliconSolar Cell with Perovskite layer for Front Surface Passivation and Ultraviolet Radiation Stability," presented at the *44th IEEE PVSC,* Washington, DC, USA, June 25th -30th, 2017.

[5] **R. Pandey**, A. Jain, and R. Chaujar, "Novel 4-terminal perovskite/SiC-based rear contact silicon tandem solar cell with 27.6% PCE," in *Photovoltaic Specialists Conference (PVSC), 2016 IEEE 43rd*, Portland, OR, USA, June 05th -10th, 2016, pp. 0812-0815.

[6] **R. Pandey**, A. Jain, A. Kumar, and Rishu Chaujar "Impact of Minority Carrier Lifetime and Temperature on SiC Based Rear Contact SiGe Solar Cell for Concentrator Photovoltaic (CPV) Applications," in *32rd European Photovoltaic Solar Energy Conference and Exhibition*, Munich, Germany, June 20th-24th, 2016, pp. 270-273.

[7] **R. Pandey** and R. Chaujar, "TCAD Analysis of Silicon-Germanium (SiGe) based Back-Contact Back-Junction (BC-BJ) solar cell as an alternative for silicon based cells," in *TechConnectWorld Innov. Conf. Expo,* Washington, DC, USA, June 14th -17th, 2015, pp. 199-202.

[8] **R. Pandey** and R. Chaujar, "Novel SiC encapsulated coaxial silicon nanowire solar cell for optimal photovoltaic performance," in *Photovoltaic Specialist Conference (PVSC), 2015 IEEE 42nd*, New Orleans, LA, USA, June 14th -19th, 2015, pp. 1-5.

[9] **R. Pandey** and R. Chaujar, "Rear contact solar cell with ZrO2 nano structured front surface for efficient light trapping and enhanced surface passivation," in *Photovoltaic Specialist Conference (PVSC), 2015 IEEE 42nd,* New Orleans, LA, USA, June 14th -19th, 2015, pp. 1-5.

[10] **R. Pandey** and R. Chaujar "TCAD Analysis of novel back-contact-back junction SiGe (BC-BJ SiGe) solar cell for improved optical and electrical characteristics," *1st International Conference On Microelectronics, Circuits And System*, July 11th -13th, Kolkata, India 2014. Vol. (1) pp. 127-129. ISBN: 8185824-46-0.

ARTICLES IN NATIONAL CONFERENCES (1)

[1] R. Pandey and R. Chaujar," SiC Encapsulation Based Coaxial Silicon Nanowire Solar Cell for Concentrated Photovoltaic Applications," *Second National Conference on Recent Developments in Electronics (NCRDE-2017)*, Department of Electronic Science, University of Delhi South Campus, New Delhi, India. February 17-18, 2017, pp. 84-87.

TABLE OF CONTENTS

APPENDIX

REPRINTS OF JOURNAL PUBLICATIONS

CHAPTER 1

INTRODUCTION

This chapter has been dedicated to the introduction of the thesis where overview, working, parameters, standard losses are reported. Chapter also includes research gaps and motivation followed by objectives and the chapter's outline.

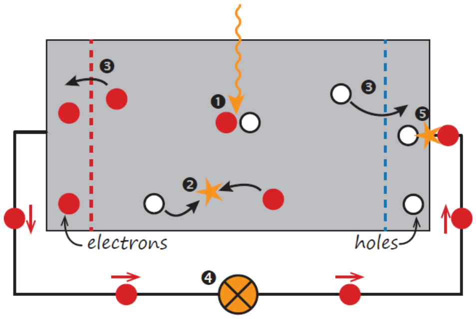

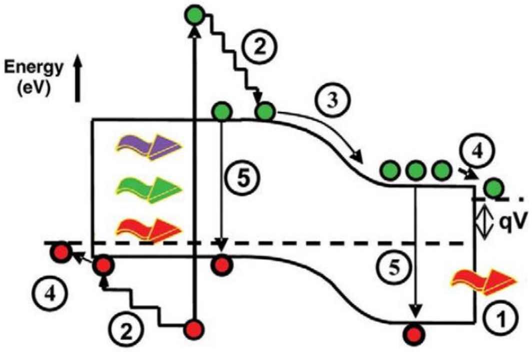

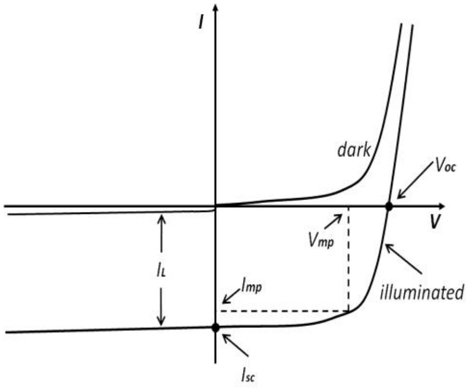

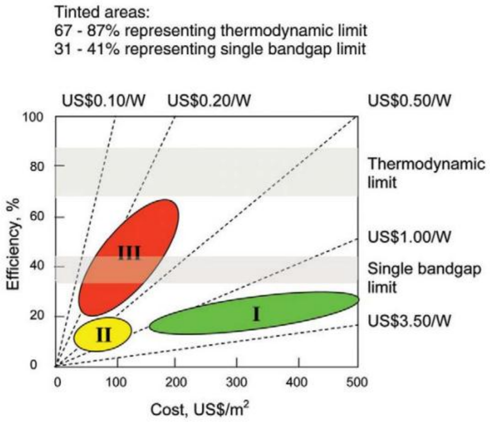

- *Overview along with strength and weakness of photovoltaic is reported.*
- *Record efficiencies of different photovoltaic technologies are provided.*
- *Research gaps and motivations are provided.*
- *Objectives and thesis outlines are provided.*

1.1: OVERVIEW OF PHOTOVOLTAIC

Earth receives almost nearly all forms of energy from the Sun. All organisms depend on solar energy to sustain their life. Solar energy is harnessed by humans to serve purposes other than biological purposes, i.e., fossil fuel and electricity generation. Also, sun's energy is utilized for producing biomass and wind energy. Industrial revolution became possible by the invention of electricity; almost all equipment and machinery needs electricity for their functioning. Thus, it is important to produce electricity at commercial scale with economical methods to make it feasible. Biomass, hydro, thermal, nuclear and wind energy are utilized to generate electricity at large scale; but some of them are not amicable for the environment, whereas others are not efficient in conversion. On the other hand, earth receives tremendous amount of solar radiation which is renewable and environmental friendly in nature. Thus, it can be used for direct production of electricity with the help of PV devices. These devices convert solar radiation directly into electricity by employing semiconductor devices, known as solar cell. The energy produced is directly proportional to the intensity of the radiation. Thus, solar cells can produce electricity in all weather conditions but with low conversion efficiency. The PV devices have following strength and weakness:

- ***Strength***
    - They are mature and highly reliable with longer lifetimes ~ 25 years
    - Requires low maintenance and automatically operated
    - Does not require fuel.
    - Environmentally amicable on comparison with conventional sources.
    - Unaffected by price hike of other energy sources

- ***Weakness***
  - Production of electricity is proportional to the intensity of radiation
  - Backup and storage is required for efficient utilization due to fluctuations
  - Expensive installation cost.
  - Some PV technologies contain hazardous material.
  - High energy need for silicon production.

Direct current (DC) electricity is produced by semiconductor with the help of chemical-electrical interaction with radiation. Mostly, Silicon is used as the base material in solar cells (ITRPV, 2016) . Following are the major technologies:

- Monocrystalline silicon cells.
- Poly-crystalline silicon cells.
- Thin film solar cells: They are fabricated by deposition of thin layer of semiconductor PV materials on a low-cost backing such as glass, stainless steel or plastic.
- Multiple junction cells: They consist of two or more stacked layers of different materials to use a wider spectrum of radiation.

With over 40 % compound annual growth rate (CAGR), from the last 15 years, Solar PV industry has become one of the fastest emerging ones in the world. Europe and Japan dominated solar cell production until 2006. However, China and Taiwan have shown rapid increase of the annual solar PV production since 2006; But, in 2014, Asian countries like India, Malaysia, Thailand, the Philippines or Vietnam have also produced PV solar cells in increased capacities. According to market forecasts, the installed PV power capacity of 235 GW at the end of 2015 could double until 2018 (Jäger-Waldau, 2016). **Figure 1.1** on page 4 shows annual production in different regions of the world.

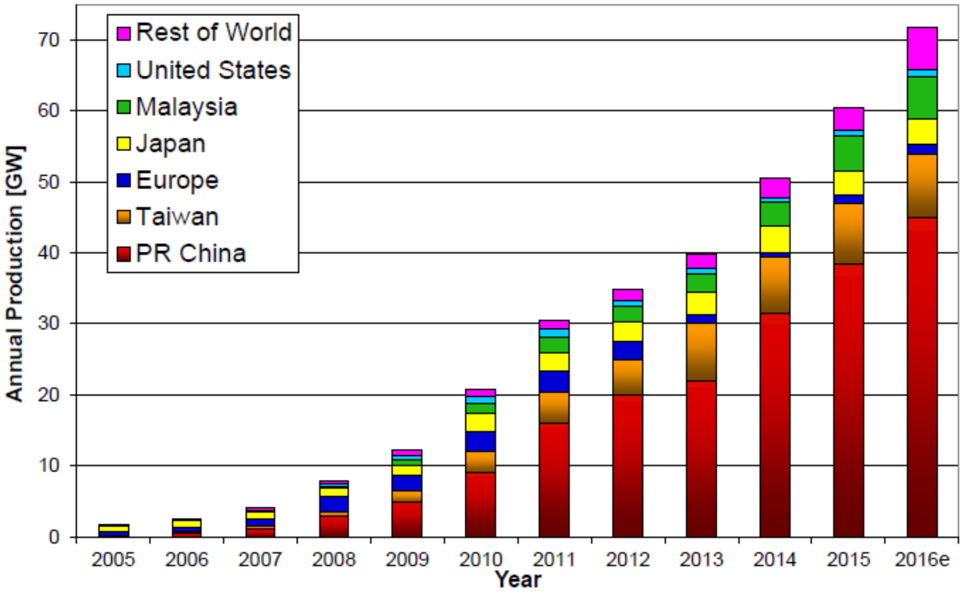

Figure 1.1: World PV cell module production from 2005 to 2016 (Jäger-Waldau, 2016).

1.2: WORKING OF SOLAR CELL

Solar cell works on the principle of PV effect, i.e. upon incidence by electromagnetic radiation, a potential difference is generated at the junction between two different materials. It is identical to photoelectric effect in which emission of electrons from material takes place after absorbing threshold frequency. This effect could be explained on the basis of quantized photons theory illustrated by Albert Einstein in 1905. The photon energy is represented by $E = h\nu$, where ν is the frequency of the light and h is Planck's constant. The PV effect can be split into three simple processes as shown in **Figure 1.2**(a-c) on page 5 (Jäger et al., 2014):

- Formation of light generated carriers in material forming junction due to the absorption of photons with appropriate energy.
- Consequent separation of the carriers generated at the junction.
- The light-generated charge carriers are collected at the terminals.

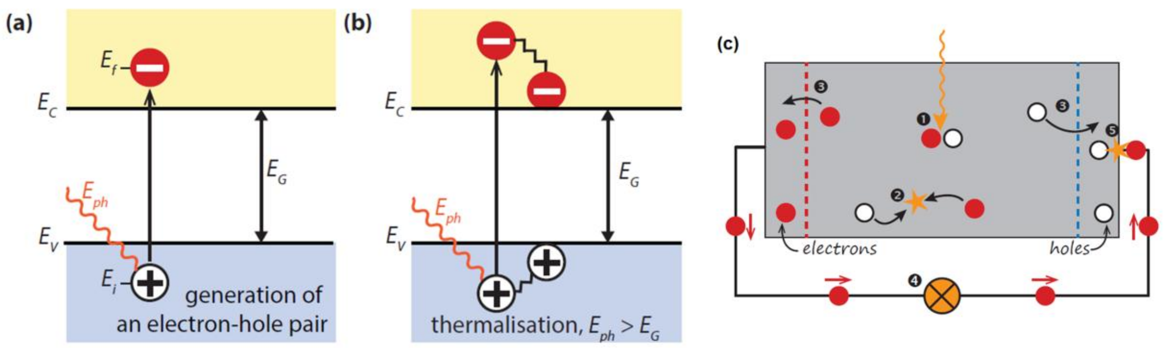

Figure 1.2: (a) Illustrations: photon absorption in semiconductor (E_{ph}= hν) (b) Thermalisation loss (E_{ph} > E_g) (c) A very simple solar cell model. ❶ Absorption leads to the generation ❷ normally, electrons and holes will combine ❸ the electrons and the holes separation by semipermeable membranes ❹ The separated electrons constitute electric current in the external circuit. ❺ Recombination with holes after flowing through the circuit (Jäger et al., 2014).

1.3: SOLAR CELL PARAMETERS

- *Quantum efficiency (QE)*= Number of carriers collected/ number of photons absorbed. Typical quantum efficiency of Si solar cell is reported in **Figure 1.3**(a) below along with carrier collection probability as a function of distance from p-n junction as reported in **Figure 1.3**(b).

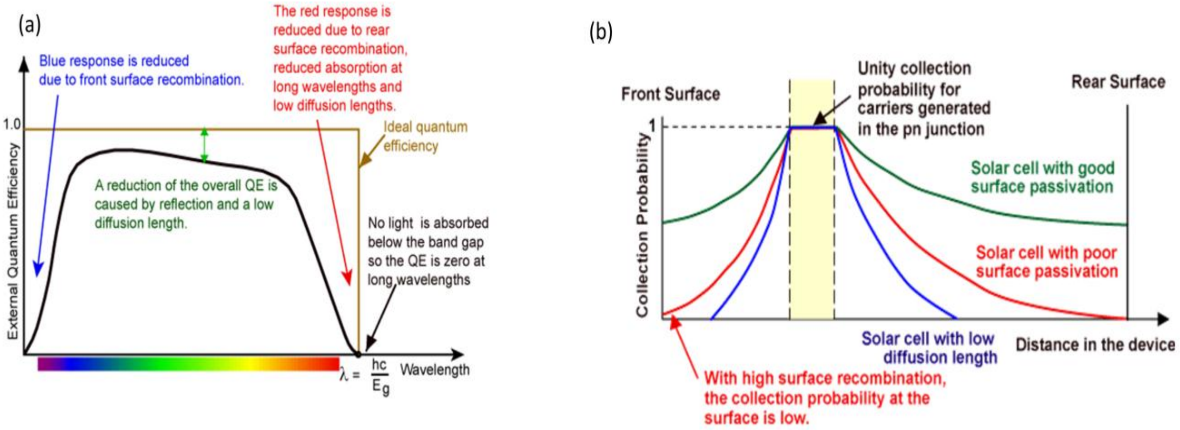

Figure 1.3: (a) The quantum efficiency of a silicon solar cell. Quantum efficiency is usually not measured much below 350 nm as the power from the air mass 1.5 (AM1.5) contained in such low wavelength is low, and (b) the carrier collection probability as a function distance from the p-n junction (Honsberg and Bowden, 2017).

- *Light generated current density, I_L (Honsberg and Bowden, 2017)*

$$I_L = q\int_0^W G(x).CP(x)dx = q\int\left[\int \alpha(\lambda)H_0 \exp(-\alpha(\lambda)x)d\lambda\right]CP(x)dx \qquad (1.01)$$

Where q is the electronic charge, W is the thickness of the device, α(λ) is the absorption coefficient, H_0 is the number of photons at each wavelength, G(x) is the generation rate, and CP (x) is the collection probability.

- *Illuminated current (I)-voltage (V) characteristics:* The I-V curve of a solar cell is the superposition of the dark (diode) and illuminated (solar cell) current (Würfel, 2008) as reported in **Figure 1.4** on page 7. Under illuminated condition, the I-V curves shift down into the fourth quadrant, and hence, power can be extracted. The illuminated I-V curve can be represented by the following equation.

$$I = I_0\left[\exp(\frac{qV}{nkT}) - 1\right] - I_L \qquad (1.02)$$

Where V is the applied voltage, n is diode ideality factor, k Boltzmann constant, T is operating temperature, and I_O is leakage current.

- Short circuit current density, $I_{SC} \approx qG(L_n + L_p)$ where L_n and L_p are the electron and hole diffusion lengths, given by $L = \sqrt{D\tau}$, D is diffusion coefficient and τ is carrier lifetimes.
- Open circuit voltage, $V_{OC} = \frac{nkT}{q}\ln(\frac{I_L}{I_0} + 1)$ (1.03)
- Fill factor, $FF = \frac{I_{mp}V_{mp}}{I_{SC}V_{OC}}$ (1.04)
- Maximum power, $P_{\max} = V_{OC}I_{SC}FF$ (1.05)

- Efficiency, $\eta = \frac{V_{OC}I_{SC}FF}{P_{in}}$ (1.06)

The input power for efficiency calculation is 0.1 W/cm^2*. Input power for 100x100 mm*^{2} *cell is 10 W and for 156 x 156 mm*^{2} *cell is 24.3 W.*

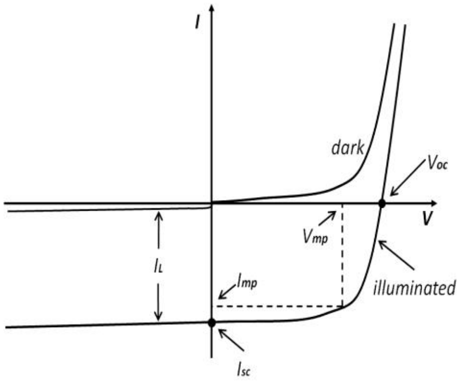

Figure 1.4: Dark and illuminated I-V curve of solar cell along with representation of some important parameters (Priambodo et al., 2013)

1.4: DIFFERENT GENERATIONS OF SOLAR CELL

Solar cells are mainly categorised in three generations as depicted in **Figure 1.5** on page 8. The first generation is relatively expensive to produce and have low efficiencies. The second generation is cheaper but produces lower efficiencies, i.e. cost per watt ($/Watt) is lower than first generation cells. The term third generation is used for highly efficient cells, and most of the technologies in this generation are not yet commercial. However a lot of research is going on in this area. The goal is to make third generation solar cells cheap to produce.

➢ *First generation solar cell:*

First generation PV cells dominate the current market which consists of Si wafers and generally shows conversion efficiency of the order of 15-20%. They reflect good performance and high stability; nonetheless, they require large energy for production and are rigid in nature.

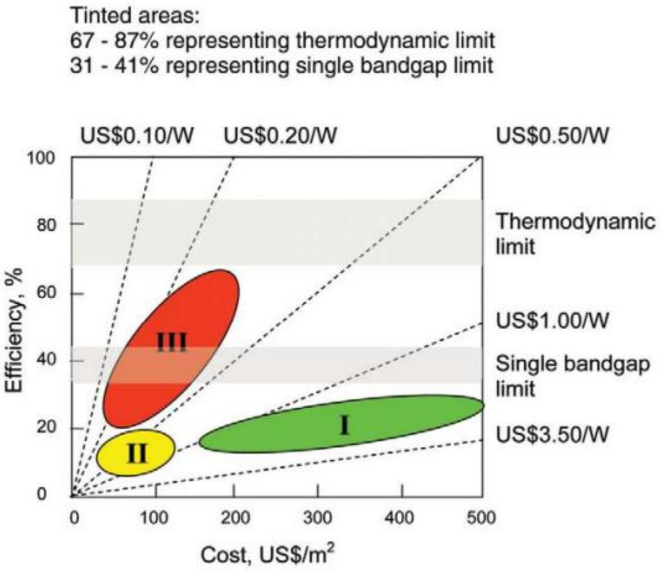

Figure 1.5: Cost efficiency scenarios for different solar cell generations (Conibeer, 2007)

- ***Second generation solar cell:***

The second generation PV cells show conversion efficiency of 10 - 15% and they contain copper indium gallium selenide (CIGS), amorphous silicon (a-Si) and cadmium telluride (CdTe) as active semiconductor material. They require less amount of material for fabrication and do not demand complex processing as needed in silicon wafers. These solar cells are flexible to some degree. However, still it requires a large amount of energy for the production of cells because their fabrication needs vacuum and high-temperature treatments.

- ***Third generation solar cell:***

Third generation PV cells consist of high-performance multi-junction PV cells which are expensive but hold a world record. They also include organic materials such as polymers or small molecules. Due to inflated production prices, most of these technologies are not commercialised yet. Perovskite solar cells also made an entry with potential to achieve efficiency > 20% on very small area. Polymer solar cells are quick and cheap as well simple to produce with the assistance of roll to roll technologies. However, their performance and stability are still inadequate as compared to other two generations. Recently, polymer solar cells have attracted a wide interest among the researchers to make it less expensive and more stable (Krebs et al., 2013). Moreover, different PV technologies are reported in **Figure 1.6** below along with their best research cell efficiencies till date (NREL, 2017).

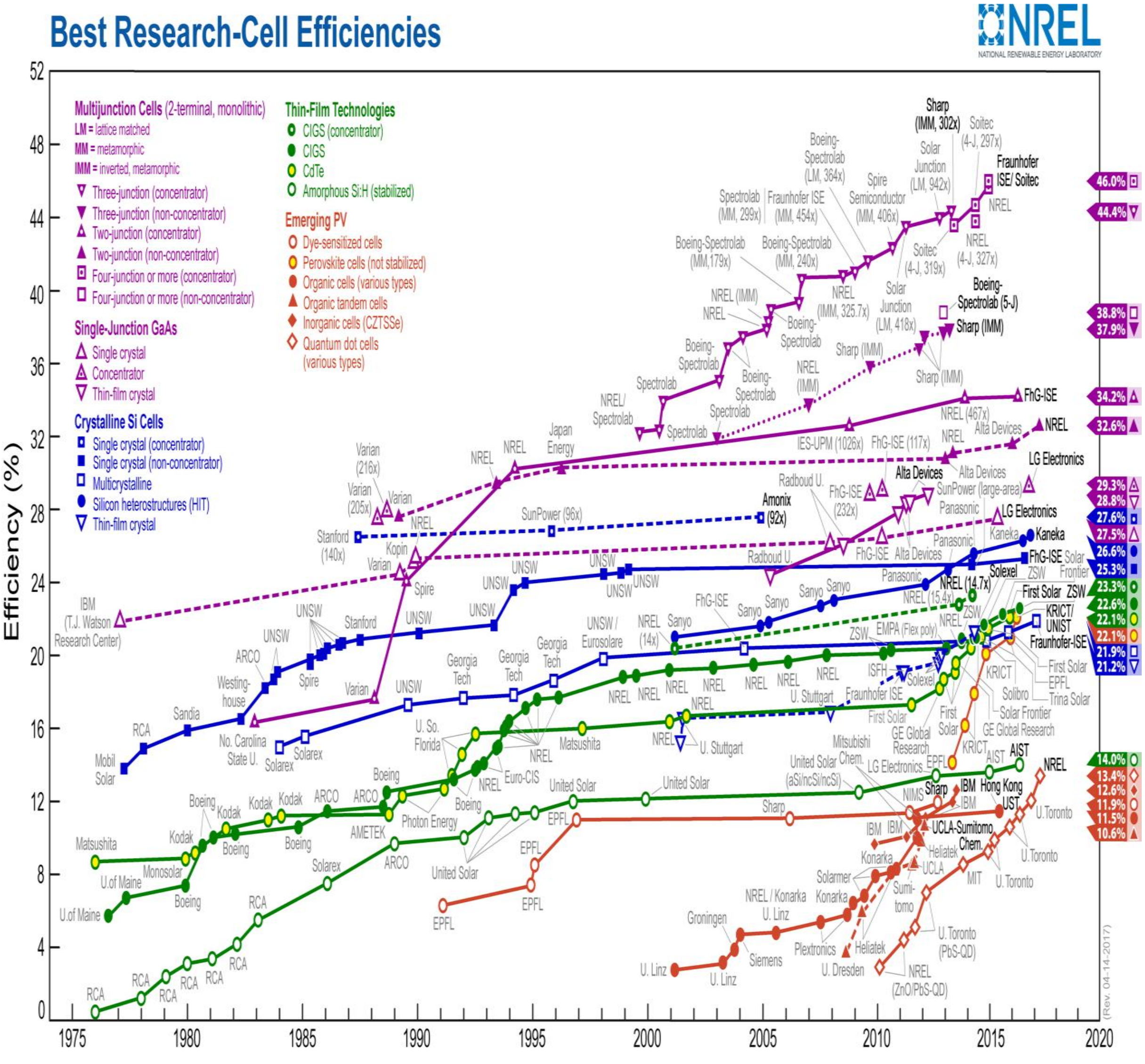

Figure 1.6: Best research cell efficiency of different type of PV technologies (NREL, 2017).

1.5: STANDARD LOSSES IN SOLAR CELL

Shockley and Queisser (SQ) predicted the efficiency limit of homojunction solar cells, which is 33% for a single junction solar cell with a bandgap of (1.4 eV) at a cell temperature of 25^{O}C illuminated by the AM 1.5G spectral irradiance (Shockley and Queisser, 1961, Rühle, 2016). There are some fundamental losses which laid the limit on the efficiency of solar cells, and the same has been reported in **Figure** 1.7 (a) below along with SQ limit and major losses as reported in **Figure 1.7** (b). The two most important loss mechanisms in single bandgap cells are the inability to absorb photons with energy less than the bandgap (loss 1) and thermalization of photon energies exceeding the bandgap (loss 2). These two mechanisms alone amount to the loss of about half of the incident solar energy in solar cell conversion to electricity as depicted in **Figure 1.7** (b). Junction (loss 3) and contact (loss 4) losses provide an insignificant reduction in overall conversion efficiencies. Another important loss process is process 5, where an electron from conduction band recombines with a hole in valence band.

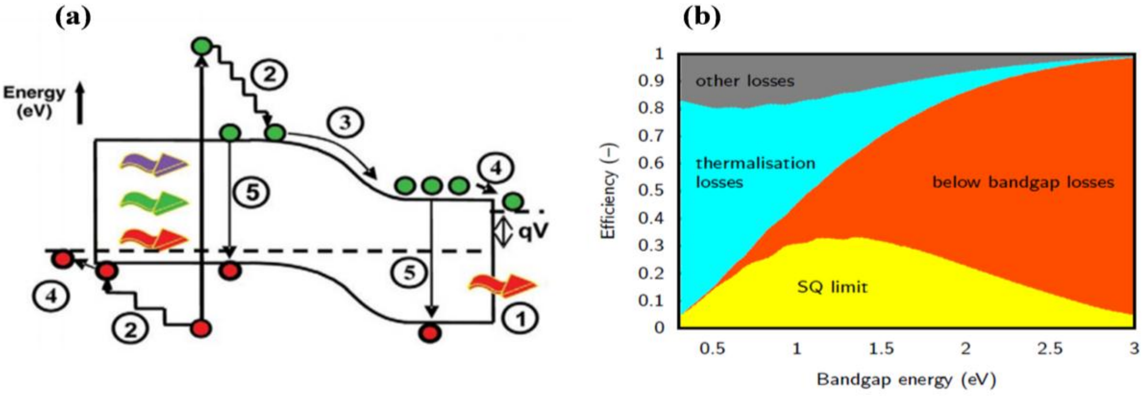

Figure 1.7: (a) Loss processes in a standard solar cell: (1) non-absorption of below bandgap photons; (2) lattice thermalization loss; (3) and (4) junction and contact voltage losses; (5) recombination loss (radiative recombination is unavoidable), and (b) The major loss mechanisms in the SQ limit. AM1.5 spectrum was used for the calculation (Conibeer, 2007, Jäger et al., 2014).

Recombination losses are further categorized as radiative, Auger, and Shockley Read Hall (SRH). In radiative recombination (unavoidable for direct bandgap semiconductor), an electron from the conduction band combines with a hole in the valence band and loses the energy of the order of the band gap. In SRH, the electron moves to an extra level in the forbidden gap releasing the energy either as a photon or multiple phonons followed by recombination with holes. SRH is prominent in less pure semiconductor solar cells, where carrier lifetime is low. Moreover, auger recombination involves three particles, where an electron recombines with the hole and gives its energy to a second electron pushing it high into the conduction band. The electron gradually gives off its energy thermally and relaxes back to the band edge. Auger recombination is most significant at elevated carrier concentrations produced by heavy doping or high level injection under concentrated sunlight. Schematic representation of radiative, SRH and Auger recombination is reported in **Figure 1.8**(a), **Figure 1.8**(b) and, **Figure 1.8**(c) below, respectively. Detailed equations and assumptions used in the thesis are reported in Appendix.

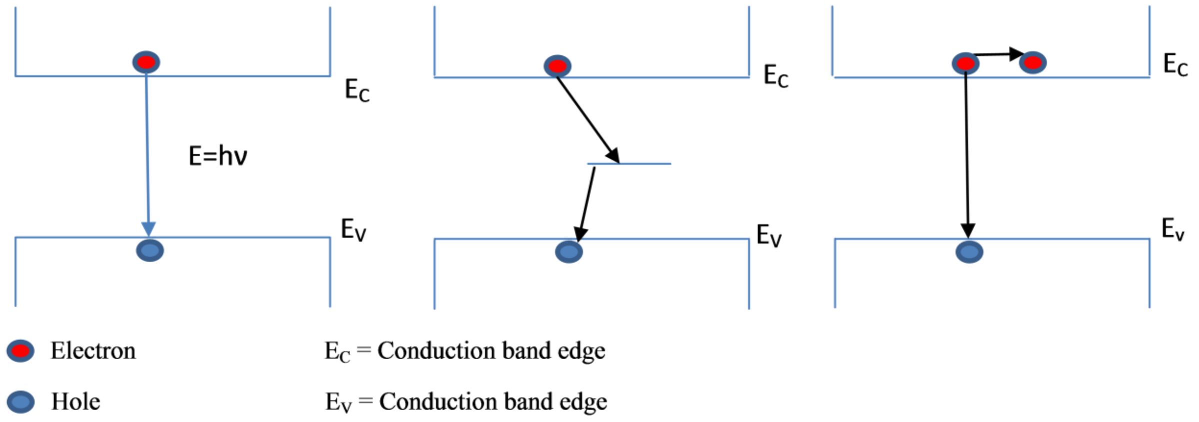

Figure 1.8: Schematic representations of (a) Radiative, (b) SRH, and, (c) Auger recombination

1.6: GAPS AND MOTIVATIONS

Silicon is the most extensively used material for solar cell production due to its abundance, reliability, nontoxicity, and mature fabrication techniques. Crystalline silicon solar cells have been dominating the PV market for several decades, with a current market share of 90% (ITRPV, 2016). The efficiency of the crystalline silicon (c-Si) solar cell has only marginally improved during the last 15 years; wafer size efficiency as high as 25.6% was obtained with a-Si/c-Si heterojunction technology (Masuko et al., 2014), and recently, record of 26.3% has been achieved on 180 cm^2 silicon heterojunction solar cell with interdigitated back contacts (Yoshikawa et al., 2017). These photoconversion efficiencies are close to the theoretical maximum efficiency of 29.4% (Richter et al., 2013). Despite this, for a PV system, fully competitive with the conventional energy source, cost-effective energy-efficient modules are required. There are different limitations of silicon PV technologies which need to be overcome simultaneously to achieve high efficiencies at reduced cost. Some of the limitations and possible solutions are as follows:

- **Absorption**: In silicon-based PV, more than 100 µm thick planar cell is required (Deinega et al., 2013), because absorption coefficient of silicon is small, to absorb the solar spectrum. Also, in order to increase the collection of the generated carriers, the dimension of the device should be comparable to the carrier diffusion length. The requirement of large volume and high-quality silicon significantly increases the module cost. Thinner silicon solar cells with high efficiency are fruitful for cost-effective energy solution (Jeong et al., 2012, van Lare et al., 2015, Jeong et al., 2013). Moreover, to maximize solar cell efficiency, it is necessary to optimize both, the device electrical characteristics and the optical absorption of thin devices (Garnett and Yang, 2010, Dwivedi et al., 2013).

Nanostructuring has been projected as an appropriate method to make thin silicon an efficient absorber. However, these cells are not efficient due to Auger and surface recombination due to large surface to volume ratio. However, few reported research work have adopted novel methods to minimize the surface recombination for nanostructured based ~300 µm thick devices, which resulted in 20% and 22% efficient cells (Ingenito et al., 2015, Savin et al., 2015). The PCEs of nanostructured Si solar cell remains below 22.2% for thick devices (Ingenito et al., 2015, Savin et al., 2015) and below 11% for thin devices (Jeong et al., 2013), except 13.7% and 15.7% reported by Jeong et al., (Jeong et al., 2013) and Branham et al., (Branham et al., 2015), respectively in the 10 µm thick devices. Therefore, to enhance the efficiency of the devices, novel front surface designs are needed to avoid absorption losses keeping the thickness and recombination losses minimal. Additionally, as silicon has absolutely low absorption coefficient particularly at higher wavelengths, high-frequency response can be improved by incorporating appropriate element which can modify its bandgap

- **Surface recombination**: In contrast with thick silicon solar cells, thin cells have large surface to volume ratio which enhances surface recombination and hence, decreases the overall performance of the devices (Jeong et al., 2013). In the 1980s, the advancement in the passivation of both surfaces leads to the power conversion efficiencies above 20%. Modern practices work towards minimizing the thickness of active materials keeping the efficiencies high; thus, passivation of both front and back surfaces are essential. In crystalline Si, recombination losses occur mainly through defect states due to indirect band gap (Chen et al., 2016) . These defects are situated within the volume and the surface. They are further divided into two categories: extrinsic (process related) and intrinsic (material related and unavoidable). High-quality silicon is free from inherent defects, and external defects can be minimized to a low level using suitable growth techniques like float-zone (FZ) (Niewelt et al., 2017). However, the situation becomes more complicated at the interface, due to non-saturated dangling bond. These defect levels promote the surface recombination losses, and they must be electronically passivated, and the passivation techniques must be stable against UV radiation. Further, most of the lower wavelength photons are absorbed near the illuminated surface, and hence, the non-metalized front surface needs to be well passivated to increase the lower wavelength response. There are two fundamental approaches to minimize the surface recombinations: (1) reduction of the density of surface states, and (2) reduction of surface concentrations of electrons or holes (Aberle, 2000). Deposition of dielectric films (Al_2O_3, SiO_2, SiN_x) is a common method to minimize the surface states. However, high-quality surface passivation cannot be maintained when exposed to UV radiation. Thus, to improve the UV stability of dielectric passivated devices, the formation of high-low junctions, i.e., p^+p and n^+n is required to reduce the concentration of charge carriers (electrons or holes) by creating a front surface field (FSF) or back surface field (BSF) (Aberle, 2000). However, presence of heavily doped front surface reduces the lower wavelength response due to the formation of the dead layer, and hence alternate UV stable passivation scheme is required which do not involve heavily doped front surface.

- **Architecture**: Conventional Si solar cells are based on front and back contact design which suffers from optoelectrical losses, and a possible solution is the introduction of rear contact architecture based cells, i.e. back-contact back-junction (BC-BJ) solar cells which have both; junction and the electrodes on the back side of the device. Since, the junction and contacts are on the back side, front surface can be designed for optimum optical performance (Diouf et al., 2009, Kerschaver and Beaucarne, 2006). It has the advantages, such as prevention of optical shading losses at the front side and higher absorption and current density. A BC-BJ solar cell with 17% efficiency working under 50 sun conditions has been reported (Schwartz and Lammert, 1975), which is intended for concentrator photovoltaic (CPV) applications. The back diffusion, contact opening, and contacts were implemented using photolithography; about six lithography steps are required to produce the cell. This fabrication technique is not compatible with the cost-effective production of the solar cell, and hence, a simplified processing of BC-BJ solar cell has been introduced (Sinton et al., 1988, Sinton and Swanson, 1990), which marks a major step toward the cost-effective BC-BJ solar cell and has been commercialized by Sunpower Corporation (Sinton et al., 1993). Today, Sunpower is the world leading manufacturer of BC-BJ solar cell. Sunpower Corp. showed in 2007 that it is possible to achieve an average cell efficiency of 22% in the mass production of BC-BJ silicon solar cell (De Ceuster et al., 2007). In the year 2014, independently confirmed conversion efficiency of 23.0% for *n*-type rear contact cell has also been reported by Feldmann et al., (Feldmann et al., 2014), at the end of the year, the interdigitated back contact solar cells developed which resulted in an independently confirmed designated-area efficiency of 24.4%. The cell is fabricated on a 230 µm thick 1.5 Ω cm *n*-type Czochralski (CZ) wafer (Franklin et al., 2016). Moreover, latest record efficiencies 25.6% (Masuko et al., 2014) and 26.3% (Yoshikawa et al., 2017) has also been obtained with the help of interdigitated back contacts heterojunction (IBC-HJ) technologies. These photoconversion efficiencies are close to the theoretical maximum efficiency of 29.4% (Richter et al., 2013). The BC-BJ solar cells are potential candidates to achieve higher efficiencies. Nevertheless, the conventional back contact solar cell has a large area which results in the higher production cost. Therefore, to make these cells further cost effective and energy efficient, the active material thickness should be reduced, i.e. energy efficient thin architecture based rear contact silicon cell is needed to reduce overall $/watt.

- **Thermalization losses**: Photoexcited carriers with excess energy, i.e. energy larger than bandgap leads to quick thermalization which is one of the major hindrances in single junction cells (Green, 2002). The thermalization losses can be minimized by splitting the solar spectrum into various ranges and each range will be utilized by well-matched bandgap cells. In available solar spectrum, small-bandgap single-junction solar cell device yields a low voltage. However, high energy photons can be absorbed by large-bandgap cell forming stacked tandem architecture and generate a high voltage as compared to the small-bandgap cell which results in efficient utilization of spectrum. Vos (Vos, 1980) predicted the efficiency limit for a tandem solar cell with optimized band gaps, and work shows it is possible to achieve 42% conversion efficiency with 2 cell stacked tandem solar cell. There are three main designs to consider when designing tandem solar cells:

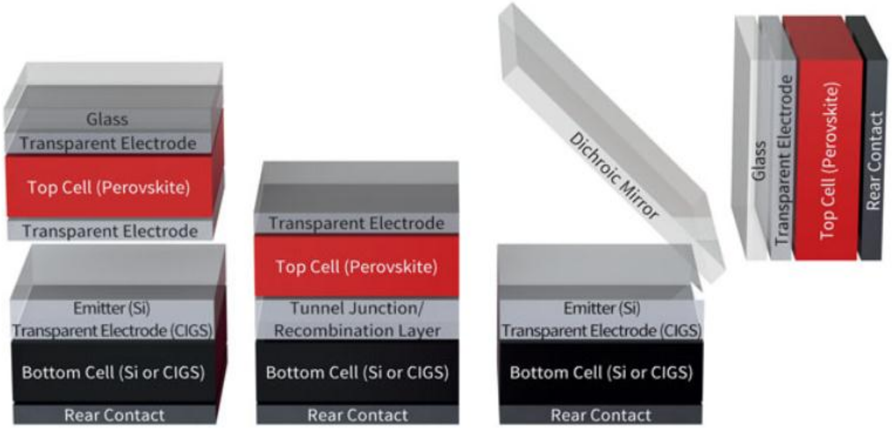

(a) **(b)** **(c)**

Figure 1.9: Different tandem architectures. (a) Mechanically stacked, (b) monolithically integrated, and (c) spectrally spilt (Bailie and McGehee, 2015).

Mechanically stacked, monolithically integrated, and spectrally split as reported in **Figure 1.9**(a), **Figure 1.9**(b), and **Figure 1.9**(c) on page 16, respectively. In mechanical stacking, top and bottom subcells are fabricated independently, and then assembled together in the module; thus gives greater process and design flexibilities. It does not require current matching between the top and bottom subcell. However, three transparent contacts are needed to maximize the optical coupling in underlying bottom subcell. These cells are also known as 4 terminal tandem solar cell, since, top and bottom subcell have separate contacts as reported in **Figure 1.9**(a). In monolithic integration, all layers are sequentially deposited on top of one another, tunnel junction is required for current matching between top and bottom subcells as depicted in **Figure 1.9**(b). These tandem devices are also known as 2 terminal tandem solar cells and require only one transparent contact. Meanwhile, perfect transparent electrode does not exist in reality and hence, removal of two electrodes will result in a higher efficiency potential. Also, cost of manufacturing becomes lower, as deposition of fewer layers is needed. Additionally, the combined advantages of monolithically integrated and mechanically stacked tandems can be acquired in spectral splitting. Nevertheless large-scale manufacturing process is uncertain. Only high concentration systems favor this architecture, which is attributed to high cost of dichroic mirrors and the physical geometry of a spectrally split system as shown in **Figure 1.9**(c). On comparing aforesaid architectures, mechanically stacked architecture is more economically and commercially viable, whose efficiency can further be enhanced by using rear contact architecture based bottom subcell, which requires only 2 transparent contacts and thus avoids the need of three transparent contacts.

1.7: OBJECTIVES

In this thesis, several schemes have been proposed to reduce the losses and achieve higher efficiencies. Moreover, the objective of the work done is briefly stated as follows:

- To minimize the losses associated with thin devices: low absorption and surface recombinations.
- To design UV stable surface passivation layer.
- To obtain higher efficiencies using heterojunction with intrinsic thin layer (HIT) based rear-contact solar cell architecture.
- To increase the optical absorption at higher wavelength by modulating the bandgap of Si.
- To minimize the thermalisation and spectrum losses using mechanically stacked perovskite/silicon and perovskite/SiGe tandem solar cell approaches.

1.8: THESIS OUTLINE

This thesis is organized into seven chapters to accommodate all the research objectives. Each chapter is organized to be fundamentally self-contained.

Chapter-2 Thesis starts with design and simulation of a novel front surface to resolve the issues associated with thin devices: low absorption and surface recombinations. Reported design balances the photonic and electronic effects together. ZrO_2 based texturing has been used along with SiC-based front

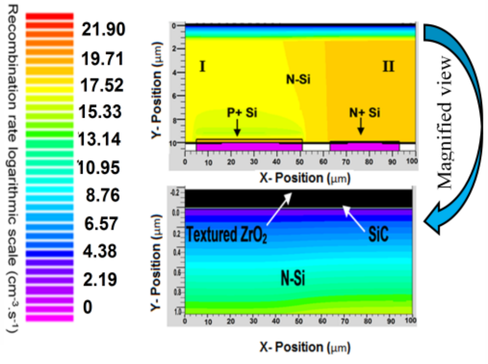

surface passivation for the suppression of interface recombination and improvement of V_{OC}. UV stability analysis has also been done.

Chapter-3 Since, tandem structure of perovskite-silicon solar cells is a promising method to achieve efficient solar energy conversion at low cost. Hence current chapter represents the application of SiC passivated rear contact silicon solar cell in mechanically stacked tandem configuration with perovskite solar cell. The focus of the work is to minimize the thermalisation losses. The impact of perovskite layer thickness, monomolecular, bimolecular, and trimolecular recombination have also been obtained on the performance of perovskite top subcell.

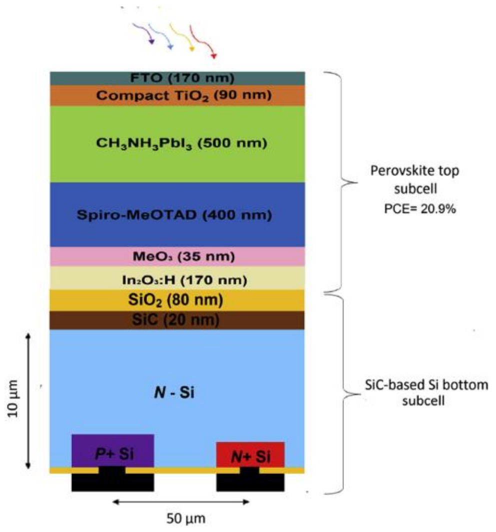

Chapter-4 The objective of this chapter is identical to the **Chapter 3** i.e., minimizing the thermalisation losses. However, the tandem architecture is slightly different, i.e., the conventional rear-contact solar cell has been replaced with SiC passivated IBC-SiHJ solar cell. Detailed analysis has been done for top and bottom subcells. Fundamental recombination dynamics are obtained. Hole transport layer (HTL) analysis has been done for perovskite top subcell, and passivation quality of SiC has been studied for IBC-SiHJ solar cells.

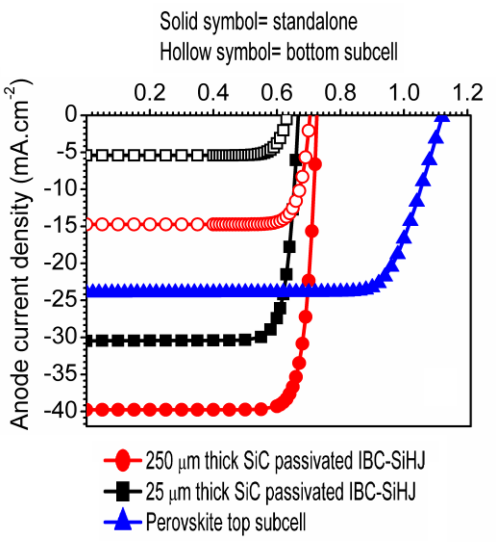

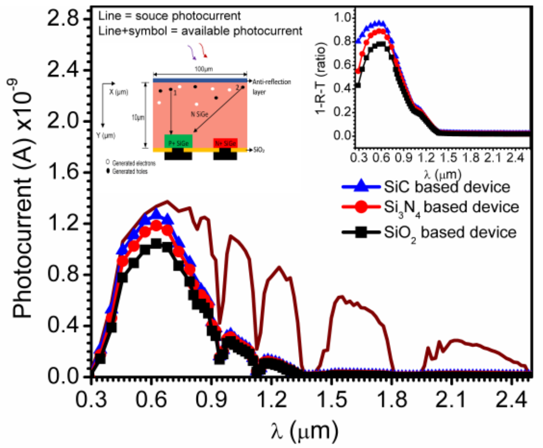

Chapter-5 Investigates the efficiency potential of SiGe material in SiC-passivated rear-contact solar cell architecture. SiGe is introduced to modulate the bandgap of Si in order to increase the optical absorption at higher wavelengths. Analysis of intrinsic and n-type wafer based SiGe solar cell has been done. Surface passivation analysis and comparison has been done with convention SiO_2 and Si_3N_4 based passivation techniques. Recombination rates, carrier distribution, and photon absorption rates within the device, are obtained.

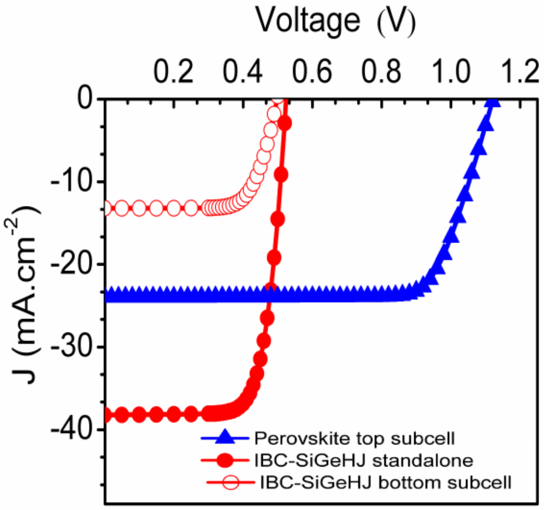

Chapter-6 Examines the efficiency potential of SiC passivated IBC-SiGeHJ solar cell in standalone as well as tandem applications. Optimization of intrinsic hydrogenated amorphous SiGe (i-a-SiGe: H) thickness, the width of *n*-type hydrogenated amorphous SiGe (n-a-SiGe: H) region, width of *p*-type hydrogenated amorphous SiGe (p-a- SiGe: H) region and pitch gap along with composition fraction has been done. It is followed by the design and analysis of mechanically stacked 4 terminal perovskite/IBC-SiGeHJ solar cells.

Finally, the research work of the thesis is briefly summarized in **Chapter -7** and future works are outlined.

1.9: REFERENCES

ABERLE, A. G. 2000. Surface passivation of crystalline silicon solar cells: a review. *Progress in Photovoltaics: Research and Applications,* 8**,** 473-487.

BAILIE, C. D. & MCGEHEE, M. D. 2015. High-efficiency tandem perovskite solar cells. *MRS Bulletin,* 40**,** 681-686.

BRANHAM, M. S., HSU, W.-C., YERCI, S., LOOMIS, J., BORISKINA, S. V., HOARD, B. R., HAN, S. E. & CHEN, G. 2015. 15.7% Efficient 10-μm-Thick Crystalline Silicon Solar Cells Using Periodic Nanostructures. *Advanced materials (Deerfield Beach, Fla.)***,** 2182-2188.

CHEN, W., DEPAUW, V., HADDAD, F., MAURICE, J.-L. & ROCA I CABARROCAS, P. 2016. Influence of anodic bonding on the surface passivation quality of crystalline silicon. *Solar Energy Materials and Solar Cells,* 157**,** 154-160.

CONIBEER, G. 2007. Third-generation photovoltaics. *Materials Today,* 10**,** 42-50.

DE CEUSTER, D., COUSINS, P., ROSE, D., VICENTE, D., TIPONES, P. & MULLIGAN, W. Low Cost, high volume production of> 22% efficiency silicon solar cells. Proceedings of the 22nd European Photovoltaic Solar Energy Conference, 2007. 816-819.

DEINEGA, A., EYDERMAN, S. & JOHN, S. 2013. Coupled optical and electrical modeling of solar cell based on conical pore silicon photonic crystals. *Journal of Applied Physics,* 113**,** 224501-224501.

DIOUF, D., KLEIDER, J. P., DESRUES, T. & RIBEYRON, P. J. 2009. Study of interdigitated back contact silicon heterojunctions solar cells by two-dimensional numerical simulations. *Materials Science and Engineering: B,* 159–160**,** 291-294.

DWIVEDI, N., KUMAR, S., BISHT, A., PATEL, K. & SUDHAKAR, S. 2013. Simulation approach for optimization of device structure and thickness of HIT solar cells to achieve ∼27% efficiency. *Solar Energy,* 88**,** 31-41.

FELDMANN, F., BIVOUR, M., REICHEL, C., HERMLE, M. & GLUNZ, S. W. 2014. Passivated rear contacts for high-efficiency n-type Si solar cells providing high interface passivation quality and excellent transport characteristics. *Solar Energy Materials and Solar Cells,* 120, Part A**,** 270-274.

FRANKLIN, E., FONG, K., MCINTOSH, K., FELL, A., BLAKERS, A., KHO, T., WALTER, D., WANG, D., ZIN, N., STOCKS, M., WANG, E.-C., GRANT, N., WAN, Y., YANG, Y., ZHANG, X., FENG, Z. & VERLINDEN, P. J. 2016. Design, fabrication and characterisation of a 24.4% efficient interdigitated back contact solar cell. *Progress in Photovoltaics: Research and Applications,* 24**,** 411-427.

GARNETT, E. & YANG, P. 2010. Light Trapping in Silicon Nanowire Solar Cells. *Nano Letters,* 10**,** 1082-1087.

GREEN, M. A. 2002. Third generation photovoltaics: solar cells for 2020 and beyond. *Physica E: Low-dimensional Systems and Nanostructures,* 14**,** 65-70.

HONSBERG, C. & BOWDEN, A. S. 2017. *Quantum Efficiency and Collection Probability* [Online]. Available: http://www.pveducation.org/.

INGENITO, A., ISABELLA, O. & ZEMAN, M. 2015. Nano-cones on micro-pyramids: modulated surface textures for maximal spectral response and high-efficiency solar cells. *Progress in Photovoltaics: Research and Applications,* 20**,** 6-6.

ITRPV, I. S. E. V. P., 2016. 2016. ITRPV.

JÄGER-WALDAU, A. 2016. PV Status Report 2016. Italy: European Commission, Joint Research Centre, Directorate C, Energy Efficiency and Renewables Unit Via Enrico Fermi 2749, TP 450 I — 21027, Ispra (VA), Italy.

JÄGER, K., ISABELLA, O., SMETS, A. H. M., SWAAIJ, R. A. C. M. M. V. & ZEMAN, M. 2014. *Solar Energy Fundamentals, Technology, and Systems,* Delft, Netherlands, Delft University of Technology.

JEONG, S., GARNETT, E. C., WANG, S., YU, Z., FAN, S., BRONGERSMA, M. L., MCGEHEE, M. D. & CUI, Y. 2012. Hybrid Silicon Nanocone–Polymer Solar Cells. *Nano Letters,* 12**,** 2971-2976.

JEONG, S., MCGEHEE, M. D. & CUI, Y. 2013. All-back-contact ultra-thin silicon nanocone solar cells with 13.7% power conversion efficiency. *Nature communications,* 4**,** 2950-2950.

KERSCHAVER, E. V. & BEAUCARNE, G. 2006. Back-contact solar cells: a review. *Progress in Photovoltaics: Research and Applications,* 14**,** 107-123.

KREBS, F. C., HÖSEL, M., CORAZZA, M., ROTH, B., MADSEN, M. V., GEVORGYAN, S. A., SØNDERGAARD, R. R., KARG, D. & JØRGENSEN, M. 2013. Freely available OPV—The fast way to progress. *Energy Technology,* 1**,** 378-381.

MASUKO, K., SHIGEMATSU, M., HASHIGUCHI, T., FUJISHIMA, D., KAI, M., YOSHIMURA, N., YAMAGUCHI, T., ICHIHASHI, Y., MISHIMA, T., MATSUBARA, N., YAMANISHI, T., TAKAHAMA, T., TAGUCHI, M., MARUYAMA, E. & OKAMOTO, S. 2014. Achievement of More Than 25% Conversion Efficiency With Crystalline Silicon Heterojunction Solar Cell. *IEEE Journal of Photovoltaics,* 4**,** 1433-1435.

NIEWELT, T., SELINGER, M., GRANT, N. E., KWAPIL, W., MURPHY, J. D. & SCHUBERT, M. 2017. Light-induced activation and deactivation of bulk defects in boron-doped float-zone silicon. *Journal of Applied Physics,* 121**,** 185702.

NREL 2017. Research Cell Efficiency Records. USA: National Renewable Energy Laboratory - National Center for Photovoltaics.

PRIAMBODO, P. S., SUKOCO, D., PURNOMO, W., SUDIBYO, H. & HARTANTO, D. 2013. Electric Energy Management and Engineering in Solar Cell System. *In:* MORALES-ACEVEDO, A. (ed.) *Solar Cells - Research and Application Perspectives.* Rijeka: InTech.

RICHTER, A., HERMLE, M. & GLUNZ, S. W. 2013. Reassessment of the Limiting Efficiency for Crystalline Silicon Solar Cells. *IEEE Journal of Photovoltaics,* 3**,** 1184-1191.

RÜHLE, S. 2016. Tabulated values of the Shockley–Queisser limit for single junction solar cells. *Solar Energy,* 130**,** 139-147.

SAVIN, H., REPO, P., VON GASTROW, G., ORTEGA, P., CALLE, E., GARÍN, M. & ALCUBILLA, R. 2015. Black silicon solar cells with interdigitated back-contacts achieve 22.1% efficiency. *Nature nanotechnology,* 10**,** 1-6.

SCHWARTZ, R. J. & LAMMERT, M. D. Silicon solar cells for high concentration applications. 1975 International Electron Devices Meeting, 1975 1975. 350-352.

SHOCKLEY, W. & QUEISSER, H. J. 1961. Detailed balance limit of efficiency of p-n junction solar cells. *Journal of applied physics,* 32**,** 510-519.

SINTON, R., VERLINDEN, P., KANE, D. & SWANSON, R. Development efforts in silicon backside-contact solar cells. Proceedings of the 8th European Photovoltaic Solar Energy Conference, 1988. 1472-6.

SINTON, R. A. & SWANSON, R. M. 1990. Simplified backside-contact solar cells. *IEEE Transactions on Electron Devices,* 37**,** 348-352.

SINTON, R. A., VERLINDEN, P. J., CRANE, R. A., SWANSON, R. M., TILFORD, C., PERKINS, J. & GARRISON, K. Large-area 21% efficient Si solar cells. Conference Record of the Twenty Third IEEE Photovoltaic Specialists Conference - 1993 (Cat. No.93CH3283-9), 10-14 May 1993 1993. 157-161.

VAN LARE, C., LENZMANN, F., VERSCHUUREN, M. A. & POLMAN, A. 2015. Dielectric Scattering Patterns for Efficient Light Trapping in Thin-Film Solar Cells. *Nano Letters,* 15**,** 4846-4852.

VOS, A. D. 1980. Detailed balance limit of the efficiency of tandem solar cells. *Journal of Physics D: Applied Physics,* 13**,** 839.

WÜRFEL 2008. *Physics of Solar Cells: From Principles to New Concepts*, Wiley Online Library.

YOSHIKAWA, K., KAWASAKI, H., YOSHIDA, W., IRIE, T., KONISHI, K., NAKANO, K., UTO, T., ADACHI, D., KANEMATSU, M., UZU, H. & YAMAMOTO, K. 2017. Silicon heterojunction solar cell with interdigitated back contacts for a photoconversion efficiency over 26%. 2**,** 17.

CHAPTER 2

REAR CONTACT SILICON SOLAR CELL WITH NOVEL FRONT SURFACE DESIGN

In this chapter, a novel front surface design has been proposed and simulated to resolve the issues associated with thin devices: low absorption and surface recombinations. ZrO_2 based texturing has been used along with SiC-based front surface passivation for the suppression of interface recombination and less absorption. Design reported in this chapter balances the photonic and electronic effects together.

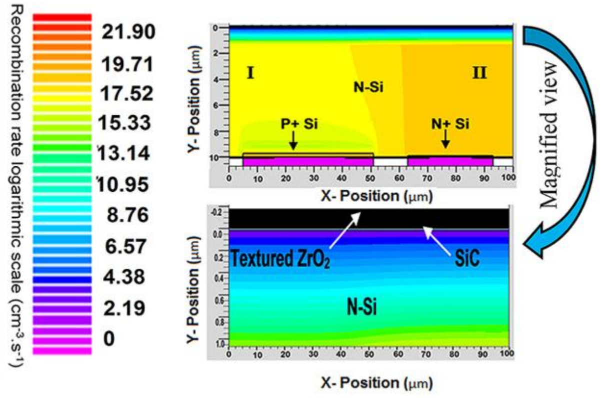

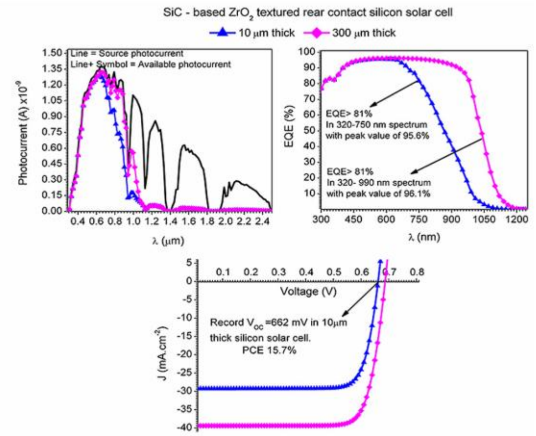

- *The innovative front surface design has been proposed for silicon solar cell.*
- *ZrO_2 based texturing has been used along with SiC-based front surface passivation.*
- *V_{OC} of 662 mV has been achieved in the sub-10-μm small device.*
- *The PCE of 15.7% has been made in the sub-10-μm small device.*
- *Moreover, a 21.6% efficient 300 μm thick device has also been designed.*

2.1: INTRODUCTION

Solar cell technology is a function of lifetime, efficiency, and cost of the device. In silicon PV technology, the thickness of typically more than 100 µm is required to absorb the solar spectrum since the absorption coefficient of silicon is small at higher wavelengths (Deinega et al., 2013). This requirement results in higher cost and hence, large-scale implementation is not economically feasible. Also, the dimension of the device should be comparable to the carrier diffusion length in order to increase the collection of the light generated carriers. Thinner silicon solar cell devices with high efficiencies are successful candidates for cost-effective energy solution (van Lare et al., 2015). Further, to maximize solar cell efficiency, it is necessary to optimize both, the device electrical characteristics and the optical absorption (Dwivedi et al., 2013, Garnett and Yang, 2010). Nanostructuring has been projected as an appropriate method to make thin silicon an efficient absorber. However, these cells are not efficient due to Auger and surface recombination as the surface to volume ratio of the cells is large. However, methods to minimize the surface recombination for nanostructured based ~300 µm thick devices have been presented which results in 20% and 22% efficient cells (Ingenito et al., 2015, Savin et al., 2015). The PCE of nanostructured Si solar cell remains below 22.2% for thick devices (Ingenito et al., 2015, Savin et al., 2015) and below 11% for thin devices (Jeong et al., 2013), except 13.7% and 15.7% reported by Jeong et al., and Branham et al., (Jeong et al., 2013, Branham et al., 2015) for the 10 µm thick devices.

The work reported in this chapter shows efficient photon absorption in the sub-10-µm-thick device. ZrO_2 based texturing has been used along with SiC-based front surface passivation. ZrO_2 is a material of high technology due to its outstanding electrical and mechanical properties and high dielectric constant. Dielectric properties ($\varepsilon \sim 25$) and large band gap (Eg ~ 6eV) suggested its potential to replace conventional SiO_2 in the advanced semiconductor device and optical applications (Garcia et al., 2006). Also, it has an excellent thermal stability; and the real index (n) values of ZrO_2 are close to the n values of nitride, which is usually used as anti-reflective coating (ARC) for silicon solar cell (Philipp, 1973, Bååk, 1982). Moreover, previous work shows that presence of thin SiC layer minimizes the reflectivity (Allen et al., 2011), and embedding 3C-SiC nanoparticles significantly reduces the photo reflectivity in UV/ visible spectrum region (Parida et al., 2013). The SiC is a wide energy band gap (E_g=2.2 eV) indirect semiconductor with high saturation velocity, high thermal conductivity and large breakdown field; hence, it is an ideal choice for high temperature, high power, high voltage electron devices. Its high melting point, chemical inertness, high wear resistance, and extreme hardness, make it possible to fabricate sensors and actuators capable of performing in harsh environments (Chung et al., 2010). Moreover, experimental work shows the feasibility of SiC formation on silicon; the SiC film formation has been done for Si solar cell passivation. The film was deposited on silicon (100) and glass substrates by radio frequency (RF) magnetron co-sputtering system (Joung et al., 2012). The rear contact silicon solar cell has been selected because it is a promising high-efficiency solar cell having both, junction and the electrodes at the back side of the device, as discussed in **Section 1.6:** of **Chapter 1** (Kerschaver and Beaucarne, 2006).

2.2: DEVICE STRUCTURE AND SIMULATION

In this section, calibrated software program is written in Silvaco ATLAS device simulator as per the already published results for 10 µm thick rear contact solar cell with AR coating (Jeong et al., 2013). The dimensions and the doping density of the planar device were identical to the referenced cell and named as Device A as shown in **Figure 2.1** on page 27.

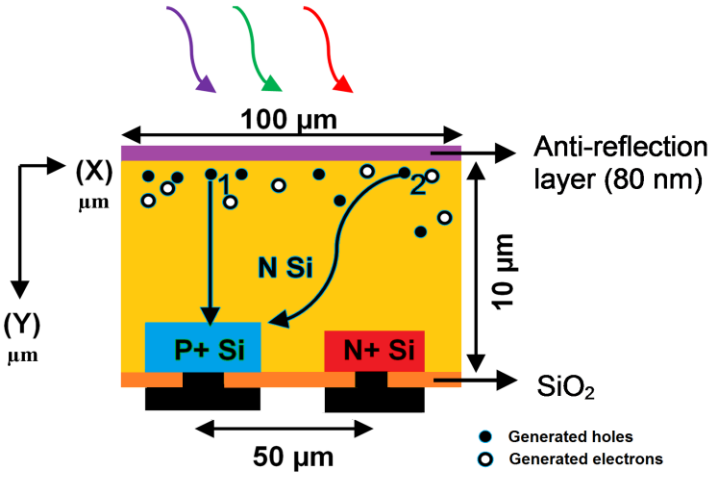

Figure 2.1: The simulated device structure, i.e. 10µm thick rear-contact silicon solar cell with the anti-reflective (AR) coating (Pandey and Chaujar, 2016b).

The device geometry in the simulation has 50-µm-wide pitch, 46µm-wide *p+*, and 30-µm-wide *n+* region. The substrate was *n-type*, with a doping density of $3\text{x}10^{15}$ cm^{-3}. The *p+* region was doped with boron with a doping density of $4\text{x}10^{20}$ cm^{-3} and a depth of 300 nm, whereas, *n+* region was doped with phosphorus with a doping density of $1\text{x}10^{20}$ cm^{-3} and a depth of 100 nm. Moreover, shunt (R_{SH}) and series (R_S) resistance of 5.69 $\text{k}\Omega.\text{cm}^2$ and $0.33\Omega.\text{cm}^2$, respectively, has also been incorporated using spice circuit simulations. Further, in the presence of heavy doping, i.e. $>10^{18}$ cm^{-3}, experimental work has shown that the *pn* product in silicon turns out to be doping dependent (Slotboom, 1977). As the doping level rises, a decrease in the bandgap occurs, where the valence band is raised by approximately the same amount as the conduction band is lowered. The discussed structure has heavily doped *p+* and *n+* regions, and so band gap narrowing effects are enabled. These effects can be described by an analytic expression relating the variation in the bandgap, ΔEg to the doping concentration, N (Slotboom and de Graaff, 1976). Furthermore, the solar cells are the carrier recombination affected devices. Therefore, Auger and SRH recombination models are selected during the simulation. Phonon transitions occur in the presence of a trap or defect within the forbidden gap of the semiconductor (Shockley and Read, 1952, Hall, 1952). The fundamental of the SRH model are the assumptions of one trap level in the forbidden band and drift-diffusion assumption for the transport of electrons and holes, and the assumption that the dynamics of the trapped carrier is quasi-stationary (Goudon et al., 2007). Moreover, capturing or emission of mobile charge carriers through three particle transition processes leads to Auger recombination, the underlying physics of such processes is still unclear, and normally qualitative understanding is sufficient as suggested by Selberherr et al. (Selberherr, 1984). The auger coefficients, C_p=9.9x10^{-32} $cm^6.s^{-1}$, and C_n=2.8x10^{-31} $cm^6.s^{-1}$ have been used for *n*-type and *p*-type silicon, respectively, at a 300K temperature (Dziewior and Schmid, 1977). The concentration-dependent mobility and field dependent mobility models have also been selected during simulation. The consistent set of models and parameters for the simulation of Si solar cell have been used as suggested in the already published article (Altermatt, 2011). Detailed equations of the models are provided in Appendix of the thesis. To obtain the current density (J)- voltage (V) curve under illumination, the standard AM1.5 solar spectrum has been used, throughout the thesis. Also, as the contact interface between metal and semiconductor is highly doped both for the $p+$ and $n+$ region, i.e. ~ 10^{20} cm^{-3}, therefore, the Ohmic contacts are used in this work. This has been done to avoid Schottky barriers, and thus unnecessarily higher computation time. Result reveals, the software program, is well calibrated within the acceptable range, which will be shown later in this Chapter.

2.3: RESULTS

The result section is divided into three parts; 1st part describes the analysis and comparison of SiC passivated device for UV stability, 2nd part deals with the designing of a

ZrO_2 textured and thin SiC-based ZrO_2 textured 10µm x 10µm thick *n-type* silicon wafer for optimal spectrum response and the 3rd part illustrates the designed ZrO_2 pattern with and without SiC to the Device A, by removing ARC layer. Additionally, ZrO_2 textured 10µm thick rear contact silicon solar cell is called as Device B, and ZrO_2 textured device with SiC layer at the ZrO_2/*n*-Si interface is termed as Device C.

2.3.1: Analysis of SiC based rear contact silicon solar cell for UV stability

As discussed in **Section 1.6:** of **Chapter 1**, there are two fundamental approaches to minimize the surface recombinations: (1) reduction of the density of surface states, and (2) reduction of surface concentrations of electrons or holes. Deposition of dielectric films (Al_2O_3, SiO_2, SiN_x) is a common method to minimize the surface states. However, high-quality surface passivation cannot be maintained when exposed to UV radiation. Thus, to improve the UV stability of dielectric passivated devices, the formation of high-low junctions, i.e. p^+p and n^+n is required to reduce the concentration of charge carriers (electrons or holes) by creating a surface field (Aberle, 2000).

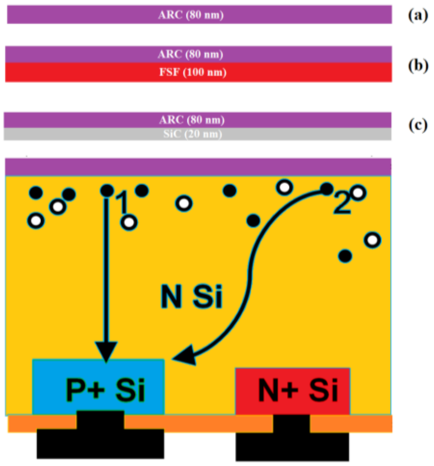

Figure 2.2: The simulated device structure with different passivation scheme (a) represents ARC, (b) represents ARC with front surface field (FSF), and (c) represents SiC with ARC, respectively.

In this section of the Chapter, simulation analysis has been done for SiC passivated rear contact silicon solar cell and performance is compared with conventional dielectric passivation and high-low junction based passivation techniques as shown in **Figure 2.2** on page 29. Initial analysis has been done at the interface. A small region at the surface is exaggerated, and photogeneration and recombination rate contour has been obtained, to understand and compare the different passivation techniques. **Figure 2.3** (a-c) below and **Figure 2.4** (a-d) on page 31 show the photon absorption and recombination rate, respectively at the interface. Results indicate that presence of SiC increases the optical coupling and hence higher photon absorption rate compared to other passivation techniques as shown in **Figure 2.3** (c). Moreover, photon absorption rate in FSF/ARC based device is slightly lower compared to ARC based device as shown in **Figure 2.3** (a) and **Figure 2.3** (b), due to the heavily doped front surface. Furthermore, surface passivation analysis at different surface recombination velocity (SRV) is reported in **Figure 2.4** (a-d). The number of surface states is incorporated in the simulations with the help of SRV parameters in the interface statement of ATLAS device simulator (see Appendix). Contour plot reported in **Figure 2.4** (a-d) has been obtained at SRV, 1×10^{4} cm.s^{-1}. The device consisting of only ARC shows higher recombination rate compared to FSF/ARC and SiC/ARC based devices, and hence more vulnerable to surface states.

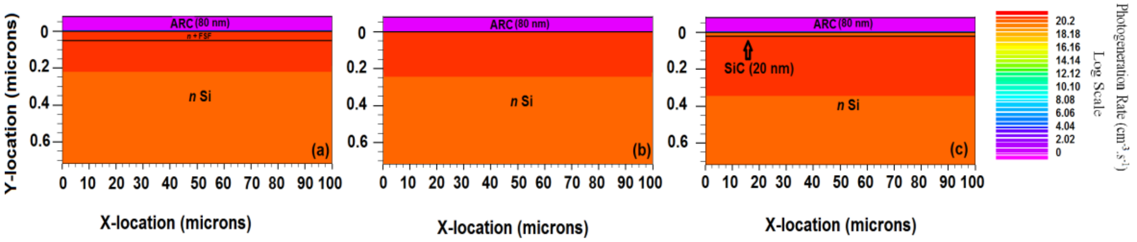

Figure 2.3: Contour representation of photogeneration rate near the interface (a) FSF/ARC based device, (b) ARC based device, and (c) SiC/ARC based device. Results are obtained under illumination on and zero applied voltage (Pandey and Chaujar, 2017).

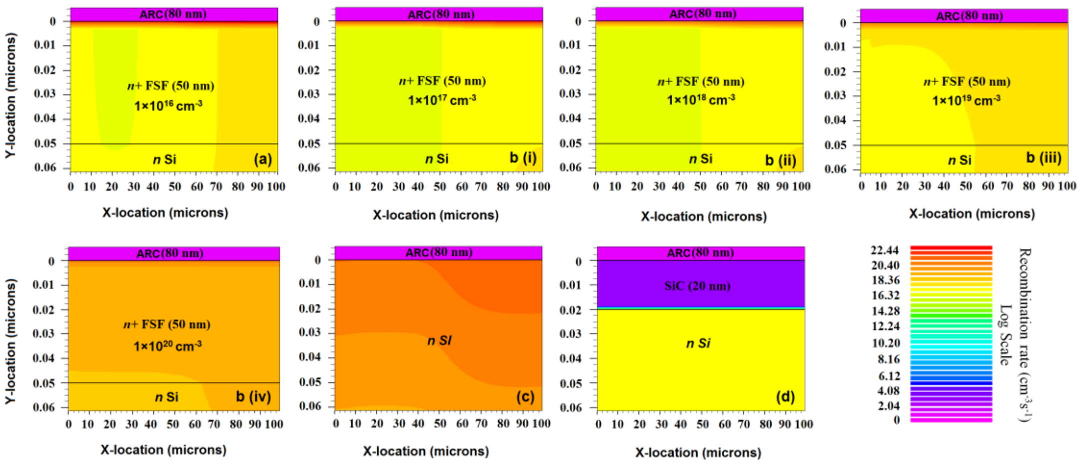

Figure 2.4: Contour representation of recombination rate near the interface (a) ARC based device, (b) FSF/ARC based device, different concentration of n+ region, i.e. FSF region is further represented in b (i-iv), and (c) SiC/ARC based device. Results are obtained under illumination and zero applied voltage (Pandey and Chaujar, 2017).

Further, spectrum response, i.e., external quantum efficiency (EQE) of the device has been obtained and reported in **Figure 2.5** (a-c) on page 32. EQE of ARC, FSF/ARC, and SiC/ARC based devices are indicated in **Figure 2.5** (a), **Figure 2.5** (b) and, **Figure 2.5** (c), respectively. Moreover, EQE of the FSF/ARC based device is obtained for different donor concentration of the front surface. To get the impact of FSF doping concentration, optical performance is achieved by varying the doping concentration (1×10^{16} cm^{-3} to 1×10^{20} cm^{-3}) and reported in **Figure 2.5** (b) (i-v). As discussed earlier, ARC coated device is vulnerable, and the same has been supported by spectrum response also. **Figure 2.5** (a) shows increasing the surface states in terms of SRV results in significant degradation in ARC based device. At a wavelength equivalent to 300 nm, the EQE of ARC-based device went to 30% from 60% as SRV changes from 1 cm/s to 10^4 cm/s. Generally, the lower wavelength response of the device is reduced due to front surface recombination, whereas midway and higher wavelength response are reduced due to lower diffusion length and transmitted photons, respectively. Nevertheless, back surface recombination also degrades higher wavelength response.

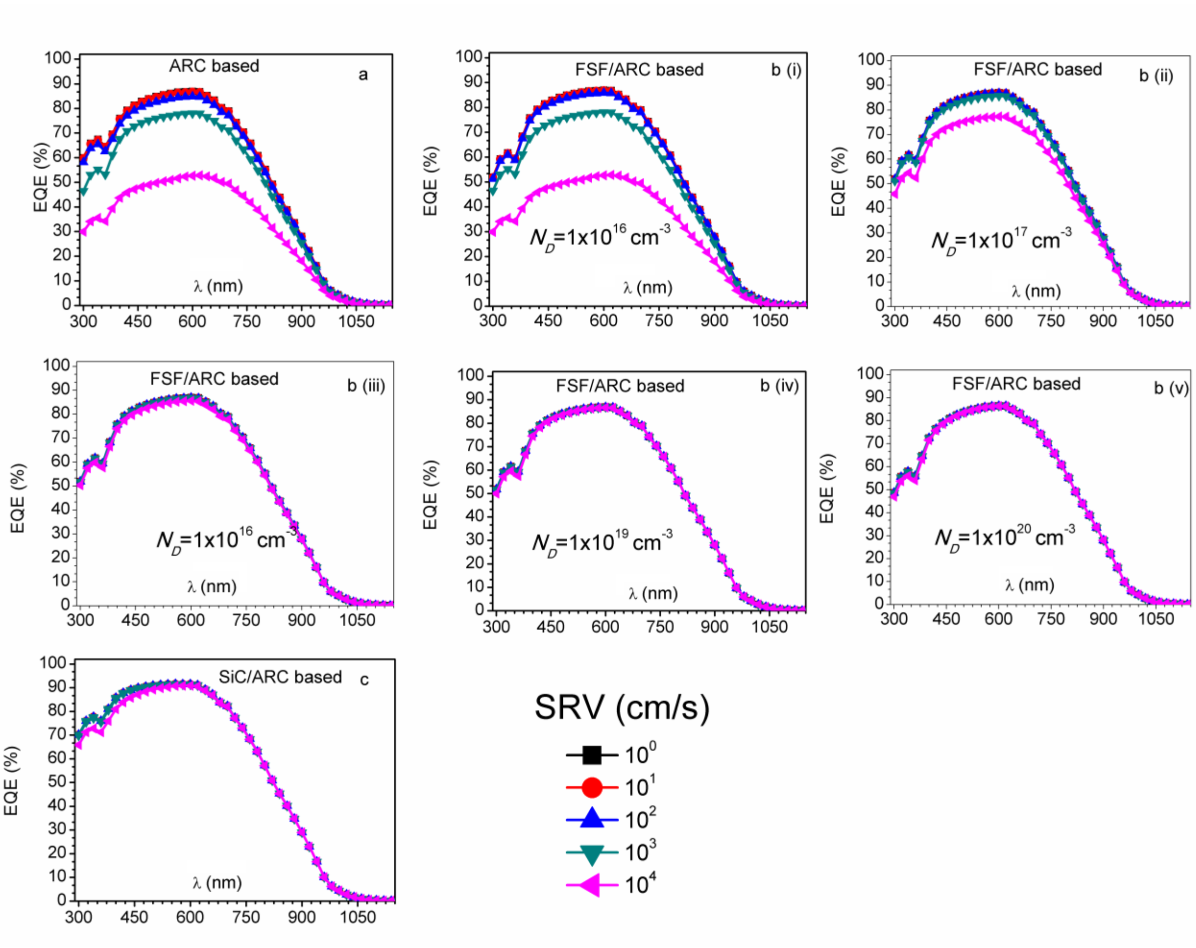

Figure 2.5: Impact of SRV on the optical performance i.e. EQE of (a) ARC based device, (b) FSF/ARC based device, different concentration of n+ region, i.e. FSF region is further represented in b (i-iv), and (C) SiC/ARC based device (Pandey and Chaujar, 2017).

Result shows, ARC coated device is unable to withstand under UV radiation and higher surface states conditions. The fundamentals of minimising the surface recombination losses are a reduction of surface states and reduction of carrier (electrons and holes) concentration at the interface. EQEs of FSF/ARC and SiC/ARC based devices shows fewer degradations, however selecting the appropriate doping concentration is an important parameter for FSF/ARC based device. Results show FSF doping concentration of 1×10^{16} cm^{-3} will not provide any spectral improvement as shown in **Figure 2.5**b (i) above, i.e., FSF is not capable of reducing the minority carrier (holes) concentration at the interface, whereas increasing the concentration will result in improvements in both lower as well as midway spectrum responses shown in **Figure 2.5**b (ii-v) on page 32. Increasing the concentration of FSF region results in the higher surface field and hence efficiently prevents the holes at the interface; and thus reduces the concentration and surface recombination, eventually, giving rise to stable spectrum response. FSF/ARC based device with appropriate doping provides UV stability as shown in **Figure 2.5**b (ii-v), however, the performance, i.e., EQE at the lower wavelength is decreased, which is attributed to the formation of dead layer at the front surface; most of the high-energy photons are absorbed near the front surface, and they get recombine as shown in **Figure 2.4**b (iii-iv) on page 31. Moreover, another passivation scheme, i.e., using SiC along with ARC coating is a possible solution to prevent the formation of the dead layer along with UV stability. **Figure 2.5** (c) shows the presence of SiC at the front surface provides significant UV stability without degrading the lower wavelength response, due to higher optical coupling and lower surface recombination as shown in **Figure 2.3** (c) on page 30 and **Figure 2.4** (d) on page 31, respectively. The SiC-based device shows EQEs >90% in the spectrum range of 480-620 nm wavelength spectrum along with good UV stability under high SRV condition. The presence of SiC prevents the movement of holes toward the interface by creating the field without the need of heavily doped front surface (Pandey and Chaujar, 2016a, Pandey and Chaujar, 2016c). However, the thickness of SiC is a critical parameter. Increasing the thickness more than 20 nm results in parasitic absorption in SiC and reduces optical coupling in underlying Si (Pandey and Chaujar, 2016c). Concluding the results obtained at the interface and spectrum response supports that SiC provides better surface stability along with good surface passivation quality.

2.3.2: Designing of SiC and textured ZrO_2 based silicon wafer

In this section, a 10µm x10µm thick *n*-type Si wafer without ARC, with ARC, textured ZrO_2 and textured ZrO_2 having SiC (20nm) layer at ZrO_2/ *n*-Si interface has been designed and simulated to obtain the spectrum response. The entire front surface of the wafer is covered with repeated ZrO_2 facet structures and optimized height, 175 nm, and width, 250 nm is used for texturing. The smaller and larger width size than 250 nm will show lower optical coupling and lower conversion efficiency, as suggested by Yoshinaga et al., (Yoshinaga et al.). In the real cell, the nanopatterns can be fabricated via inexpensive and scalable imprinting technique. The complex refractive index of various materials has been obtained from SOPRA database (Atlas, 2017) and reported in **Figure 2.6** (a-b) below. As wavelength changes from 300 to 1200 nm, the refractive index, n of ZrO_2 changes from 2.45-2.17 as shown in **Figure 2.6** (a). The n values of ZrO_2 are close to the n values of nitride, which is usually used as AR coating for silicon solar cell (Philipp, 1973, Bååk, 1982).

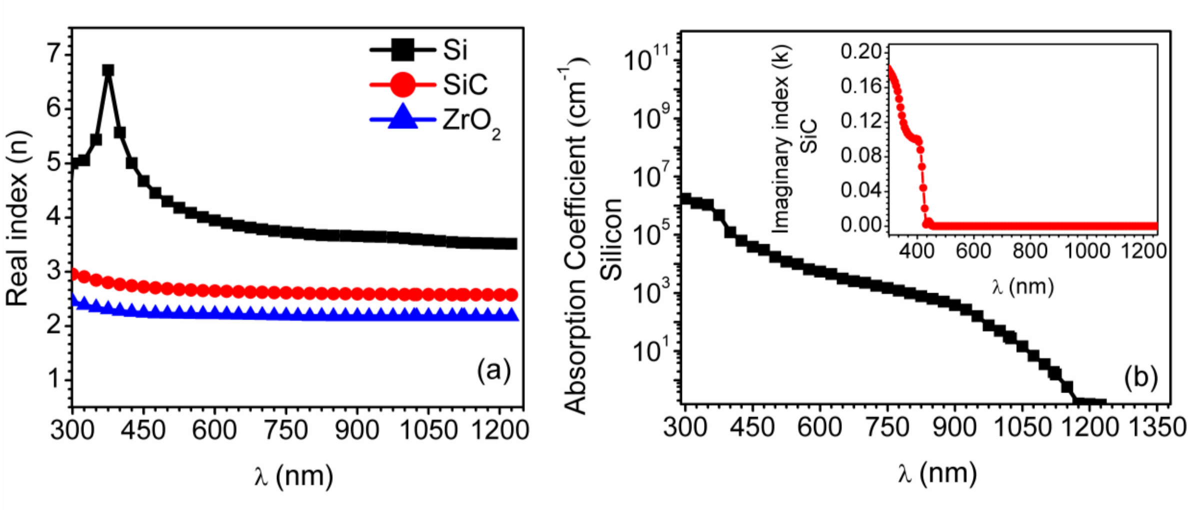

Figure 2.6: Wavelength-dependent optical properties of the materials used in simulation: (a) Real index, and (b) Absorption coefficient of silicon. Inset shows the extinction coefficient of SiC (Pandey and Chaujar, 2016b).

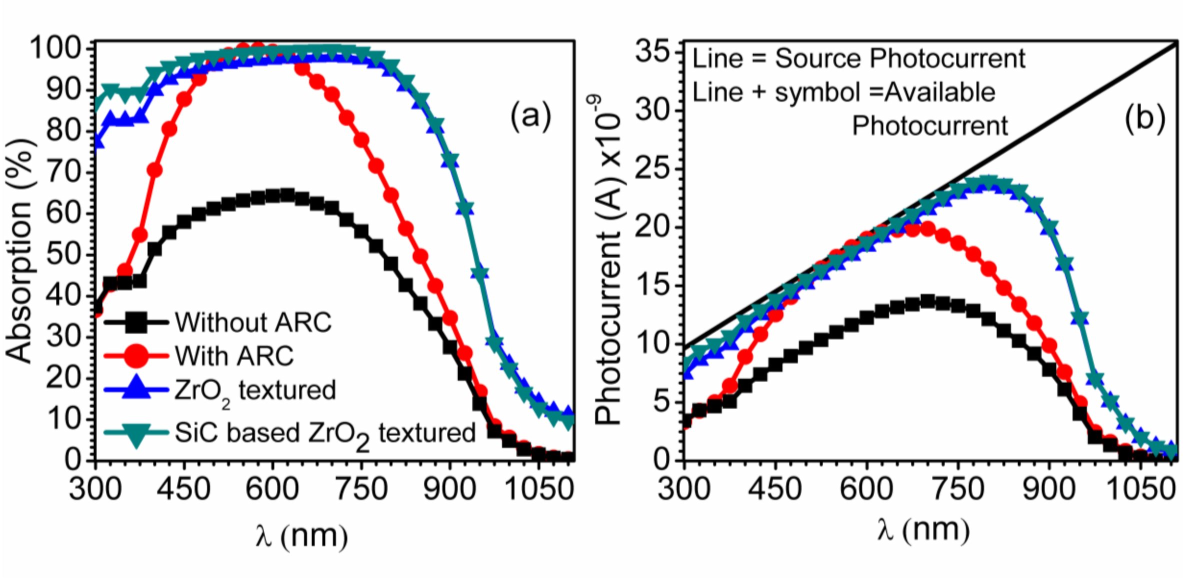

Figure 2.7: Spectral response of (10 µm × 10 µm) thick Si wafer with different types of front surfaces (a) Absorption, and (b) Source and available photocurrent. Si_3N_4 was used with the thickness of 80nm for AR layer (Pandey and Chaujar, 2016b).

Further, the spectral response of Si wafers is obtained and presented in **Figure 2.7** (a-b) above. Result shows, planar silicon wafer without coating is highly reflective, i.e. absorption is small in the range of 300-1000 nm wavelength spectrum. Also, ARC layer based Si wafer shows > 96% absorption in the spectrum range of 500-625 nm wavelength. Lower and higher wavelength response is however not remarkable. The ZrO_2 textured wafer exhibits improved optical behavior compared to ARC based wafer due to anti-reflection and light scattering as shown in **Figure 2.7** (a). This concludes that higher absorption is achieved in the ZrO_2 textured wafer, which further results in higher available photocurrent shown in **Figure 2.7** (b). Results also indicate that throughout the spectrum range (300-1000 nm), ZrO_2 textured wafer shows enhanced absorption as compared to ARC coated wafer. At a wavelength equivalent to 300 nm, 77% absorption is achieved in the silicon wafer. Also, photon absorption > 82% has been achieved in the spectrum range of 325-850 nm wavelengths with a maximum of 98.2%. This shows spectrum response has been improved due to ZrO_2 textured front surface. Further, optical behavior of SiC-based ZrO_2 textured wafer has also been obtained. The efficiency of a solar cell is directly related to the amount of light entering the cell. An antireflection coating is used to reduce the reflection of the useful light while not absorbing it. It has been shown that the photon coupling in the underlying substrate is higher for 20 nm thick SiC-based device (Pandey and Chaujar, 2016c); Also, increasing the SiC thickness results in parasitic absorbance in SiC, and lower photon coupling in the underlying substrate. Since absorbance directly depends on the thickness of the material, it results in lower short-circuit current density and power conversion efficiency (Pandey and Chaujar, 2016c). Therefore, the thickness of SiC used in the simulation is only 20 nm whose absorption is negligible hence; optical coupling in underlying silicon is higher. Also, the optical properties, i.e. refractive index and extinction coefficient (k) required for an AR coating depends on the refractive index of the underlying substrate, encapsulated cover, and the operating wavelengths. The material having low absorption of useful light is needed, to reduce the absorption of useful light in ARC. Therefore, low k values are required, k value of 0.01 corresponds to less than 1% absorption, since absorption coefficient, $\alpha=4\pi k/\lambda$. **Figure 2.6** (a) and **Figure 2.6** (b) on page 34 shows that SiC has n values between 2.9 and 2.5 in the spectrum range of 300 -1200 nm and k of less than 0.01 for the wavelengths greater than 430 nm. Also, according to the patented work of Allen et al. (Allen et al., 2011), SiC film having n between 2.7 and 2.3 and k of less than 0.01 at a wavelength of 630 nm is a good candidate for anti-reflective coating for solar cells. This confirms that presence of SiC will not degrade the optical behaviors of ZrO_2 based wafer. Moreover, a contour plot of photons absorption rate in the wafers is also shown in **Figure 2.8** (a-d) on page 37. Higher photons coupling has been observed in both ZrO_2 based and SiC-based ZrO_2 textured wafer, which results in higher absorption rate as well as higher absorption depth compared to ARC based device, as shown in **Figure 2.8**c&d and **Figure 2.8**g&h below.

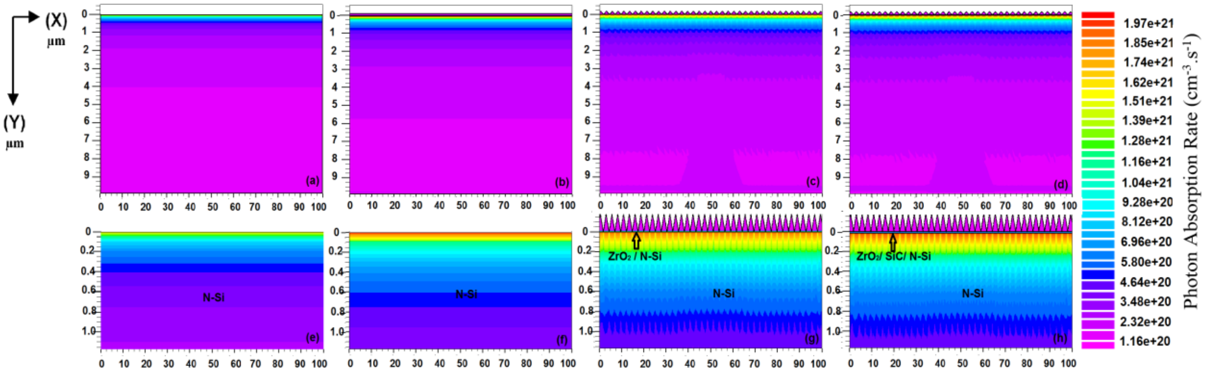

Figure 2.8: Photon absorption rate ($cm^{-3}.s^{-1}$) in the silicon wafer with the different type of front surface: (a) Without ARC, (b) with ARC, (c) ZrO_2 textured, and (d) SiC-based ZrO_2 textured. Fig. 2.8 (e-h) shows the magnified view near the interface for uncoated, ARC based, ZrO_2 textured, and SiC based ZrO_2 textured wafers, respectively (Pandey and Chaujar, 2016b).

2.3.3: SiC based rear contact solar cells with ZrO_2 textured front surface

Spectral results as discussed in previous sections show that the optical performance of Si wafer is significantly improved in the case of ZrO_2 textured front surface. Therefore, ARC coating of Device A is replaced with ZrO_2 textured front surface with rest of the device parameters being the same. In this section, the performance of two ZrO_2 textured solar cells has been obtained, one with 20nm thick SiC layer at the interface (Device C) and another without SiC layer at the interface (Device B) and obtained results are compared with planar rear contact device as shown in **Figure 2.1** on page 27. Device B and Device C have been simulated with the help of calibrated program written for Device A. Results of the previous section shows, an amalgamation of thin SiC layer does not degrade the optical behavior of the wafer. Hence, both the devices, i.e. Device B and Device C shows significant improvement in device photovoltaic parameters: in terms of J_{SC}, V_{OC}, FF, and PCE compared to Device A.

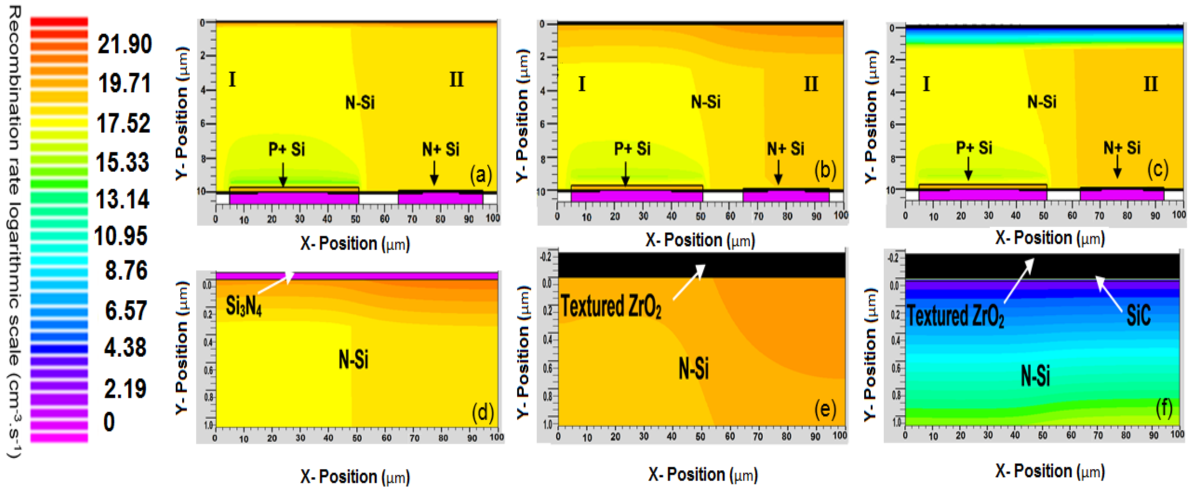

Figure 2.9: Contour representation of Recombination rate ($cm^{-3}.s^{-1}$): (a) Si_3N_4 coated device, (b) ZrO_2 textured device, and (c) SiC-based ZrO_2 textured device. Fig. 2.07 (d-f) shows the magnified view of Si_3N_4/N-Si, ZrO_2/N-Si, and ZrO_2/SiC/N-Si interfaces, respectively (Pandey and Chaujar, 2016b).

Further, **Figure 2.9**(a-f) above shows the contour plot of recombination rate in Device A, Device B, and Device C, respectively. The device architecture is such that the holes generated at point 1, in **Figure 2.1** on page 27 need to travel shorter to arrive at $n — p+$ interface, whereas the holes generated at point 2, needs to travel a greater lateral distance. Under short-circuit condition, a space charge region is formed around the junction having an associated electric field that collects the generated electron-hole pairs, and the collection is complete near $p+$ region. However, outside the $p+$ region, the substrate is neutral, and the collection will be by diffusion of electrons and holes towards the field region where they will be collected and separated. The electrons and holes generated in a region greater than the diffusion length will never reach the junction, and the recombination process will balance out. This results in higher recombination rate in region II compared to the region I, shown in **Figure 2.9**(a-f). Further, **Figure 2.9**c&f indicates that significant improvement in surface recombination has been obtained in Device C compared to Device A and Device B. The analysis reveals that recombination rate near the SiC/*n*-Si interface is small compared to the bulk region (*n*-Si) of the device. The presence of SiC creates an electric field at the interface and is directed from SiC to Si, rendering it energetically unfavorable for holes transport to SiC/*n*-Si interface, resulting in a low concentration of holes at the passivating interface (Pandey and Chaujar, 2016a, Pandey and Chaujar, 2016c). Thus, sinking the holes concentration at the interface will produce higher concentration difference between electrons and holes, and results in lower surface recombination rate (Aberle, 2000). Results conclude that presence of ZrO_2 textured front surface increases the optical response and presence of SiC at the ZrO_2/*n*-Si interface minimizes the surface recombination. Therefore, the dual advantage has been obtained with the help of SiC and ZrO_2.

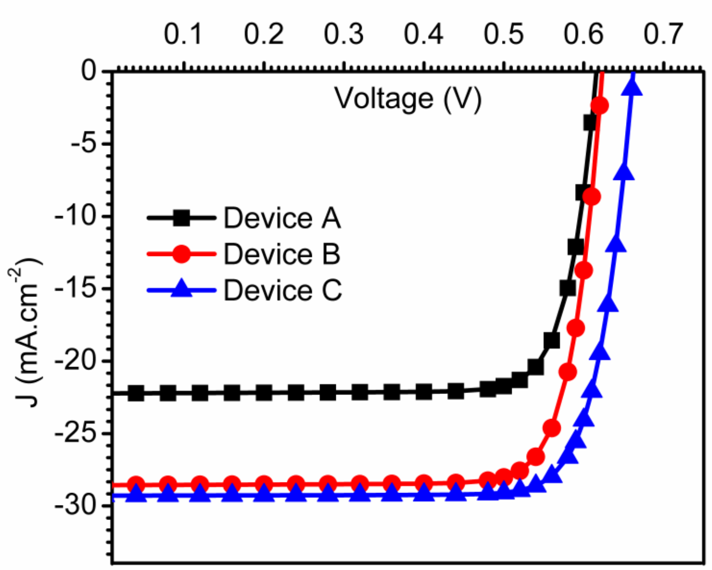

Figure 2.10: Current density-voltage (J-V) curve under illumination for different devices: (a) Si_3N_4 coated device, (b) ZrO_2 textured device, and (c) SiC-based ZrO_2 textured device (Pandey and Chaujar, 2016b).

Further, the J-V curve is presented in **Figure 2.10** above for Device A, Device B, and Device C. Correspondingly, the photovoltaic parameters are concluded in **Table 2-1** on page 40. The J-V curve of Device A is identical to the J-V curve of the planar 10-µm-thick solar cell with anti-reflection layer, presented by Jeong et al. (Jeong et al., 2013). This also validates the calibration of the software program. Moreover, lower recombination and higher photogeneration lead to improved J_{SC} and V_{OC} in Device B and Device C compared to Device A. The J_{SC}, V_{OC} of 28.6 mA.cm^{-2},623 mV and 29.3 mA.cm^{-2},662 mV have been obtained in Device B and Device C, respectively, as shown in **Figure 2.10** on page 39. Hence, 32% higher J_{SC} and 7% higher V_{OC} has been obtained in Device C compared to Device A. Also, the V_{OC} of the Device C is 6 % higher compared to Device B which shows that the presence of SiC in ZrO_2 textured rear contact device significantly boost the photovoltaic performance of the device by suppressing the surface recombination. The overall PCE of the Device C is 42% and 11% higher compared to Device A and Device B respectively.

TABLE 2-1: PHOTOVOLTAIC PARAMETERS OF 10μm THICK DEVICES: DEVICE A, DEVICE B, AND DEVICE C CORRESPONDS TO Si_3N_4 COATED, ZrO_2 TEXTURED, AND SiC-BASED ZrO_2 TEXTURED DEVICES, RESPECTIVELY (PANDEY AND CHAUJAR 2016B).

Device	J_{SC} (mA.cm^{-2})	V_{OC} (mV)	FF (%)	PCE (%)
Reference cell (Jeong et al., 2013)	22.2	615	80.2	10.9
Device A	22.2	616	80.8	11.0
Device B	28.6	623	80.9	14.4
Device C	29.3	662	80.9	15.7
Periodic nanostructure based silicon solar cell (Branham et al., 2015)	33.9	589	78.5	15.7

Also, the impact of minority carrier lifetime (τ) has been studied to obtain the effect of material quality on PV parameters, and the results are presented in **Figure 2.11**(a-d) on page 41. The discussed device is thin compared to conventional silicon solar cells and hence, the device can be fabricated with inexpensive, less pure material. Also, the charge carriers in discussed device need to diffuse shorter length whereas, in conventional rear contact device, a long carrier lifetime is required to collect the carrier because the thickness is usually >150μm.

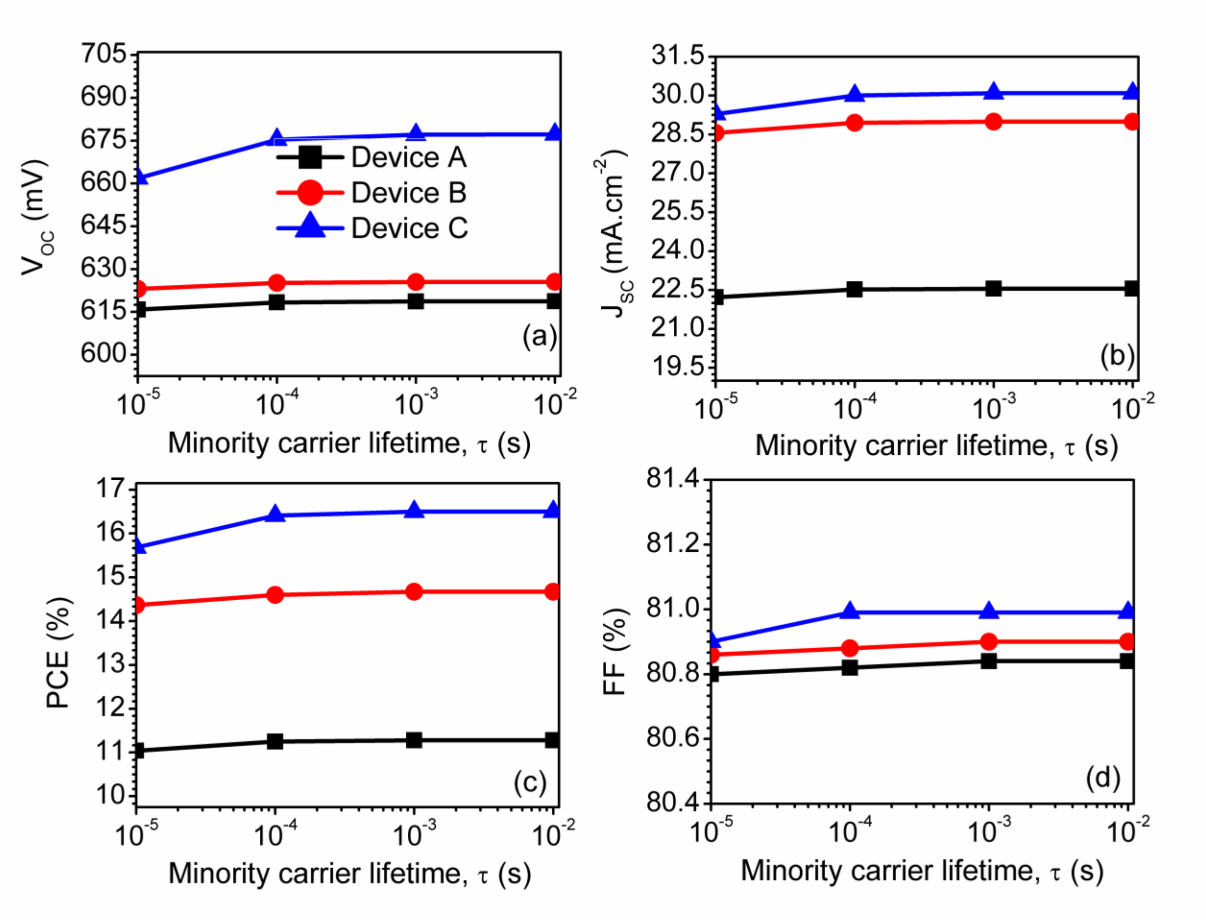

Figure 2.11: Impact of minority carrier lifetime on photovoltaic parameters of Si_3N_4 coated, ZrO_2 textured, and SiC-based ZrO_2 textured devices: (a) V_{OC}, (b) J_{SC}, (c) PCE and (d) FF (Pandey and Chaujar, 2016b).

This results in, increased module cost since high- purity material is required. Results show that the impact of minority carrier lifetime is negligible on all the three devices. However, the overall photovoltaic parameters of the Device C are superior compared to Device A and Device B. At τ equivalent to 10^{-2} s, the PCE of 11.3%, 14.7%, and 16.5% have been obtained in Device A, Device B, and Device C respectively, whereas, for τ equivalent to 10^{-5} s, the values are 11.0%, 14.4%, and 15.7%, respectively. This shows only 4% change in PCE is observed for Device C, as carrier lifetime changes from 10^{-2} s to 10^{-5} s. All the photovoltaic parameters of Device C are good compared to Device A and Device B as shown in **Figure**

2.11(a), **Figure 2.11**(b), **Figure 2.11**(c), and **Figure 2.11**(d) on page 41, respectively. The results discussed above show that the performance of silicon solar cell is improved with the help of SiC-based ZrO_2 texturing; however, optical absorption falls to lower values in the wavelength range of 900-100 nm, whereas simulated spectrum goes up to 1200 nm. The absorption coefficient of silicon is small at a higher wavelength (Green and Keevers, 1995, Green, 2008) and hence to increase the absorption up to 1200 nm, thicker silicon is required. Therefore, a 300μm thick SiC-based ZrO_2 textured rear-contact solar cell has also been designed and it's optical, as well as electrical parameters, are compared with 10 μm thick device as discussed above.

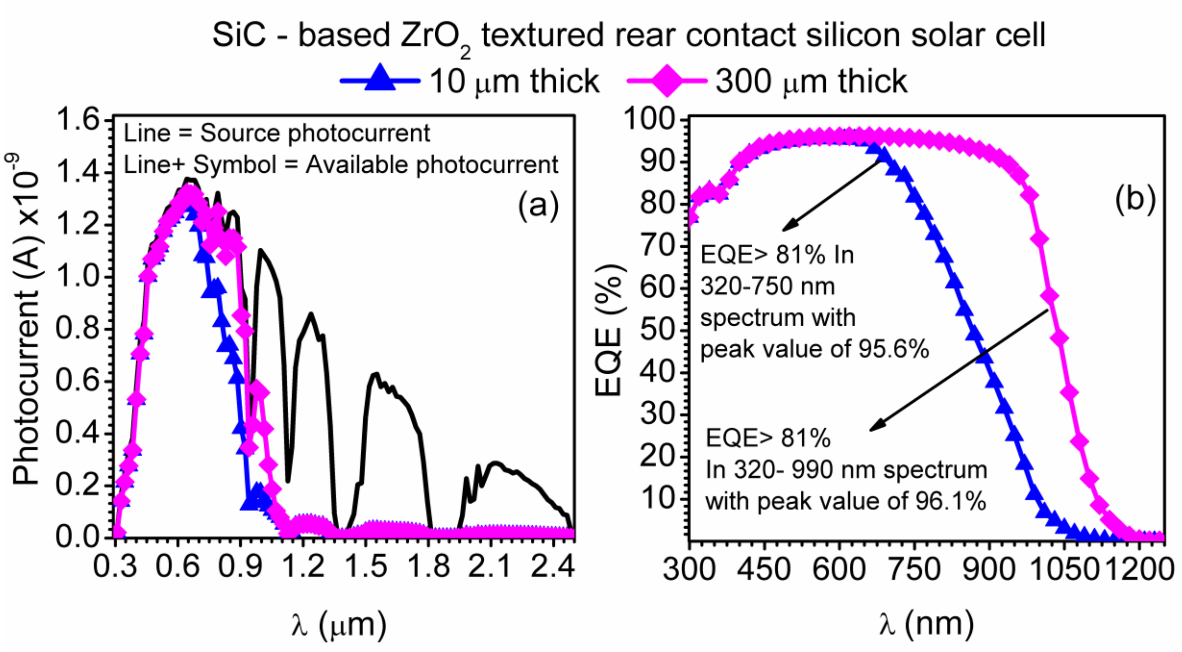

Figure 2.12: (a) Available photocurrent in the 10μm and 300μm thick SiC-based ZrO_2 textured devices, respectively under AM1.5 illumination, and (b) EQE of the 10μm and 300μm thick SiC-based ZrO_2 textured devices, respectively (Pandey and Chaujar, 2016b).

In addition, **Figure 2.12** (a-b) above shows the optical behavior of the devices, i.e. 10 microns and 300 micron thick devices, respectively. The available photocurrent (I_A) is shown in **Figure 2.12**(a) along with source photocurrent (I_S) of the spectrum. Improved available photocurrent has been obtained in 300 µm thick device in higher wavelength regime. The EQEs of the two devices have also been obtained and presented in **Figure 2.12**(b) on page 42. Results show, significant improvement in the higher wavelength region. The EQE fall to lower values at higher wavelength compared to 10-micron thick device, as shown in **Figure 2.12**(b). Further, J-V curve of the devices is presented in **Figure 2.13** below. Results indicate that improved optical response of 300µm thick device leads to significant improvement in J_{SC}. The minority carrier lifetime of 1ms has been selected for the thicker device to prevent the bulk recombination of generated carriers. The J_{SC} (39.40 mA.cm^{-2}), V_{OC} (687mV), FF (80%), and PCE (21.6%) have been obtained. In experimental work, modulated surface textured (MST) based rear contact device shows J_{SC}, V_{OC}, FF, and PCE values of 40.5 mA.cm^{-2}, 635 mV, 77%, and 19.8%, respectively (Ingenito et al., 2015). This shows that simulated results are in good agreement with experimental results. The V_{OC} value of the experimental device is lower compared to the device under investigation.

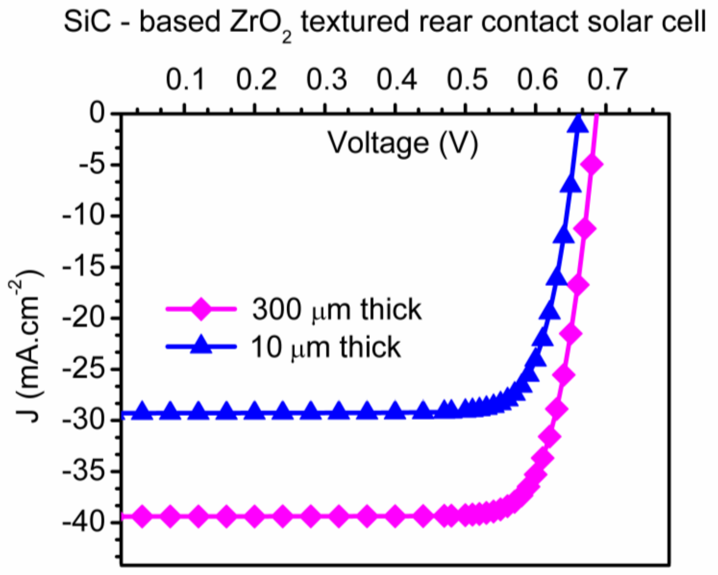

Figure 2.13: J-V curve under illumination for different devices: (a) Si_3N_4 coated device, (b) ZrO_2 textured device, and (c) SiC-based ZrO_2 textured device (Pandey and Chaujar, 2016b).

Results conclude that the optimum surface passivation has been achieved in this work compared to experimental results due to the presence of SiC. This shows that the amalgamation of SiC in experimental devices can significantly suppress the carrier recombination at the interface and lead to higher open circuit voltage. The photovoltaic parameters of the 300 µm thick device simulated in this work are shown in **Table 2-2** below along with already available experimental results.

TABLE 2-2: PHOTOVOLTAIC PARAMETERS OF 300 µm THICK SiC-BASED REAR CONTACT SILICON SOLAR CELL ALONG WITH ALREADY PUBLISHED EXPERIMENTAL RESULTS (PANDEY AND CHAUJAR 2016B).

Device	Thickness (µm)	J_{SC} (mA.cm^{-2})	V_{OC} (mV)	FF (%)	PCE (%)
SiC based ZrO_2 textured	300	39.4	687	80.0	21.6
MST based device (Ingenito et al., 2015)	285±25	40.5	635	77.0	19.8

2.4: SUMMARY

This chapter presents an efficient optical absorption and improved surface passivation in sub-10µm-thick Si solar cell device. Primarily a calibrated software program is written as per the results already published and then SiC-based passivation scheme has been discussed with rear contact silicon solar cell and optical performance is compared with conventional dielectric and FSF based passivation scheme. UV stability and superior optical response have been achieved in SiC-based device. Further, ZrO_2 textured and SiC-based front surface are designed for the silicon wafer, and spectrum response is obtained. The wafer shows absorption (87%) at short wavelengths (300 nm). Results show that throughout the wavelength spectrum 300-1000 nm, i.e. (UV-Visible-Infrared), ZrO_2 textured wafer having thin SiC at the interface (ZrO_2/n-Si) shows significant improvement in optical absorption. Hence, ZrO_2 textured SiC-based rear-contact solar cell device has been designed and simulated to achieve higher optical absorption, lower interface recombination, and improved V_{OC}. The device exhibits external quantum efficiency > 81% in the spectrum range of 320-720 nm wavelength spectrums with a maximum of 95.6% at wavelength 560 nm. This results in enhanced photovoltaic parameters compared to the conventional rear-contact solar cell with AR coating. The J_{SC} and V_{OC} of 29.3 mA.cm^{-2}, 661 mV have been obtained. This results in 15.7% PCE in the sub-10µm-thick rear contact silicon solar cell. Further, to utilize the higher wavelength photons, a 21.6% efficient 300µm thick device has also been designed and simulated. Results show that if fabricated experimentally it can prove to be a cost-effective solution for energy efficient applications.

Further, application of SiC passivated rear contact silicon solar cell in tandem configuration with perovskite top subcell has been discussed in next chapter and the focus of the work is to minimize the thermalisation losses.

2.5: REFERENCES

ABERLE, A. G. 2000. Surface passivation of crystalline silicon solar cells: a review. *Progress in Photovoltaics: Research and Applications,* 8**,** 473-487.

ALLEN, S., AWAD, Y., GAUMOND, A. & DAVIES, M. 2011. Silicon carbide-based antireflective coating. Google Patents.

ALTERMATT, P. P. 2011. Models for numerical device simulations of crystalline silicon solar cells—a review. *Journal of Computational Electronics,* 10**,** 314-330.

BÅÅK, T. 1982. Silicon oxynitride; a material for GRIN optics. *Applied optics,* 21**,** 1069-72.

BRANHAM, M. S., HSU, W.-C., YERCI, S., LOOMIS, J., BORISKINA, S. V., HOARD, B. R., HAN, S. E. & CHEN, G. 2015. 15.7% Efficient 10-µm-Thick Crystalline Silicon Solar Cells Using Periodic Nanostructures. *Advanced materials (Deerfield Beach, Fla.)***,** 2182-2188.

CHUNG, G. S., KIM, K. S. & YAKUPHANOGLU, F. 2010. Electrical characterization of Au/3C-SiC/n-Si/Al Schottky junction. *Journal of Alloys and Compounds,* 507**,** 508-512.

DEINEGA, A., EYDERMAN, S. & JOHN, S. 2013. Coupled optical and electrical modeling of solar cell based on conical pore silicon photonic crystals. *Journal of Applied Physics,* 113**,** 224501-224501.

DWIVEDI, N., KUMAR, S., BISHT, A., PATEL, K. & SUDHAKAR, S. 2013. Simulation approach for optimization of device structure and thickness of HIT solar cells to achieve ∼27% efficiency. *Solar Energy,* 88**,** 31-41.

DZIEWIOR, J. & SCHMID, W. 1977. Auger coefficients for highly doped and highly excited silicon. *Applied Physics Letters,* 31**,** 346-346.

GARCIA, J. C., SCOLFARO, L. M. R., LINO, A. T., FREIRE, V. N., FARIAS, G. A., SILVA, C. C., ALVES, H. W. L., RODRIGUES, S. C. P. & DA SILVA, E. F. 2006. Structural, electronic, and optical properties of ZrO_2 from ab initio calculations. *Journal of Applied Physics,* 100**,** 104103-104103.

GARNETT, E. & YANG, P. 2010. Light Trapping in Silicon Nanowire Solar Cells. *Nano Letters,* 10**,** 1082-1087.

GOUDON, T., MILJANOVIĆ, V. & SCHMEISER, C. 2007. On the Shockley–Read–Hall Model: Generation-Recombination in Semiconductors. *SIAM Journal on Applied Mathematics,* 67**,** 1183-1201.

GREEN, M. A. 2008. Self-consistent optical parameters of intrinsic silicon at 300K including temperature coefficients. *Solar Energy Materials and Solar Cells,* 92**,** 1305-1310.

GREEN, M. A. & KEEVERS, M. J. 1995. Optical properties of intrinsic silicon at 300 K. *Progress in Photovoltaics: Research and Applications,* 3**,** 189-192.

HALL, R. 1952. Electron-Hole Recombination in Germanium. *Physical Review,* 87**,** 387-387.

INGENITO, A., ISABELLA, O. & ZEMAN, M. 2015. Nano-cones on micro-pyramids: modulated surface textures for maximal spectral response and high-efficiency solar cells. *Progress in Photovoltaics: Research and Applications*, 20**,** 6-6.

JEONG, S., MCGEHEE, M. D. & CUI, Y. 2013. All-back-contact ultra-thin silicon nanocone solar cells with 13.7% power conversion efficiency. *Nature communications,* 4**,** 2950-2950.

JOUNG, Y.-H., KANG, H., KIM, J., LEE, H.-S., LEE, J. & CHOI, W. 2012. SiC formation for a solar cell passivation layer using an RF magnetron co-sputtering system. *Nanoscale Research Letters,* 7**,** 22-22.

KERSCHAVER, E. V. & BEAUCARNE, G. 2006. Back-contact solar cells: a review. *Progress in Photovoltaics: Research and Applications,* 14**,** 107-123.

PANDEY, R. & CHAUJAR, R. 2016a. Front Surface Passivation Scheme for Back-Contact Back-Junction (BC-BJ) Silicon Solar Cell. *Advanced Science Letters,* 22**,** 815-820.

PANDEY, R. & CHAUJAR, R. 2016b. Numerical simulation of rear contact silicon solar cell with a novel front surface design for the suppression of interface recombination and improved absorption. *Current Applied Physics,* 16**,** 1581-1587.

PANDEY, R. & CHAUJAR, R. 2016c. Rear contact SiGe solar cell with SiC passivated front surface for >90-percent external quantum efficiency and improved power conversion efficiency. *Solar Energy,* 135**,** 242-252.

PANDEY, R. & CHAUJAR, R. 2017. Rear Contact Silicon Solar Cell with SiC Based Front Surface Passivation for Ultraviolet Radiation Stability *9th International conference on Advanced Nanomaterials, University of Aveiro, Portugal*

PARIDA, B., CHOI, J., LIM, G. & KIM, K. 2013. Enhanced Visible Light Absorption by 3C-SiC Nanoparticles Embedded in Si Solar Cells by Plasma-Enhanced Chemical Vapor Deposition. *Journal of Nanomaterials,* 2013**,** 1-10.

PHILIPP, H. R. 1973. Optical Properties of Silicon Nitride. *Journal of The Electrochemical Society,* 120**,** 295-295.

SAVIN, H., REPO, P., VON GASTROW, G., ORTEGA, P., CALLE, E., GARÍN, M. & ALCUBILLA, R. 2015. Black silicon solar cells with interdigitated back-contacts achieve 22.1% efficiency. *Nature nanotechnology,* 10**,** 1-6.

SELBERHERR, S. 1984. *Analysis and Simulation of Semiconductor Devices,* Vienna, Springer Vienna.

SHOCKLEY, W. & READ, W. 1952. Statistics of the Recombinations of Holes and Electrons. *Physical Review,* 87**,** 835-842.

SLOTBOOM, J. W. 1977. The pn-product in silicon. *Solid-State Electronics,* 20**,** 279-283.

SLOTBOOM, J. W. & DE GRAAFF, H. C. 1976. Measurements of bandgap narrowing in Si bipolar transistors. *Solid-State Electronics,* 19**,** 857-862.

SOFTWARE, D. S. 2013. ATLAS User ' s Manual. 567-1000.

VAN LARE, C., LENZMANN, F., VERSCHUUREN, M. A. & POLMAN, A. 2015. Dielectric Scattering Patterns for Efficient Light Trapping in Thin-Film Solar Cells. *Nano Letters,* 15**,** 4846-4852.

YOSHINAGA, S., ISHIKAWA, Y., ARAKI, S. & URAOKA, Y. Light trapping effect of nanoimprinted-textured crystalline silicon solar cells. 2013/06//. IEEE, 1310-13.

CHAPTER 3

SiC Passivated Rear Contact Silicon Solar Cell in Tandem Configuration with Perovskite Top Subcell

This chapter represents the application of SiC passivated rear contact silicon solar cell in mechanically stacked tandem configuration with perovskite solar cell. The focus of the work is to minimize the thermalisation losses as discussed in **Chapter 1**. The tandem structure of perovskite-silicon solar cells is a promising method to achieve efficient solar energy conversion at low costs.

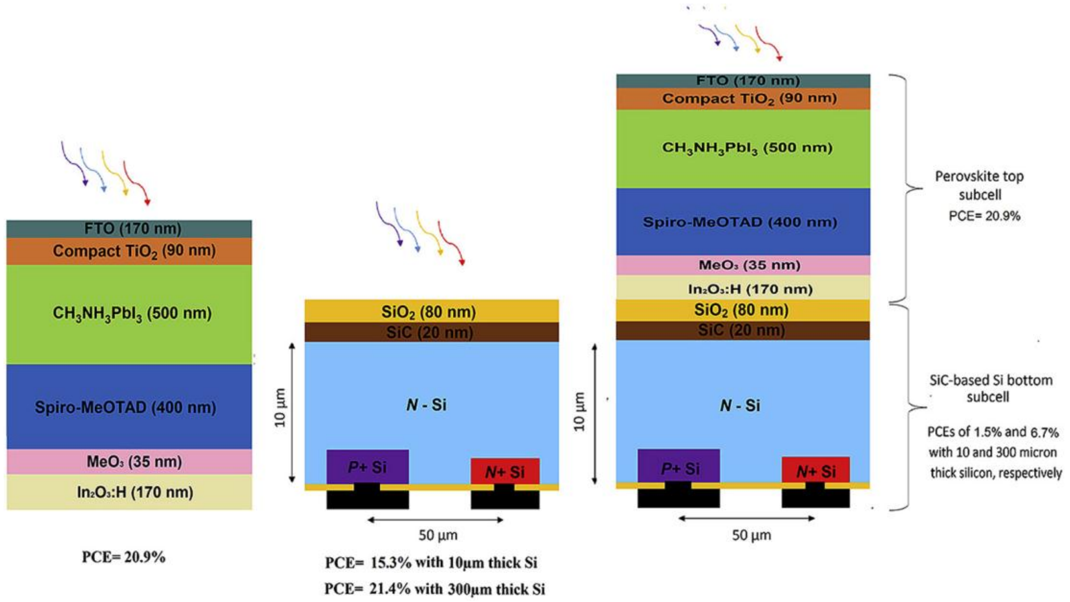

- *Innovative perovskite/silicon based 4-terminal tandem cell has been proposed and simulated.*
- *20.9% efficient perovskite cell has been designed for top subcell.*
- *PCEs of 27.6% and 22.4% have been achieved with 300 μm and 10 μm thick silicon bottom subcells.*
- *Result shows, proposed design can be a good candidate to obtain ultra-high efficiencies*

3.1: INTRODUCTION

Refining the performance of PV devices is crucial to surge their competitiveness with a conventional source of electricity. Crystalline silicon solar cells have dominated the PV market for decades, with 90% current market share (Loper et al., 2014, ITRPV, 2016). The efficiency of the crystalline silicon solar cell has only marginally improved during the last 15 years, wafer size efficiency as high as 25.6% has been reported with amorphous silicon (a-Si)/c-Si hetero-junction technology (Masuko et al., 2014). Moreover, recently a record of 26.3% has been achieved on 180 cm^2 crystalline silicon solar cell (Yoshikawa et al., 2017) which is close to the theoretical maximum efficiency of 29.4% (Richter et al., 2013). However, to make photovoltaic fully competitive with the conventional energy source, further cost effective energy efficient module is required. Photoexcited carriers with excess energy, i.e. energy larger than bandgap leads to quick thermalization which is one of the major hindrances in single junction cells (Green, 2002). The thermalization losses can be minimized by splitting the solar spectrum into various ranges and each range will be utilized by well-matched bandgap cells. This idea seems to be suggested in 1955, and same has been published in 1960 (Jackson, 1960), although, not getting much attention at that time. Moon et al. (Moon et al., 1978), demonstrated that high efficiencies could be achieved by employing this idea, which led to, widespread interest. Initially, spectrum splitting approaches are used using spectrally sensitive mirrors; later it was realized that stacking of the cells on one another could lead to spectral filtering by placing the largest bandgap cell on the top (Jackson, 1960). A single-junction small-bandgap solar cell device produces a low voltage from the available solar spectrum, whereas, the stacked tandem architecture uses a large-bandgap cell to absorb the high-energy photons, generating a higher voltage from these photons than the small-bandgap cell, thus, resulting in efficient utilization of solar spectrum.

Therefore, to obtain the higher efficiency at lower cost, Si-based tandem approaches have been proposed, which combine a silicon cell with a low-cost cell with wide-bandgap (1.6e - 1.9 eV) absorber material to form a tandem cell. Commonly, III-V semiconductors have been used on top of silicon to make a tandem cell; however, their large area production is costly and challenging (Bailie and McGehee, 2015). The emergence of organic-inorganic halide perovskite solar cell drastically changes the situation. The methylammonium-lead-halide, $CH_3NH_3PbX_3$ (X=Br, I) perovskite has a tunable band gap, ranging from 1.6 to 2.3 eV depending on halide composition. The solar cell based on organometal halides represents an emerging PV technology. Optical absorption of methylammonium-lead-halide on nanocrystalline titanium oxide (TiO_2) surface produces the PCE of 3-4%, in a liquid-based dye-sensitized solar cell (DSSC), as first discovered in 2009. Further, by optimizing the perovskite coating condition, the PCE has been doubled after two years. However, owing to stability issue, liquid-based perovskite receives little attention. In 2012, a long-term stable perovskite solar cell was developed with PCE of 10%, by substituting the solid hole conductor with liquid electrolytes. The notable improvement in PCE achieved in the past few years suggests that it is a capable candidate for the next-generation PV technology (Park, 2014). In the year 2015, the certified efficiency has reached 20.1% (Yang et al., 2015a). Recently, record PCEs of 20.8% and 21.1% have been achieved in perovskite solar cells (Bi et al., 2016, Saliba et al., 2016).

The emphasis of this chapter is on designing and simulations of 4-terminal mechanically stacked perovskite/SiC-passivated rear contact silicon tandem solar cell. In the four-terminal tandem configuration, the cells are connected independently and hence avoids the need for current matching between the top and bottom subcell, thus giving greater design flexibility as discussed in **Section 1.6:** of **Chapter 1**. Previously, in tandem based approach, 13.7% efficient 2-terminal perovskite/silicon multijunction solar cell enabled by a silicon tunnel junction has been reported (Mailoa et al., 2015). Moreover, 21.2% and 19.2% efficient monolithic perovskite/silicon tandem solar cells with a cell area of 0.17 cm^2 and 1.22 cm^2 respectively, have been proposed in the literature (Werner et al., 2015). Previous research work shows perovskite based cell is a good candidate to be used in 2, 4- terminal tandem configuration with silicon cell to produce an efficient cell under illumination (Sheng et al., 2015). Therefore, the work reported in this chapter proposes a new 4-terminal perovskite/silicon-based tandem device for energy efficient applications. The $CH_3NH_3PbI_3$ based perovskite solar cell has been used as the top subcell, and SiC passivated rear contact Si solar cell as discussed in **Chapter 2** has been utilized for the bottom subcell. The realistic TCAD design and analysis has been done for perovskite solar cell to understand the physical processes in the device and to make reliable predictions of the behavior before discussing the same in the tandem configuration. The results section of the chapter is divided into two parts: Analysis of perovskite top subcell; and Analysis of SiC-based silicon bottom subcell along with 4-terminal perovskite/SiC-based silicon tandem solar cell.

3.2: DEVICE STRUCTURE, MODELS AND METHODS

Optical absorption by a thin film of $CH_3NH_3PbI_3$ at room temperature creates free mobile charges with high yield within a few picoseconds. These charge carriers have high mobilities that lead to micrometer diffusion length and microsecond timescale recombination time (Carlito et al., 2016). Therefore, carrier recombination plays a significant role that determines the ultimate performance of the perovskite based devices. For instance, SRH recombination usually determines the carrier lifetime and hence, directly impacts diffusion lengths of the carriers in solar cell. Refining material quality can significantly reduce the SRH and other defect-related carrier recombination channels, leaving the other fundamental recombination channels: Auger and radiative recombination to limit carrier lifetimes. The following equation can quantitatively describe the carrier dynamics in perovskite device according to different recombination mechanisms (Wehrenfennig et al., 2014a) :

$$\frac{dn(t)}{dt} = -C.n^3 - B.n^2 - A.n \tag{3.01}$$

In the above equation, n (t) is the charge carrier density and A, B, and C denotes the first, second, and third order decay constants, i.e., monomolecular, bimolecular and trimolecular recombination rate constants. Literature reports, first order recombination can be attributed to geminate and/or SRH recombinations, whereas bimolecular and trimolecular recombinations attributed to radiative and Auger recombination of free electrons and holes, respectively (Yang et al., 2015b). With the rapid progress in perovskite-based solar cell device performance, critical studies, i.e., device simulation considering the impact of the various recombination mechanisms on photovoltaic device parameters is lagging. In this Chapter, TCAD analysis has been done for perovskite top subcell with the help of Silvaco ATLAS device simulator to study the photophysical properties and the performance of $CH_3NH_3PbI_3$ based perovskite solar cell. The parameters, i.e., constants for each model have been obtained from experimentally available data as reported in (Yang et al., 2015b, Wehrenfennig et al., 2014a).

Moreover, **Figure 3.1**(a-c) on page 53 represents the simulated device structure. Perovskite top subcell as reported in **Figure 3.1**(a) comprises of fluorine doped tin oxide

(FTO) based front contact. Compact TiO_2 is *n*- type, with a doping density of 5×10^{19} cm^{-3}, whereas $CH_3NH_3PbI_3$ and Spiro-MeOTAD are *p*-type with a doping density of 2.14×10^{19} cm^{-3} and 3×10^{18} cm^{-3} respectively. Moreover, in a four-terminal tandem configuration, the perovskite top subcell requires two transparent contacts to facilitate the optical coupling in underlying bottom subcell. Therefore, molybdenum trioxide (MoO_3) buffer layer based hydrogenated indium oxide (In_2O_3: H) rear transparent electrode has been used for perovskite cell, as reported by Fu et al. (Fu et al., 2015). Further, bottom subcell device as presented in **Figure 3.1**(b) below is identical to Device C as discussed in **Chapter 2**; however, ZrO_2 textured surface and external resistances have been omitted to avoid complexity, higher computation time and resistive losses respectively. Additionally, **Figure 3.1**(c) shows the final 4-terminal mechanically stacked perovskite/SiC-passivated rear contact silicon tandem solar cell.

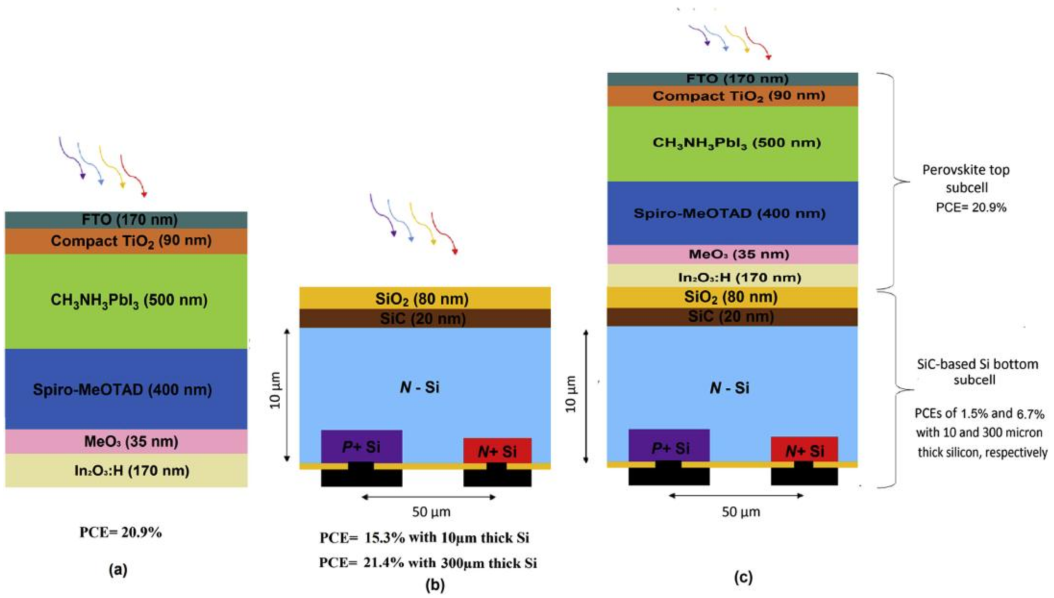

Figure 3.1: The device structures used in simulation: (a) perovskite top subcell with indium oxide (In_2O_3: H) as a transparent rear electrode, (b) SiC-based silicon bottom subcell and (c) mechanically stacked perovskite/silicon tandem cell (Pandey and Chaujar, 2016) .

The Poisson's equation is solved along with electron and hole continuity equations (see Appendix) to obtain the J-V curve. Additionally, when models are enabled, SRH, auger, and radiative recombination rates are included in the recombination terms in the carrier continuity equations. Perovskite top subcell is simulated based on the recombination dynamics in $CH_3NH_3PbI_3$ with the help of SRH, Auger, and radiative recombination models to account for monomolecular, bimolecular and trimolecular recombinations in the perovskite top subcell, whereas concentration dependent SRH, Auger, concentration dependent mobility and bandgap narrowing models have been used for the bottom silicon solar cell. The radiative recombination model is omitted for silicon solar cell since it is an indirect bandgap semiconductor.

TABLE 3-1: MATERIAL PARAMETERS USED DURING SIMULATION (PANDEY AND CHAUJAR, 2016).

Material		Compact TiO_2	$CH_3NH_3PbI_3$	Spiro-MeOTAD	Silicon	SiC
Dielectric Constant		100	30	3	11.8	9.72
Band Gap (eV)		3.2	1.5	2.91	1.12	2.2
Electron Affinity (eV)		4	3.93	2.2	4.17	4.2
Thickness (µm)		0.09	0.5	0.4	10, 300	0.02
Electron, Hole mobility (cm2/V·s)		0.006, 0.006	50,50	0.0001, 0.0001	1417, 470	1000, 50
Effective conduction band (DOS) (cm^{-3})		1×10^{21}	2.5×10^{20}	2.5×10^{20}	2.76×10^{19}	6.4×10^{18}
Effective valence band (DOS) (cm^{-3})		2×10^{20}	2.5×10^{20}	2.5×10^{20}	1.02×10^{19}	1.6×10^{18}
Conduction tail states	$N^{c\text{-}tail}\ A$ (cm^{-3})	10^{14}	10^{14}	10^{14}	n/a	n/a
	$E^{c\text{-}tail}\ A$ (eV)	0.01	0.015	0.01	n/a	n/a
Valence tail states	$N^{v\text{-}tail}\ D$ (cm^{-3})	10^{14}	10^{14}	10^{14}	n/a	n/a
	$E^{v\text{-}tail}\ D$ (eV)	0.01	0.015	0.01	n/a	n/a
Acceptor-like (A) dangling bond states	$N^{db}\ A$ (cm^{-3})	10^{17}	10^{14}	10^{16}	n/a	n/a
	$E^{db}\ A$ (eV)	1.1	1.2	1.1	n/a	n/a
	$\sigma^{db}\ A$ (eV)	0.1	0.1	0.1	n/a	n/a
Donor-like (D) dangling bond states	$N^{db}\ D$ (cm^{-3})	10^{17}	10^{14}	10^{16}	n/a	n/a
	$E^{db}\ D$ (eV)	1.1	1.2	1.1	n/a	n/a
	$\sigma^{db}\ D$ (eV)	0.1	0.1	0.1	n/a	n/a

Further, material parameters used in the simulation are reported in **Table 3-1** on page 54; Parameters for perovskite cell as reported in **Table 3-1** has been obtained from already published results (Liu et al., 2014). Added, optical properties of the material used in the simulations are shown in **Figure 3.2**(a-f) below. The n, k values of perovskite, Spiro-MeOTAD, TiO_2, FTO, MoO_3, In_2O_3: H, Si and SiC are reported in **Figure 3.2**(a), **Figure 3.2**(b), **Figure 3.2**(c), **Figure 3.2**(d), **Figure 3.2**(e), **Figure 3.2**(e) inset, and **Figure 3.2**(f) including inset, respectively.

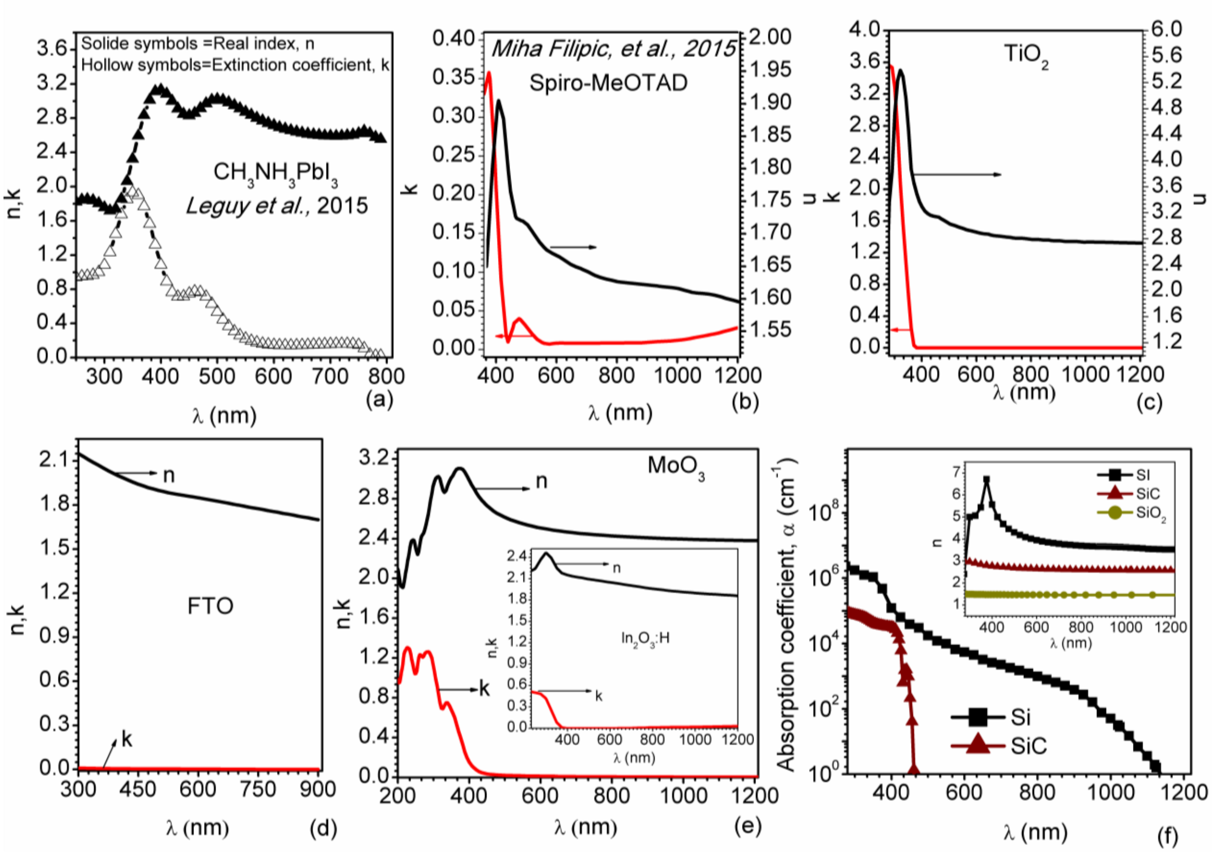

Figure 3.2: The optical properties used in simulation: (a) n, k of $CH_3NH_3PbI_3$ obtained from (Leguy et al., 2015) (b) n, k of Spiro-MeOTAD obtained from (Filipič et al., 2015), (c) n, k of TiO_2, (d) n, k of FTO, (e) n, k of MoO_3. Inset shows the n, k of In_2O_3: H and (f) absorption coefficient of silicon and SiC. Inset shows real index of Si, SiC, and SiO_2 respectively (Pandey and Chaujar, 2016, Yoshikawa et al., 2017).

3.3: RESULTS

Result section of the chapter is divided into two parts: 1st comprehensive analysis of perovskite top subcell has been done, where the impact of perovskite layer thickness, monomolecular, bimolecular, and trimolecular recombination have been obtained on the performance of perovskite top subcell. 2nd part deals with the analysis of mechanically stacked 4-terminal perovskite/silicon tandem solar cell, and the performance of the bottom subcell has been obtained for both standalone and tandem configurations. Moreover, the impact of carrier lifetime has been studied to get the effect of material quality on the performance of bottom subcell.

3.3.1: Analysis of perovskite top subcell

The thickness of the top subcell is a critical parameter in tandem configuration since absorption is directly related to the absorption coefficient and thickness of the material. Hence, thickness of top subcell plays a crucial role in determining the efficiency of bottom subcell. A much thicker perovskite layer will limit the optical absorption in underlying bottom subcell, due to parasitic absorption. Nevertheless, thinner perovskite layer will result in insufficient absorption in top subcell, which eventually leads to lower efficiencies. Hence, detailed thickness analysis has been performed and the spectrum response, i.e. external quantum efficiency, EQE along with J-V curve of the device is presented in **Figure 3.3**(a) and **Figure 3.3**(b) on page 57, respectively. The result shows that thin perovskite layer based device is not proficient to absorb the photons of the visible spectrum and hence shows inferior photovoltaics performance as observed in J-V curve reported in **Figure 3.3**(b). Frequency response indicated in **Figure 3.3**(a) reveals that top subcell having perovskite thickness < 400nm is not capable of utilizing the spectrum efficiently. Therefore, substantial improvement in frequency response can be obtained by increasing the thickness of the perovskite layer, as shown in **Figure 3.3**(a) below.

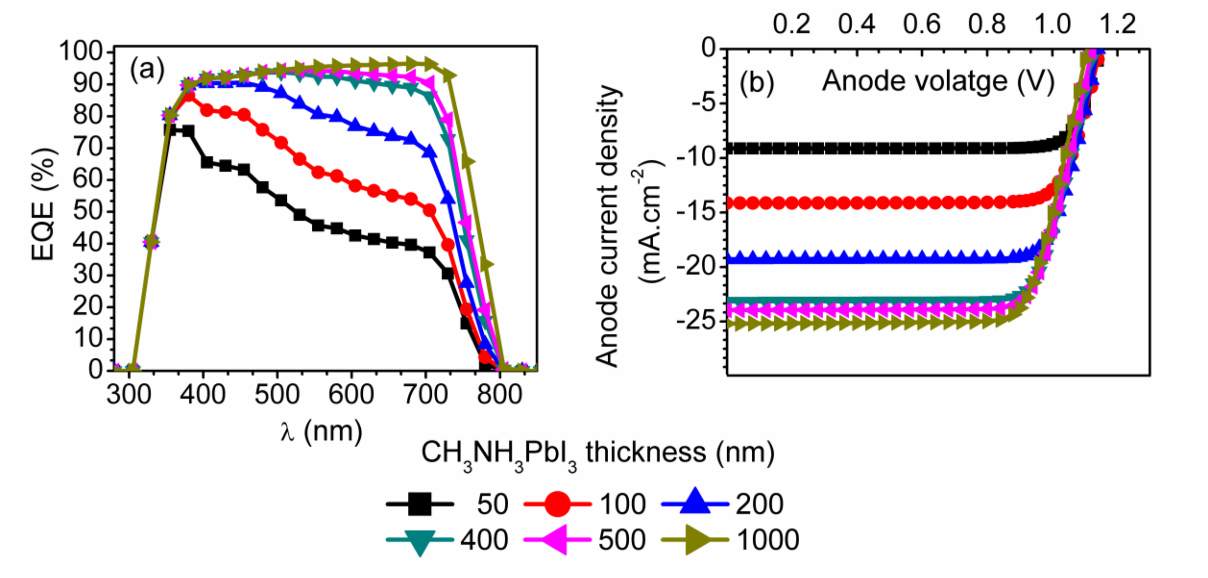

Figure 3.3: Impact of perovskite layer thickness on perovskite top subcell: (a) EQE, and (b) J-V curve (Pandey and Chaujar, 2016).

Additionally, considerable improvement in current density has also been observed as represented in **Figure 3.3**(b) above; whereas, V_{OC} decreases slightly. This can be attributed to increased carrier recombination in a thicker film. Further, increasing the thickness from 400 to 1000 nm does not provide any substantial improvement. Hence, further analysis has been done with 500 nm thick layer of perovskite. The simulation results obtained in this chapter are in agreement with the fact that increasing the thickness of perovskite, results in higher PCE as reported in the literature (Laban and Etgar, 2013, Etgar et al., 2012, Sun et al., 2014). Moreover, the efficiency limit for 500 nm thick perovskite solar cell having a perfect mirror at the rear side has been predicted by detailed, balanced models, which shows J_{SC}, V_{OC}, FF, and PCE of 25.97 mA.cm^{-2}, 1.315 V, 91%, and 30.0%, respectively (Sha et al., 2015), while top subcell (which do not include perfect mirror at rear side) simulated in this work, displays J_{SC},

V_{OC}, FF, and PCE of 24.06 mA cm^{-2}, 1.315 V, 82%, and 25.9%, respectively, as shown in **Figure 3.4** (a) below.

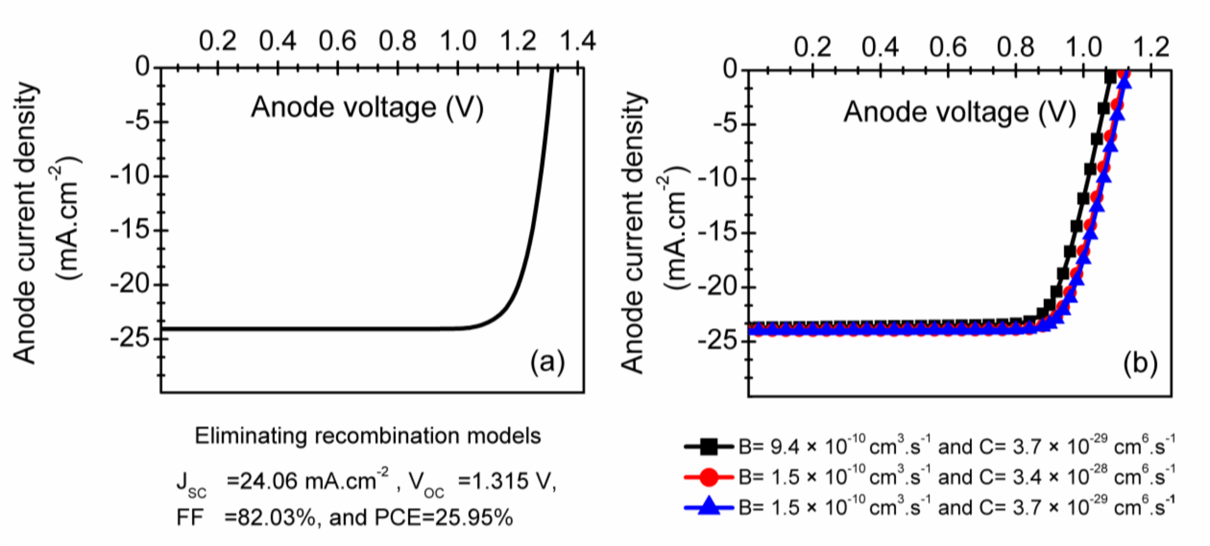

Figure 3.4: (a) The J-V curve of the perovskite top subcell, by eliminating the recombination models and (b) J-V curve of the perovskite top cell with different bimolecular and trimolecular carrier recombination coefficient as reported in (Yang et al., 2015c, Wehrenfennig et al., 2014a, Pandey and Chaujar, 2016).

The J-V curve presented in **Figure 3.4** (a) above has been obtained by assuming high-quality perovskite layer and eliminating the recombination models such as Auger and radiative recombination. This exercise has been done to observe the impact of these fundamental recombination dynamics on the performance of top subcell. Moreover, recombination dynamics has been included in the simulation, with the help of recombination models and three J-V curves are obtained with different second and third order recombination rate constants, i.e. B and C. The constants B and C have been obtained from experimental data as suggested in literature (Yang et al., 2015c, Wehrenfennig et al., 2014a). SRH recombination model has been modeled with carrier lifetimes of 10^{-6} s. The J-V curves reported in **Figure 3.4** (b) shows considerable degradation when recombination dynamics are incorporated in the perovskite layer. The square and circular mark J-V curves are based on the constants reported by Wehrenfennig et al. (Wehrenfennig et al., 2014a) and Yang et. al. (Yang et al., 2015c), respectively, whereas, to obtain optimum performance, triangular symbol based J-V curve is also simulated by selecting the smaller values of the constants as shown in **Figure 3.4** (b) on page 58. The PCEs of 19.7%, 20.9%, and 21.0% have been obtained, which has been reported in **Table 3-2** below.

TABLE 3-2: PHOTOVOLTAIC PARAMETERS OF PEROVSKITE SOLAR CELL: CHARGE CARRIER DECAY CONSTANT HAS BEEN OBTAINED FROM EXPERIMENTALLY AVAILABLE DATA FROM (YANG ET AL., 2015C, WEHRENFENNIG ET AL., 2014A, PANDEY AND CHAUJAR, 2016).

Charge Carrier Decay Constants		Photovoltaic Parameters			
2^{nd} order, B ($cm^3\ s^{-1}$)	3^{rd} order, C ($cm^6\ s^{-1}$)	J_{SC} ($mA.cm^{-2}$)	V_{OC} (V)	FF (%)	PCE (%)
9.4×10^{-10}	3.7×10^{-29}	23.70	1.08	76.7	19.7
1.5×10^{-10}	3.4×10^{-28}	23.95	1.12	77.8	20.9
1.5×10^{-10}	3.7×10^{-29}	23.96	1.13	77.8	21.0

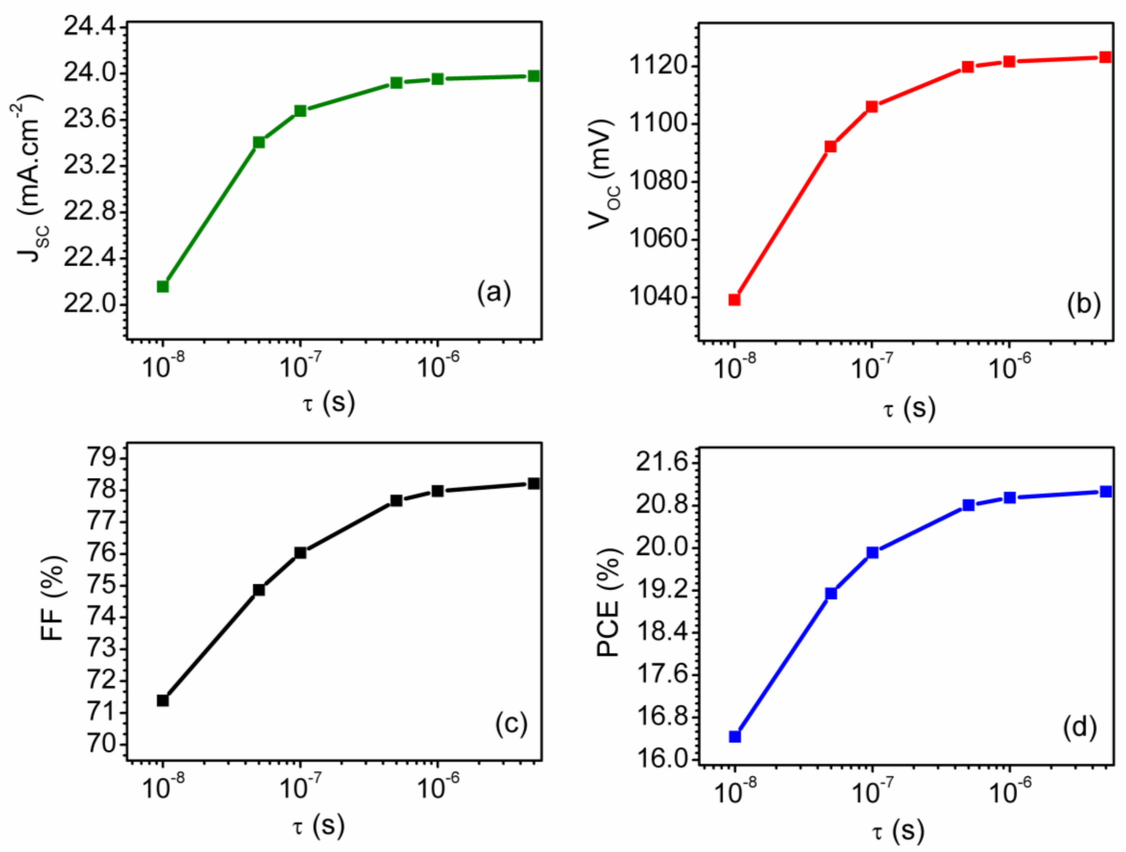

Figure 3.5: The impact of first order recombination lifetime on the device photovoltaic parameters for perovskite top subcell: (a) J_{SC}, (b) V_{OC}, (c) FF, and (d) PCE (Pandey and Chaujar, 2016).

Moreover, the inclusion of SRH recombination model provides the freedom to obtain the impact of material quality on the performance of the device, since SRH recombination is defect-limited and proportional to the defect density. Literature reports, first order recombination lifetime in perovskite ranges from 10 to 10^3 ns (Zhu et al., 2015, Wehrenfennig et al., 2014b, Shi et al., 2015). Thus, the impact of perovskite material quality on the photovoltaic parameters has been achieved by varying the carrier lifetime from 10 ns to 5×10^3 ns and presented in **Figure 3.5** (a-d) on page 59. Photovoltaic parameters: J_{SC}, V_{OC}, FF and, PCE is reported in **Figure 3.5** (a), **Figure 3.5** (b), **Figure 3.5** (c) and, **Figure 3.5** (d), respectively. Result shows as the lifetime changes from 5×10^{-6} s to 5×10^{-8} s, the change in J_{SC}, V_{OC}, FF, and PCE are 23.98 to 23.40 mA cm^{-2} , 1.12 to 1.09 V, 78.2% to 74.8%, and 21.0% to 19.1%, respectively. The reduction of 2.4%, 2.6%, 4.3%, and 9.0% in J_{SC}, V_{OC}, FF, and PCE has been observed, respectively. Nevertheless, as the lifetime of the carriers further changes from 5×10^{-8} s to 10^{-8} s, the decrease in J_{SC}, V_{OC}, FF, and PCEs is 5.3%, 4.6%, 4.6%, and 14.1%, respectively as shown in **Figure 3.5** (a-d). The analysis of material quality concludes that the diffusion length of light generated carriers is inadequate for 5×10^{-8} s and 10^{-8} s lifetime based perovskite material, and hence significant degradation is observed, particularly at 10^{-8} s lifetime as shown in **Figure 3.5** (a-d). The photovoltaic parameters of perovskite device with 10^{-6} s lifetime simulated in this work are nearly equivalent to mixed cation high-performance perovskite solar cells with record PCEs of 20.8% and 21.1% reported by Bi et al. (Bi et al., 2016, Saliba et al., 2016). While, the performance of lower lifetime based perovskite cell is also in close approximation with the experimentally available data reported by Liu et al. (Liu et al., 2013).

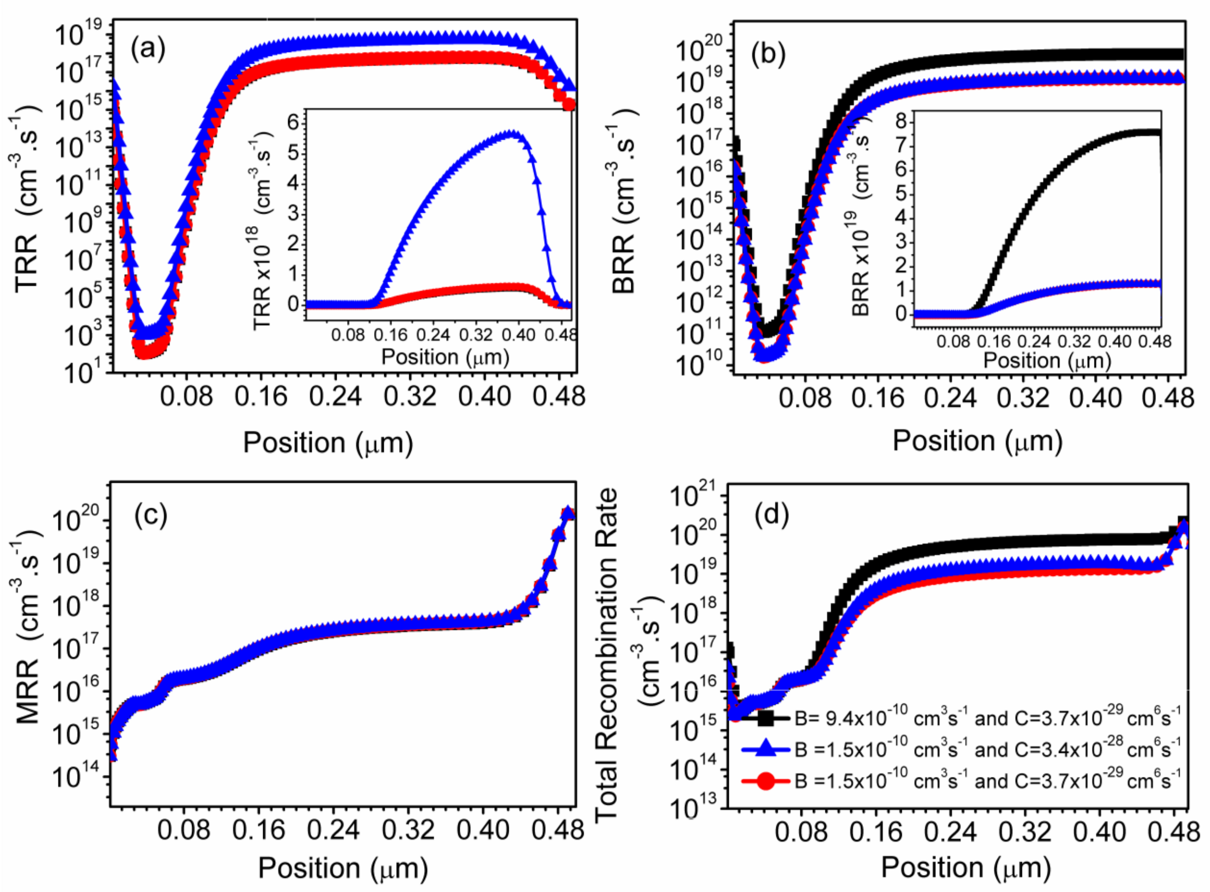

Figure 3.6: The carrier recombination rate inside the perovskite region with different bimolecular and trimolecular carrier recombination coefficient as reported in the literature (Yang et al., 2015c, Wehrenfennig et al., 2014a). (a) Trimolecular recombination rate (TRR); Inset shows the data on linear scale, (b) bimolecular recombination rate (BRR); Inset shows the data on linear scale, (c) monomolecular recombination rate (MRR) and, (d) total recombination rate inside the perovskite region. Analysis has been done under short circuit condition with standard AM1.5 illumination. Also, fixed first order recombination lifetime 10^{-6}s has been used during simulation (Pandey and Chaujar, 2016).

Additionally, fundamental recombination dynamics inside the perovskite region has also been obtained and presented in **Figure 3.6**(a-d) above. Trimolecular, bimolecular, monomolecular and, total recombination rates are reported in **Figure 3.6**(a), **Figure 3.6**(b), **Figure 3.6**(c) and, **Figure 3.6**(d), respectively. J-V curves as reported in **Figure 3.4**(b) on page 58 and recombination rate reported in **Figure 3.6**(b) above shows that the influence of trimolecular (Auger) recombination is lesser compared to bimolecular (radiative) recombination, on the photovoltaic parameters. The magnitude of BRR is higher compared to TRR as depicted in **Figure 3.6**(a-b) on page 61, which is attributed to the direct band gap of perovskite material. Therefore, Auger recombination is sufficiently suppressed, and this has also been verified by experimental results reported by Xing et al. (Xing et al., 2014), though, the influence of trimolecular recombination is not ignorable at high charge carrier density (Wehrenfennig et al., 2014a). Moreover, MRR is same for all the three cases, since fix carrier lifetime 10^{-6} has been used during analysis, **Figure 3.6**(c). **Figure 3.6**(d) shows overall recombination rate near compact TiO_2-perovskite interface is lower and gradually increases as we move away from the interface. To understand the behavior further, thorough analysis of recombination rates along with carrier distribution inside perovskite layer is done in the next Chapter.

3.3.2: Study of 4-terminal perovskite/SiC-based silicon tandem solar cell

This section of the chapter demonstrates mechanically stacked four-terminal tandem solar cell based on perovskite as top cell and SiC-passivated silicon cell as bottom subcell, as schematically shown in **Figure 3.1**(c) on page 53. In experimental approaches, both top and bottom subcells are separately handled and then assembled together to form a four-terminal mechanically stacked tandem devices, hence both subcells are electrically independent. The performance of each subcell is evaluated, and the addition of the two gives the overall efficiency in a tandem configuration. Two different devices have been used for bottom subcell, i.e., 10 and 300-µm thick silicon wafer-based devices are used. The performance of bottom silicon subcell is evaluated with perovskite top subcell (**Figure 3.1**a on page 53) as a filter under standard AM1.5 illumination. The motivation to design SiC-based silicon cell is to suppress the surface recombinations and improvement of V_{OC}, as discussed in **Chapter 2**.

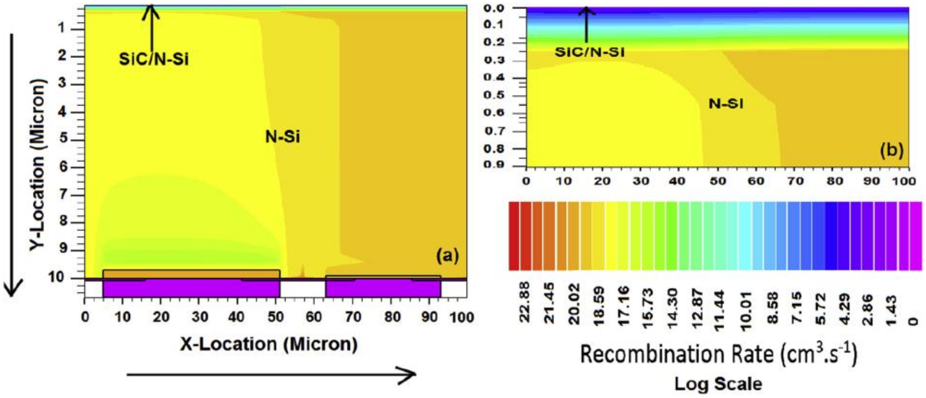

Figure 3.7: **(a) The contour representation of recombination rate in SiC-based bottom silicon subcell, (b) magnified view near SiC/n-Si interface (Pandey and Chaujar, 2016).**

Further, the recombination rate contour for the bottom silicon solar cell is shown in **Figure 3.7** above, which validates the improvements in surface passivation. The recombination dynamics as observed in bottom subcell show significant reduction in surface recombination compared to the bulk region of the device. Moreover, for detailed explanations of recombination inside the device, please refer **Section 2.3.3: Chapter 2**. Additionally, optical performance, i.e., EQEs of perovskite top subcell and silicon bottom subcell is obtained under tandem configuration and reported in **Figure 3.8**(a) on page 64. The result shows that 10 µm thick Si-based bottom subcell device is not proficient in absorbing higher wavelength photon compared to 300-µm thick device. Improved optical absorption results in higher EQEs in thicker device, since photon absorbance is directly related to the absorption coefficient and the thickness of the material used. This leads to the superior photovoltaic performance of 300 µm thick Si bottom subcell based tandem device. Moreover, photovoltaic parameters of the device is summarized in **Table 3-3** on page 65 for both standalone and tandem configuration.

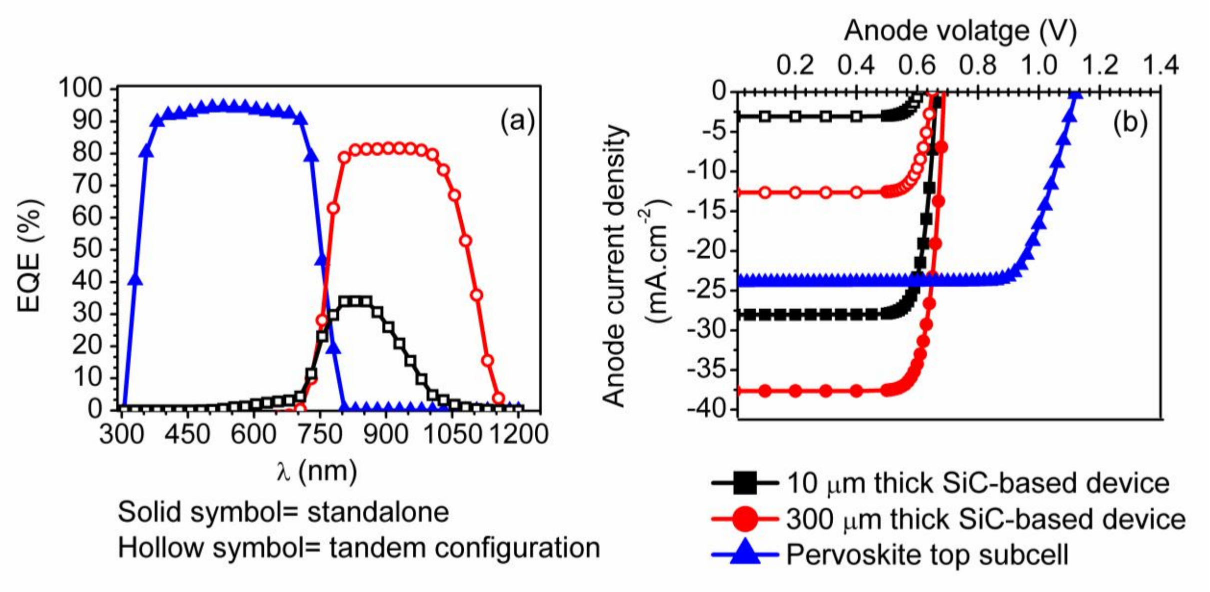

Figure 3.8: (a) EQE of perovskite top subcell and SiC-based silicon bottom subcell in tandem configuration, and (b) J-V curve of perovskite and silicon cell in stand-alone and tandem configuration (Pandey and Chaujar, 2016).

Further, to understand the impact of using perovskite cell as a filter, the performance of Si cell without perovskite filter has also been obtained and reported in **Figure 3.8**(b) above. The stand-alone configuration of bottom subcell leads to, J_{SC} of 28.08 mA.cm^{-2} and 37.64 mA.cm^{-2} in 10 µm and 300-µm thick wafer based rear-contact solar cells, respectively as shown in **Figure 3.8**(b). After adding the perovskite top cell, the J_{SC} of bottom Si cell went down to 3.06 mA.cm^{-2} and 12.61 mA.cm^{-2} for 10 and 300 µm thick devices respectively, which is attributed to reduced light intensity. The reduction in FF and V_{OC} are only marginal, resulting in 1.5% and 6.7% efficient Si-based bottom subcells, as shown in **Table 3-3** on page 65. Thus, together with the 20.9% efficiency of perovskite top subcell, this results in 22.4% and 27.6% efficient tandem devices with 10 and 300-µm thick silicon-based bottom subcells, respectively. This is a considerable improvement as compared to transparent perovskite solar cell and c-Si solar cell operated individually. Moreover FF under standalone as reported in

Table 3-3 shows higher value compared to the devices simulated in **Chapter 2**, due to the absence of external electrical resistances; however, V_{OC} of the device remain unaltered. Additionally, removal of ZrO_2 texturing resulted in lower J_{SC}.

TABLE 3-3: PHOTOVOLTAIC PARAMETERS OF THE DEVICES IN STAND-ALONE AND TANDEM CONFIGURATIONS (PANDEY AND CHAUJAR, 2016).

Solar cells	J_{SC} (mA.cm^{-2})	V_{OC} (mV)	FF (%)	PCE (%)
Perovskite top subcell	23.95	1121	77.8	20.9
Silicon bottom cell 10 micron (stand-alone)	28.08	662	82.3	15.3
Silicon bottom cell 10 micron (tandem)	3.06	606	81.8	1.5
Silicon bottom cell 300 micron (stand-alone)	37.64	688	82.9	21.4
Silicon bottom cell 300 micron (tandem)	12.61	649	82.3	6.7
4-terminal using 10 micron thick Si bottom subcell				20.9+1.5=22.4
4-terminal using 300 micron thick Si bottom subcell				20.9+6.7=27.6

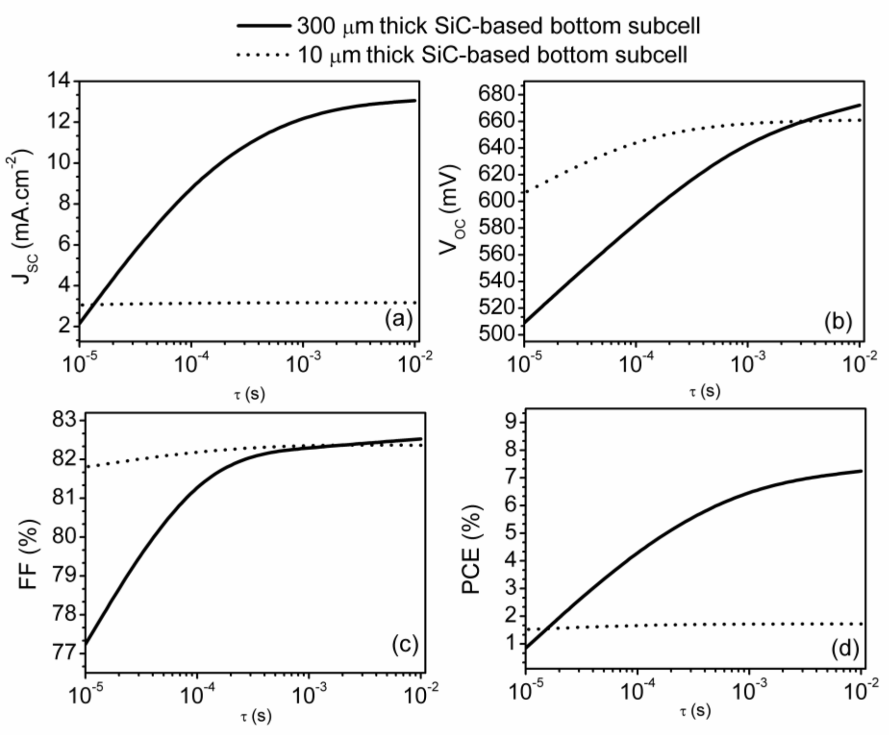

Figure 3.9: Impact of carrier lifetime on the performance of bottom silicon subcell under tandem configuration: (a) J_{SC}, (b) V_{OC}, (c) FF, and (d) PCE (Pandey and Chaujar, 2016).

Moreover, the influence of carrier lifetime has been studied to obtain the effect of material quality on the performance of bottom subcell, and the results are reported in **Figure 3.9**(a-d) on page 65. Photovoltaic parameters: J_{SC}, V_{OC}, FF, PCE is reported in **Figure 3.9**(a), **Figure 3.9**(b), **Figure 3.9**(c), and **Figure 3.9**(d), respectively. The 10 µm thick device is thin compared to conventional ~300 µm thick silicon solar cells and hence, the device can be fabricated with inexpensive, less pure material. Also, the charge carriers need to diffuse shorter length whereas, in 300 mm thick device, a long carrier lifetime is required to collect the light generated carriers. Therefore, the photovoltaic performance of thinner device shows the negligible impact of material quality, whereas significant degradation has been observed in the thicker device as reported in **Figure 3.9**(a-d). Results show for lower carrier lifetime (10^{-5} s) the performance of 300 µm thick is lower compared to 10 µm thick device, due to higher bulk recombination of the carrier in the thicker device, since lifetime is small. The desired material quality and the device can be selected from **Figure 3.9**(d) depending upon the application. Overall efficiency in tandem configuration can be obtained by adding the efficiencies of bottom subcell and perovskite top cell.

3.4: SUMMARY

A unique 27.6% efficient, 4-terminal mechanically stacked perovskite/SiC-passivated rear contact silicon tandem device has been suggested and simulated. The bottom subcell used in the analysis is identical to the SiC passivated device discussed in the previous chapter, and semitransparent perovskite top subcell with efficiency of 20.9% has been designed for perovskite-silicon tandem structure. The perovskite-silicon tandem architecture is a favorable method for low cost energy conversion. In the four-terminal tandem configuration, top and bottom subcells are connected independently and hence avoids the need for current matching between upper and lower subcell, consequently, gives greater design flexibility. Thorough TCAD analysis has been performed to predict the behavior of the devices. The impact of perovskite layer thickness, monomolecular, bimolecular, and trimolecular recombination have also been obtained on the performance of top subcell. The presence of SiC significantly suppressed the interface recombination in bottom silicon subcell. The influence of silicon material quality on the performance of bottom silicon subcell has also been obtained. The simulation analysis displays, PCE of 27.6% and 22.4% with 300 µm and 10 µm thick rear contact Si bottom subcell, respectively. This is a substantial improvement compared to the transparent perovskite solar cell, and c-Si solar cell operated separately. Moreover, despite the exciting results achieved in this chapter, conventional rear-contact solar cell shows low V_{OC} and has high complexity in fabrication; while, IBC-SiHJ solar cells which use low-temperature processes have excellent performance, i.e., high V_{OC}, and better rear surface passivation due to deposited i-a-Si: H. Hence, next chapter deals with the analysis of SiC passivated IBC-SiHJ solar cell as a bottom subcell under perovskite solar cell to achieve further ultra-high efficiencies.

3.5: REFERENCES

BAILIE, C. D. & MCGEHEE, M. D. 2015. High-efficiency tandem perovskite solar cells. *MRS Bulletin,* 40**,** 681-686.

BI, D., TRESS, W., DAR, M. I., GAO, P., LUO, J., RENEVIER, C., SCHENK, K., ABATE, A., GIORDANO, F., CORREA BAENA, J.-P., DECOPPET, J.-D., ZAKEERUDDIN, S. M., NAZEERUDDIN, M. K., GRÄTZEL, M. & HAGFELDT, A. 2016. Efficient luminescent solar cells based on tailored mixed-cation perovskites.

CARLITO, S. P., JR., YUXI, T., VILLY, S. & IVAN, G. S. 2016. Excited state and charge-carrier dynamics in perovskite solar cell materials. *Nanotechnology,* 27**,** 082001.

ETGAR, L., GAO, P., XUE, Z., PENG, Q., CHANDIRAN, A. K., LIU, B., NAZEERUDDIN, M. K. & GRÄTZEL, M. 2012. Mesoscopic CH3NH3PbI3/TiO2 heterojunction solar cells. *Journal of the American Chemical Society,* 134**,** 17396-9.

FILIPIČ, M., LÖPER, P., NIESEN, B., DE WOLF, S., KRČ, J., BALLIF, C. & TOPIČ, M. 2015. CH(3)NH(3)PbI(3) perovskite / silicon tandem solar cells: characterization based optical simulations. *Optics express,* 23**,** A263-78.

FU, F., FEURER, T., JÄGER, T., AVANCINI, E., BISSIG, B., YOON, S., BUECHELER, S. & TIWARI, A. N. 2015. Low-temperature-processed efficient semi-transparent planar perovskite solar cells for bifacial and tandem applications. *Nature Communications,* 6**,** 8932-8932.

GREEN, M. A. 2002. Third generation photovoltaics: solar cells for 2020 and beyond. *Physica E: Low-dimensional Systems and Nanostructures,* 14**,** 65-70.

ITRPV, I. S. E. V. P., 2016. 2016. ITRPV.

JACKSON, E. D. 1960. Solar energy converter. Google Patents.

LABAN, W. A. & ETGAR, L. 2013. Depleted hole conductor-free lead halide iodide heterojunction solar cells. *Energy & Environmental Science,* 6**,** 3249-3249.

LEGUY, A. M. A., HU, Y., CAMPOY-QUILES, M., ALONSO, M. I., WEBER, O. J., AZARHOOSH, P., VAN SCHILFGAARDE, M., WELLER, M. T., BEIN, T., NELSON, J., DOCAMPO, P. & BARNES, P. R. F. 2015. Reversible Hydration of CH 3 NH 3 PbI 3 in Films, Single Crystals, and Solar Cells. *Chemistry of Materials,* 27**,** 3397-3407.

LIU, F., ZHU, J., WEI, J., LI, Y., LV, M., YANG, S., ZHANG, B., YAO, J. & DAI, S. 2014. Numerical simulation: Toward the design of high-efficiency planar perovskite solar cells. *Applied Physics Letters,* 104**,** 253508-253508.

LIU, M., JOHNSTON, M. B. & SNAITH, H. J. 2013. Efficient planar heterojunction perovskite solar cells by vapour deposition. *Nature,* 501**,** 395-398.

LOPER, P., NIESEN, B., MOON, S. J., MARTIN DE NICOLAS, S., HOLOVSKY, J., REMES, Z., LEDINSKY, M., HAUG, F. J., YUM, J. H., DE WOLF, S. & BALLIF, C. 2014. Organic-inorganic halide perovskites: Perspectives for silicon-based tandem solar cells. *IEEE Journal of Photovoltaics,* 4**,** 1545-1551.

MAILOA, J. P., BAILIE, C. D., JOHLIN, E. C., HOKE, E. T., AKEY, A. J., NGUYEN, W. H., MCGEHEE, M. D. & BUONASSISI, T. 2015. A 2-terminal perovskite/silicon multijunction solar cell enabled by a silicon tunnel junction. *Applied Physics Letters,* 106**,** 121105.

MASUKO, K., SHIGEMATSU, M., HASHIGUCHI, T., FUJISHIMA, D., KAI, M., YOSHIMURA, N., YAMAGUCHI, T., ICHIHASHI, Y., MISHIMA, T., MATSUBARA, N., YAMANISHI, T., TAKAHAMA, T., TAGUCHI, M., MARUYAMA, E. & OKAMOTO, S. 2014. Achievement of More Than 25% Conversion Efficiency With Crystalline Silicon Heterojunction Solar Cell. *IEEE Journal of Photovoltaics,* 4**,** 1433-1435.

MOON, R., JAMES, L., VANDER PLAS, H., YEP, T., ANTYPAS, G. & CHAI, Y. Multigap solar cell requirements and the performance of AlGaAs and Si cells in concentrated sunlight. 13th Photovoltaic specialists conference, 1978. 859-867.

PANDEY, R. & CHAUJAR, R. 2016. Numerical simulations: Toward the design of 27.6% efficient four-terminal semi-transparent perovskite/SiC passivated rear contact silicon tandem solar cell. *Superlattices and Microstructures,* 100**,** 656-666.

PARK, N.-G. 2014. Perovskite solar cells: an emerging photovoltaic technology. *Materials Today,* 18**,** 65-72.

RICHTER, A., HERMLE, M. & GLUNZ, S. W. 2013. Reassessment of the Limiting Efficiency for Crystalline Silicon Solar Cells. *IEEE Journal of Photovoltaics,* 3**,** 1184-1191.

SALIBA, M., MATSUI, T., SEO, J. Y., DOMANSKI, K., CORREA-BAENA, J. P., NAZEERUDDIN, M. K., ZAKEERUDDIN, S. M., TRESS, W., ABATE, A., HAGFELDT, A. & GRATZEL, M. 2016. Cesium-containing triple cation perovskite solar cells: improved stability, reproducibility and high efficiency. *Energy Environ Sci,* 9**,** 1989-1997.

SHA, W. E. I., REN, X., CHEN, L. & CHOY, W. C. H. 2015. The efficiency limit of CH3NH3PbI3 perovskite solar cells. *Applied Physics Letters,* 106**,** 221104-221104.

SHENG, R., HO-BAILLIE, A. W., HUANG, S., KEEVERS, M., HAO, X., JIANG, L., CHENG, Y.-B. & GREEN, M. A. 2015. Four-Terminal Tandem Solar Cells Using CH3NH3PbBr3 by Spectrum Splitting. *The journal of physical chemistry letters,* 6**,** 3931-3934.

SHI, D., ADINOLFI, V., COMIN, R., YUAN, M., ALAROUSU, E., BUIN, A., CHEN, Y., HOOGLAND, S., ROTHENBERGER, A., KATSIEV, K., LOSOVYJ, Y., ZHANG, X., DOWBEN, P. A., MOHAMMED, O. F., SARGENT, E. H. & BAKR, O. M. 2015. Low trap-state density and long carrier diffusion in organolead trihalide perovskite single crystals. *Science,* 347**,** 519-522.

SUN, S., SALIM, T., MATHEWS, N., DUCHAMP, M., BOOTHROYD, C., XING, G., SUM, T. C. & LAM, Y. M. 2014. The origin of high efficiency in low-temperature solution-processable bilayer organometal halide hybrid solar cells. *Energy & Environmental Science,* 7**,** 399-399.

WEHRENFENNIG, C., EPERON, G. E., JOHNSTON, M. B., SNAITH, H. J. & HERZ, L. M. 2014a. High Charge Carrier Mobilities and Lifetimes in Organolead Trihalide Perovskites. *Advanced Materials,* 26**,** 1584-1589.

WEHRENFENNIG, C., LIU, M., SNAITH, H. J., JOHNSTON, M. B. & HERZ, L. M. 2014b. Homogeneous emission line broadening in the organo lead halide perovskite CH3NH3PbI3-xClx. *Journal of Physical Chemistry Letters,* 5**,** 1300-1306.

WERNER, J., WENG, C.-H., WALTER, A., FESQUET, L., SEIF, J. P., DE WOLF, S., NIESEN, B. & BALLIF, C. 2015. Efficient Monolithic Perovskite/Silicon Tandem Solar Cell With Cell Area > 1 cm 2. *The Journal of Physical Chemistry Letters,* 7**,** acs.jpclett.5b02686-acs.jpclett.5b02686.

XING, G., MATHEWS, N., LIM, S. S., YANTARA, N., LIU, X., SABBA, D., GRÄTZEL, M., MHAISALKAR, S. & SUM, T. C. 2014. Low-temperature solution-processed wavelength-tunable perovskites for lasing. *Nature materials,* 13**,** 476-80.

YANG, W. S., NOH, J. H., JEON, N. J., KIM, Y. C., RYU, S., SEO, J. & SEOK, S. I. 2015a. High-performance photovoltaic perovskite layers fabricated through intramolecular exchange. *Science.***,** science.aaa9272-science.aaa9272.

YANG, Y., YANG, M., LI, Z., CRISP, R., ZHU, K. & BEARD, M. C. 2015b. Comparison of Recombination Dynamics in CH3NH3PbBr3 and CH3NH3PbI3 Perovskite Films: Influence of Exciton Binding Energy. *Journal of Physical Chemistry Letters,* 6**,** 4688-4692.

YANG, Y., YANG, M., LI, Z., CRISP, R., ZHU, K. & BEARD, M. C. 2015c. Comparison of Recombination Dynamics in CH 3 NH 3 PbBr 3 and CH 3 NH 3 PbI 3 Perovskite Films: Influence of Exciton Binding Energy. *The Journal of Physical Chemistry Letters*, 6**,** acs.jpclett.5b02290-acs.jpclett.5b02290.

YOSHIKAWA, K., KAWASAKI, H., YOSHIDA, W., IRIE, T., KONISHI, K., NAKANO, K., UTO, T., ADACHI, D., KANEMATSU, M., UZU, H. & YAMAMOTO, K. 2017. Silicon heterojunction solar cell with interdigitated back contacts for a photoconversion efficiency over 26%. 2**,** 17032.

ZHU, H., FU, Y., MENG, F., WU, X., GONG, Z., DING, Q., GUSTAFSSON, M. V., TRINH, M. T., JIN, S. & ZHU, X. Y. 2015. Lead halide perovskite nanowire lasers with low lasing thresholds and high quality factors. *Nature materials*, 14**,** 636-42.

CHAPTER 4

SiC PASSIVATED IBC-SiHJ SOLAR CELL IN TANDEM CONFIGURATION WITH PEROVSKITE TOP SUBCELL

Although the objective of this chapter is identical to the previous Chapter, i.e., minimizing the thermalisation losses, the tandem architecture is slightly different, i.e., the bottom rear-contact solar cell has been replaced with IBC-SiHJ solar cell. This is due to the fact that conventional rear-contact solar cell shows lower V_{OC} and has high complexity in fabrication, whereas, IBC-SiHJ solar cells use low-temperature processes and have excellent performance, i.e., high V_{OC}, and better rear surface passivation due to deposited i-a-Si: H.

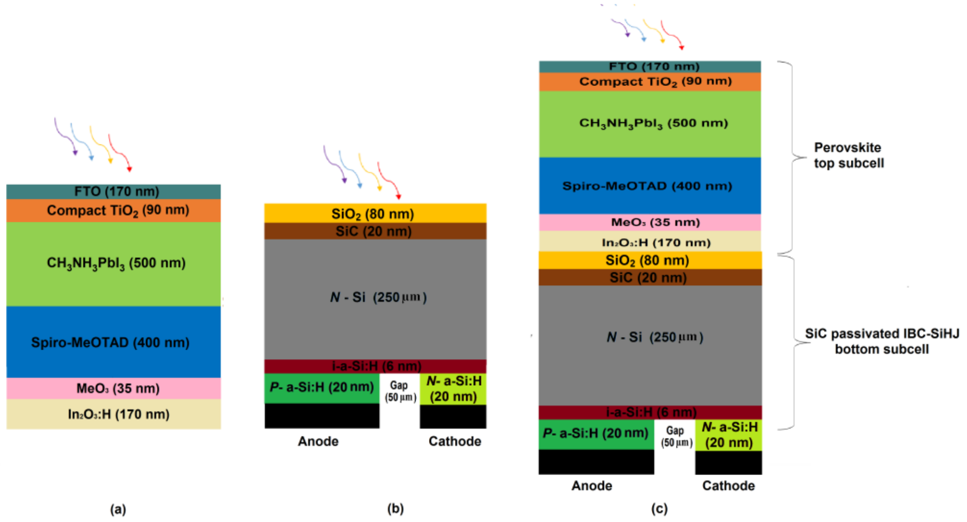

- *Perovskite/IBC-SiHJ based 4-terminal tandem cell has been proposed and simulated.*
- *Fundamental recombination dynamics are obtained inside the device.*
- *HTL analysis has been done for perovskite top subcell.*
- *Passivation quality of SiC has been studied for IBC-SiHJ solar cells.*
- *PCEs of 29.5% and 23.7% have been achieved with 250 µm/25 µm thick bottom subcells.*

4.1: INTRODUCTION

Heterojunction structures are the favorable contenders for higher conversion efficiencies in silicon PV technologies (Lu et al., 2007, Yang et al., 2015a). Crystalline and amorphous silicon constitutes the two different types of materials in heterojunction silicon solar cells. The combination of p-type and n-type materials forms a-Si/c-Si heterojunction solar cell similar to diode structure. c-Si is a substrate on top of which a-Si layer is deposited. The research work on the analysis of a-Si/c-Si heterojunction began more than 46 years ago. The fabrication of a-Si/c-Si heterojunction was first reported by Grigorivici et al. (Grigorovici et al., 1968), who synthesized the heterojunction by evaporation of amorphous non hydrogenated silicon on top of p-type/ n-type c-Si substrate with different resistivities, and consequently annealing the sample at either 290^0 C or 500^0 C. The aim of their study focused on determining transport mechanism in a-Si layer but the presented fabrication method produced a highly defective a-Si layer. They concluded better rectification in a-Si/n-type c-Si heterojunction as compared to the a-Si/p-type c-Si heterojunction. Fuhs et al. (Fuhs et al., 1974) showed first deposition of hydrogenated amorphous silicon (a-Si:H) on c-Si which resulted in lesser defect density. Few years later, large band gap of a-Si: H generated wide interest in use of a-Si: H/c-Si heterojunction in PV applications. With the first model of a-Si: H/c-Si heterojunction solar cells, an efficiency of over 15 % have been demonstrated (Schröder et al., 2001).

In the beginning, it was found that V_{OC} and FF of the a-Si/c-Si heterojunction based solar cells were lower than those of conventional diffused p-n junction based solar cells. It is the result of recombination process which occurs in the depletion region of the a-Si/c-Si heterojunction. Additionally, the doped a-Si layer contains significant amount of midgap states which may eventually increase the leakage current by the tunneling process. A spacer with less density of trap levels can be inserted to suppress this tunneling process (Fahrner, 2011). On considering this fact, Taguchi et al. (Taguchi et al., 2000) inserted a pristine a-Si layer between the n-type c-Si and p-type a-Si that leads to clampdown of the backward current density and thus progresses the Voc and solar cell performances. The structure is known as HIT that abbreviates as Heterojunction with an Intrinsic Thin-layer (Taguchi et al., 2000) . A very thin intrinsic a-Si layer is inserted between p-type a-Si and n-type c-Si to form this structure. At low temperature process, higher efficiencies with no complicated structures make HIT a favorable candidate for PV applications. Moreover, optical absorption loss occurs in conventional HIT structure due to absorption in a-Si: H emitter and intrinsic layers along with shading loss by metal grids. These issues can be resolved using IBC design that was proposed by Lammert et al. (Schwartz and Lammert, 1975, Lammert and Schwartz, 1977). This design contains contact as well as junction on its back side which provides independent control for better optical performance at illuminated side and enhanced low series resistance electrical performance on the back side as discussed in **Section 1.6:** of **Chapter 1**.

Incorporation of HIT design to IBC cells result in interdigitated back contact silicon heterojunction, IBC-SiHJ solar cells. Due to outstanding performance and simple low temperature process, the IBC-SiHJ solar cell consisting of thin layers of a-Si:H deposited made it most favorable technological solution in PV market (Taira et al., 2007). A record 25.6 % conversion efficiency was achieved by Panasonic Corporation on an industrial sized (143.7 cm^2) solar cell based monocrystalline- ‘HIT’ (Masuko et al., 2014). The main contributors to this increased efficiency were mitigation of optical loss, resistance loss and recombination loss. The advantages of IBC were incorporated into IBC-SiHJ solar cell having all the contacts at back of the device, which led to higher J_{SC} by eliminating contact shading and heterojunction silicon cell with high V_{OC} due to the enhanced surface passivation of the deposited i-a-Si: H layer (Lammert and Schwartz, 1977, Smith et al., 2012, Cousins et al., 2010).

Moreover, perovskite/silicon tandem solar cell discussed in the previous chapter contains diffused p-n junction which shows lower V_{OC} and has high complexity in fabrication, whereas high processing temperature (800ºC) is avoided in IBC-SiHJ solar cell which is essential to develop standard diffused homojunction cells and contact. Warping and cracking of thin wafers at high temperature processing can be eliminated in IBC-SiHJ structure as the processing steps are performed at 200ºC. It is easier to control the position of the *p*- and *n*-type doped layers by using the process of deposition in place of diffusion, which lowers the probability of shunting between the emitter and base contacts (Lu et al., 2007). Henceforth, this chapter deals with design and simulations of mechanically stacked perovskite/ SiC-passivated IBC-SiHJ tandem solar cell for ultra-high efficiencies under single AM1.5 irradiance. Analysis of SiC-based front passivation has also been discussed for bottom IBC-SiHJ solar cell and performance is compared with convention ARC based passivation scheme. Moreover, the analysis of perovskite top subcell reported in this chapter is the continuation of **Chapter 3**.

4.2: DEVICE STRUCTURE, MODELS AND METHODS

Figure 4.1(a-c) on page 75 represents the simulated device structures. Perovskite top subcell is identical to as discussed in **Chapter 3** and shown in **Figure 4.1**(a), whereas bottom IBC-SiHJ subcell along with mechanically stacked 4-terminal tandem cell is shown in **Figure 4.1**(b) and **Figure 4.1**(c), respectively. The device structure has been designed using the

ATHENA process simulator (Silvaco, 2015). The dimensions, and material parameters as reported in **Table 4-1** on page 76 are obtained from already published simulation work reported by Belarbi et al. (Belarbi et al., 2016), the doping density 2.14×10^{16} cm^{-3} and 4.8×10^{18} cm^{-3} have been used for n-type c-Si and n-type a-Si:H, respectively. The width 180 µm and 950 µm have been used for n-type a-Si: H and n-type a-Si: H, respectively, and the width of the gap region is 50 µm. After successfully re-obtaining the results as reported by Belarbi et al. (Belarbi et al., 2016), ARC is replaced with a 20-nm thick SiC layer along with 80-nm-thick SiO_2-based encapsulation. The modified device is shown in **Figure 4.1**(b) below.

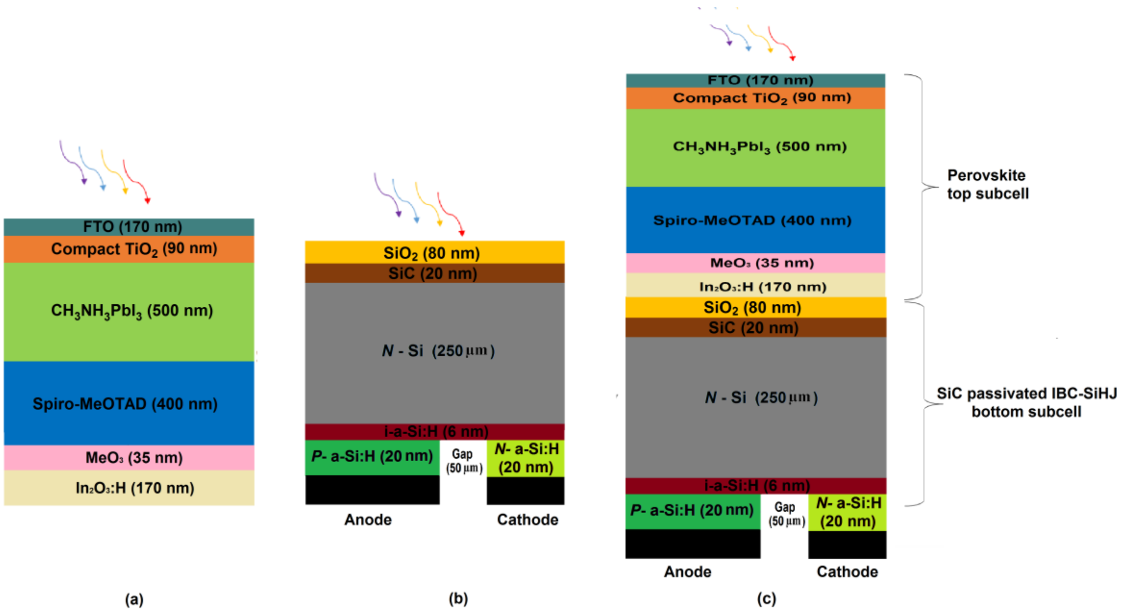

Figure 4.1: Device structures used in simulation: (a) perovskite top subcell with indium oxide (In_2O_3: H) as a transparent rear electrode, (b) SiC-based IBC-SiHJ bottom subcell and (c) mechanically stacked perovskite/ IBC-SiHJ tandem cell (Pandey and Chaujar, 2017) .

Moreover, to obtain the J-V curve under AM1.5 illumination, the Poisson equation is solved along with the electron and hole continuity equations (see Appendix). The perovskite top subcell cell is simulated, based on the recombination dynamics in $CH_3NH_3PbI_3$ with the help of SRH, Auger, and radiative recombination models to account for monomolecular, bimolecular, and trimolecular recombinations as discussed in **Chapter 3**, whereas for the bottom IBC-SiHJ cell, Bohm quantum potential combined with drift-diffusion accounts for quantum correction and carriers distribution are solved by Fermi statistics (Atlas, 2017, Iannaccone et al., 2004). The concentration-dependent SRH, concentration-dependent mobility, and Auger recombination are activated for the bottom IBC-SiHJ solar cell. The radiative recombination model is omitted for the IBC-SiHJ cell since silicon is an indirect bandgap semiconductor and band to band recombination is insignificant.

TABLE 4-1: MATERIAL PARAMETERS FOR IBC-SIHJ SOLAR CELL USED DURING SIMULATION (BELARBI ET AL., 2016, PANDEY AND CHAUJAR, 2017).

Material		*n* type a-Si:H	Buffer a-Si:H	*p* type a-Si:H	Interface defects
Dielectric Constant		11.9	11.9	11.9	
Band Gap (eV)		1.70	1.70	1.70	1.17
Electron Affinity (eV)		3.9	3.9	3.9	
Thickness (µm)		0.02	0.006	0.02	0.001
Effective conduction band (DOS) (cm^{-3})		2.5×10^{20}	2.5×10^{20}	2.5×10^{20}	
Effective valence band (DOS) (cm^{-3})		2.5×10^{20}	2.5×10^{20}	2.5×10^{20}	
Conduction tail states	$N^{c\text{-}tail}\ A$ (cm^{-3})	10^{21}	10^{18}	10^{21}	0
	$E^{c\text{-}tail}\ A$ (eV)	0.12	0.09	0.07	0.07
Valence tail states	$N^{v\text{-}tail}\ D$ (cm^{-3})	10^{21}	10^{18}	10^{21}	0
	$E^{v\text{-}tail}\ D$ (eV)	0.12	0.09	0.12	0.12
Acceptor-like (A) dangling bond states	$N^{db}\ A$ (cm^{-3})	10^{19}	10^{16}	10^{19}	2.4×10^{16}
	$E^{db}\ A$ (eV)	0.7	1.1	1.3	0.5
	$\sigma^{db}\ A$ (eV)	0.2	0.15	0.2	0.2
Donor-like (D) dangling bond states	$N^{db}\ D$ (cm^{-3})	10^{19}	10^{16}	10^{19}	2.4×10^{16}
	$E^{db}\ D$ (eV)	0.45	0.9	1.1	0.5
	$\sigma^{db}\ D$ (eV)	0.2	0.15	0.2	0.2

Further, the description of the material parameters used in the simulation is shown in **Table 4-1** above. The material and models parameters employed in simulations for the perovskite top subcell are identical as reported in **Table 3-1** on page 54 of **Chapter 3**. The optical properties for $CH_3NH_3PbI_3$, Spiro-MeOTAD, MoO_3, In_2O_3:H, TiO_2, FTO, c-Si, SiC and, SiO_2 are also identical to as reported in **Figure 3.2** on page 55 of **Chapter 3**, whereas optical properties of a-Si: H, have been used from the SOPRA database of the Silvaco ATLAS library (Atlas, 2017).

4.3: RESULTS

Result section of the chapter is divided into three parts: Comprehensive analysis of fundamental recombination and carrier distribution inside perovskite layer together with the study of hole transport layer, HTL layer and counter electrode (CE) work function; Analysis and comparison of SiC- passivated IBC-SiHJ solar cell; and Investigates the efficiency potential of mechanically stacked 4-terminal perovskite/SiC-passivated IBC-SiHJ based tandem solar cell.

4.3.1: Comprehensive investigation of fundamental recombination and carrier distribution inside perovskite layer

As discussed in the introduction section of the ongoing Chapter, the analysis of perovskite cell is the continuation of **Chapter 3**. This section gives the detailed discussion of recombination dynamics along with carrier distribution inside the perovskite layer. For better understanding, contour representation of MRR in the $CH_3NH_3PbI_3$ layer has been obtained for three carrier lifetimes and presented in **Figure 4.2**(a-c) on page 78, and data plot is shown in **Figure 4.3**(a) on page 78. The MRR for 10^{-6} s, 10^{-7} s and, 10^{-8} s lifetime based devices are reported in **Figure 4.2**(a), **Figure 4.2**(b) and, **Figure 4.2**(c), respectively. The recombination parameter is obtained under short-circuit condition with illumination. **Figure 4.2**(a-c) and **Figure 4.3**(a) clearly shows that the higher recombination rate is observed when carrier lifetime is equivalent to 10^{-8} s compared to 10^{-7} s and 10^{-6} s lifetime based devices, which is attributed to small diffusion length, which also validates the results reported in **Figure 3.5** on page 59 of **Chapter 3**.

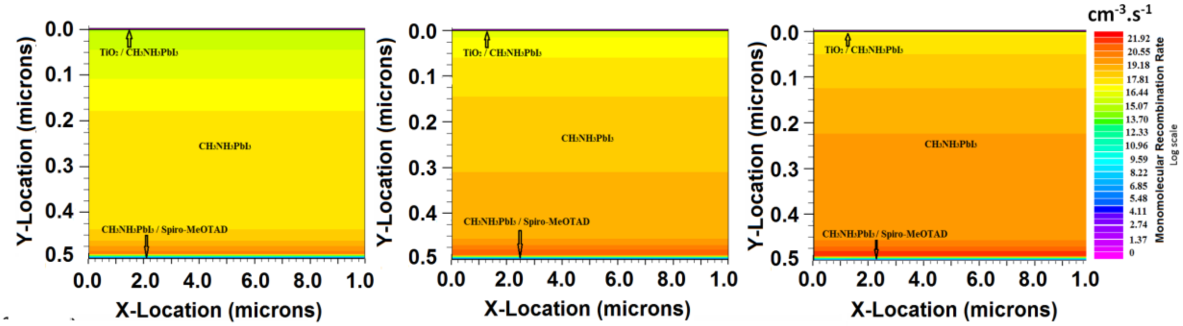

(a) (b) (c)

Figure 4.2: (a-c) Contour representation of monomolecular recombination rate inside the perovskite region with varying values of first order recombination lifetime, i.e. 10^{-6} s, 10^{-7} s, and 10^{-8} s, respectively (Pandey and Chaujar, 2017).

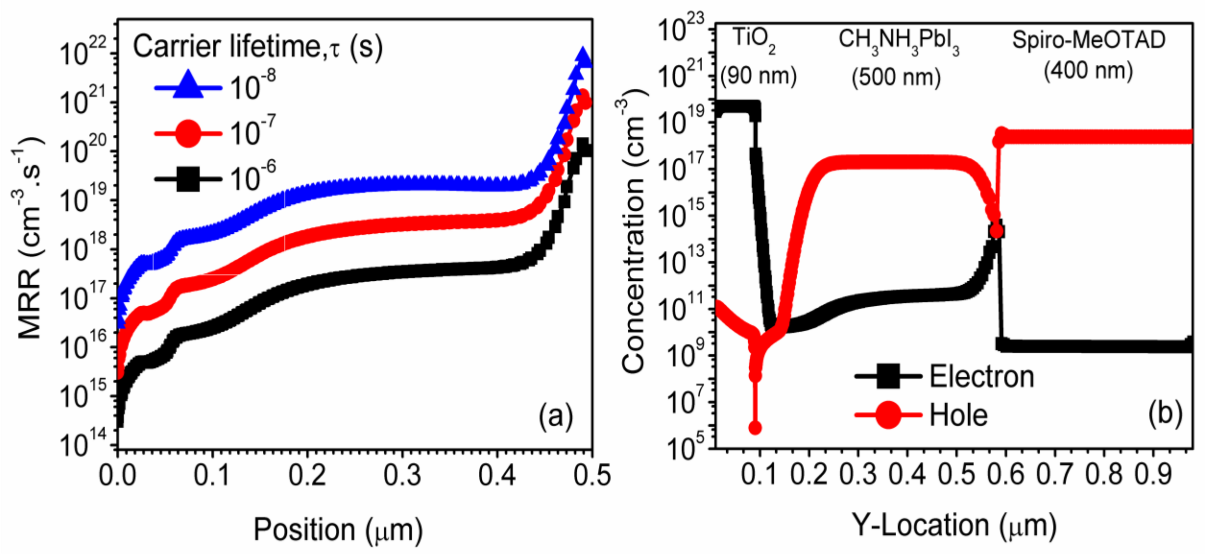

Figure 4.3: (a) X-Y representation of monomolecular recombination rate, the position in perovskite region is shown on X-axis and recombination rate is shown on y-axis and (b) show the carrier concentration in perovskite top subcell device, lifetime 10^{-6} s has been used. All the date has been obtained under short circuit condition with illumination (on) (Pandey and Chaujar, 2017).

Moreover, the MRR is lower at the TiO_2 (electron transport layer, ETL) / $CH_3NH_3PbI_3$ interface, increases in the bulk of the device and becomes maximum near the $CH_3NH_3PbI_3$ / Spiro-MeOTAD (HTL) interface. The distribution is obtained under short-circuit condition with illumination. Therefore, under short-circuit condition, the associated electric field of TiO_2 (ETL)/ $CH_3NH_3PbI_3$ interface collects the generated minority carrier electrons from the electron-hole (e-h) pair, and the collection is complete in near interface (ETL/perovskite). However, the region outside the (ETL/perovskite) interface is neutral, and the collection will be by diffusion towards the field area, where they will be separated and collected. Therefore, the areas closer to the (ETL/perovskite) interface will have lower recombination rate as shown in **Figure 4.2**(a-c) and **Figure 4.3** (a) on page 78. Furthermore, carrier concentration inside the device has also been obtained and presented in **Figure 4.3** (b); the carrier lifetime 10^{-6} s has been used for further analysis. Near ETL/perovskite interface electron concentration is less compared to the bulk region and perovskite/HTL interface, since outside the interface, the collection will be by diffusion of electrons towards the field area where it will be collected. The electrons that are generated in a region greater than the diffusion length are balanced by recombination process. Hence, there is a lateral concentration gradient for electrons, showing the lateral flow of electrons to the collecting junction. This also validates the higher MRR near perovskite/HTL interface as shown in **Figure 4.2**(a-c) and **Figure 4.3** (a).

Moreover, the contour representation of BRR and TRR has also been obtained in perovskite layer for three different devices viz. Device I, Device II and, Device III and presented in **Figure 4.4** on page 80. Device I is based on TRR and BRR coefficients of $3.4\text{x}10^{-28}$ $cm^6.s^{-1}$ and $1.5\text{x}10^{-10}$ $cm^3.s^{-1}$ (Yang et al., 2015a), Device II is based on TRR and BRR coefficients $3.7\text{x}10^{-29}$ $cm^6.s^{-1}$ and $9.4\ \text{x}10^{-10}$ $cm^3.s^{-1}$ (Wehrenfennig et al., 2014a), and

Device III is based on TRR and BRR recombination coefficients $3.7\text{x}10^{-29}$ $\text{cm}^6.\text{s}^{-1}$ and 1.5 $\text{x}10^{-10}$ $\text{cm}^3.\text{s}^{-1}$. **Figure 4.4**I(a), **Figure 4.4**II(a) and, **Figure 4.4**III(a) represents the TRR inside the perovskite layer of the Device I, Device II and, Device III, respectively, whereas **Figure 4.4**I(b), **Figure 4.4**II(b) , **Figure 4.4**II(b) shows BRR of the corresponding devices.

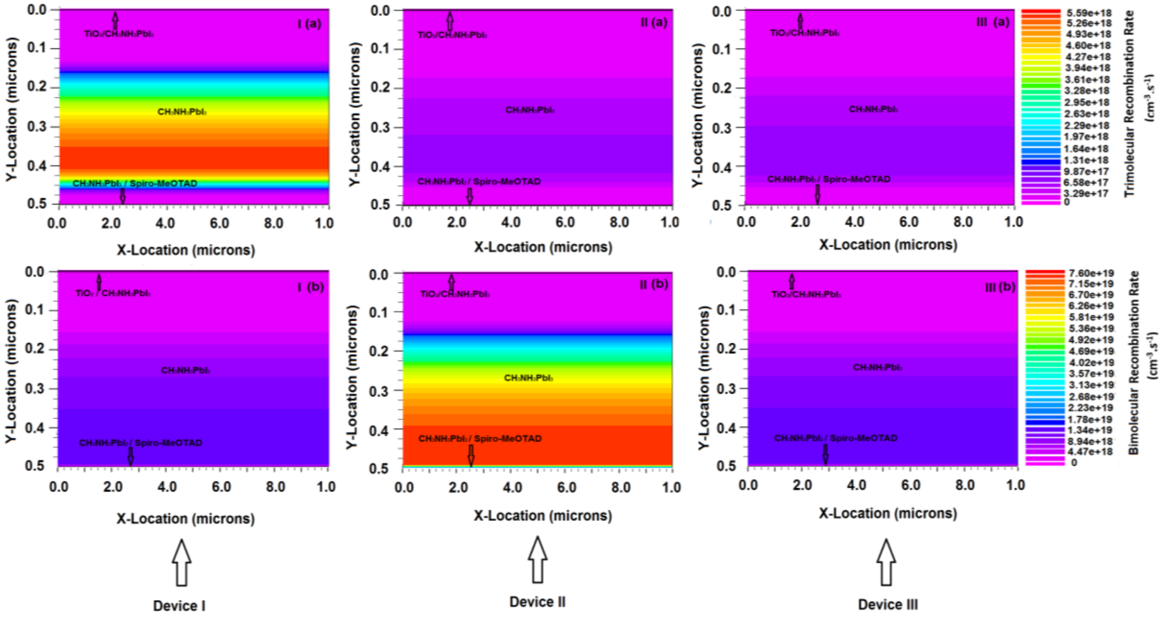

Figure 4.4: The contour representation of TRR and BRR inside the perovskite layer. I(a), II(a) and, III(a) shows the TRR of the Device I, Device II and, Device III respectively, whereas I(b), II(b) and, III(b) represents the BRR of the Device I, Device II and, Device III respectively. Device I is based on recombination coefficients $3.4\text{x}10^{-28}$ $\text{cm}^6.\text{s}^{-1}$ and $1.5\text{x}10^{-10}$ $\text{cm}^3.\text{s}^{-1}$, Device II is based on recombination coefficients $3.7\text{x}10^{-29}$ $\text{cm}^6.\text{s}^{-1}$ and 9.4 $\text{x}10^{-10}$ $\text{cm}^3.\text{s}^{-1}$, and Device III is based on recombination coefficients $3.7\text{x}10^{-29}$ $\text{cm}^6.\text{s}^{-1}$ and 1.5 $\text{x}10^{-10}$ $\text{cm}^3.\text{s}^{-1}$ (Yang et al., 2015a, Wehrenfennig et al., 2014a, Pandey and Chaujar, 2017).

Further, higher TRR and lower BRR is obtained in the Device I compared to Device II, since third order recombination rate is 9.2 times higher and second order recombination rate is 6.3 times lower compared to device II. Parameters suggested by Yang et al. (Yang et al., 2015b) has higher third order recombination coefficient and lower second order recombination coefficient compared to parameters reported by Wehrenfennig et al. (Wehrenfennig et al., 2014b). Hence, perovskite device simulations on the basis of parameters reported by Yang et al. (Yang et al., 2015a) shows superior photovoltaic performance as indicated in **Figure 3.4** on page 58 and **Table 3-2** on page 59 of **Chapter 3**. Results also demonstrate the magnitude of TRR is lower compared to BRR, as shown in in **Figure 4.4** on page 80, which validates the data plot of recombination rates reported in **Figure 3.6** on page 61 of **Chapter 3**. Hence, the significant efficiency limiting factor for perovskite cell is radiative recombination, and the statement is well supported by experimental results (Xing et al., 2014). However, in defected perovskite layer having 10^{-8} s carrier lifetime, monomolecular recombination plays a significant role in performance degradation as discussed earlier.

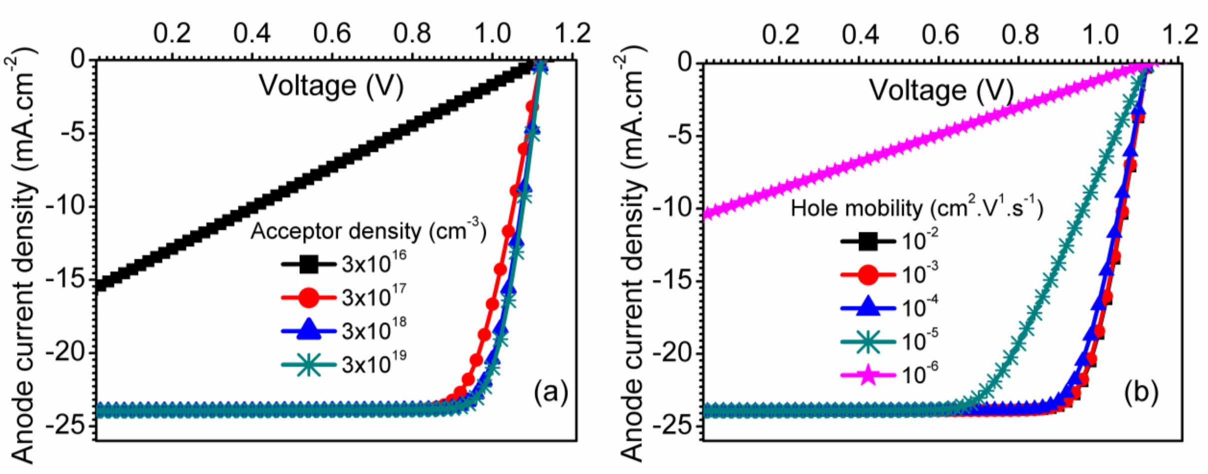

Figure 4.5: The J-V curves of the perovskite top cell (a) varying acceptor density in HTL layer with constant mobility of 10^{-4} cm^{2}.V.s^{-1} and (b) varying hole mobility in HTL layer with constant acceptor density of 3 x 10^{18} cm^{-3} (Pandey and Chaujar, 2017).

Additionally, the analysis of HTL and CE has also been done. The effect of doping and hole mobility in Spiro-MeOTAD (HTL) on device performance has been obtained and presented **Figure 4.5**(a-b) on page 81. The J-V curve improves by increasing the acceptor doping in HTL as shown in **Figure 4.5**(a), since for low acceptor concentration the series resistance of HTL is high. Further, the hole mobility of HTL has an appreciable effect on the performance of the device. The basic role of this layer is to extract the holes from electron-hole pair reaching the (perovskite/HTL) interface. Therefore, HTL must be a good hole conductor, to perform its hole collecting function well. Also, it must not allow the stack up of the holes in it near the interface. However, if this occurs because of low hole mobility, the free holes will recombine with free electrons on both sides of the interface and thus would lead to a decrease in collector current. Another effect also comes into the play, having low hole mobility results in increased resistance causing a larger voltage drop for the same cell current. Thus, the increased series resistance of the cell leads to decrease in FF of the device. So the effect of hole mobility is a twofold, i.e., decrease in both the collected current as well as FF of the device, as shown in **Figure 4.5**(b) on page 81.

Moreover, the effect of the counter electrode, CE work function has also been discussed. The performance of the device degrades with decreasing the work function. The distribution of electric field examined in HTL layer near the HTL/CE interface by exaggerating small region near HTL/CE interface as reported in **Figure 4.6(a-h)** on page 83. The contour representation of electric field with CE work function of 4.3eV, 4.9eV, 5.0eV, and 5.1eV is reported in **Figure 4.6(a)**, **Figure 4.6(b)**, **Figure 4.6(c)**, and **Figure 4.6(d)**, respectively, whereas corresponding data has also been reported in **Figure 4.6(e)**, **Figure 4.6(f)**, **Figure 4.6(g)**, and **Figure 4.6(h)**, respectively. Results reveal that direction of the field near HTM/CE interface becomes negative when the work function value is below 5.0 eV, which means the electric field direction is directed from CE to HTL, rendering it energetically unfavorable for hole transport to the electrode and hence increase the series resistance. This attributed to the possible formation of the Schottky junction at the HTL/CE interface, which further results in decreased FF as reported in **Figure 4.7** on page 83.

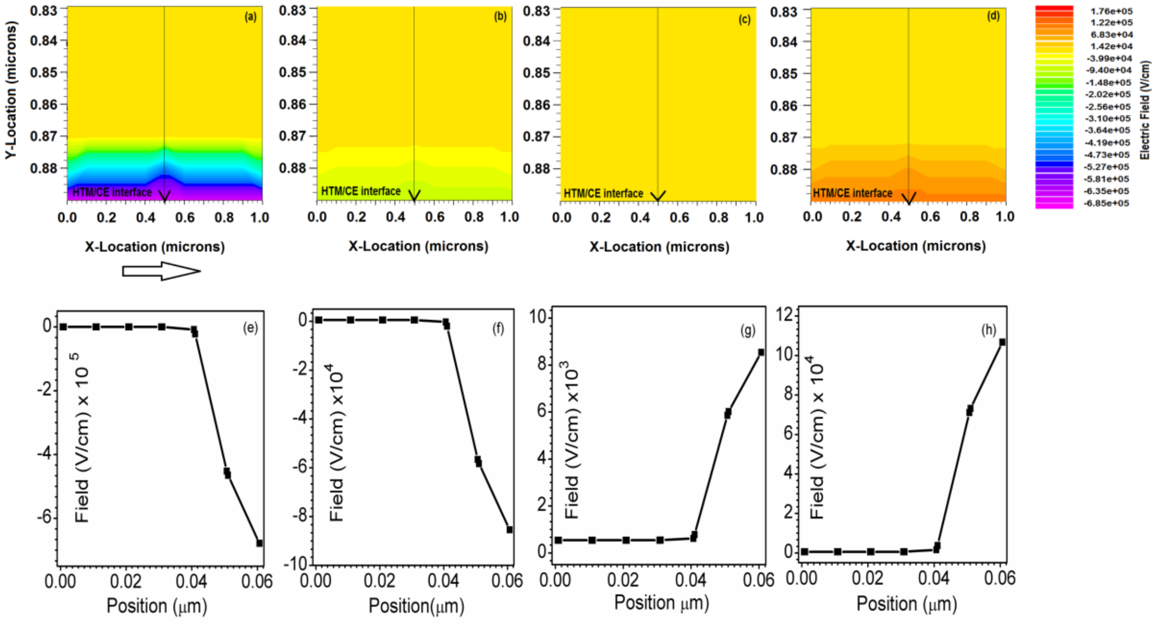

Figure 4.6: The contour representation of electric field near HTL/CE interface with different CE work functions (a) 4.3eV, (b) 4.9eV, (c) 5.0eV, and (d) 5.1eV respectively, and the corresponding data has also been presented in (e), (f), (g), and (h), respectively using cutline of contour representation as shown (a-d) (Pandey and Chaujar, 2017).

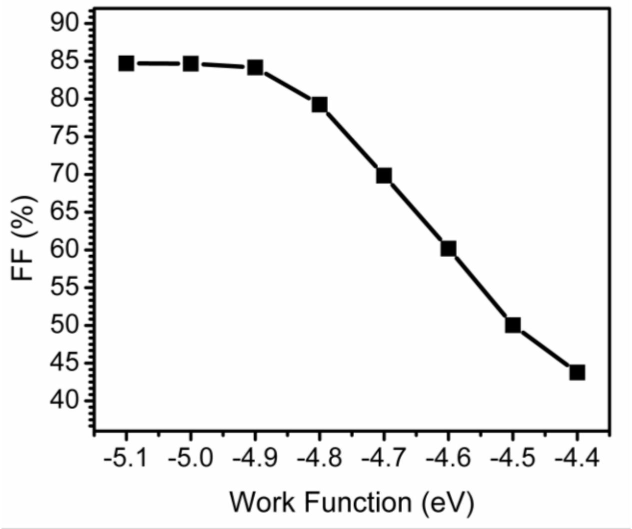

Figure 4.7: Impact of CE metal work function on FF of the perovskite device (Pandey and Chaujar, 2017).

The impact of acceptor density, hole mobility in HTL, and CE work function on the photovoltaic performance of perovskite top cell shows identical behavior as reported by Liu et al. (Liu et al., 2014), using AMPS (analysis of microelectronic and photonic structures)-1D device simulator.

4.3.2: Analysis and comparisons of SiC passivated IBC-SiHJ bottom subcell

In this section, the performance of SiC-based IBC-SiHJ has been compared with conventional ARC based IBC-SiHJ and the external quantum efficiency, EQE and J-V curves have been obtained for both the devices as reported in **Figure 4.8**(a-b) below. **Figure 4.8**(a) shows, EQE of the SiC passivated IBC-SiHJ device is higher as compared to ARC based device since the presence of SiC increases the optical coupling in the underlying substrate as discussed in **Chapter 2**, and supported by previous publications (Allen and Awad, 2009, Pandey and Chaujar, 2016).

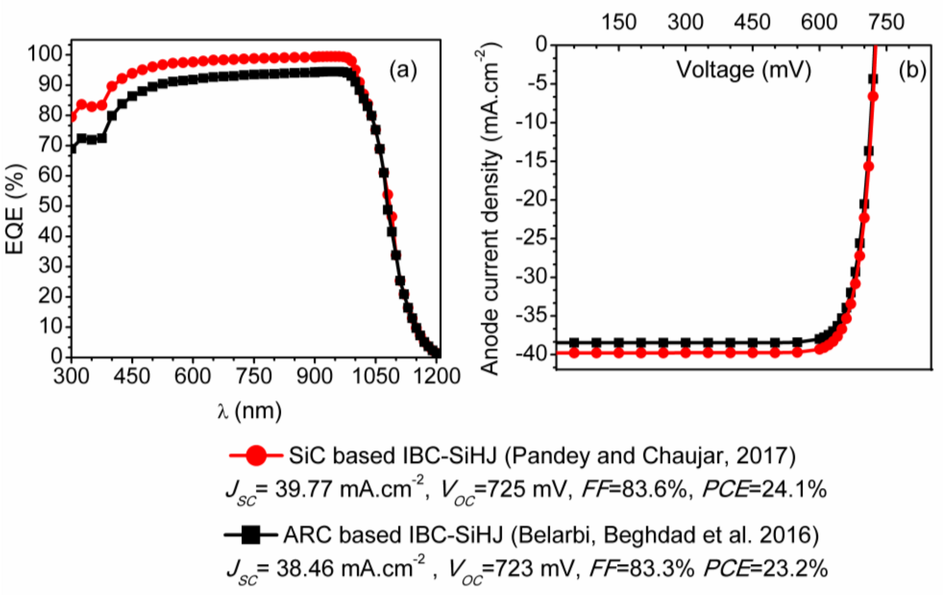

Figure 4.8: Comparison of the optical and electrical behavior of SiC and ARC based IBC-SiHJ subcell in the standalone configuration: (a) EQE and (b) J-V curve. Analysis has been done with surface recombination velocity, SRV (10 cm/s) (Pandey and Chaujar, 2017).

Further, at wavelength equivalent of 300 nm, the EQE of the SiC-based device is 79% whereas in ARC based; it is 69%. This results in 14.5% higher EQE in the SiC passivated device. Also, EQE of the SiC-based device is greater than 79% in the spectrum range of (300-1040) nm wavelength, as shown in **Figure 4.8**(a) on page 84. The higher optical performance leads to higher J_{SC}; the J_{SC} values of 38.46 mA.cm^{-2} and 39.77 mA.cm^{2} has been obtained in ARC and SiC-based devices, respectively, as shown in **Figure 4.8**(b). 24.1% PCE has been achieved in SiC passivated IBC-SiHJ solar cell compared to 23.2% in ARC based IBC-SiHJ solar cell. The advantage of using the SiC-based IBC-SiHJ device is that it provides dual benefits in terms of increased optical behavior as well as enhanced front surface passivation quality as discussed in **Chapter 2**.

4.3.3: Examination of 4-terminal perovskite/SiC-passivated IBC-SiHJ tandem solar cell

In this section, a 4-terminal perovskite/SiC-passivated IBC-SiHJ based mechanically stacked tandem device has been designed and analyzed using numerical simulation. The procedure of analysis is similar to the **Chapter 3**; tandem device simulated in this section is reported in **Figure 4.1**(c) on page 75, which comprises perovskite as top subcell and SiC passivated IBC-SiHJ solar cell bottom subcell. The performance of IBC-SiHJ bottom cell is directly measured by placing perovskite device as a filter under standard AM1.5 illumination, to simulate the condition when IBC-SiHJ is positioned as bottom subcell. For bottom subcell, two types of the IBC-SiHJ solar cell has been used, one with the thickness of 250µm and second with the thickness of 25µm. This results in two 4-terminal tandem devices. All the dimensions of 250 µm thick device have been reduced 10 times except the gap width, to obtain 25 µm thick IBC-SiHJ solar cell. The carrier lifetime of 10^{-5} s is used for 25 µm thick device since lower diffusion length is required compared to 250-micron thick device. The 25 µm thick device is thin compared to conventional 250 µm thick silicon solar cells, and hence, the device can be fabricated with inexpensive, less pure material. The performance of IBC-SiHJ solar cells has been obtained for both standalone as well as bottom subcell conditions for the comparisons and presented in **Figure 4.9** (a-c) below.

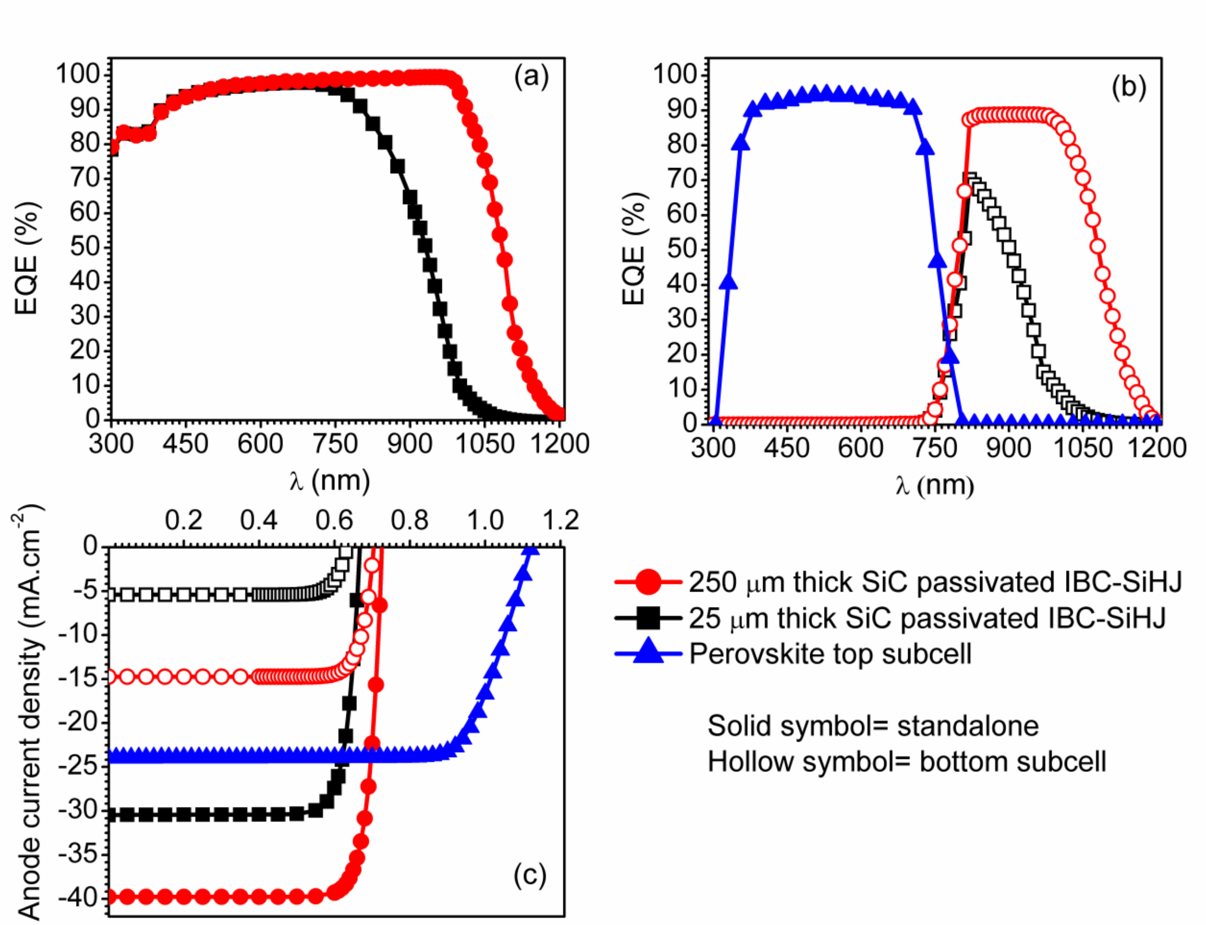

Figure 4.9: (a) EQE of 250 µm and 25 µm thick SiC passivated IBC-SiHJ solar cell under standalone conditions. (b) EQE of perovskite top subcell and IBC-SiHJ bottom subcells in a tandem configuration. (c) The J-V curve of IBC-SiHJ cells in stand-alone and bottom subcell configuration along with J-V curve of perovskite top subcell (Pandey and Chaujar, 2017).

Figure 4.9(a) above shows the spectral response of IBC-SiHJ solar cells in standalone condition. The result indicates that the optical performance of 25 µm thick device is inferior compared 250 µm thick device. The EQE starts to fall at a lower wavelength in the case of 25 µm thick device. This shows that 25-micron thick subcell device is not capable of absorbing high energy photon compared to 250-micron thick device as shown in **Figure 4.9** (a-b) on page 86, since photon absorbance is directly related to the absorption coefficient and the thickness of the material used. This will lead to the superior photovoltaic performance of 250-micron thick bottom subcell based tandem device. Moreover, **Figure 4.9**(c) shows the performance of bottom subcell cell with and without perovskite filter. In stand-alone configuration, the J_{SC} of 39.77mA.cm^{-2} and 30.45mA.cm^{-2} have been obtained in 250 micron and 25-micron thick bottom subcells, respectively as shown in **Figure 4.9**(c). After adding the perovskite top cell, the J_{SC} of bottom subcell decreases to 14.74 mA.cm^{-2} and 5.42 mA.cm^{-2} for 250 micron and 25 micron thick devices respectively, due to reduced light intensity. The decrease in V_{OC} is only marginal, resulting in 8.6% and 2.8% efficient two bottom subcells. Therefore, together with the 20.9% efficiency of perovskite top subcell, this results in 29.5% and 23.7% efficient tandem device with 250-micron and 25-micron thick bottom subcells, respectively. This is a substantial improvement as compared to transparent perovskite solar cell and c-Si solar cell operated individually. The photovoltaic parameters of tandem devices are shown in **Table 4-2** below.

TABLE 4-2: PHOTOVOLTAIC PARAMETERS OF THE DEVICES IN STAND-ALONE AND TANDEM CONFIGURATIONS (PANDEY AND CHAUJAR, 2017).

Solar cells	J_{SC} (mA.cm^{-2})	V_{OC} (mV)	FF (%)	PCE (%)
Perovskite top subcell	23.95	1121	77.8	20.9
IBC-SiHJ bottom cell 25 micron (stand-alone)	30.45	667	82.3	16.7
IBC-SiHJ bottom cell 25 micron (tandem)	5.42	632	81.6	2.8
IBC-SiHJ bottom cell 250 micron (stand-alone)	39.77	725	83.6	24.1
IBC-SiHJ bottom cell 250 micron (tandem)	14.74	704	82.7	8.6
4-terminal using 10 micron thick Si bottom subcell				20.9+2.8=23.7
4-terminal using 300 micron thick Si bottom subcell				20.9+8.6=29.5

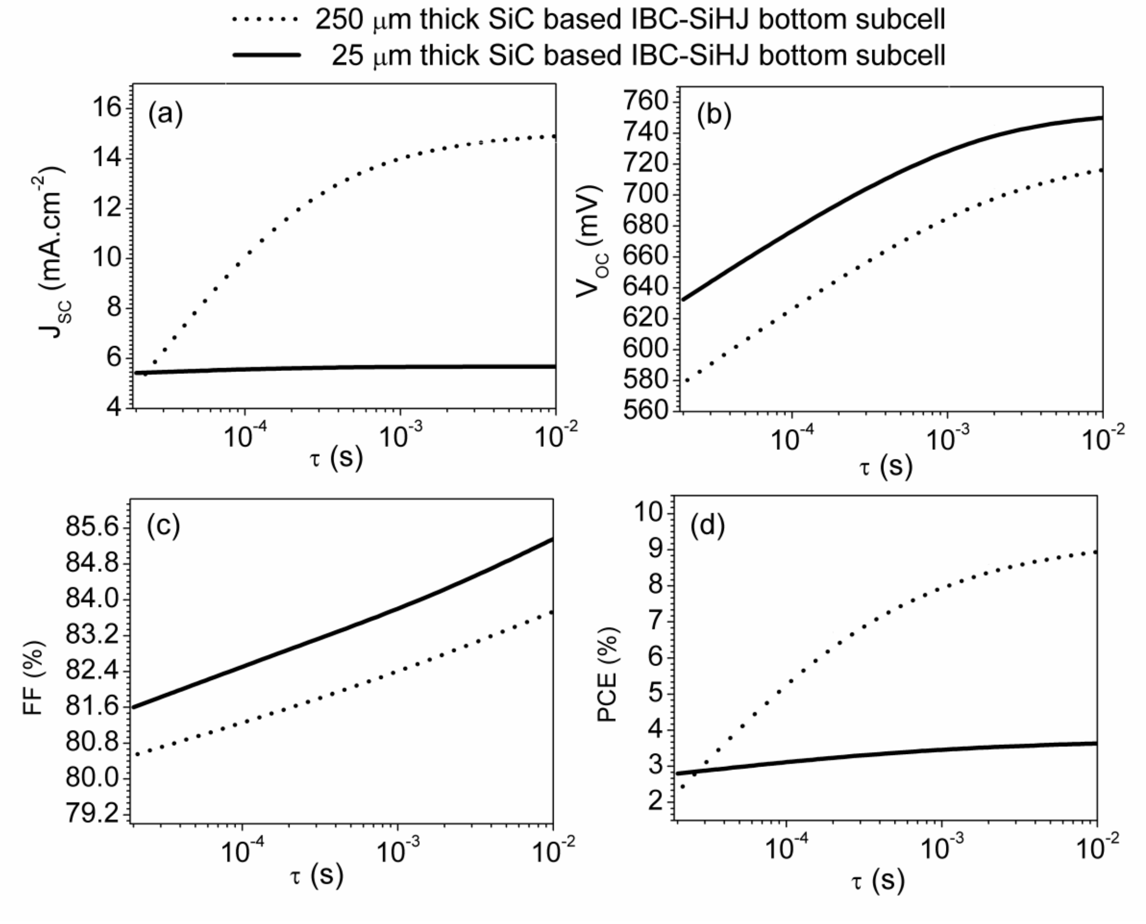

Figure 4.10: The impact of carrier lifetime on the performance of IBC-SiHJ bottom subcells in a tandem configuration: (a) J_{SC}, (b) V_{OC}, (c) FF, and (d) PCE (Pandey and Chaujar, 2017).

Moreover, the impact of material quality has also been obtained on the performance of IBC-SiHJ solar cells. Therefore, the bottom subcell has been simulated with different carrier lifetimes to get the impact of material (c-Si) quality, and results are reported in **Figure 4.10**(a-d) above. Impact of lifetime on photovoltaic parameters: J_{SC}, V_{OC}, FF, and PCE is reported in **Figure 4.10**(a), **Figure 4.10**(b), **Figure 4.10**(c), and **Figure 4.10**(d), respectively. The charge carriers need to diffuse a shorter length in the thinner device. Therefore, the PV performance of smaller device shows the negligible impact of material quality, whereas significant degradation has been observed in the thicker device, as shown in **Figure 4.10**(a) - **Figure 4.10**(d). Results show that for lower carrier lifetime (2 × 10^{-5} s), the performance of a 250-

μm-thick device is lower compared to a 25-μm-thick device, due to higher bulk recombination of the carrier in the thicker device, since lifetime is small. The V_{OC} values of the thinner device are higher compared to the thicker device as shown in **Figure 4.10**(a) on page 88. Since the 25-μm-thick device has 10 times smaller substrate, the charge-carrier concentration in the 25-μm-thick device is higher than the 250-μm-thick device, which led to higher V_{OC}. The desired material quality and the device can be selected from **Figure 4.10**, depending upon the application. Total efficiency in a tandem configuration can be obtained by adding the efficiencies of the bottom subcell and perovskite top cell.

4.4: SUMMARY

This chapter presents TCAD design of a 29.5% efficient mechanically stacked perovskite / IBC-SiHJ tandem device. Results show, PCE of 29.5 % and 23.7% with 250 μm and 25 μm thick IBC-SiHJ bottom subcells, respectively. Semitransparent perovskite top subcell with the efficiency of 20.9% has been designed for perovskite-silicon tandem structure. Thorough TCAD analysis has been performed to predict the behavior of the devices. All the basic recombination rates along with carrier distribution are obtained and reported to understand the recombination processes inside the perovskite top subcell. The performance of top subcell has been obtained for different acceptor densities and hole motilities in HTL, along with the impact of counter electrode work function. Increasing the acceptor density and hole mobility in HTL beyond $3\times10^{16}\,\text{cm}^{-3}$ and $10^{-5}\,\text{cm}^{2}.\text{V}^{1}.\text{s}^{-1}$ shows significant improvement in the performance of perovskite top subcell. Electric field distribution near HTL/CE shows CE work function value > 4.9 eV is required for the efficient extraction of holes from HTL. For bottom subcell, 24.1% efficient individually operated IBC-SiHJ solar cell is combined in mechanically stacked four terminal tandem configuration with 20.9%

efficient perovskite top subcell. SiC passivated IBC-SiHJ bottom subcell shows good photovoltaic parameters compared to ARC based IBC-SiHJ solar cell. The optical and electrical behavior of the devices has been obtained for both standalone as well as tandem configuration. Results reveal that discussed tandem device may open a new door for the cost-effective and energy efficient applications.

In the previous three chapters, SiC passivated rear contact silicon solar cells are designed for standalone as well as tandem configuration. However, the absorption coefficient of silicon is small at higher wavelengths; therefore thick silicon wafers are required to obtained greater efficiencies in both standalone as well as tandem configuration as discussed in current chapter and **Chapter 3**. However, thicker silicon wafer eventually increases the module cost. Hence, low bandgap (<1.1eV) materials are required to increase the absorption of sunlight at higher wavelengths while keeping the thickness low, and $Si_{1-X}Ge_X$ can be used for the same. Therefore, the next two chapters deals with design and simulations of SiC passivated rear contact SiGe solar cells for standalone and tandem configuration.

4.5: REFERENCES

ALLEN, S. & AWAD, Y. 2009. Silicon carbide-based antireflective coating. *US Patent App. 12/994,973*.

ATLAS 2017. ATLAS User ' s Manual. 567-1000.

BELARBI, M., BEGHDAD, M. & MEKEMECHE, A. 2016. Simulation and optimization of n-type interdigitated back contact silicon heterojunction (IBC-SiHJ) solar cell structure using Silvaco Tcad Atlas. *Solar Energy,* 127**,** 206-215.

COUSINS, P. J., SMITH, D. D., LUAN, H. C., MANNING, J., DENNIS, T. D., WALDHAUER, A., WILSON, K. E., HARLEY, G. & MULLIGAN, W. P. Generation 3: Improved performance at lower cost. 2010 35th IEEE Photovoltaic Specialists Conference, 20-25 June 2010 2010. 000275-000278.

FAHRNER, W. R. 2011. *Amorphous Silicon / Crystalline Silicon Heterojunction Solar Cells*, Springer.

FUHS, W., NIEMANN, K. & STUKE, J. 1974. Heterojunctions of amorphous silicon and silicon single crystals. *Bull Am Phys Soc* 19**,** 6.

GRIGOROVICI, R., CROITORU, N., MARINA, M. & NASTASE, L. 1968. Heterojunctions between amorphous Si and Si single crystals. *Rev Roum Phys,* 13**,** 9.

IANNACCONE, G., CURATOLA, G. & FIORI, G. Effective Bohm Quantum Potential for device simulators based on drift diffusion and energy transport. Simulation of Semiconductor Processes and Devices, 2004. 275-278.

LAMMERT, M. D. & SCHWARTZ, R. J. 1977. The interdigitated back contact solar cell: A silicon solar cell for use in concentrated sunlight. *IEEE Transactions on Electron Devices,* 24**,** 337-342.

LIU, F., ZHU, J., WEI, J., LI, Y., LV, M., YANG, S., ZHANG, B., YAO, J. & DAI, S. 2014. Numerical simulation: Toward the design of high-efficiency planar perovskite solar cells. *Applied Physics Letters,* 104**,** 253508.

LU, M., BOWDEN, S., DAS, U. & BIRKMIRE, R. 2007. Interdigitated back contact silicon heterojunction solar cell and the effect of front surface passivation. *Applied Physics Letters,* 91**,** 063507.

MASUKO, K., SHIGEMATSU, M., HASHIGUCHI, T., FUJISHIMA, D., KAI, M., YOSHIMURA, N., YAMAGUCHI, T., ICHIHASHI, Y., MISHIMA, T., MATSUBARA, N., YAMANISHI, T., TAKAHAMA, T., TAGUCHI, M., MARUYAMA, E. & OKAMOTO, S. 2014. Achievement of More Than 25% Conversion Efficiency With Crystalline Silicon Heterojunction Solar Cell. *IEEE Journal of Photovoltaics,* 4**,** 1433-1435.

PANDEY, R. & CHAUJAR, R. 2016. Rear contact SiGe solar cell with SiC passivated front surface for >90-percent external quantum efficiency and improved power conversion efficiency. *Solar Energy,* 135**,** 242-252.

PANDEY, R. & CHAUJAR, R. 2017. Technology computer aided design of 29.5% efficient perovskite/interdigitated back contact silicon heterojunction mechanically stacked tandem solar cell for energy-efficient applications. *Journal of Photonics for Energy,* 7**,** 022503-022503.

SCHRÖDER, B., WEBER, U., LEDERMANN, A., SEITZ, H., KUPICH, M. & MUKHERJEE, C. Progress in thin-film-silicon-based solar cells prepared by thermo-catalytic CVD. Proceedings of the 17th European photovoltaic conference, , 2001 Muenchen, Germany pp. 2850.

SCHWARTZ, R. J. & LAMMERT, M. D. Silicon solar cells for high concentration applications. 1975 International Electron Devices Meeting, 1975 1975. 350-352.

SILVACO 2015. *ATHENA User's Manual, 2D PROCESS SIMULATION SOFTWARE,* Santa Clara, CA 95054 Silvaco.

SMITH, D. D., COUSINS, P. J., MASAD, A., WALDHAUER, A., WESTERBERG, S., JOHNSON, M., TU, X., DENNIS, T., HARLEY, G., SOLOMON, G., RIM, S., SHEPHERD, M., HARRINGTON, S., DEFENSOR, M., LEYGO, A., TOMADA, P., WU, J., PASS, T., ANN, L., SMITH, L., BERGSTROM, N., NICDAO, C., TIPONES, P. & VICENTE, D. Generation

III high efficiency lower cost technology: Transition to full scale manufacturing. 2012 38th IEEE Photovoltaic Specialists Conference, 3-8 June 2012 2012. 001594-001597.

TAGUCHI, M., KAWAMOTO, K., TSUGE, S., BABA, T., SAKATA, H., MORIZANE, M., UCHIHASHI, K., NAKAMURA, N., KIYAMA, S. & OOTA, O. 2000. HITTM cells—high-efficiency crystalline Si cells with novel structure. *Progress in Photovoltaics,* 8**,** 503-514.

TAIRA, S., YOSHIMINE, Y., BABA, T., TAGUCHI, M., KANNO, H., KINOSHITA, T., S., H., M. & E., T., M 2007. Our approaches for

achieving HIT solar cells with more than 23% efficiencies. *In: Proceedings of the 22nd EPVSEC.*

WEHRENFENNIG, C., EPERON, G. E., JOHNSTON, M. B., SNAITH, H. J. & HERZ, L. M. 2014a. High Charge Carrier Mobilities and Lifetimes in Organolead Trihalide Perovskites. *Advanced Materials,* 26**,** 1584-1589.

WEHRENFENNIG, C., EPERON, G. E., JOHNSTON, M. B., SNAITH, H. J. & HERZ, L. M. 2014b. High Charge Carrier Mobilities and Lifetimes in Organolead Trihalide Perovskites. *Advanced Materials,* 26**,** 1584-1589.

XING, G., MATHEWS, N., LIM, S. S., YANTARA, N., LIU, X., SABBA, D., GRÄTZEL, M., MHAISALKAR, S. & SUM, T. C. 2014. Low-temperature solution-processed wavelength-tunable perovskites for lasing. *Nature materials,* 13**,** 476-80.

YANG, Y., YANG, M., LI, Z., CRISP, R., ZHU, K. & BEARD, M. C. 2015a. Comparison of Recombination Dynamics in CH 3 NH 3 PbBr 3 and CH 3 NH 3 PbI 3 Perovskite Films: Influence of Exciton Binding Energy. *The Journal of Physical Chemistry Letters,* 6**,** acs.jpclett.5b02290-acs.jpclett.5b02290.

YANG, Y., YANG, M., LI, Z., CRISP, R., ZHU, K. & BEARD, M. C. 2015b. Comparison of Recombination Dynamics in CH 3 NH 3 PbBr 3 and CH 3 NH 3 PbI 3 Perovskite Films: Influence of Exciton Binding Energy. *The Journal of Physical Chemistry Letters,* 6**,** acs.jpclett.5b02290.

CHAPTER 5

REAR CONTACT SiGe SOLAR CELLS WITH SiC PASSIVATED FRONT SURFACE FOR IMPROVED CONVERSION EFFICIENCY

Silicon shows lower photon absorption at higher wavelengths due to small absorption coefficient, and to increase the absorption of sunlight while keeping the thickness low, small bandgap (<1.1 eV) material is required. Hence, this chapter along with next chapter of the thesis investigates the efficiency potential of SiGe material in SiC-based rear-contact solar cell architectures for standalone as well as tandem applications.

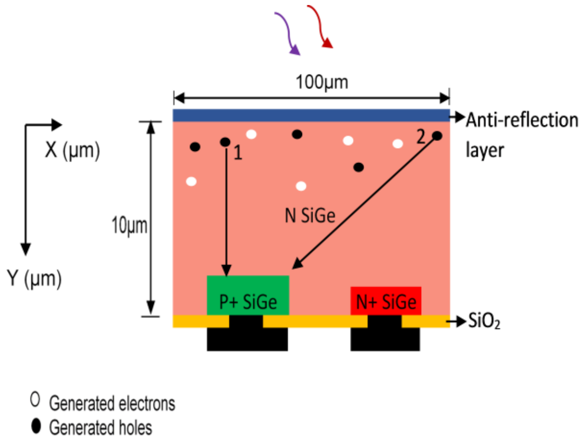

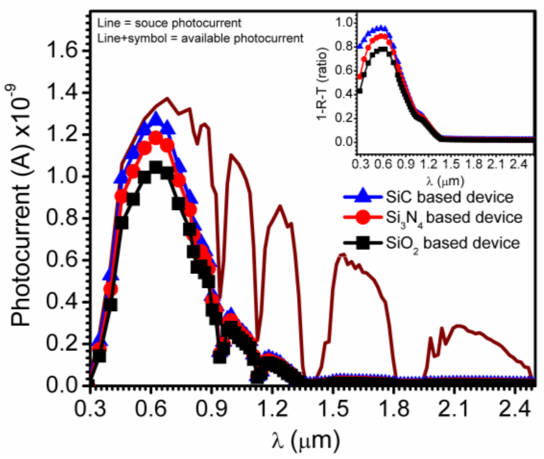

- *Innovative SiC-based rear contact SiGe Solar cells have been designed and simulated.*
- *EQE > 90% has been achieved in 400–650 nm wavelength spectrums.*
- *PCE of 15.4% has been achieved in 10 μm thick rear contact SiGe solar cell.*
- *Result reveals remarkably lower surface recombination and higher optical coupling.*
- *The device has also been analyzed for concentrator photovoltaics, CPV applications*

.

5.1: INTRODUCTION

Although, one of the most abundant element available on Earth's crust is silicon, fabrication of Si wafers are expensive, complex and time consuming (Fisher et al., 2012, Shimura, 2012). Miniaturization of active material used in solar PV devices is one of the crucial steps toward the reduction of cost, i.e., $/Watt (Garnett and Yang, 2010). Nevertheless, it is very difficult task to improve the efficiency of the cell while reducing its thickness, since photon absorption directly depends on the absorption coefficient and the thickness of the material. In c-Si PV technology, the solar cell is constructed using c-Si which has absolutely low absorption coefficient particularly at higher wavelengths (Green and Keevers, 1995), and hence the energy of the visible part of the spectrum utilized by the solar cell is less than 50%. High absorption material can be chosen to oppose a substantial reduction of efficiency in thickness of small layer (Das and Choudhary, 2013). Thin film solar cell made up of III–V compound shows higher efficiency because of their enhanced absorption and thus made them a common choice (Conibeer, 2007). Unfortunately, this technology is not suitable for marketable applications because they are very expensive and the cost is a grave concern to use them for terrestrial use (Yamaguchi, 2003). The magnitude of absorption in germanium, Ge is approximately 1 to 2 orders better than that of silicon, that is higher for 1.1 to 3.5 eV photon energy levels (Humlíček et al., 1989, Ahuja et al., 2003). Also, Ge offers outstanding absorption at 0.6 eV, i.e. low energy level (the long wavelengths) on the contrary to Si. However, Ge does not absorb wavelengths corresponding to less than 0.6 eV and Si does not capture the long wavelength resulting in energy less than about 1.1 eV. Thus, wavelengths ranging from 0.6 to 1.1 eV can be absorbed by Ge which cannot be achieved by Si (Bulletin, 2003). Around the world, various academic and industrial research groups are interested in reaping the benefits from the combination of both. PV cells can be manufactured at cheaper cost by enhancing the thin-film of c-Si via SiGe. The integration of SiGe alloy introduces enhancement in the near-infrared response via the reduced bandgap. PVs with superior adsorption characteristics and enhanced conversion efficiency can be achieved using SiGe, which makes it a promising candidate. However, SiGe solar cells are not used practically due to crystal quality deficiency and losses incurred in V_{OC}. Presently, high-frequency transistors are made up of SiGe and their potential is also being explored for solar cells (Ouellette, 2002, Kasap and Capper, 2007). Doping with Ge modifies the electrical properties of Si because number of electrons in Ge is higher than that of Si which results in higher conductivity at any given temperature. As both Ge and Si have similar physical and electrical properties, the fabrication of SiGe becomes easier in process. Illuminating the solar cell results in high intensity degradation which is suppressed by SiGe due to its greater mechanical strength (Yang et al., 2010). However, Silicon wafer is much cheaper as compared to Ge doped wafer (Chen and Yangoran, 2010), but current research work demonstrate it to be a potential candidate for energy efficient applications. Overall $/Watt of the device may be reduced by development of new cost-solar effective energy effective method in future.

Moreover, considering the fact discussed above, this chapter instigates the application of SiGe alloy in rear contact architecture based solar cell (Kerschaver and Beaucarne, 2006), to obtain the improved performances at higher wavelengths while avoiding complex texturing schemes. Initially, 10×10 µm thick SiGe wafer is designed with antireflective passivation layer (ARPL) followed by the representation of SiC-passivated rear contact SiGe solar cells to achieve higher efficiencies in sub 10 micron thick devices. Intrinsic and n-type wafer based device has been discussed. The optimization has been done along with surface passivation and optical absorption analysis of SiC passivation scheme. On the other hand, the proposed device has also been analyzed for CPV applications.

5.2: DEVICE STRUCTURE AND METHODS

The architecture of the device is identical to as discussed in **Chapter 2** of the thesis. However, Si has been replaced by SiGe and resulted devices are presented in **Figure 5.1**(a-b) below. The $Si_{0.9}Ge_{0.1}$ was used, with a very small Ge content, since increasing the Ge content, decreases the band gap of SiGe, which further results in lower open circuit voltage. Two different types of SiGe based rear-contact solar cell device has been designed one with intrinsic (i)-SiGe wafer and another with n-type SiGe wafer as shown in **Figure 5.1**(a) and **Figure 5.1**(b), respectively. All the material parameters for SiGe used in the simulation is obtained from experimentally available data (NSM, 2016).

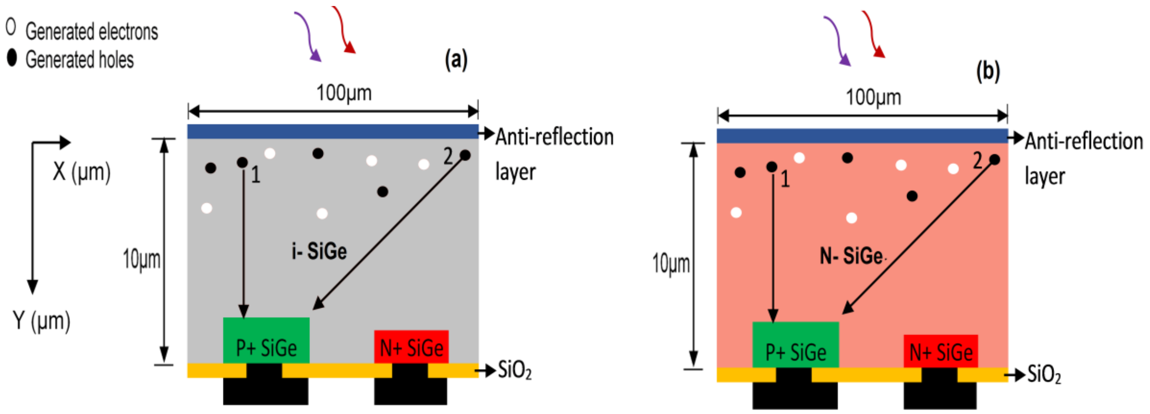

Figure 5.1: Rear contact SiGe solar cell with a 70nm thick antireflection layer on top, oxide layer has been used for back surface passivation. The region denoted by black color shows the ohmic contact to *n*+ and *p*+ regions: (a) intrinsic wafer based and (b) n-type wafer based device (Pandey and Chaujar, 2016a, Pandey and Chaujar, 2016b).

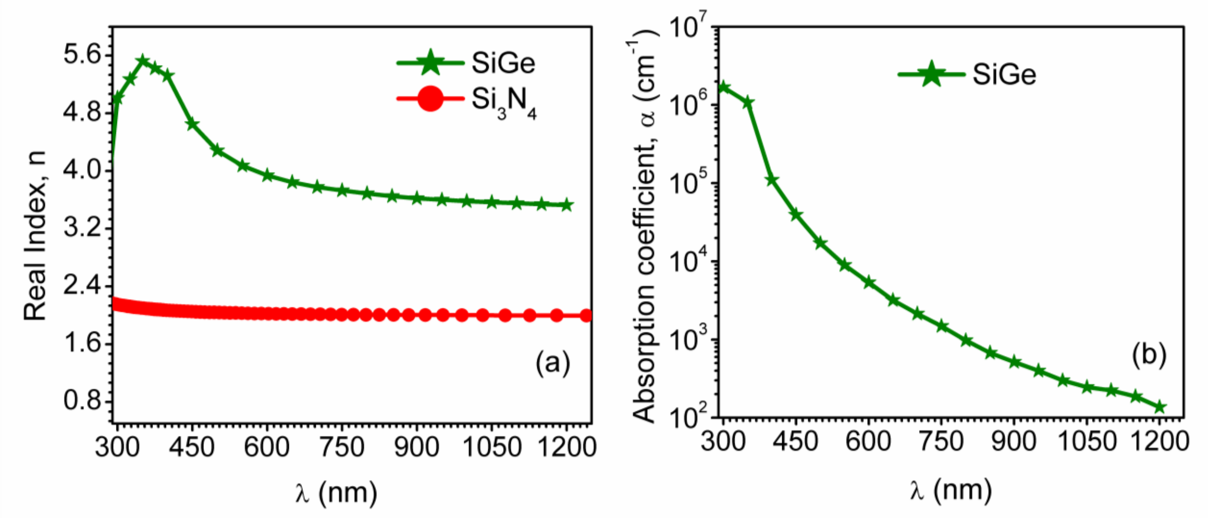

Figure 5.2: Optical properties, i.e. wavelength dependent (a) real index, n for SiGe and Si_3N_4 and (b) absorption coefficients of SiGe (Pandey and Chaujar, 2016b).

Further, the optical properties of Si_3N_4 and SiGe are reported in **Figure 5.2** (a-b) above. The real index values of Si_3N_4 and SiGe are indicated in **Figure 5.2**(a), whereas absorption coefficient of SiGe is shown in **Figure 5.2**(b). Moreover, optical properties of SiO_2 and SiC are identical as reported in **Figure 3.2**(f) on page 55 of **Chapter 3**. The analyses of i-SiGe and n-type SiGe wafer-based devices are reported in **Section 5.3.1:** and **Section 5.3.2:** , respectively. In **Section 5.3.1:** initial study has been done on the rear side of the device, i.e., energy band diagram has been obtained from *p+-i-n+* region to understand the movement of the carriers. Moreover, a new ARPL has also been designed for SiGe wafer using SiC, SiO_2 and Si_3N_4 layers; followed by its amalgamation to the SiGe based device. Added, impact carrier lifetime has also been obtained. Furthermore, **Section 5.3.2:** reports the optical and electrical analysis of n-type SiGe wafer based rear contact device, along with optimization, and at the end of the section, CPV application has also been discussed at different operating temperatures.

5.3: RESULTS

5.3.1: *Analysis of i-SiGe wafer based rear-contact solar cell*

This section includes the band diagram analysis along with designing of antireflective passivation layer with the help of SiC, Si_3N_4, and SiO_2 layers. Moreover, the impact of carrier lifetime has also been obtained. Initially, the energy band diagrams from *p*+ – *i* – *n*+ regions are examined under illuminated conditions, to analyze the motion of the carriers. **Figure 5.3** below shows if an electron (hole) is generated in the *i* region, it finds built-in potential at *i/p*+ (*i/n*+) interface and hence, will not travel towards *p*+ (*n*+) side. However as there is no barrier near *i/n*+ (*i/p*+) interface, it can quickly move toward *n*+ (p+) region as depicted in **Figure 5.3**. Hence, the *n*+ *(p+)* regions act as back surface field, BSF for holes (electrons).

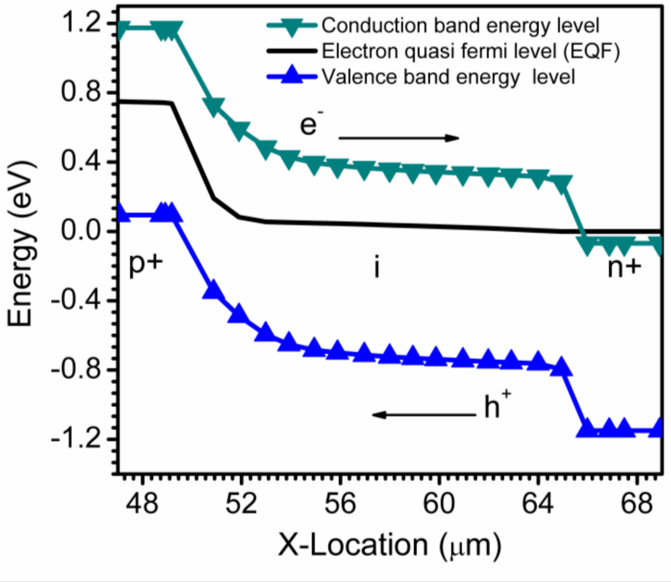

Figure 5.3: Illuminated energy band diagram of rear contact i-SiGe solar cell, data is obtained from *p*+-*i*-*n*+ region, i.e., at the rear side of the device (Pandey and Chaujar, 2016a).

Moreover, after analyzing the energy band, an antireflective passivation layer has also been designed for SiGe wafer using carbide, oxide, and nitride layers; and its application is discussed for rear contact SiGe solar cell, later in the section. Prior to the application of ARPL on the actual device, early analysis has been done on 10×10 µm thick intrinsic SiGe wafer, and spectrum response, i.e., reflectivity and available photocurrent are obtained in the wavelength spectrum and presented in **Figure 5.4** (a-b) below with different ARPLs. Wavelength vs. Reflectivity and available photocurrent, I_A of the wafer with different ARPL is reported in **Figure 5.4** (a) and **Figure 5.4** (b), respectively, whereas wavelength dependent source photocurrent I_S is presented in **Figure 5.4** (b) inset.

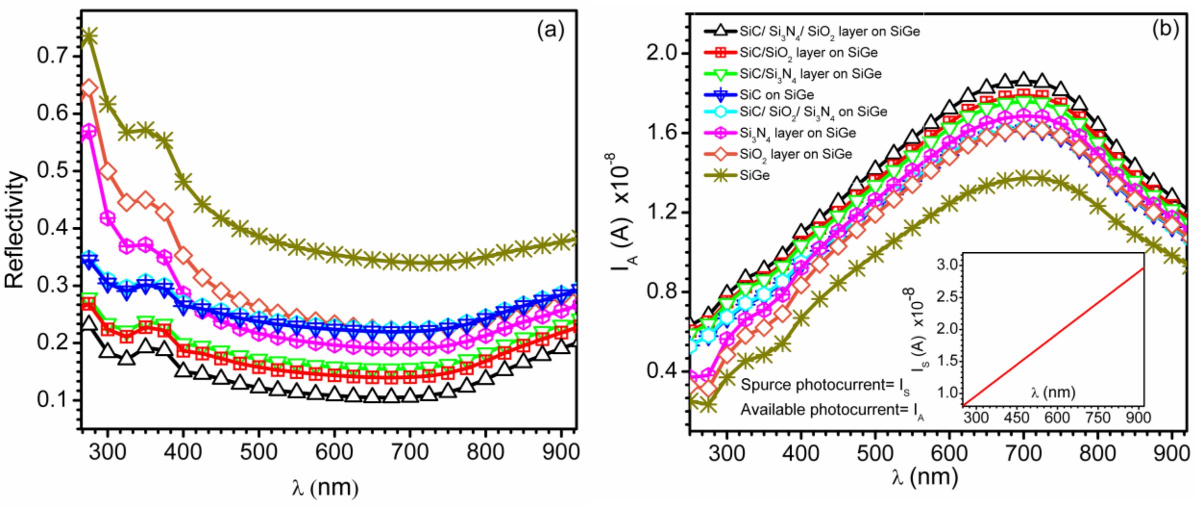

Figure 5.4: Spectrum response of (10 × 10) µm thick *i-SiGe* wafer with different ARPLs. (a) Reflectivity w.r.t wavelengths and (b) Available photocurrent w.r.t wavelengths: Inset shows source photocurrent w.r.t wavelengths (Pandey and Chaujar, 2016a).

Results as reported in **Figure 5.4** (a) above indicate a significant decrease in photo reflectivity in UV region due to the presence of SiC. However, results also indicate SiC is reflective in the visible region. Therefore, only SiC layered device shows lower I_A in the visible spectrum shown in **Figure 5.4** (b). Hence, to resolve the problem, oxide and nitride coated layers are placed on SiC, which results in better absorption as shown in **Figure 5.4** (a). Nevertheless, results indicate SiO_2 coated SiC provide better absorption compared to Si_3N_4

coated SiC. Moreover, SiGe wafer without any coating layer is highly reflective as depicted in **Figure 5.4** (a) on page 99, whereas, the highest optical coupling is observed in $SiC/Si_3N_4/SiO_2$ coated SiGe wafer compared to other layers and, hence I_A is close to I_S as reported in **Figure 5.4** (b) including inset. Likewise, results also indicate that SiC/SiO_2 coated SiGe wafer shows approximately same response as $SiC/Si_3N_4/SiO_2$ coated SiGe. This indicates SiC/SiO_2 coated SiGe can be used instead of $SiC/Si_3N_4/SiO_2$ coated SiGe in order to avoid complexity.

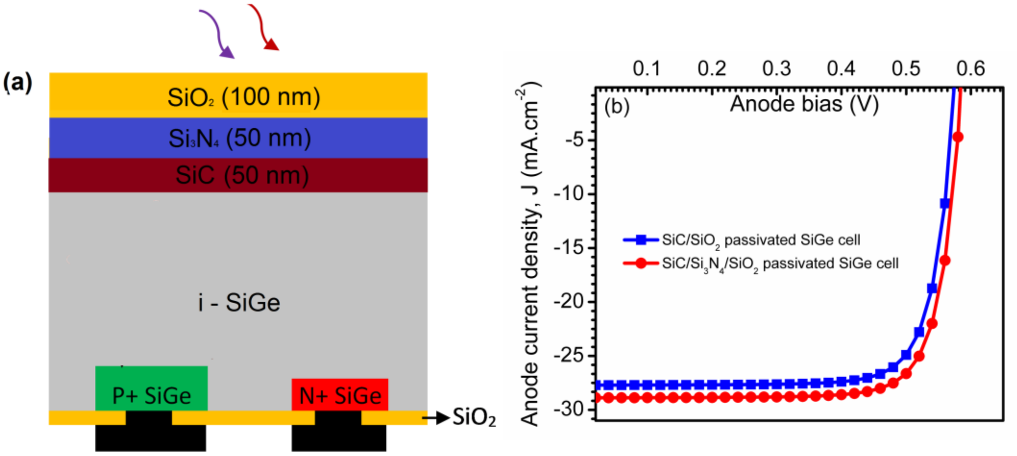

Figure 5.5: (a) Rear contact i-SiGe solar cell with $SiC/Si_3N_4/SiO_2$ based ARPL and (b) illuminated J-V curve of rear contact i-SiGe device with two different ARPLs (Pandey et al., 2016).

TABLE 5-1: COMPARISONS OF PHOTOVOLTAIC PARAMETERS OF 10μm THICK REAR CONTACT-i-SiGe SOLAR CELL WITH TWO DIFFERENT ARPLS (PANDEY AND CHAUJAR, 2016B)

Device	J_{SC} ($mA.cm^{-2}$)	V_{OC} (mV)	FF (%)	PCE (%)
$SiC/Si_3N_4/SiO_2$ based ARPL	28.9	585	79.1	13.4
SiC/SiO_2 based ARPL	27.7	575	78.8	12.5

Further, the designed ARPLs are introduced to the device and analysis has been done with two different front surfaces one with $SiC/Si_3N_4/SiO_2$ based front surface as depicted in **Figure 5.5**(a) above and another with SiC/SiO_2. The J-V curves of the devices are reported in

Figure 5.5(a) on page 100, and photovoltaic parameters are summarized in **Table 5-1** on page 100. Results validate superior performance in SiC/Si_3N_4/SiO_2 based ARPL, which led to 13.4% PCE, whereas 12.5% has been observed in SiC/SiO_2 based ARPL. These results indicated that efficiencies > 13% can be achieved in sub 10 microns thick regime without the need of complex texturing, which is required for thin silicon solar cells.

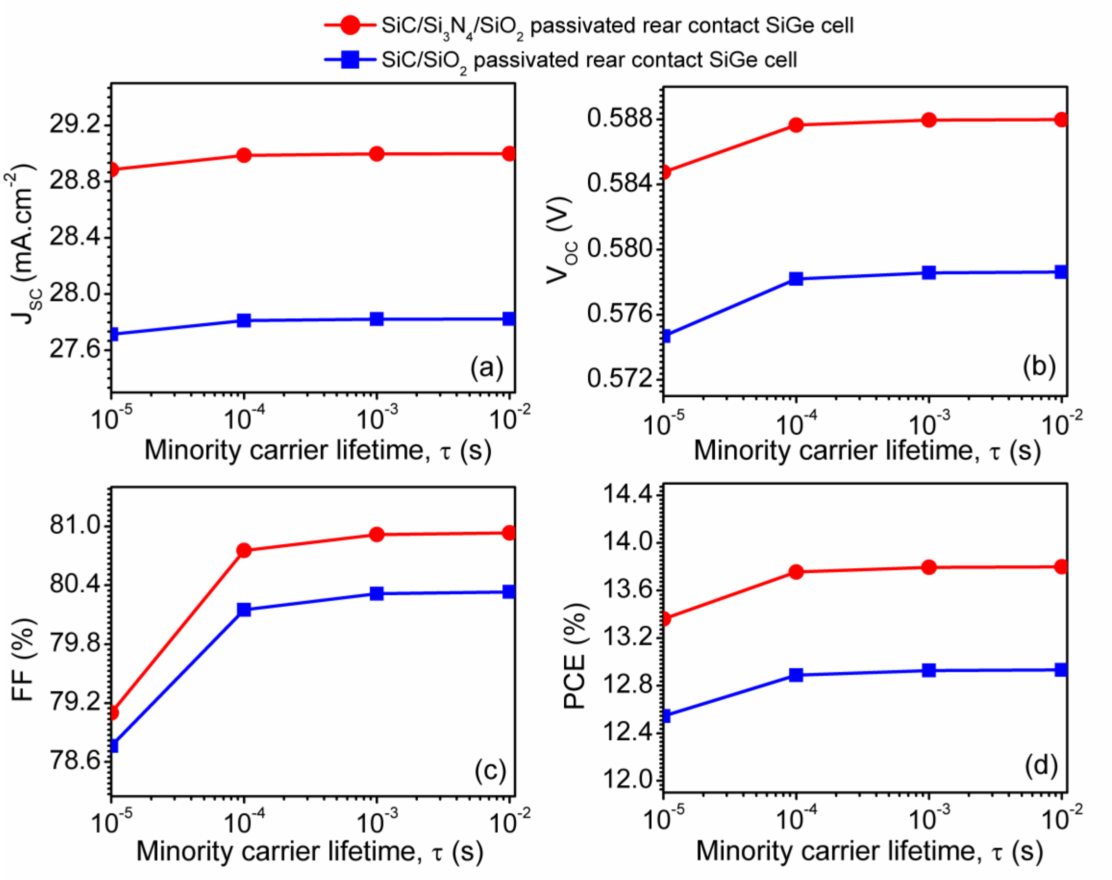

Figure 5.6: Impact of minority carrier lifetime on device photovoltaic parameters: (a) J_{SC}, (b) V_{OC}, (c) FF, and (d) PCE (Pandey et al., 2016).

Nevertheless, the impact of material quality has also been obtained, and performances of the devices are reported in **Figure 5.6**(a-d) above. The PV parameters: J_{SC}, V_{OC}, FF, and PCE are reported in **Figure 5.6**(a), **Figure 5.6** (b), **Figure 5.6** (c), and **Figure 5.6**(d), respectively. Result reveals that the parameters are less impacted by τ variations, as τ changes from 10^{-2} s to 10^{-5} s, change in J_{SC}, V_{OC}, FF and PCE are 0.4%, 0.5%, 2.2% and 3.2%, respectively. Concluding the present section reflects 13.4%, 12.5% efficient 10µm thick i-SiGe wafer based rear-contact solar cells. However, results reported in **Figure 5.5**(b) and **Table 5-1** on page 100 shows that the V_{OC} values are < 600 mV and this is attributed to lower built-in potential at the collecting junction due to intrinsic wafer, since V_{OC} of the device directly depends on the built-in potential at the collecting junction. On considering this fact, intrinsic wafer can be replaced by n-type or p-type wafer to improve the V_{OC}. In a standard solar cell, p-type wafer has been preferred, and hence the diffusion length of minority carrier (electrons) in p-type wafer is higher than the diffusion length of minority carrier (holes) in n-type wafer. However, in large-scale production, it is difficult to avoid chemical and mechanical imperfection to the wafer. Here, lies the big advantage of n-type wafer solar cells. The performance of n-type cell is less vulnerable to chemical and mechanical imperfections. The n-type cell has several advantages over p-type cells. They are less affected by light-induced degradation (Glunz et al., 1999, Tjahjono and Cotter, 2005), and hence, next section is dedicated to study of the n-type wafer based rear contact SiGe solar cell, to obtain higher V_{OC}.

5.3.2: Study of n- SiGe wafer based rear-contact solar cell

The simulated device structure used in this section is represented in **Figure 5.1**(b) on page 96, n-type SiGe wafer has been used with a doping density of 3×10^{15} cm^{-3}, doping density is identical to the doping of n-Si wafer which is used in **Chapter 2**. The un-optimized diffusion depth of 3µm and 2.5µm has been used for initial analysis, which will be optimized further. At first, analysis of the device has been done with Si_3N_4 based ARC layer and external quantum efficiency, EQE is reported in **Figure 5.7** on page 103. The device shows superior EQE, and remarkably it achieved EQE>76% in the spectrum range of 400-700 nm wavelength, shown in **Figure 5.7** below. At wavelength equivalent to 400 nm, proposed device shows EQE of the order of 78% that is at least 12% higher than other Si nanostructured solar cells (Oh et al., 2012) and 18% greater than that of planar 10 µm thick Si cell with anti-reflection coating (Jeong et al., 2013). Nevertheless, results reflect > 20% EQE at a wavelength equivalent to 1000 nm and more than 10% EQE at a wavelength of 1200 nm, which clearly indicates superior optical performance compared to Si-based device, whose EQE falls below 5% for the wavelengths greater than 1000 nm as reported in **Figure 2.5** on page 32 of **Chapter 2**. Improved performance is attributed to the higher absorption coefficient in SiGe compared to Si at higher wavelengths.

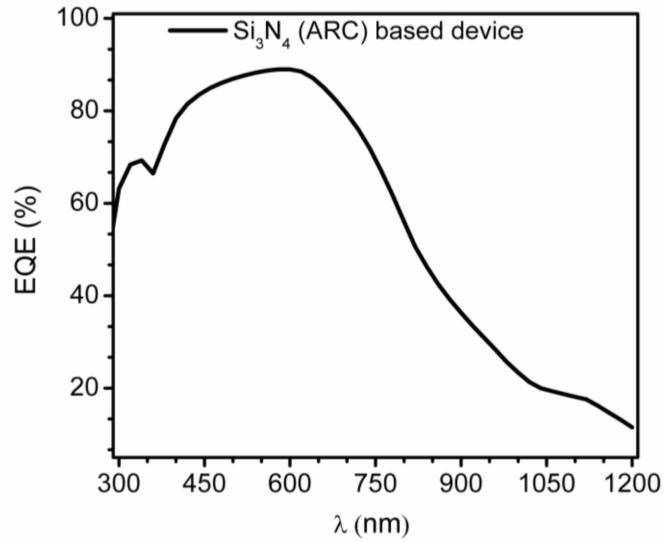

Figure 5.7: EQE of rear contact n-type SiGe solar cell with 70 nm thick Si_3N_4 based ARC layer.

Moreover, to understand the movement and recombination process of minority carriers (holes) inside the device, contour representation of recombination rate is obtained as reported in **Figure 5.8**(a-b) on page 104 along with energy band diagram and hole concentration as depicted in **Figure 5.9** (a-c) on page 105. At the interface, the holes that are generated at point 1 need to travel the shorter diffusion length, to arrive at collecting junction (*n/p+*

interface) compared to holes that are created at point 2 shown in **Figure 5.1**(b) on page 96. These results in decreased collection probability in region II, therefore, higher recombination rate is observed in region II compared to the region I, as shown in **Figure 5.8** (a-b) below. Region, I and region II, is defined in the *n*-type region only; they do not include the *p*+ and *n*+ type regions.

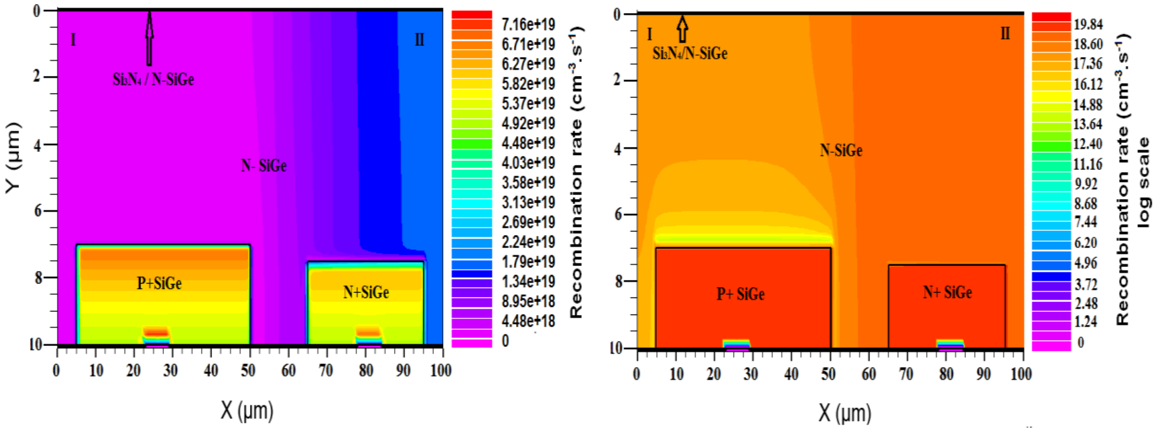

(a) (b)

Figure 5.8: Recombination rate contour (cm^{-3}.s^{-1}) of illuminated Si$_3$N$_4$ ARC based rear contact SiGe solar cell under short circuit condition: (a) linear scale, and (b) log scale (Pandey and Chaujar, 2016b).

Moreover, the energy band diagram which of consists valance band (E$_V$), conduction band (E$_C$), electron quasi-Fermi (EQF), and hole quasi-Fermi (HQF) level examined at the rear side under dark and illuminated conditions, respectively are reported in **Figure 5.9**(a-b) on page 105. It is clearly observed that due to heavily doped *p*+/*n*+ regions, EQF (HQF) lies within the E$_C$ (E$_V$) in *n*+ (*p*+) region as shown in **Figure 5.9**(a), and upon illumination, their position remains unchanged. However, the HQF (EQF) moves closer to the E$_V$ (E$_C$) in *n*+ (*p*+) region as shown in **Figure 5.9**(b). The shift in the Fermi levels is attributed to the generation of electron-hole pair throughout the device, upon illumination. Moreover, hole concentration is reported in **Figure 5.9**(c), to understand the recombination dynamics and carrier movement. The formation of space charge region with the associated electric field at *n/p+* interface collects and separates electron-hole pairs within the vicinity of the interface; however, outside the interface the substrate is neutral, and the collection will be by diffusion. The carriers that are generated far away from the interface are not able to arrive at the collecting junction. Hence, recombination process will balance out as already explained in **Section 2.3.3:** of **Chapter 2**. Near *p+/n* interface, hole concentration is less compared to the bulk of *n-type* region and *n/n+* interface; since outside the collecting interface, the collection will be by diffusion of electrons towards the field area where it will be collected as discussed above. The holes that are generated in a region greater than the diffusion length are balanced by recombination process. Hence, there is a lateral concentration gradient for holes, showing the lateral flow of holes to the collecting (*n/p+*) junction. Moreover, this also validates higher recombination rate in II region of the device as shown in **Figure 5.8**(a-b) on page 104.

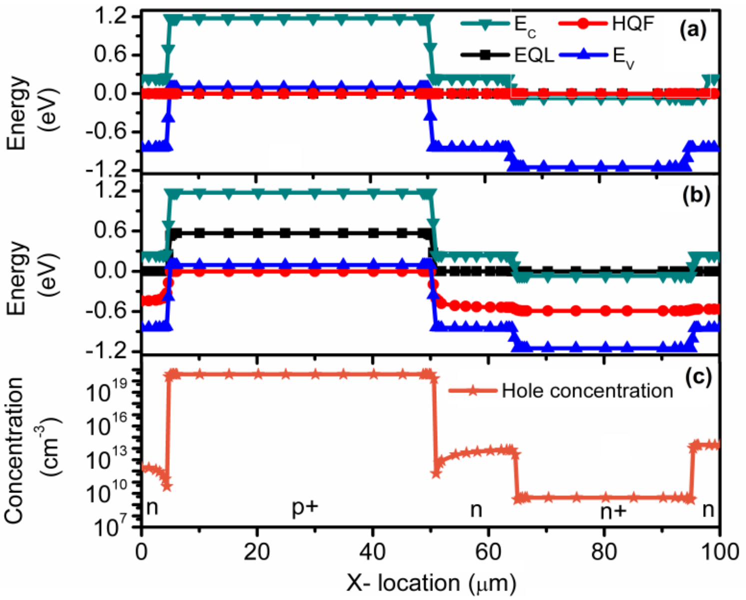

Figure 5.9: Energy band diagram of rear contact n type SiGe solar cell, data is obtained at the rear side of the device under (a) dark and (b) illuminated conditions, respectively. Moreover hole concentration is reported in (c).

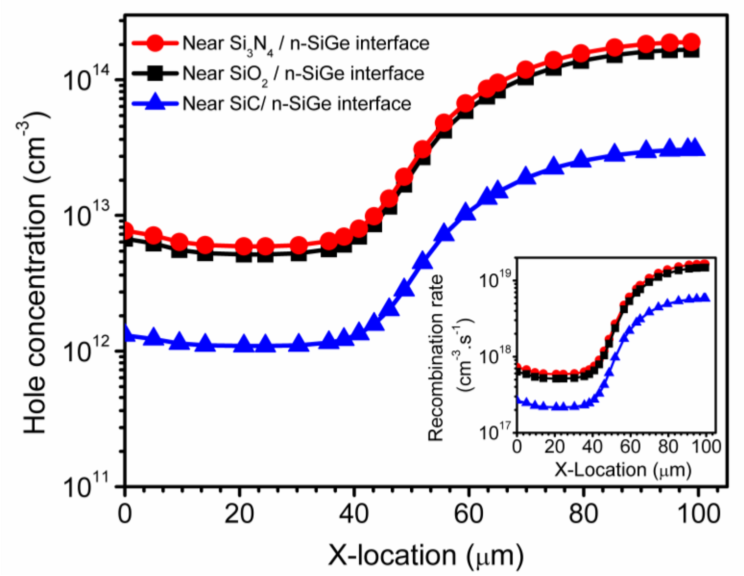

Figure 5.10: Hole concentration and recombination rate (inset) near the interface of SiC, Si_3N_4 and SiO_2 passivated devices. Data has been obtained from location (0, 0.2) to (100, 0.2) under illumination with short circuit condition (Pandey and Chaujar, 2016b).

Additionally, different front surface passivation schemes have been discussed and compared. The front surface investigation has been done for three interfaces viz. SiC/n-SiGe, SiO_2/n-SiGe, and Si_3N_4/n-SiGe, and relevant parameters are obtained as reported in **Figure 5.10** above and **Figure 5.11** on page 107. Recalling the concept discussed in the **Chapter 2**, efficient surface passivation can be achieved by (1) minimizing the density of surface states and (2) reducing the surface concentration of the carriers (electrons or holes), and thus, minority carrier (hole) concentration near the interfaces are obtained and reported in **Figure 5.10**. Result shows, minority carrier concentration are drastically reduced at the SiC/*n*-SiGe interface compared to SiO_2 and Si_3N_4 based passivation layers, which displays that SiC prevents the minority carriers (holes) to reach the SiC/*n*-SiGe interface, and hence lower surface recombination rate is observed at interface as depicted in **Figure 5.10** (inset). This is due to the positive electric field at the interface as reported in **Figure 5.11** on page 107. The electric field direction is directed from SiC to SiGe, rendering it energetically unfavorable for hole transport to SiC/n-SiGe interface, resulting in a low concentration of holes at the front surface.

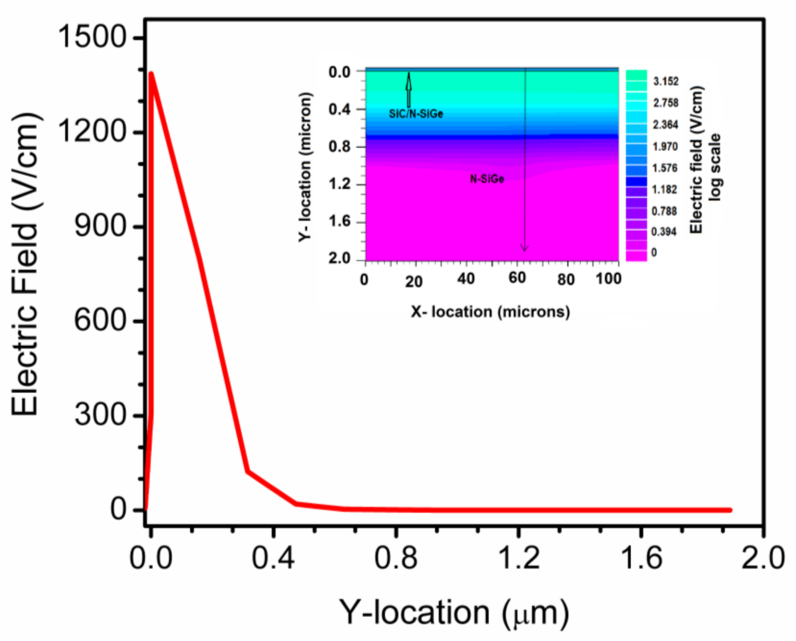

Figure 5.11: Distribution of electric field near the (SiC/n-SiGe) interface. Inset shows the contour representation of electric field. Data is obtained under illumination with zero-bias voltage (Pandey and Chaujar, 2016b).

Nevertheless, contour representation of recombination rate is also reported in **Figure 5.12** on page 108. **Figure 5.12**(a), **Figure 5.12**(b), and **Figure 5.12**(c) displays the recombination rate for SiO_2 passivated, Si_3N_4 passivated, and SiC passivated devices, respectively. Also magnified view of the interface is also reported in **Figure 5.12**(d), in case of SiC passivated device. Sinking the hole concentration at the interface will produce higher concentration difference between electrons and holes, and thus results in lower surface recombination rate, which also validated the data reported in **Figure 5.10** (inset) on page 106. Results shows, the concentration difference between electron and hole is larger in SiC passivated device compared to SiO_2 and Si_3N_4 based devices; thus, results in lower surface recombination rate, as shown in the **Figure 5.12**(c-d) below. In SiC layered device, approximately ten times lower hole concentration is obtained near the interface (SiC/n-SiGe), compared to the bulk (*n*-SiGe) region of the device. This shows that the presence of SiC reduces the concentration of minority carriers only at the interface. Lower recombination at the interface ensures that generated carrier will contribute more external current and recombination current density will be suppressed. Moreover, higher recombination rate is observed in II region compared to I region. This is attributed to diffusion of holes towards the collecting junction (*p+/n*). Lateral hole concentration gradient as reported in **Figure 5.10** on page 106 shows lateral hole flow to the junction.

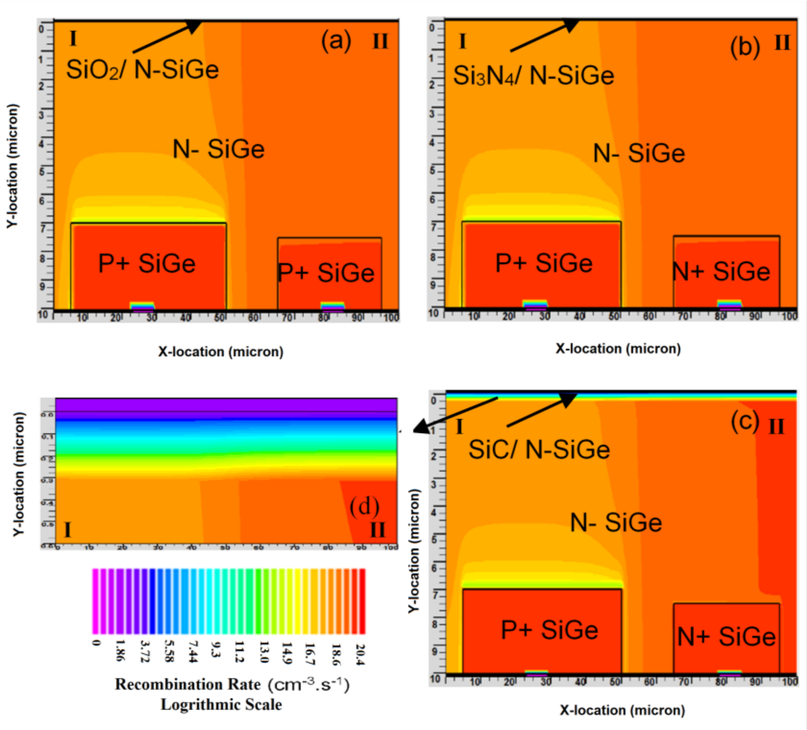

Figure 5.12: Contour plot of recombination rate ($cm^{-3}.s^{-1}$) in the log scale, (a) SiO_2 passivated rear contact SiGe solar cell, (b) Si_3N_4 passivated rear contact SiGe solar cell, (c) SiC passivated rear contact SiGe solar cell and (d) Magnified view of (SiC/ n-SiGe) interface in case of SiC passivated device. Data has been obtained under illumination with zero-bias voltage (Pandey and Chaujar, 2016b).

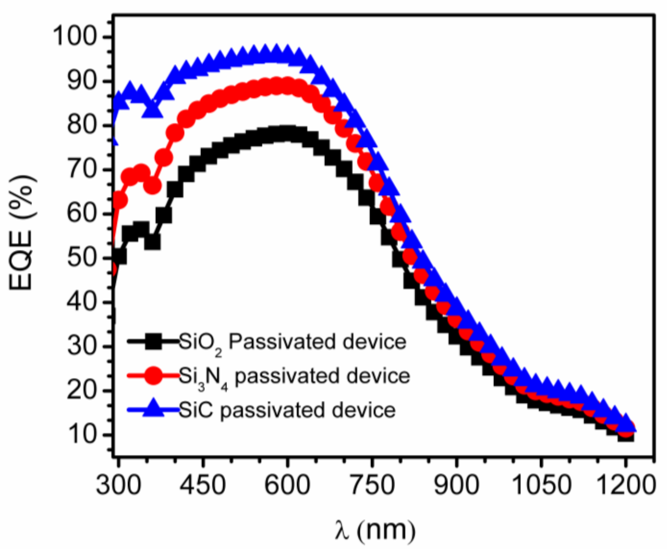

Figure 5.13: EQEs of SiC, Si_3N_4, and SiO_2 passivated rear contact SiGe solar cells (Pandey and Chaujar, 2016b).

Moreover, the spectrum response has been obtained for SiO_2, Si_3N_4, and SiC passivated devices and EQE with different front surface passivation layers are shown in **Figure 5.13** above. Result shows, significant improvement in blue response, as well as midway response, in SiC layered device compared to other devices. EQE>80% is achieved in the wavelength range of 300-720 nm. At wavelength equivalent to 550 nm, the device exhibits EQE of the order of 95% which is 25.5% and 10.2 % higher than SiO_2 and Si_3N_4 layered devices, respectively. Moreover, at the smaller wavelength (300 nm), 35%, and 70% higher EQE has been obtained compared to respective devices shown in **Figure 5.13**.

In addition, the performance of a solar cell is directly related to the amount of light entering the cell, however, wavelength dependent extinction coefficient as reported in **Figure 2.6** on page 34 of **Chapter 2** shows that SiC has higher absorption coefficient at lower wavelengths, whereas it is desired that SiC should be transparent in the simulated spectrum. The absorbance of a material is directly related to the absorption coefficient and thickness of the material used. This suggests that to minimize the absorption and increase the transparency, thinner SiC layer should be employed. This phenomenon sets the limit on the thickness of SiC. The SiC layer utilized in the simulation is only 20 nm thick whose absorbance is negligible. However, consequences of using thicker SiC layer have also been discussed. Four SiC-based *n-type* SiGe wafer has been designed with a different thickness of SiC, i.e., 20 nm, 40 nm, 80 nm, and 160 nm, and photon absorption rate has been obtained in underlying SiGe wafer as shown in **Figure 5.14** (a), **Figure 5.14** (b), **Figure 5.14** (c), and **Figure 5.14** (d) below, respectively. The contour representation indicates that the photon coupling in underlying SiGe is higher for 20 nm thick SiC layered wafer, however, increasing the thickness results in absorbance in SiC and hence, lower optical coupling in underlying SiGe. The 160 nm thick SiC layered wafer shows worst optical behavior compared to other wafers as shown in **Figure 5.14** (a-d).

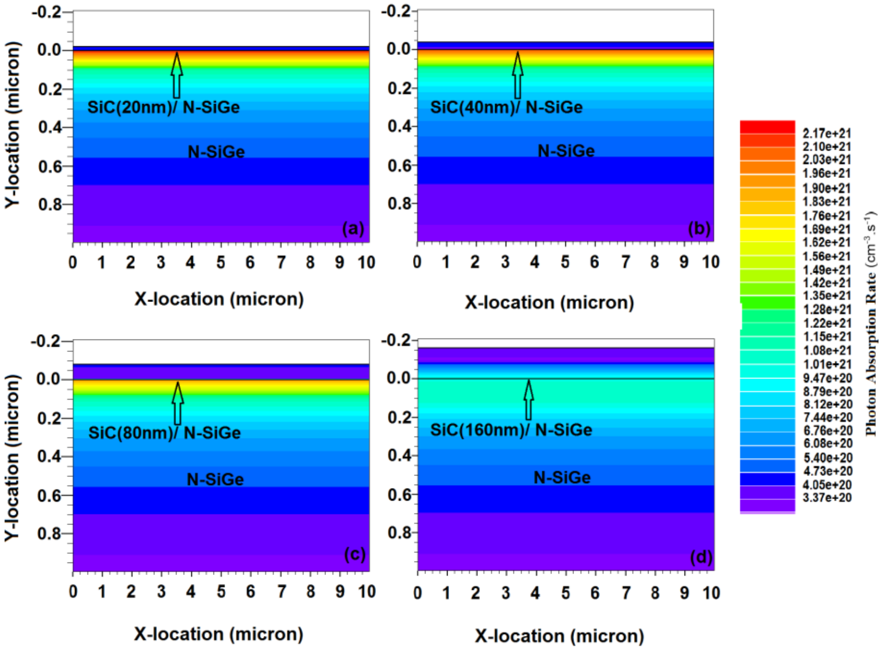

Figure 5.14: The contour representation of photon absorption rate (cm^{-3}.s^{-1}) in underlying SiGe with different SiC thicknesses: (a) 20 nm, (b) 40 nm, (c) 80nm, and (d) 160 nm (Pandey and Chaujar, 2016b).

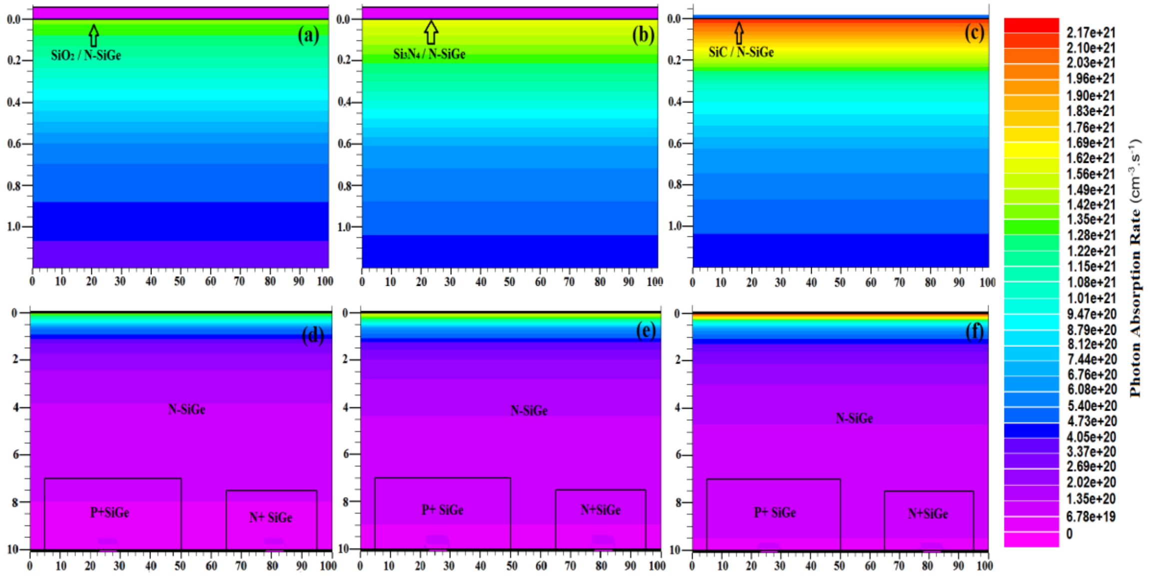

Figure 5.15: The contour representation of photon absorption rate ($cm^{-3}.s^{-1}$) in rear contact SiGe solar cell: (a) magnified view near the (SiO_2/*n*-SiGe) interface in SiO_2 passivated device, (b) magnified view near the (Si_3N_4 /*n*-SiGe) interface in Si_3N_4 passivated device, (c) magnified view near the (SiC /*n*-SiGe) interface in SiC passivated device, and Fig. 5.15 d,e, and f show the SiO_2, Si_3N_4, and SiC passivated device on full scale. Data has been obtained under illumination with zero-bias voltage (Pandey and Chaujar, 2016b).

Meanwhile, the photon absorption contour is also obtained for all the devices, and same has been presented in **Figure 5.15**(a-f) above. **Figure 5.15**(a), **Figure 5.15**(b), and **Figure 5.15**(c) shows the exaggerated view of photon absorption rate at the interface of SiO_2, Si_3N_4, and SiC passivated devices as reported in **Figure 5.15**(d), **Figure 5.15**(e), and **Figure 5.15**(f), respectively. Results reveal that higher photon absorption rate is achieved in SiC layered device. The device shows, 12.5% and 5% higher photon absorption rate compared to SiO_2 and Si_3N_4 layered devices, respectively as shown in **Figure 5.15** (d-f). Moreover, **Figure 5.15**(a) shows higher absorption at the front surface. This validates the higher optical coupling of photons with lower wavelengths. In addition, **Figure 5.16** on page 112 shows the source photocurrent of the AM1.5 spectrum, along with the ratio of I_A to I_S. The improved optical behavior of the device results in higher available photocurrent, which further increases the I_A/I_S ratio. Result shows, > 80% ratio with a maximum value of 95.7% in the spectrum range of 289-735 nm wavelengths, thus, reflecting an excellent spectrum response of SiC passivated device.

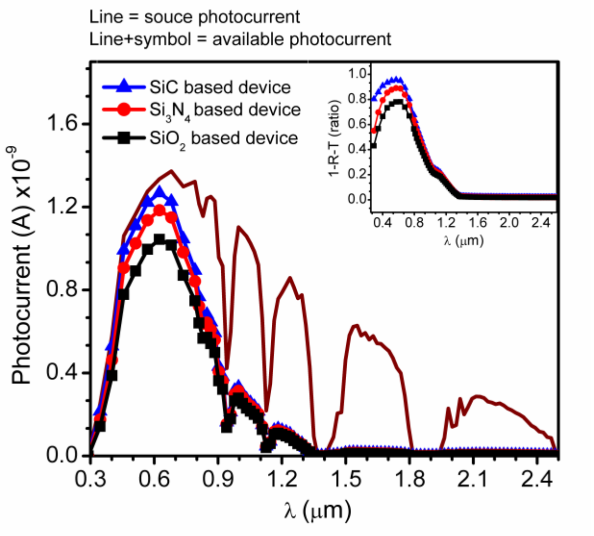

Figure 5.16: Comparison of spectrum response under AM1.5 illumination for rear contact SiGe solar cell with SiC, Si_3N_4, and SiO_2 passivation layers. The inset shows the I_A/I_S ratio for all the three devices (Pandey and Chaujar, 2016b).

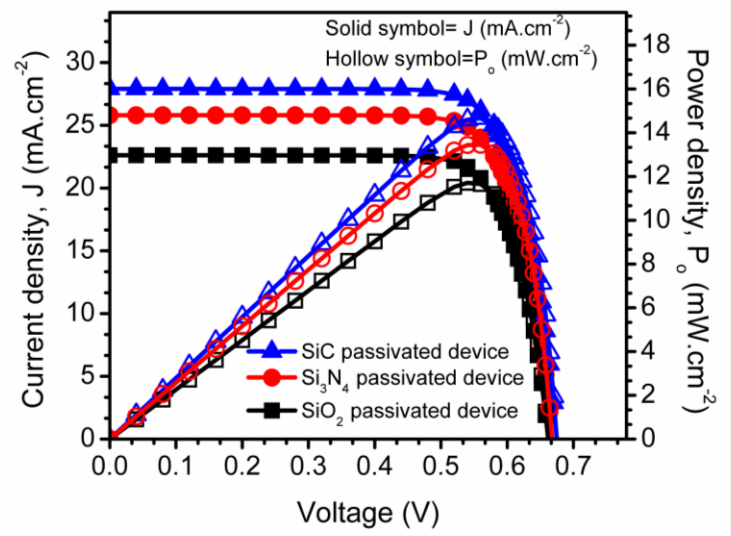

Figure 5.17: Illuminated J-V and P_O-V curve of rear contact SiGe solar cell with SiC, Si_3N_4, and SiO_2 passivation layers (Pandey and Chaujar, 2016b).

The most important part of the solar cell design is its J–V characteristics. Any design must have a higher J_{SC} and a higher V_{OC}. The J-V characteristic of the device is simulated under AM1.5 illumination with optical power 0.1W/cm^2 and presented in **Figure 5.17** on page 112. The J_{SC} and V_{OC} in SiC layered device is 28 mAcm^{-2} and 668 mV, whereas J_{SC} , V_{OC} in SiO_2 and Si_3N_4 layered devices are 22.6 mAcm^{-2} , 662 mV, and 25.8mAcm^{-2} , 667mV respectively. Thus, SiC layered device shows 24% and 8% higher J_{SC} compared to respective devices. A detailed comparison of electrical parameters is provided in **Table 5-2** below.

TABLE 5-2: COMPARISONS OF PHOTOVOLTAIC PARAMETERS OF 10µm THICK REAR CONTACT SiGe SOLAR CELL WITH SiO_2, Si_3N_4 AND SiC BASED PASSIVATION LAYERS (PANDEY AND CHAUJAR, 2016B)

Device	J_{SC} (mA.cm^{-2})	V_{OC} (mV)	FF (%)	PCE (%)
SiO_2 layered	22.6	662	78.2	11.7
Si_3N_4 layered	25.8	667	78.0	13.5
SiC layered	28.0	668	78.6	14.7

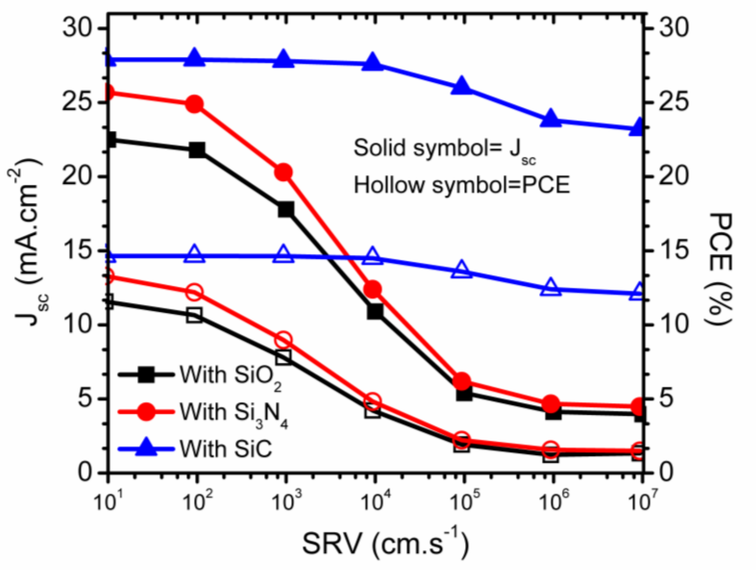

Figure 5.18: Impact of surface recombination velocity on rear contact SiGe solar cell with different passivation layers. J_{SC} and PCE are presented on primary and secondary axis, respectively.

Additionally, the impact of surface recombination velocity (SRV) on J_{SC} and PCE has been obtained which is presented **Figure 5.18** on page 113. At SRV equivalent to 10^2 $cm.s^{-1}$, the difference between available photocurrent and short circuit current is 2.2 $mA.cm^{-2}$ in SiC layered device whereas the difference of ~ 7 $mA.cm^{-2}$ has been observed in SiO_2 and Si_3N_4 layered devices. This shows that recombination and the parasitic absorption losses are higher in respective devices, compared to SiC layered device. Also, when SRV changes from 10^1 $cm.s^{-1}$ to 10^7 $cm.s^{-1}$, the PCE and J_{SC} went down to 12.1% and 23.2 $mA.cm^{-2}$, respectively in SiC layered device, whereas these values are 1.33% and 3.97 $mA.cm^{-2}$ and 1.5% and 4.49 $mA.cm^{-2}$ in SiO_2 and Si_3N_4 layered devices, respectively. Results reveal that characteristics of the device are less affected by SRV. Also, result shows that new surface passivation scheme is useful when the surface to volume ratio of the device is large, i.e., for a thin device; since thin devices suffer from higher surface recombination. Furthermore, the effect of diffusion depth has also been investigated. The best device i.e., SiC passivated device has been selected for analysis. Recombination rate with different *p+/n+* diffusion depth viz. 3µm/2.5µm, 1.5µm/1.25µm, 0.75µm/0.63µm, 0.38µm/0.32µm, and 0.19µm/0.16µm are reported in **Figure 5.19**(a), **Figure 5.19**(b), **Figure 5.19**(c), **Figure 5.19**(d), and **Figure 5.19**(e), respectively on page 115. The recombination rate in *p+* and the *n+* region is higher because of the heavily doped region (~10^{20} cm^{-3}) and larger diffusion depth in Y- direction. Therefore, the diffusion depth of *p+* and *n+* region has been minimized to reduce the recombination rate in these areas. The PCE of 15.4 %, i.e., 4.7% higher than initial value (14.7%) is obtained by reducing the diffusion depth of the regions. **Figure 5.19** (a-e) shows carrier recombination is reduced by reducing the diffusion depth of *p+* and *n+* regions. The impact of diffusion depth on device photovoltaic parameters is presented in **Table 5-3** on page 116.

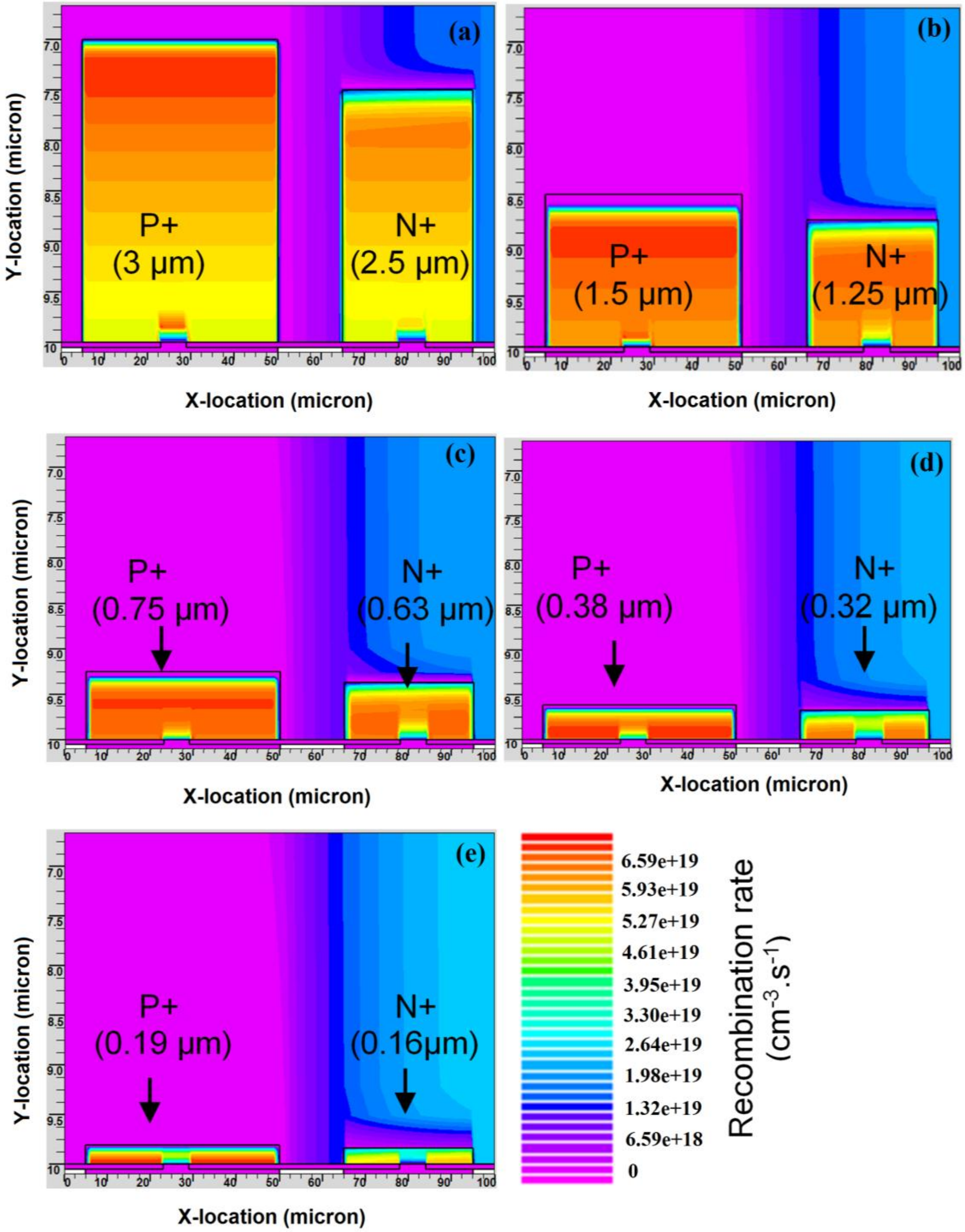

Figure 5.19: Recombination rate (cm^{-3} s^{-1}) contour of SiC passivated rear contact SiGe solar cell with different diffusion depth of *p*+ and *n*+ regions: (a) p+/n+ is 3µm/2.5µm, (b) p+/n+ is 1.5µm/1.25µm, (c) p+/n+ is 0.75µm/0.63µm, (d) p+/n+ is 0.38µm/0.32µm, and (e) p+/n+ is 0.19µm/0.16µm. Data has been obtained under illumination with zero-bias voltage (Pandey and Chaujar, 2016b).

TABLE 5-3: IMPACT OF *n*+ AND *p*+ REGIONS DIFFUSION DEPTH ON PHOTOVOLTAIC PARAMETERS OF SiC PASSIVATED 10µm THICK REAR CONTACT SiGe SOLAR CELL (PANDEY AND CHAUJAR, 2016B)

S. No.	Regions	Thickness (µm)	J_{SC} ($mA.cm^{-2}$)	V_{OC} (mV)	FF (%)	PCE (%)
1	*p*+	3.0	28.0	668	78.6	14.70
	n+	2.5				
2	*p*+	1.5	28.9	666	78.6	15.13
	n+	1.25				
3	*p*+	0.75	29.3	666	78.3	15.30
	n+	0.63				
4	*p*+	0.38	29.5	666	78.3	15.37
	n+	0.32				
5	*p*+	0.19	29.6	667	78.2	15.41
	n+	0.16				

In the last exercise of the Chapter, the application of SiC passivated rear contact SiGe solar cell for CPV use has been discussed. Altering the irradiance on a solar cell varies all solar cell parameters, including J_{SC}, V_{OC}, FF, PCE, series and shunt resistances. The light intensity on a solar cell is called the number of suns, where one- sun corresponds to standard illumination at AM1.5, or $100mW/cm^2$. The PV module intended to work under one- sun is called a "flat plate" while those using more than one- sun or concentrated sunlight are called "concentrator.” Further, concentrators have some advantages in terms of higher efficiency than a one-sun solar cell and the lower cost. The J_{SC} of a solar cell depends linearly on irradiance. This indicates, device operating under 10 suns would have 10 times the J_{SC} as the same device under one sun operation. However, this will not result in increased PCE, since the incident power also increases linearly. The efficiency benefits arise from the open-circuit voltage, as V_{OC} increases logarithmically with light intensity (Würfel, 2008). Therefore, the impact of irradiance and temperature on the devices is obtained, and the results are presented in **Figure 5.20**(a-c) on page 117. The device is simulated up to 20-suns ($2 W/cm^2$) condition at room temperature (300K). Nevertheless, temperature also increases as a function of input optical power per unit area. Hence, cell operating at higher concentration levels require complex cooling system, and overall cost of the PV module will be increased. In literature, the silicon-based concentrator solar cell with the efficiencies range of (15-27.5) % has been reported for the concentration level of (20-150) suns (Sinton et al., 1986, Cuevas et al., 1990, Lammert and Schwartz, 1977, Wenham and Green, 1995, Zhao et al., 1990), whereas simulation analysis reported in this chapter achieves V_{OCs} of 766 mV, 800 mV and PCEs of 18.37%, 19.32% at 10-sun and 20-sun conditions, respectively as shown in **Figure 5.20** (a) below.

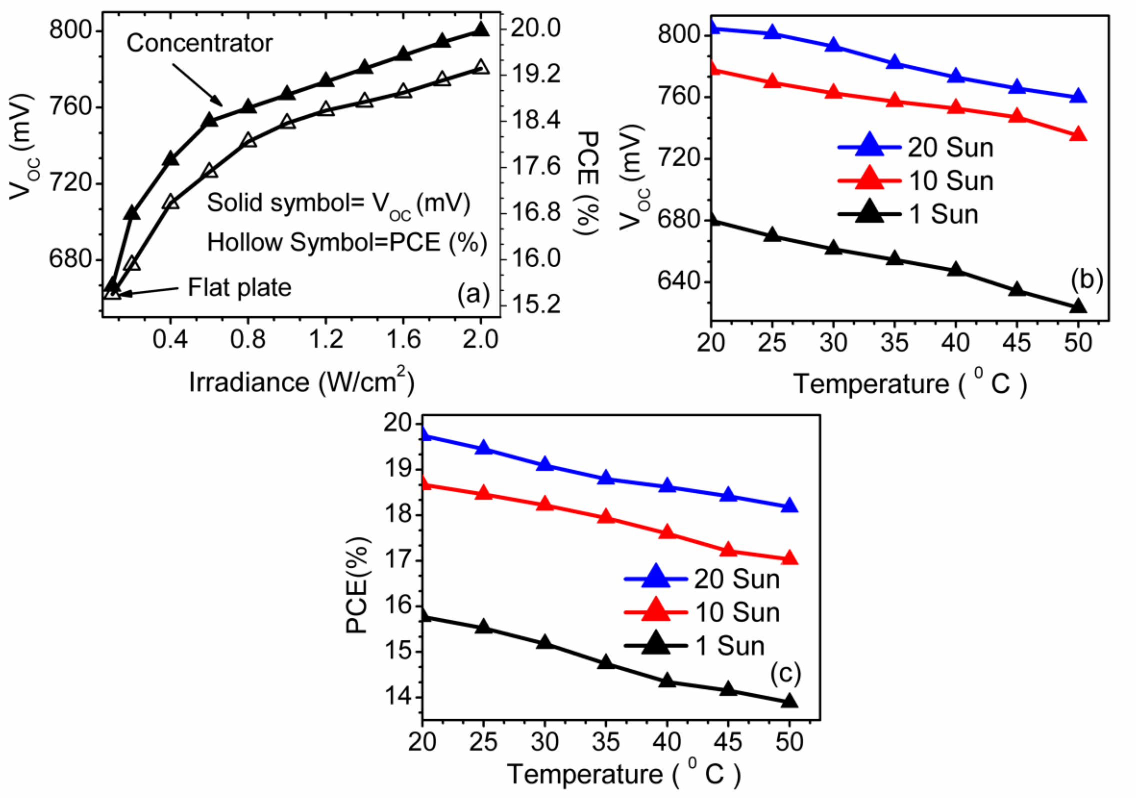

Figure 5.20: Impact of irradiance and temperature on SiC passivated rear contact SiGe solar cell: (a) effect of irradiance on V_{OC} and PCE, (b) effect of temperature on V_{OC} for 1 sun, 10 suns and 20 suns conditon, respectively (c) effect of temperature on PCE for 1 sun, 10 suns and 20 suns condition, respectively (Pandey and Chaujar, 2016b).

Further, results show 10.2% and 13.7% higher PCE at the concentration levels of 4, 6 suns compared to the 1-sun condition. Moreover, the desired concentration level can be selected from the **Figure 5.20**(a) on page 117 depending upon applications. Besides, the impact of temperature on device parameters: V_{OC}, PCE, and FF for three different conditions (1-sun, 10-suns, and 20-suns) have also been analyzed. Since, under concentrated light device temperature increases, although, it can be avoided by using a suitable cooling system (Royne et al., 2005). The device performance degrades as the temperature increases as shown in **Figure 5.20** (b-c), since intrinsic carrier concentration increase at higher temperatures. Therefore, bandgap decreases, which further results in decrease in V_{OC}, as shown in **Figure 5.20**(b). The V_{OC} values of 804 mV, 778 mV, 680 mV and PCE values of 19.75%, 18.67%, 15.77 % is obtained at 20°C for 20-sun, 10-sun and 1-sun conditions respectively, whereas 760 mV, 735 mV, 623 mV and 18.2%, 17%, 13.9% is obtained at 50^0C. Results show, as the temperature increases from 20^0C - 45^0C, 10.2% decrease in PCE is obtained for flat plate cell, whereas 7.8% and 6.7% decrease in PCE is obtained for the same cell operating at 10-suns and 20-suns, as shown in **Figure 5.20**(c). Further, all the results of this section conclude that PCE of 19.3% is obtained at 20-suns in the sub 10µm thick device, which suggests that the proposed device can be a good candidate for the flat plate as well as low concentrator applications.

5.4: SUMMARY

In this Chapter, 10 µm thick rear contact SiGe based solar cell devices have been discussed with SiC-based front surface passivation for the suppression of interface recombination as well as improvement of J_{SC} and V_{OC}. The design principle presented here balance the electronic and photonic effects together and is a significant step to develop highly efficient thin solar cells. Initially, intrinsic wafer based rear contact SiGe solar cell has been designed with SiC, SiO_2, and Si_3N_4 based ARPLs. Photo reflectance is significantly reduced in the UV/visible spectral region due to the presence of SiC. Energy band analysis has been done to understand the movement of carriers. Moreover, the impact of material quality has also been discussed. In second approach, intrinsic wafer has been replaced with n-type SiGe, to obtain further high V_{OC}. Detailed analysis such as energy band, hole concentration, electric field, and recombination rates are achieved inside the device to understand the behavior of the device. Spectrum analysis resulted in EQE> 90% in the range of 400–650 nm wavelength. Also, at wavelengths equivalent to 300 nm, SiC passivated device shows EQE of 85%. The presence of SiC as a surface passivation layer shows enhanced surface characteristics in terms of reduced surface recombination and higher photon absorption rate. Moreover, optimization of diffusion depth of the device resulted in 15.4% PCE under standard AM1.5 illumination. Nevertheless, the proposed device has also been analyzed for CPV applications, resulting in 18.4% and 19.3% efficiencies at 1 W/cm^2 (10 suns, 27^{O}C) and 2 W/cm^2 (20 suns, 27^{O}C) respectively.

The improved performance of the device in sub 10 µm thick regime is attributed to the superior absorption coefficient of SiGe compared to Si. Absorption at the higher wavelength is obtained without the need of thick wafer and complex texturing scheme. Now, evoking the concept of perovskite-based tandem devices, the perovskite top cell utilizes the lower wavelength photons, and to absorb the higher wavelength photons, thicker silicon cells are required. These issues can be resolved by using SiGe which is capable of absorbing higher wavelength photons in compact architecture. Therefore, in order to explore this, next chapter proposes IBC-SiGeHJ bottom subcell based 4-terminal perovskite/SiGe tandem solar cell, to boost the efficiencies of tandem solar cell.

5.5: REFERENCES

AHUJA, R., PERSSON, C., SILVA, A. F. D., ALMEIDA, J. S. D., ARAUJO, C. M. & JOHANSSON, B. 2003. Optical properties of SiGe alloys. *Journal of Applied Physics,* 93**,** 3832-3836.

BULLETIN, P. 2003. SiGe: a key to unlocking the potential of solar cells. *Photovoltaics Bulletin,* 2003**,** 7-9.

CHEN, G. & YANGORAN, D. 2010. Germanium Doped Czochralski Silicon. *In:* CHU, P. K. (ed.) *Advances in Solid State Circuit Technologies.* Rijeka: InTech.

CONIBEER, G. 2007. Third-generation photovoltaics. *Materials Today,* 10**,** 42-50.

CUEVAS, A., SINTON, R. A., MIDKIFF, N. E. & SWANSON, R. M. 1990. 26-percent efficient point-junction concentrator solar cells with a front metal grid. *IEEE Electron Device Letters,* 11**,** 6-8.

DAS, M. K. & CHOUDHARY, S. K. 2013. Ge-content dependent efficiency of Si/SiGe heterojunction solar cell. *Applied Physics A,* 112**,** 543-548.

FISHER, G., SEACRIST, M. R. & STANDLEY, R. W. 2012. Silicon crystal growth and wafer technologies. *Proceedings of the IEEE,* 100**,** 1454-1474.

GARNETT, E. & YANG, P. 2010. Light trapping in silicon nanowire solar cells. *Nano letters,* 10**,** 1082-1087.

GLUNZ, S. W., REIN, S., KNOBLOCH, J., WETTLING, W. & ABE, T. 1999. Comparison of boron- and gallium-doped p-type Czochralski silicon for photovoltaic application. *Progress in Photovoltaics: Research and Applications,* 7**,** 463-469.

GREEN, M. A. & KEEVERS, M. J. 1995. Optical properties of intrinsic silicon at 300 K. *Progress in Photovoltaics: Research and Applications,* 3**,** 189-192.

HUMLÍČEK, J., GARRIGA, M., ALONSO, M. I. & CARDONA, M. 1989. Optical spectra of SixGe1−x alloys. *Journal of Applied Physics,* 65**,** 2827-2832.

JEONG, S., MCGEHEE, M. D. & CUI, Y. 2013. All-back-contact ultra-thin silicon nanocone solar cells with 13.7% power conversion efficiency. *Nature communications,* 4**,** 2950-2950.

KASAP, S. & CAPPER, P. 2007. *Springer Handbook of Electronic and Photonic*

Materials Springer US, Boston, MA, pp. 481–498 (accessed February 26, 2016).

KERSCHAVER, E. V. & BEAUCARNE, G. 2006. Back-contact solar cells: a review. *Progress in Photovoltaics: Research and Applications,* 14**,** 107-123.

LAMMERT, M. D. & SCHWARTZ, R. J. 1977. The interdigitated back contact solar cell: A silicon solar cell for use in concentrated sunlight. *IEEE Transactions on Electron Devices,* 24**,** 337-342.

NSM, A. 2016. NSM Archive - Silicon Germanium (SiGe).

OH, J., YUAN, H.-C. & BRANZ, H. M. 2012. An 18.2%-efficient black-silicon solar cell achieved through control of carrier recombination in nanostructures. *Nature nanotechnology,* 7**,** 743-8.

OUELLETTE, J. 2002. Silicon-germanium gives semiconductors the edge. *Industrial Physicist,* 8**,** 4.

PANDEY, R. & CHAUJAR, R. 2016a. Novel back-contact back-junction SiGe (BC-BJ SiGe) solar cell for improved power conversion efficiency. *Microsystem Technologies,* 22**,** 2673-2680.

PANDEY, R. & CHAUJAR, R. 2016b. Rear contact SiGe solar cell with SiC passivated front surface for >90-percent external quantum efficiency and improved power conversion efficiency. *Solar Energy,* 135**,** 242-252.

PANDEY, R., JAIN, A., KUMAR, A. & CHAUJAR, R. IMPACT OF MINORITY CARRIER LIFETIME AND TEMPERATURE ON SiC BASED REAR CONTACT SiGe SOLAR CELL FOR CONCENTRATOR PHOTOVOLTAIC (CPV) APPLICATIONS. European Photovoltaic Solar Energy Conference and Exhibition, 2016 2016 Munich, Germany. 270-273.

ROYNE, A., DEY, C. & MILLS, D. 2005. Cooling of photovoltaic cells under concentrated illumination: a critical review. *Solar Energy Materials and Solar Cells,* 86**,** 451-483.

SHIMURA, F. 2012. *Semiconductor silicon crystal technology*, Elsevier.

SINTON, R. A., KWARK, Y. K. Y., GAN, J. Y. & SWANSON, R. M. 1986. 27.5-Percent Silicon Concentrator Solar Cells. *IEEE Electron Device Letters,* 7**,** 567-569.

TJAHJONO, B. S. & COTTER, J. E. 19.2% efficiency n-type laser-grooved silicon solar cells. 2005 2005. IEEE, 983-986.

WENHAM, S. & GREEN, M. A. 1995. Large area, concentrator buried contact solar cells. *IEEE Transactions on Electron Devices,* 42**,** 144-149.

WÜRFEL 2008. *Physics of Solar Cells: From Principles to New Concepts*, Wiley Online Library.

YAMAGUCHI, M. 2003. III–V compound multi-junction solar cells: present and future. *Solar Energy Materials and Solar Cells,* 75**,** 261-269.

YANG, D., YU, X., LI, X., WANG, P. & WANG, L. Germanium-doped crystal silicon for solar cells. 2010/11// 2010. IEEE, 1994-1994.

ZHAO, J., WANG, A. & GREEN, M. A. 24% efficient PERL structure silicon solar cells. 1990 1990. IEEE, 333-335.

CHAPTER 6

SIC PASSIVATED IBC-SiGeHJ SOLAR CELL IN TANDEM CONFIGURATION WITH PEROVSKITE TOP SUBCELL

In perovskite/silicon tandem solar cell, to absorb the photons of higher wavelength, i.e. >800 in bottom subcell, thickness more than 250 μm is required since the absorption coefficient of silicon is small at a higher wavelength. This eventually increases the module cost. These issues can be fixed by using a different material which has higher optical absorption compared to silicon at higher wavelengths. The use of SiGe cell as a bottom cell is a possible solution to enhance the absorption and boost the efficiencies.

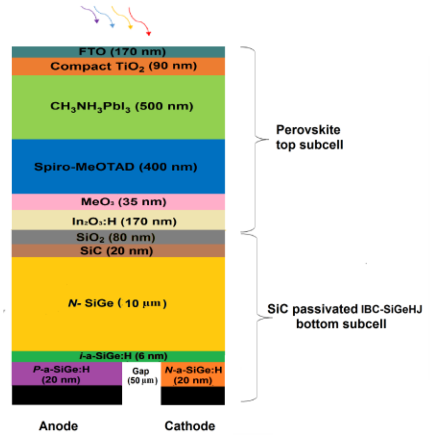

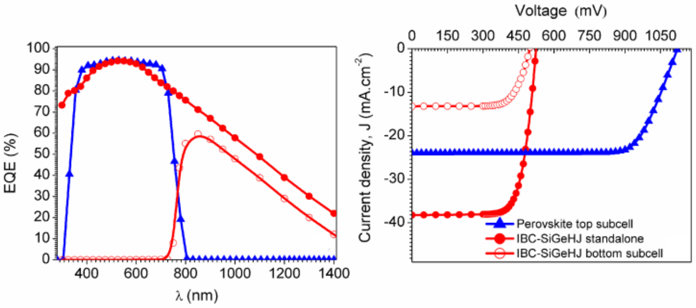

- *Innovative $Si_{0.75}Ge_{0.25}$ based IBC-HJ solar cell been proposed and simulated.*
- *Optimization has been done for 10 μm thick IBC-SiGeHJ.*
- *In combination with perovskite top subcell, further 25.7% PCE demonstrated.*
- *Results shows, proposed design can be a good candidate to obtained ultra-high efficiencies.*

6.1: INTRODUCTION

In the PV technologies, thickness of the active material plays a crucial role in determining the efficiency (Pandey and Chaujar, 2017b, Pandey and Chaujar, 2016b, Pandey and Chaujar, 2016a, Garnett and Yang, 2010). Increasing the thickness of active material significantly improves the optical performance of the device; however requirement of large and high quality material increase the module cost also as well (Branham et al., 2015, Jeong et al., 2013). Silicon is the most commonly used material in PV technologies (ITRPV, 2016), and after 61 years of research, the PCEs of Si solar cell is slowly approaching the Auger-recombination-constrained Shockley–Queisser limit of 29.8% (Polman et al., 2016, Tiedje et al., 1984). To further increase the efficiencies while simultaneously reducing the cost per kWh, new strategies such as tandem configurations (Bailie and McGehee, 2015, Tiedje et al., 1984) have to be applied as discussed in **Chapter 3** and **Chapter 4**. In c-Si based tandem approaches, a low cost wide-bandgap (1.6-1.9 eV) absorber material based top subcell is required (Werner et al., 2015), and perovskite based solar cells are the potential candidates to fulfill the requirement (Park, 2014). Previous research work shows significant improvement in the overall PCEs of perovskite/silicon based tandem devices, under single AM1.5 irradiance (Mailoa et al., 2015, Werner et al., 2015, Sheng et al., 2015).

Moreover, in perovskite/silicon tandem solar cell, the perovskite top cell utilize the lower wavelength photons. Whereas, to absorb the photons of higher wavelength, i.e. > 800 , thickness more than 250 μm is required since the absorption coefficients of silicon is small at a higher wavelength (Green and Keevers, 1995, Green, 2008). Work reported in **Chapter 3** shows 29.5% and 23.7% conversion efficiencies in 250 μm and 25 μm thick IBC-SiHJ bottom subcell based tandem devices, respectively (Pandey and Chaujar, 2017b).

Approximately 20% decrease in PCE has been observed, which clearly indicates decreasing the thickness of bottom subcell surely saves the material cost, but consequently affects the overall conversion efficiencies also. Hence, further refinements are required in perovskite/silicon based tandem device to improve the efficiencies while keeping the thickness of bottom subcell low. These issues can be fixed by using a different material which has higher optical absorption compared to silicon at higher wavelengths (Bulletin, 2003). Results reported in **Chapter 5** shows that the use of SiGe cell as a bottom cell is a possible solution to enhance the absorption at a higher wavelength while keeping the thickness low (Pandey and Chaujar, 2016c). The experimentally available data shows, the absorption coefficients of SiGe is greater than Si in the higher wavelength region. Hence, SiGe can efficiently absorb the photon of wavelengths > 800 nm (non-utilized photons by top subcell) compared to Si.

Further, work reported in this chapter presents IBC-SiGeHJ solar cell for standalone and mechanically stacked tandem applications, to make a SiGe based bottom subcell, a novel device has been designed, where SiGe material is introduced to IBC-HJ architecture (Taguchi et al., 2000, Schwartz and Lammert, 1975, Lammert and Schwartz, 1977), and resulted device is named as IBC-SiGeHJ solar cell (Pandey and Chaujar, 2017a). 10µm thick SiGe solar cell has been used as bottom subcell, which is ~ (25-30) times thinner than conventional Si solar cell which is used as bottom subcell in perovskite/silicon tandem solar cell. This indicates that the proposed device significantly saves the material required for the fabrication. However, the cost of germanium doped wafer is higher compared to a silicon wafer, though present work shows a tandem device made using SiGe cell can be a good candidate for energy efficient applications, and future development of cost effective energy efficient methods may decrease the overall dollar per watt ($/W) of the device. Detailed analysis has been done for SiGe cell, before placing it as bottom subcell in tandem device. Optimization has been done for both standalone and tandem conditions where thickness of i-a-SiGe: H, width of n-type (back surface field), width of p-type (emitter), gap width, and composition fraction have been optimized for improved conversion efficiency. Further, to prevent the front surface recombination, SiC-based front surface passivation has been used for bottom subcell (Pandey and Chaujar, 2016a, Pandey and Chaujar, 2016c).

6.2: DEVICE STRUCTURE, MODELS AND METHODS

The simulated device structures are reported in **Figure 6.1**(a-c) below, perovskite top subcell, IBC-SiGeHJ bottom subcell, and 4-terminal tandem cell have been shown in Fig. **Figure 6.1**(a), **Figure 6.1**(b), and **Figure 6.1**(c), respectively. The top subcell is identical as used in **Chapter 3** and **Chapter 4**.

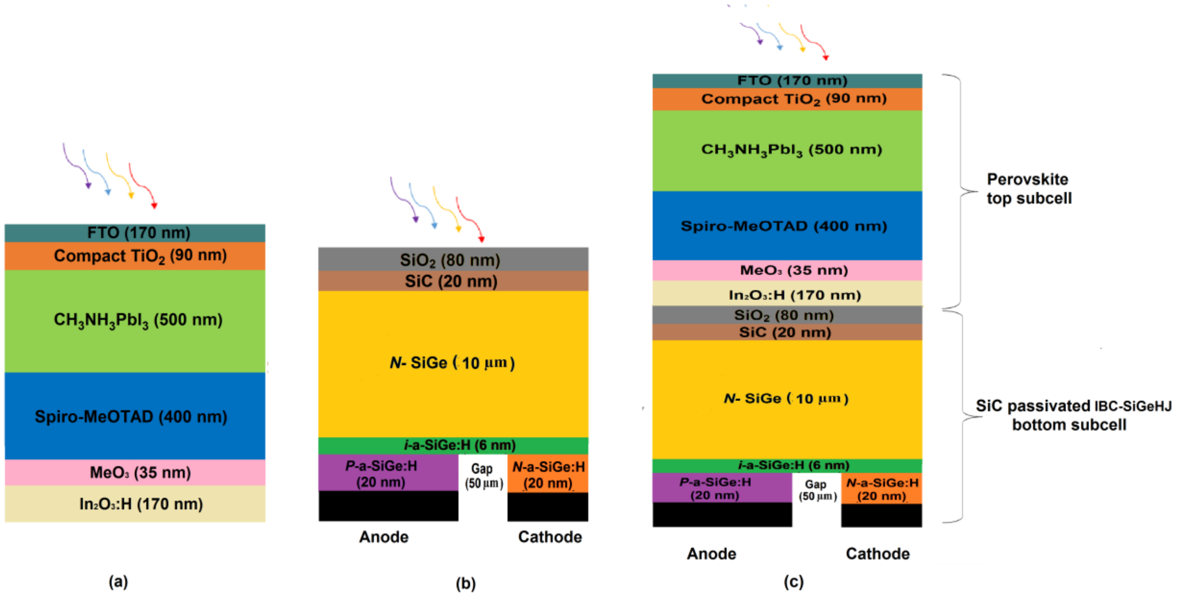

Figure 6.1: Device structures used in simulations (a) semitransparent perovskite top subcell, with FTO and In_2O_2: H based front and rear contact (b) IBC-SiGeHJ bottom subcell, and (c) 4-terminal mechanically stacked tandem solar cell (Pandey and Chaujar, 2017a).

ATHENA process simulator has been used to design the devices (Silvaco, 2015). The doping of *n-type* SiGe and *n-type* a-SiGe:H is 2.14×10^{16} cm^{-3} and 4.8×10^{18} cm^{-3}, respectively and that of *p-type* a-SiGe:H is 2×10^{19} cm^{-3}. The gap width is 50 µm and width of *p-type* a-SiGe: H, *n-type* a-SiGe: H is 100 µm and 25µm respectively. Models for bottom subcell are identical as used for IBC-SiHJ solar cell in **Chapter 4**; however material parameters for SiGe is reported in **Table 6-1** below, whereas models and material parameters for top subcell are identical as used in **Chapter 3**.

TABLE 6-1: MATERIAL PARAMETERS USED DURING SIMULATION (PANDEY AND CHAUJAR, 2017A, ATLAS, 2017).

Material		A	B	C	D	E
Dielectric Constant		12.9	11.9	11.9	11.9	
Band Gap (eV)		0.94	1.60	1.60	1.60	0.99
Electron Affinity (eV)		4.17	4.0	4.0	4.0	
Thickness (µm)		10	0.02	0.006	0.02	0.001
Electron, Hole mobility (cm^2/V·s)		1430, 480	20, 2	20, 2	20, 2	n/a
Effective conduction band (DOS) (cm^{-3})		2.36× 10^{19}	2.5× 10^{20}	2.5× 10^{20}	2.5× 10^{20}	n/a
Effective valence band (DOS) (cm^{-3})		9.30× 10^{18}	2.5× 10^{20}	2.5× 10^{20}	2.5× 10^{20}	n/a
Conduction tail states	$N^{c\text{-}tail}\ A$ (cm^{-3})	n/a	10^{21}	10^{18}	10^{21}	0
	$E^{c\text{-}tail}\ A$ (eV)	n/a	0.07	0.09	0.07	0.07
Valence tail states	$N^{v\text{-}tail}\ D$ (cm^{-3})	n/a	10^{21}	10^{18}	10^{21}	0
	$E^{v\text{-}tail}\ D$ (eV)	n/a	0.12	0.09	0.12	0.12
Acceptor-like (A) dangling bond states	$N^{db}\ A$ (cm^{-3})	n/a	10^{19}	10^{16}	10^{19}	2.4× 10^{16}
	$E^{db}\ A$ (eV)	n/a	0.7	1.1	1.3	0.5
	$\sigma^{db}\ A$ (eV)	n/a	0.2	0.15	0.2	0.2
Donor-like (D) dangling bond states	$N^{db}\ D$ (cm^{-3})	n/a	10^{19}	10^{16}	10^{19}	2.4× 10^{16}
	$E^{db}\ D$ (eV)	n/a	0.45	0.9	1.1	0.5
	$\sigma^{db}\ D$ (eV)	n/a	0.2	0.15	0.2	0.2

A=$Si_{0.85}Ge_{0.15}$, *B*= *n*- type a- $Si_{0.85}Ge_{0.15}$:H, *C*= Buffer a- $Si_{0.85}Ge_{0.15}$:H, *D*= *p*- type a- $Si_{0.85}Ge_{0.15}$:H, E=Interface defects

In this chapter, the optimization has been performed for IBC-SiGeHJ solar cell initially, where thickness of i-a-SiGe: H, width of n-type (back surface field), width of p-type (emitter), gap width, and composition fraction have been optimized for improved conversion efficiency. Further, IBC-SiGeHJ cell is placed under top subcell and a fresh optimization has been done again under reduced light intensity, followed by the final design of 4- terminal mechanically stacked perovskite/IBC-SiGeHJ tandem solar cell.

6.3: RESULTS

Result section of the chapter is divided into two parts: Comprehensive analysis and optimization of 10 μm thick IBC-SiGeHJ solar cell is reported in **Section 6.3.1:** and examination of perovskite/IBC-SiGeHJ mechanically stacked tandem solar cell is presented in **Section 6.3.2:**

6.3.1: Comprehensive study and optimization of 10 μm thick IBC-SiGeHJ bottom subcell.

This section of the chapter deals with the optimization of IBC-SiGeHJ bottom subcell, i.e., the thickness of i-a-SiGe: H, width of back surface field (BSF), width of emitter, gap width, and composition fraction have been optimized for improved efficiency. The simulation analysis of the IBC-SiGeHJ solar cell has been performed and the J-V curve with different i-a-SiGe: H thicknesses have been reported in **Figure 6.2** on page 128. The basic role of i-a-SiGe: H layer is to minimize the recombination at the a-SiGe/SiGe region, however it also reduces the conduction of light generated carriers and hence leads to increase series resistance. Result displays, increasing the thickness of a-SiGe: H layer leads to decrease in FF as depicted in **Figure 6.2**, which is attributed to increased series resistance. Nevertheless, at a thickness equivalent to 20 nm, “S” shaped J-V curve with low FF has been observed, which is confirmed by the already available results of 200-micron thick silicon-based device with the same architecture as reported by Meijun et al. (Meijun Lu, 2007).

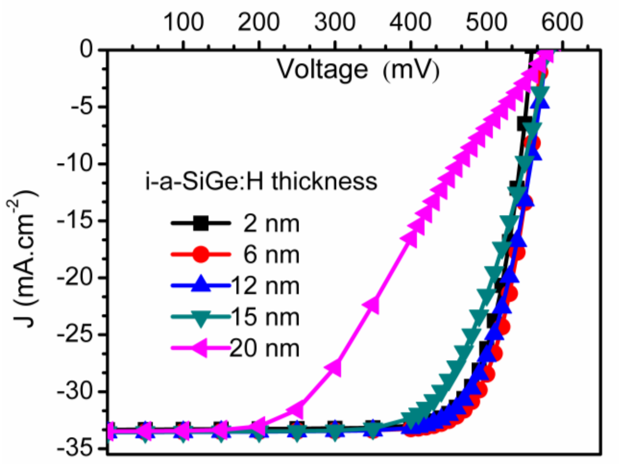

Figure 6.2: Impact of i-a-SiGe: H thickness on the current density (J) - voltage (V) curve of IBC-SiGeHJ solar cell (Pandey and Chaujar, 2017a).

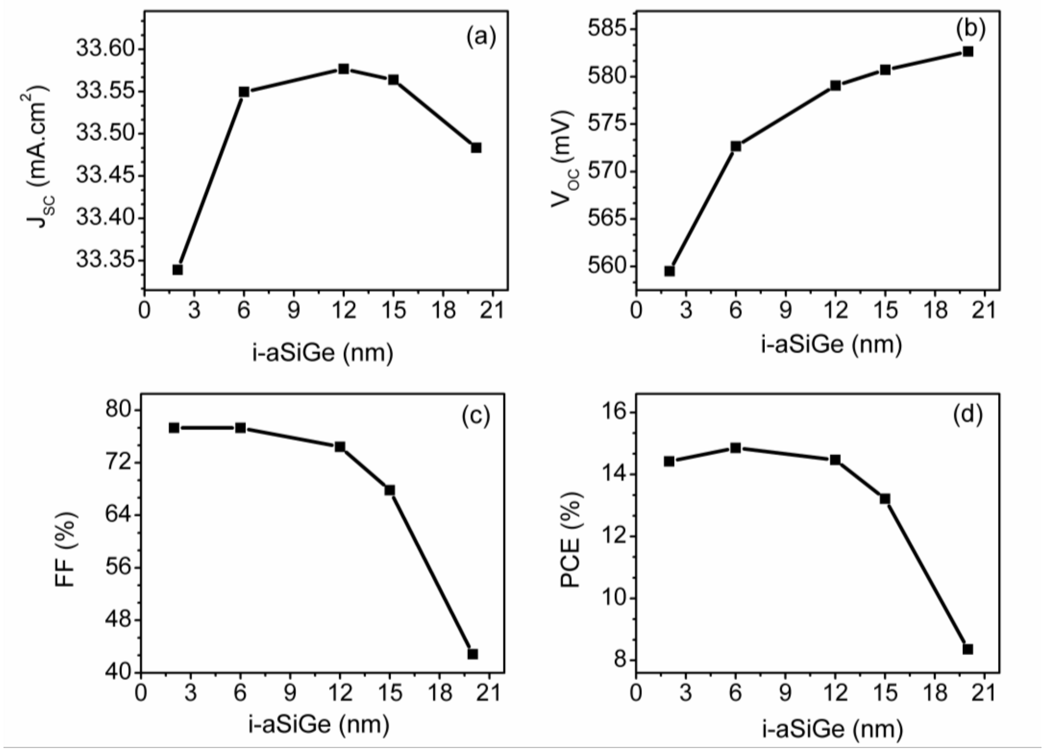

Figure 6.3: Impact of i-a-SiGe: H thickness on PV parameters: (a) J_{SC}, (b) V_{OC}, (c) FF, and (d) PCE. Results are obtained under standalone conditions (Pandey and Chaujar, 2017a).

Moreover, the influence of i-a-SiGe: H thickness on the photovoltaic parameters: J_{SC}, V_{OC}, FF, and PCE are shown in **Figure 6.3**(a), **Figure 6.3**(b), **Figure 6.3**(c), and **Figure 6.3**(d), respectively on page 128. Very minute impact has been observed on J_{SC}, whereas result shows a slight improvement in V_{OC} on increasing the thickness of i-a SiGe: H as depicted in **Figure 6.3**(a) and **Figure 6.3**(b), respectively, which is due to enhanced passivation quality and also supported by already published results (Thibaut et al., 2011). However, an increase in V_{OC} is not sufficient to mitigate the decrease in FF as reported in **Figure 6.3**(c) and hence, the overall PCE reduces by increasing the thickness of i-a-SiGe: H, as shown in **Figure 6.3**(d).

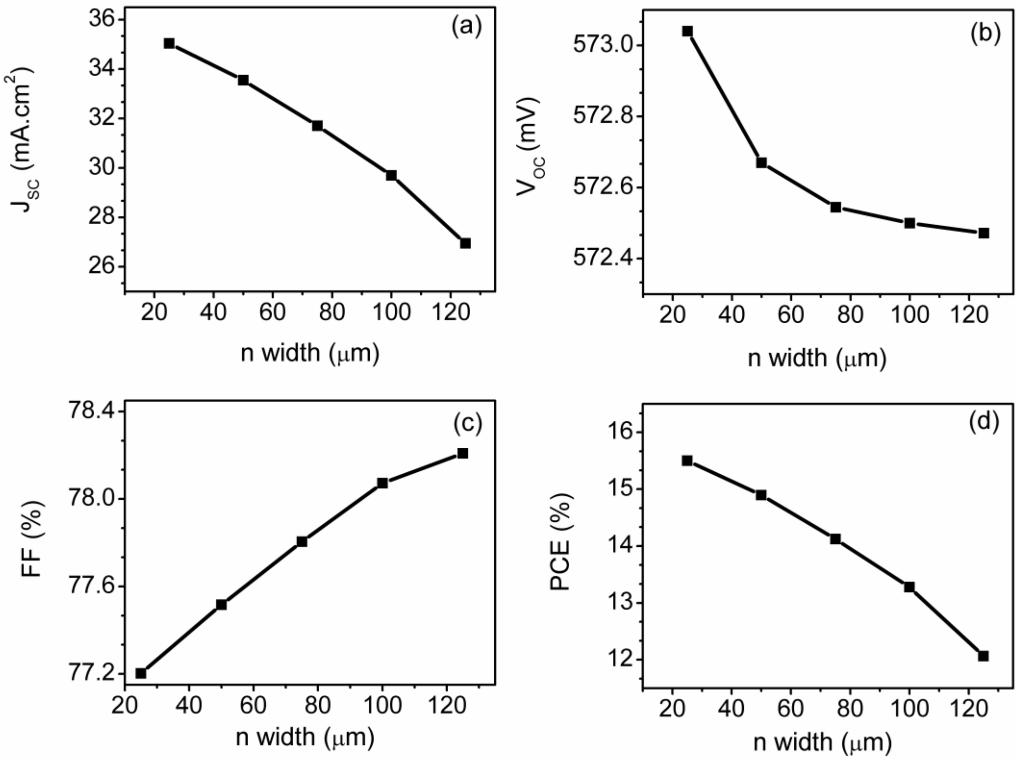

Figure 6.4: Impact of n strip width on PV parameters: (a) J_{SC}, (b) V_{OC}, (c) FF, and (d) PCE. Results are obtained under standalone condition (Pandey and Chaujar, 2017a).

Moreover, the width of n-strip, p- strip, and the gap has also optimized, and the results are shown in **Figure 6.4** above – **Figure 6.7** on page 132. The J_{SC} data w.r.t n-strip width is reported in **Figure 6.4** (a) on page 129. Increasing n-strip width considerably reduces J_{SC} and to understand the effect of n- strip width, contour representation of recombination rate; and the vector representation of conduction current have also been obtained and shown in **Figure 6.5**(a-c) below. To obtain the results, a very small region near the back side of the device is exaggerated as shown in **Figure 6.5**(a-c). Recombination rate with 25 micron, 75 micron, and 125 micron *n* strip width is reported in **Figure 6.5**(a), **Figure 6.5**(b), and **Figure 6.5**(c), respectively.

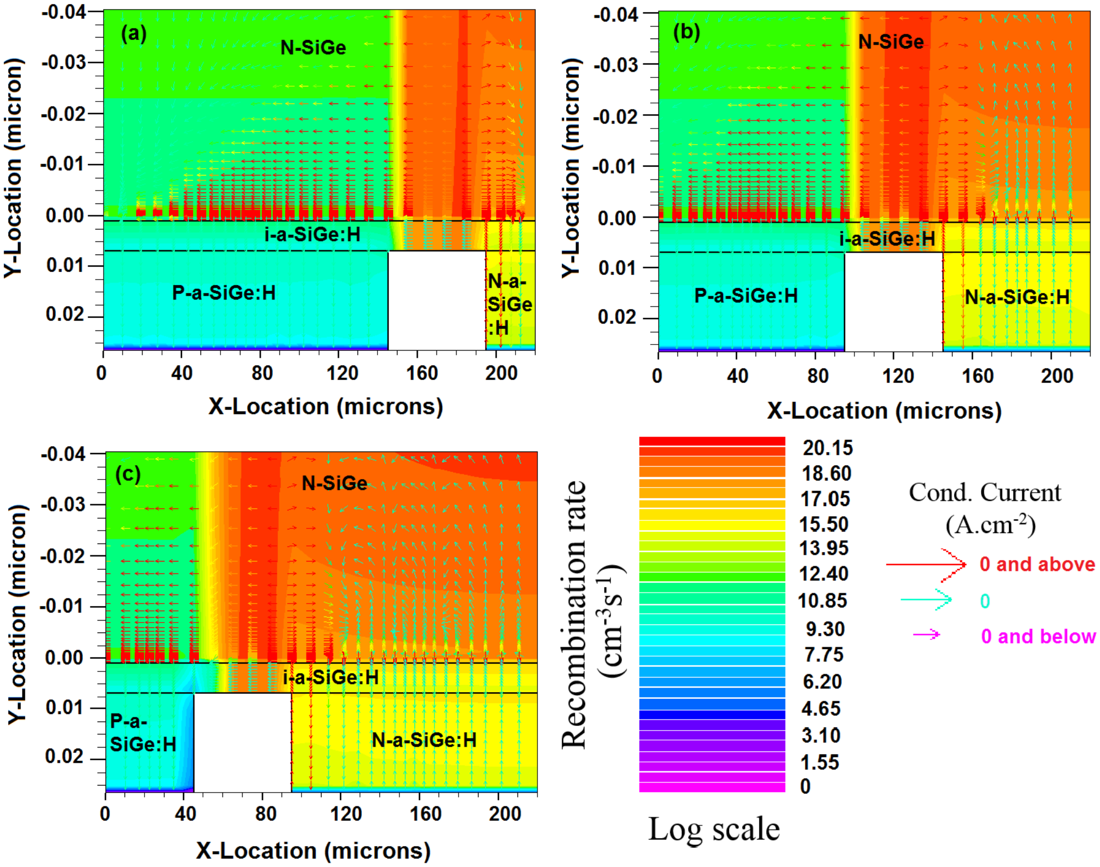

Figure 6.5: Contour representation of recombination rate with different n-strip widths (a) 25 micron, (b) 75 micron, and (d) 125 micron (Pandey and Chaujar, 2017a).

Increasing n- strip width will decrease the carrier collection probability of p-strip region, since the minority carriers that are generated near or at n-strip region requires to travel not only vertical to the rear junction but also laterally to arrive at the collecting junction, i.e. p-strip. Increasing n-width results in longer traveling distance for minority carrier, and hence the probability of carrier recombination is higher, as shown in **Figure 6.5**(a-c) on page 130. Higher the recombination rate, lower will be the conduction current density, and the direction of the conduction current density is shown in **Figure 6.5**(a-c). The FF and V_{OC} remain almost unaffected due to good surface passivation quality as depicted in **Figure 6.4** (b) &(c) on page 129, and thus the overall PCE decreases by increasing the n strip width as reported in **Figure 6.4**(d).

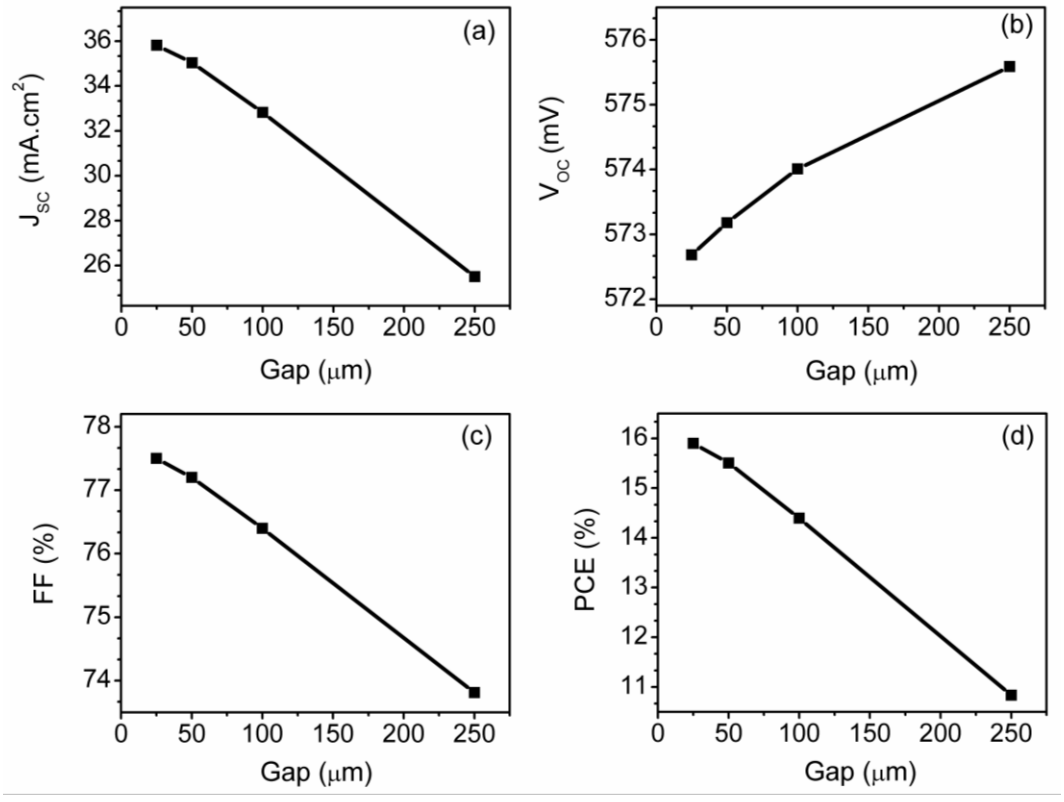

Figure 6.6: Impact of gap width on PV parameters: (a) J_{SC}, (b) V_{OC}, (c) FF, and (d) PCE. Results are obtained under standalone condition (Pandey and Chaujar, 2017a).

Further, the impact of gap width is studied in **Figure 6.6**(a-d) on page 131. Increasing the gap width will increase the lateral distance and series resistance for minority carrier that is generated at or near the BSF region. Therefore, increasing the gap width will decrease J_{SC} and FF as reported in **Figure 6.6**(a) and **Figure 6.6**(c), respectively. Slight improvement in V_{OC} is also observed as depicted in **Figure 6.6**(b). The overall impact of gap is reported in **Figure 6.6**(d), and results show PCE decrease as gap width increases.

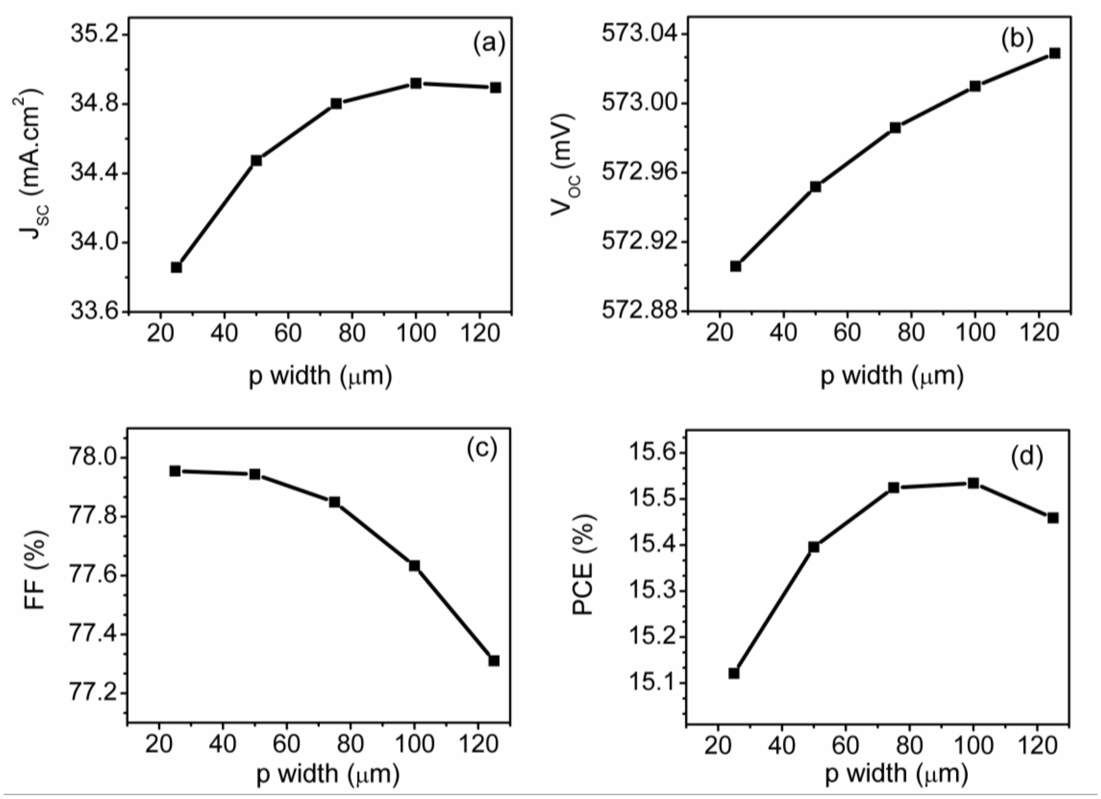

Figure 6.7: Impact of p strip width on PV parameters: (a) J_{SC}, (b) V_{OC}, (c) FF, and (d) PCE. Results are obtained under standalone condition (Pandey and Chaujar, 2017a).

Moreover, at the end of the optimization process, the impact of p-strip width has also been obtained, and results show that the 100 micron thick p-strip is optimum to give a good performance, as reflected in J_{SC}, V_{OC}, FF, and PCE reported in **Figure 6.7**(a), **Figure 6.7**(b), **Figure 6.7**(c), and **Figure 6.7**(d) above, respectively. Concluding the section gives the optimized dimensions for 10 microns thick IBC-SiGeHJ solar cell, i.e. width of BSF, gap, and emitter regions are 25 micron, 50 microns, and 100 microns respectively.

6.3.2: Examination of semitransparent Perovskite/IBC-SiGeHJ mechanically stacked tandem solar cell

In this section, a novel semi-transparent perovskite/IBC-SiGeHJ mechanically stacked tandem solar cell device has been simulated for ultra-high conversion efficiencies. A 20.9% efficient organic-inorganic halide semitransparent perovskite solar cell has been used as top subcell as reported by Pandey et al. (Pandey and Chaujar, 2016b), whereas 10 micron thick IBC-SiGeHJ solar cell has been used as bottom subcell. Four-terminal device simulated in this section is already reported in **Figure 6.1**(c) on page 125. The technique of simulation for tandem architecture is identical to **Chapter 3** and **Chapter 4**, where, top subcell is simulated individually, whereas bottom subcell has been simulated by placing perovskite as a filter. The addition of the PCE of perovskite top subcell and IBC-SiGeHJ bottom subcell in tandem configuration gives the overall PCE of the tandem device.

In the previous section, the optimization of IBC-SiGeHJ solar cell for standalone applications has been done under the full AM1.5 spectrum. Moreover, in this section, fresh optimization for IBC-SiGeHJ has been done under filtered spectrum by top subcell, and results are reported in **Figure 6.8**(a-d) on page 134 - **Figure 6.11**(a-d) on page 135. Parameters such as J_{SC}, V_{OC}, FF, and PCE are reported in part (a), (b), (c), and (d) of the Figures. Results show that the behavior of bottom subcell device is identical as obtained in standalone condition. However, the magnitude of PV parameters is lower, particularly J_{SC} as shown in **Figure 6.8**(a), **Figure 6.9**(a), **Figure 6.10**(a), and **Figure 6.11**(a).The decrease in J_{SC} is attributed to reduced light intensity in the presence of perovskite top subcell.

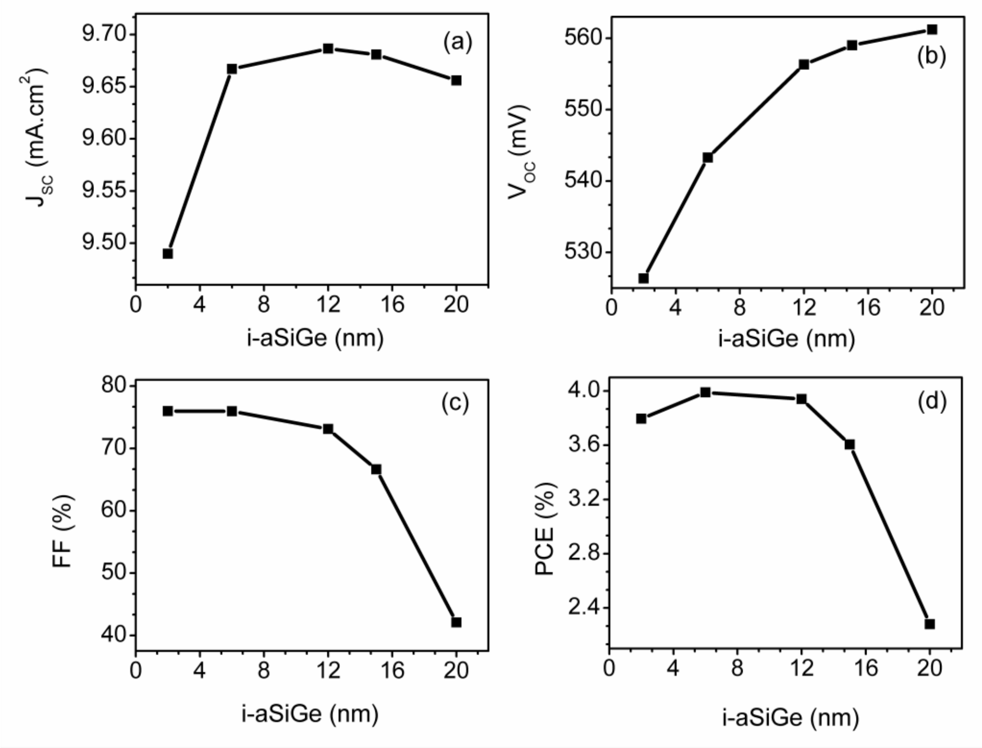

Figure 6.8: Impact of i-a-SiGe: H thickness on PV parameters: (a) J_{SC}, (b) V_{OC}, (c) FF, and (d) PCE. Results are obtained under tandem conditions (Pandey and Chaujar, 2017a).

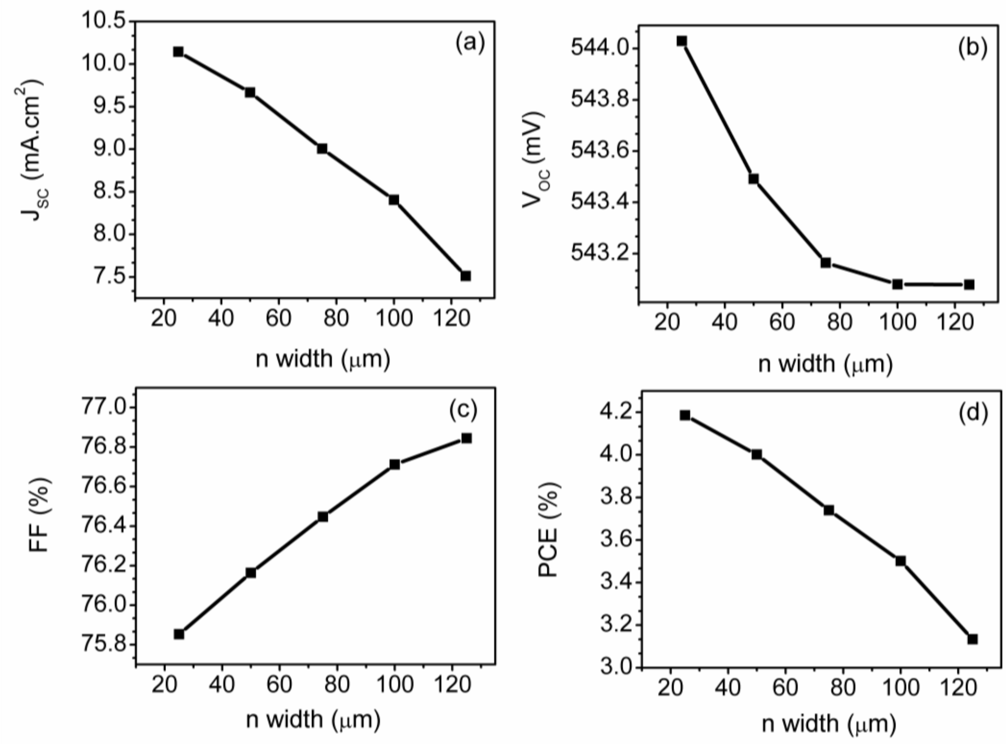

Figure 6.9: Impact of n strip width on PV parameters: (a) J_{SC}, (b) V_{OC}, (c) FF, and (d) PCE. Results are obtained under tandem condition (Pandey and Chaujar, 2017a).

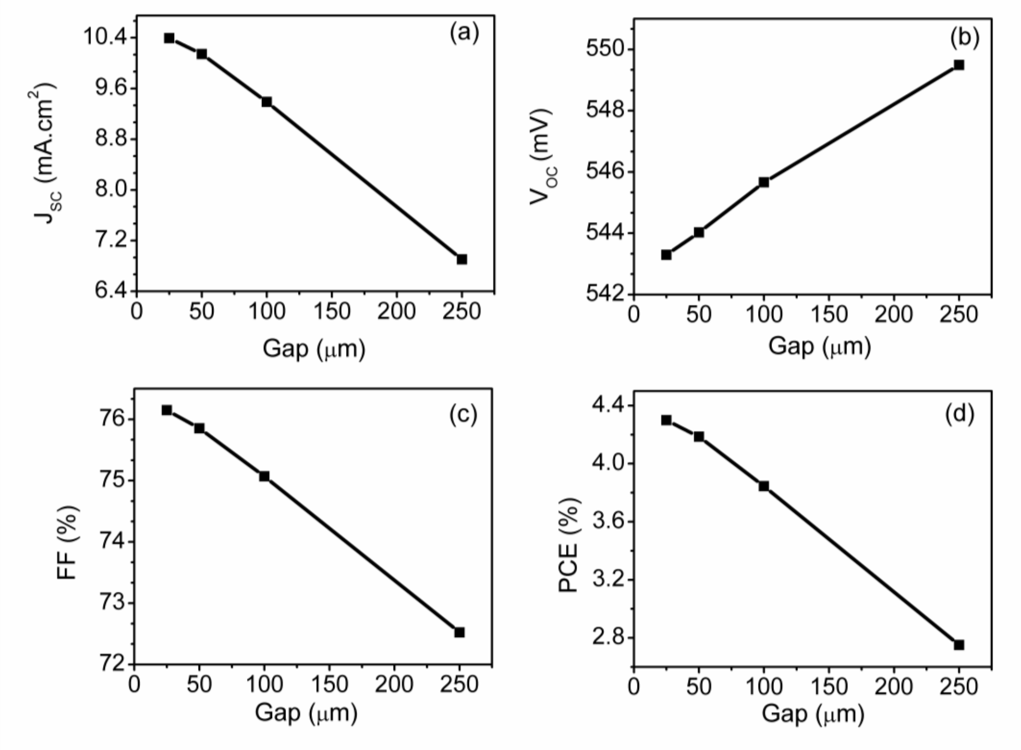

Figure 6.10: Impact of gap width on PV parameters: (a) J_{SC}, (b) V_{OC}, (c) FF, and (d) PCE. Results are obtained under standalone condition (Pandey and Chaujar, 2017a).

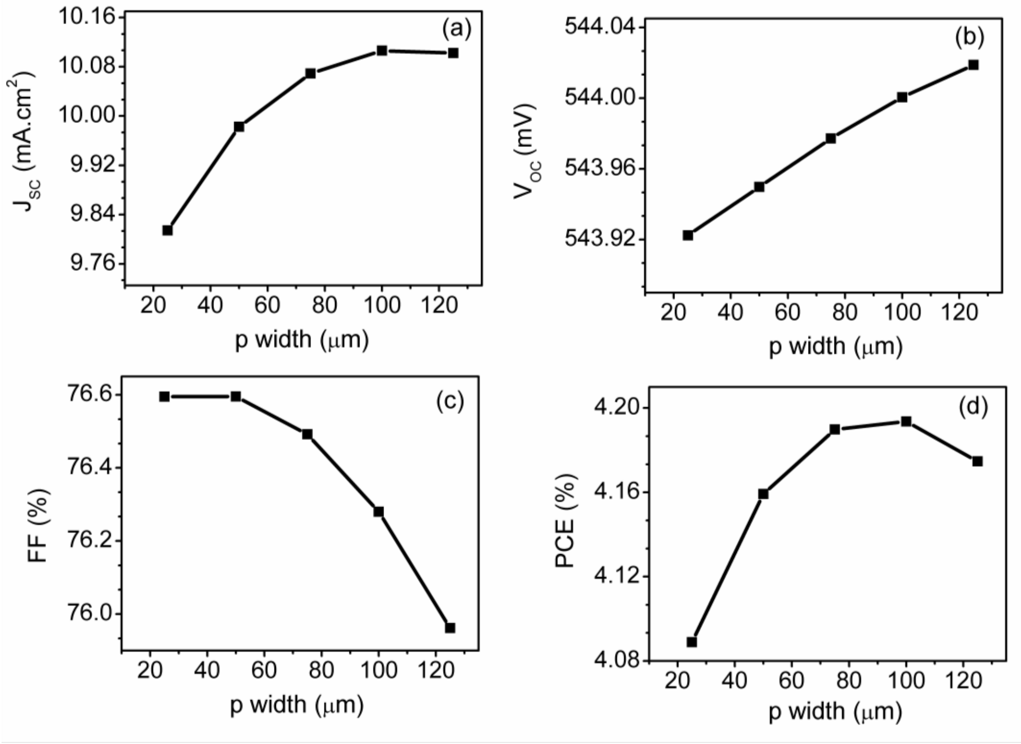

Figure 6.11: Impact of p strip width on PV parameters: (a) J_{SC}, (b) V_{OC}, (c) FF, and (d) PCE. Results are obtained under standalone condition (Pandey and Chaujar, 2017a).

Results reported in **Figure 6.8**(a-d) on page 134 - **Figure 6.11**(a-d) on page 135 shows that optimized dimensions under filtered spectrum are same as obtained for the stand-alone case. This validates that optimized dimensions, i.e. the width of BSF, gap, and emitter regions 25 microns, 50 microns, and 100 microns respectively, hold good for both standalone as well as bottom subcell conditions.

Further, the impact of composition fraction (*x*) on the performance of bottom IBC-Si$_{1-x}$Ge$_x$HJ solar cell has been studied for both standalone as well as tandem configuration. The performance of bottom subcell device has been obtained with three different composition fractions, i.e. *x*=0, 0.15, and 0.25. The optical properties, i.e. complex reflective indices used in the simulation have been obtained from SOPRA database of ATLAS library (Atlas, 2017), and reported in **Figure 6.12** below. The wavelength dependent real and imaginary index as a function of composition fraction is reported in **Figure 6.12** and **Figure 6.12**(inset), respectively.

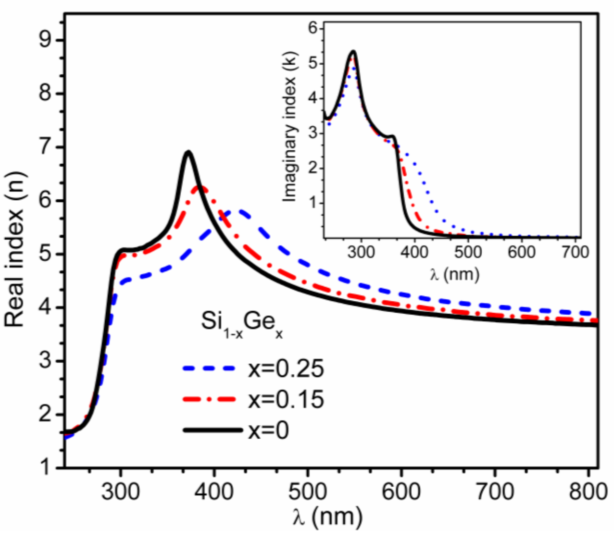

Figure 6.12: Optical properties i.e. real and imaginary indices (inset) of Si$_{1-x}$Ge$_x$ as a function composition fraction (Pandey and Chaujar, 2017a).

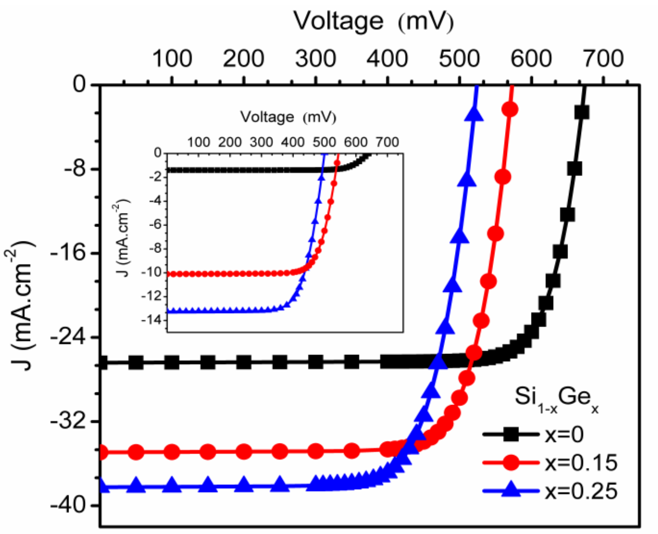

Figure 6.13: J-V curve of $Si_{1-x}Ge_x$ based bottom subcell device with different composition fraction, under standalone condition. Inset shows the J-V curve under tandem configuration (Pandey and Chaujar, 2017a).

Furthermore, the J-V for bottom subcell under standalone and tandem configuration with different composition fraction is shown in **Figure 6.13** above and **Figure 6.13**(inset), respectively. Increasing the composition fraction results in higher optical absorption, and hence results in higher J_{SC}; however, bandgap also reduces which further results in lower V_{OC}. This has been verified in the J-V curve reported in **Figure 6.13** including inset. Bottom subcell in standalone condition shows the J_{SC} (V_{OC}) values 26.4 mA.cm^{-2} (674mV), 34.9 mA.cm^{-2} (573mV), and 38.2 mA.cm^{-2} (524mV) with x=0, 0.15, and 0.25 composition fractions, respectively; as shown in **Figure 6.13**, and hence resulted in 14.4%, 15.5%, and 14.9% PCE for composition values of 0, 0.15, and 0.25, respectively. This concludes that under the standalone condition the optimum performance has been obtained for the composition fraction of 0.15. However, under tandem configuration with x=0, 0.15, and 0.25, the bottom subcell shows J_{SC} (V_{OC}) values of 1.4 mA.cm^{-2} (640 mV), 10.1 mA.cm^{-2} (544mV), and 13.2 mA.cm^{-2} (498 mV), respectively as depicted in **Figure 6.13**(inset), which resulted in

0.7%, 4.2%, and 4.8% PCE. Photovoltaic parameters of bottom subcell in standalone and bottom subcell operating conditions with different *x* values are reported in **Table 6-2** below.

Table 6-2: PHOTOVOLTAIC PARAMETERS OF IBC-SiGe BOTTOM SUBCELL WITH DIFFERENT COMPOSITION FRACTION (PANDEY AND CHAUJAR 2017A)

IBC-$Si_{1-x}Ge_x$HJ		J_{SC} (mA.cm^{-2})	V_{OC} (mV)	FF (%)	PCE (%)
x=0	standalone	26.4	674	81.1	14.4
	under tandem	1.4	640	79.6	0.7
x=0.15	standalone	34.9	573	77.4	15.5
	under tandem	10.1	544	76.9	4.2
x=0.25	standalone	38.2	524	74.5	14.9
	under tandem	13.2	498	73.2	4.8
Perovskite top subcell		23.9	1121	77.8	20.9
Mechanically stacked perovskite/IBC-$Si_{1-x}Ge_x$HJ tandem solar cell					20.9+4.8=25.7

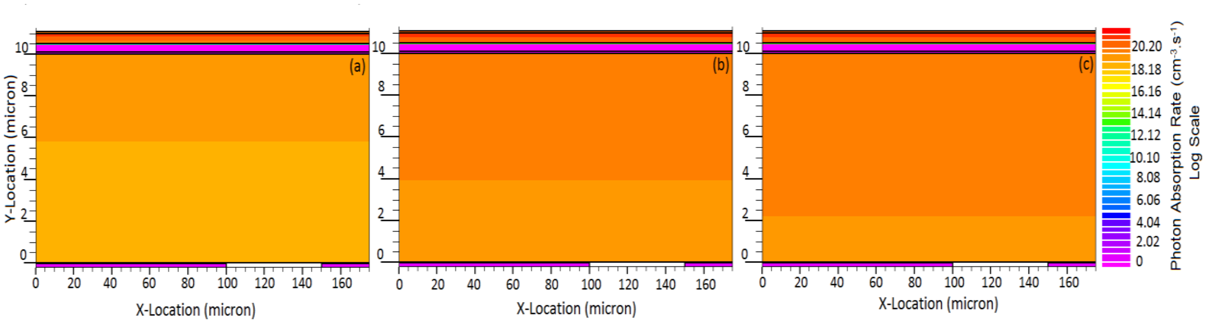

Figure 6.14: Photon absorption rate (cm^{-3}.s^{-1}) in bottom subcell under filtered spectrum by perovskite top subcell, with different *x* values. (a) *x*=0, (b) *x*=0.15, and (c) *x*=0.25. Regions above 10 μm in Y-locations represents perovskite top filter, and below 10 μm represents bottom IBC-SiGeHJ solar cell (Pandey and Chaujar, 2017a).

Result shows, under tandem configuration, optimum performance is obtained for *x*=0.25, due to improved optical absorption at a higher wavelength in $Si_{0.75}Ge_{0.25}$ and hence leads to higher J_{SC} under bottom subcell. In order to verify this, contour representation of photon absorption rate has been obtained in the bottom subcell device under tandem configuration and reported in **Figure 6.14** (a-b) above. The result shows higher photon coupling in bottom subcell for *x* value of 0.25, due to superior optical absorption in $Si_{0.75}Ge_{0.25}$ compared to other two composition fraction values. Simulation results show that IBC-$Si_{0.85}Ge_{0.15}$HJ solar cell shows optimum performance in standalone condition, whereas IBC-$Si_{0.75}Ge_{0.25}$HJ solar cell superior performance under tandem configuration.

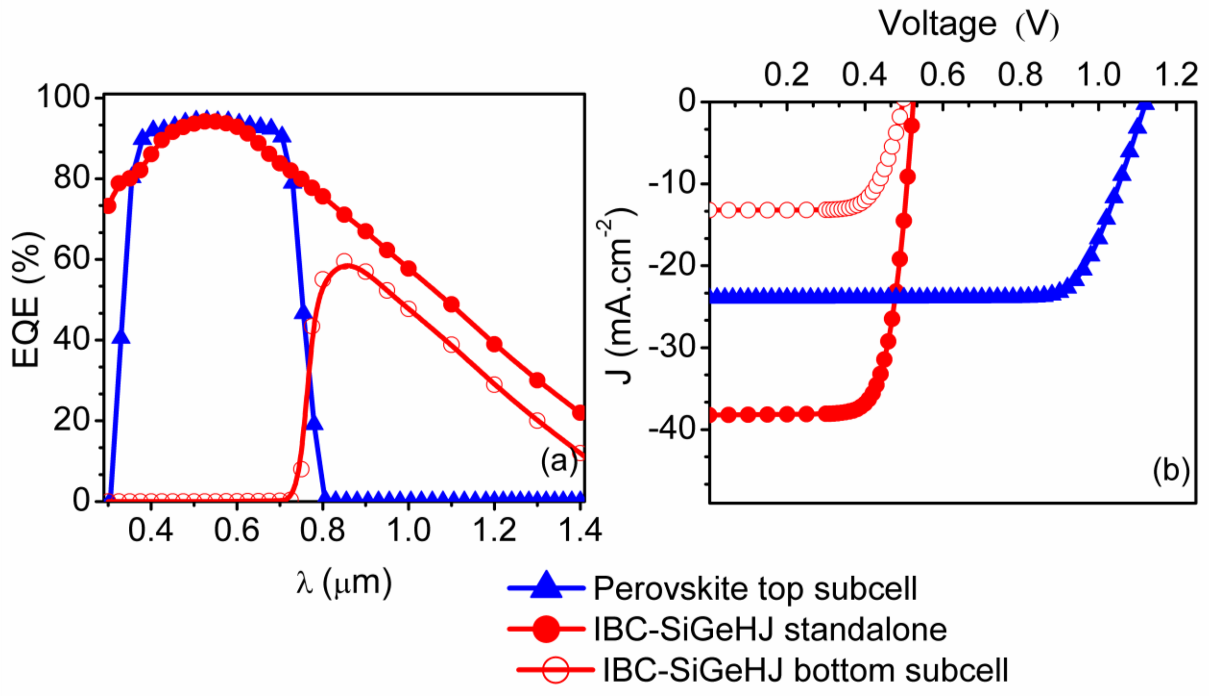

Figure 6.15: (a) Spectrum response, i.e. EQE of perovskite top subcell and IBC-$Si_{0.75}Ge_{0.25}$HJ bottom subcell in tandem and standalone configuration. (b) The J-V curve of top subcell and bottom subcell under illumination (Pandey and Chaujar, 2017a).

Further, simulation results are obtained for the final tandem device and reported in **Figure 6.15**(a-b) above. The spectrum response, i.e. external quantum efficiency, EQE of the perovskite top subcell, IBC-$Si_{0.75}Ge_{0.25}$HJ standalone, and IBC-$Si_{0.75}Ge_{0.25}$HJ as a bottom subcell in the tandem configuration are shown in **Figure 6.15**(a). The perovskite top subcell shows the EQE up to 800 nm, which are in good agreement with already published experimental results (Yin et al., 2016, Lin et al., 2015, Yang et al., 2015). Bottom subcell operated standalone shows EQE in the lower wavelength as well as higher wavelength region.

However, when operated in tandem configuration as a bottom subcell, the EQE at lower wavelengths disappears, due to the presence of perovskite top subcell. Since, up to 800 nm, top subcell absorbs the solar spectrum. However, a wavelength greater than 800 nm will be available for bottom subcell, as shown in **Figure 6.15**(a) on page 139. J-V curve of the final tandem device is shown in **Figure 6.15**(b) and corresponding photovoltaic parameters are shown in **Table 6-2** on page 138.

6.4: SUMMARY

In this Chapter, a novel 10 micron thick IBC-$Si_{1-x}Ge_x$HJ solar cell device has been designed and simulated for standalone and four-terminal mechanically stacked tandem applications. Optimization of i-a-SiGe: H thickness, width of n-a-SiGe: H region, p-a-SiGe: H region and gap along with composition fraction led to 15.5% PCE in a stand-alone configuration, whereas in combination with perovskite top subcell, further 25.7% PCE is demonstrated in four-terminal tandem configuration. In perovskite-based tandem devices, the spectrum till 800 nm wavelength will be absorbed by perovskite top subcell whereas wavelength greater than 800 nm will be available for bottom subcell. Therefore the use of SiGe ensures higher absorption compared to Si-based IBC solar cell since the presence of Ge increases the optical absorption at higher wavelengths, which results in higher J_{SC}. The spectrum, as well as the electrical behavior of the devices, has been obtained to understand the device operation in both tandem as well as standalone conditions. Under tandem configuration, 4.8% PCE has been simulated in bottom subcell, which combines with 20.9% PCE of perovskite top subcell to give overall conversion efficiency of 25.7% (20.9% top subcell + 4.8% bottom subcell). 10µm thick IBC-$Si_{0.75}Ge_{0.25}$HJ solar cell has been used as bottom subcell in perovskite/SiGe tandem solar cell which is ~ (25-30) times thinner than conventional Si solar cell and is used as a bottom subcell in perovskite/silicon tandem solar cell, and hence, significantly saves the material. The results reveal that the proposed 4-terminal mechanically stacked perovskite/IBC-SiGeHJ tandem device may open new doors for the energy efficient applications.

Moreover, next chapter concludes all the work done in the thesis and gives future prospective of discussed solutions.

6.5: REFERENCES

NSM Archive - Silicon Germanium (SiGe) - Optical properties.

ATLAS 2017. ATLAS User ' s Manual. 567-1000.

BAILIE, C. D. & MCGEHEE, M. D. 2015. High-efficiency tandem perovskite solar cells. *MRS Bulletin,* 40**,** 681-686.

BRANHAM, M. S., HSU, W.-C., YERCI, S., LOOMIS, J., BORISKINA, S. V., HOARD, B. R., HAN, S. E. & CHEN, G. 2015. 15.7% Efficient 10-μm-Thick Crystalline Silicon Solar Cells Using Periodic Nanostructures. *Advanced materials (Deerfield Beach, Fla.)***,** 2182-2188.

BULLETIN, P. 2003. SiGe: a key to unlocking the potential of solar cells. *Photovoltaics Bulletin,* 2003**,** 7-9.

GARNETT, E. & YANG, P. 2010. Light trapping in silicon nanowire solar cells. *Nano letters,* 10**,** 1082-1087.

GREEN, M. A. 2008. Self-consistent optical parameters of intrinsic silicon at 300K including temperature coefficients. *Solar Energy Materials and Solar Cells,* 92**,** 1305-1310.

GREEN, M. A. & KEEVERS, M. J. 1995. Optical properties of intrinsic silicon at 300 K. *Progress in Photovoltaics: Research and Applications,* 3**,** 189-192.

ITRPV, I. S. E. V. P., 2016. 2016. ITRPV.

JEONG, S., MCGEHEE, M. D. & CUI, Y. 2013. All-back-contact ultra-thin silicon nanocone solar cells with 13.7% power conversion efficiency. *Nature communications,* 4**,** 2950-2950.

LAMMERT, M. D. & SCHWARTZ, R. J. 1977. The interdigitated back contact solar cell: A silicon solar cell for use in concentrated sunlight. *IEEE Transactions on Electron Devices,* 24**,** 337-342.

LIN, Q., ARMIN, A., NAGIRI, R. C. R., BURN, P. L. & MEREDITH, P. 2015. Electro-optics of perovskite solar cells. *Nat Photon,* 9**,** 106-112.

MAILOA, J. P., BAILIE, C. D., JOHLIN, E. C., HOKE, E. T., AKEY, A. J., NGUYEN, W. H., MCGEHEE, M. D. & BUONASSISI, T. 2015. A 2-terminal perovskite/silicon multijunction solar cell enabled by a silicon tunnel junction. *Applied Physics Letters,* 106**,** 121105.

MEIJUN LU, S. B., UJJWAL DAS, AND ROBERT BIRKMIRE 2007. A-SI/C-SI HETEROJUNCTION FOR INTERDIGITATED BACK CONTACT SOLAR CELL *Pro. 22nd European PVSEC,* 22**,** 4.

PANDEY, R. & CHAUJAR, R. 2016a. Numerical simulation of rear contact silicon solar cell with a novel front surface design for the suppression of interface recombination and improved absorption. *Current Applied Physics,* 16**,** 1581-1587.

PANDEY, R. & CHAUJAR, R. 2016b. Numerical simulations: Toward the design of 27.6% efficient four-terminal semi-transparent perovskite/SiC passivated rear contact silicon tandem solar cell. *Superlattices and Microstructures,* 100**,** 656-666.

PANDEY, R. & CHAUJAR, R. 2016c. Rear contact SiGe solar cell with SiC passivated front surface for >90-percent external quantum efficiency and improved power conversion efficiency. *Solar Energy,* 135**,** 242-252.

PANDEY, R. & CHAUJAR, R. 2017a. Numerical simulations of novel SiGe-based IBC-HJ solar cell for standalone and mechanically stacked tandem applications. *Materials Research Bulletin,* 93**,** 282-289.

PANDEY, R. & CHAUJAR, R. 2017b. Technology computer aided design of 29.5% efficient perovskite/interdigitated back contact silicon heterojunction mechanically stacked tandem solar cell for energy-efficient applications. *Journal of Photonics for Energy,* 7**,** 022503-022503.

PARK, N.-G. 2014. Perovskite solar cells: an emerging photovoltaic technology. *Materials Today,* 18**,** 65-72.

POLMAN, A., KNIGHT, M., GARNETT, E. C., EHRLER, B. & SINKE, W. C. 2016. Photovoltaic materials: Present efficiencies and future challenges. *Science,* 352.

SCHWARTZ, R. J. & LAMMERT, M. D. Silicon solar cells for high concentration applications. 1975 International Electron Devices Meeting, 1975 1975. 350-352.

SHENG, R., HO-BAILLIE, A. W., HUANG, S., KEEVERS, M., HAO, X., JIANG, L., CHENG, Y.-B. & GREEN, M. A. 2015. Four-Terminal Tandem Solar Cells Using CH3NH3PbBr3 by Spectrum Splitting. *The journal of physical chemistry letters*, 6**,** 3931-3934.

SILVACO 2015. *ATHENA User's Manual, 2D PROCESS SIMULATION SOFTWARE,* Santa Clara, CA 95054 Silvaco.

TAGUCHI, M., KAWAMOTO, K., TSUGE, S., BABA, T., SAKATA, H., MORIZANE, M., UCHIHASHI, K., NAKAMURA, N., KIYAMA, S. & OOTA, O. 2000. HITTM cells—high-efficiency crystalline Si cells with novel structure. *Progress in Photovoltaics,* 8**,** 503-514.

THIBAUT, D., SYLVAIN, D. V., FLORENT, S., DJICKNOUM, D., DELFINA, M., MARIE, G.-F., JEAN-PAUL, K. & JEAN, R. P. 2011. Development of Interdigitated Back Contact Silicon Heterojunction (IBC Si-HJ) Solar Cells. *Energy Procedia,* 8**,** 294-300.

TIEDJE, T., YABLONOVITCH, E., CODY, G. D. & BROOKS, B. G. 1984. Limiting efficiency of silicon solar cells. *IEEE Transactions on electron devices,* 31**,** 711-716.

WERNER, J., WENG, C.-H., WALTER, A., FESQUET, L., SEIF, J. P., DE WOLF, S., NIESEN, B. & BALLIF, C. 2015. Efficient Monolithic Perovskite/Silicon Tandem Solar Cell With Cell Area > 1 cm 2. *The Journal of Physical Chemistry Letters*, 7**,** acs.jpclett.5b02686-acs.jpclett.5b02686.

YANG, W. S., NOH, J. H., JEON, N. J., KIM, Y. C., RYU, S., SEO, J. & SEOK, S. I. 2015. High-performance photovoltaic perovskite layers fabricated through intramolecular exchange. *Science.***,** science.aaa9272.

YIN, X., CHEN, P., QUE, M., XING, Y., QUE, W., NIU, C. & SHAO, J. 2016. Highly Efficient Flexible Perovskite Solar Cells Using Solution-Derived NiOx Hole Contacts. *ACS Nano,* 10**,** 3630-6.

CHAPTER 7

SUMMARY AND OUTLOOK

This chapter gives complete summary and outlook of the research work reported in the thesis.

- *Research work is briefly summarized*
- *Possible future work is projected*

7.1: SUMMARY

In this thesis, several approaches for improving solar efficiency with careful design have been proposed. These approaches attempt to improve the solar cell current, solar cell voltage, light absorption, surface recombination, and UV stability. Finally, the mechanically stacked tandem architecture addresses thermalization and lack of absorption losses for improved efficiency. In this chapter, each approach is briefly reviewed, and opportunities for future work in each area are also identified.

We first considered resolving the issues associated with thin devices such as low absorption and high surface recombination. These issues have been resolved in **Chapter 2** with the help of novel front surface design where ZrO_2 based texturing has been used along with SiC-based front surface passivation for the suppression of interface recombination and improvement of V_{OC}. The device under investigation shows V_{OC} of 662 mV in the sub-10 µm-thick rear contact silicon solar cell. Presence of ZrO_2 and SiC significantly improves the optical as well as the electrical behavior of the device. Photon absorption ~ 87% is obtained at short wavelengths (300 nm). A device containing thin SiC at the interface (ZrO_2/ n-Si) shows significant improvement throughout the wavelength spectrum 300-1000 nm, i.e. (UV-Visible-Infrared) and leads to EQE > 81% in the spectrum range of 320-720 nm wavelength spectrums with a maximum of 95.6% at wavelength 560 nm. UV stability has also been obtained under high surface recombination velocity conditions. These improvements lead to 15.7% efficient rear contact silicon solar cell, in the sub-10 µm-thick regime. Moreover, **Chapter 2** includes 21.6% efficient 300 µm thick device by introducing the same front surface design to a 300 µm thick device. Furthermore, application of SiC passivated rear contact solar cell in tandem configuration with perovskite top subcell has been discussed in **Chapter 3** where the focus is to minimize the thermalisation losses. The tandem structure of perovskite-silicon solar cells is a promising method to achieve efficient solar energy conversion at low cost. In the four-terminal tandem configuration, the cells are connected independently and hence avoids the need for current matching between top and bottom subcell, thus giving greater design flexibility. A novel four-terminal perovskite/SiC-based rear contact silicon tandem solar cell device has been proposed and simulated to achieve higher conversion efficiencies under single AM1.5 illumination. Initially, 20.9% efficient semitransparent perovskite top subcell has been designed for top subcell followed by the analysis of perovskite/silicon tandem architecture. The simulation analysis shows, PCEs of 27.6% and 22.4% with 300 µm and 10 µm thick rear contact Si bottom subcell, respectively. This is a substantial improvement compared to transparent perovskite solar cell and c-Si solar cell operated individually. The impact of perovskite layer thickness, monomolecular, bimolecular, and trimolecular recombination have also been obtained on the performance of perovskite top subcell.

Moreover, despite the exciting results achieved in **Chapter 3**, conventional rear-contact solar cell shows low V_{OC} and has high complexity in fabrication. IBC-SiHJ solar cells which use low-temperature processes have excellent performance, i.e., high V_{OC}, and better rear surface passivation due to deposited i-a-Si: H. Hence, analysis of SiC passivated IBC-SiHJ solar cell as a bottom subcell under perovskite solar cell has been done in **Chapter 4** to achieve further ultra-high efficiencies, wherein, the analysis of perovskite top subcell is the continuation of **Chapter 3**. All the basic recombination rates along with carrier distribution are obtained and reported to understand the recombination processes inside the perovskite top subcell. The performance of top subcell has been obtained for different acceptor densities and hole mobility in HTL, along with the impact of counter electrode work function. Increasing the acceptor density and hole mobility in HTL beyond 3×10^{16} cm^{-3} and 10^{-5} cm^{2}.V^{1}.s^{-1} shows significant improvement in the performance of perovskite top subcell. Electric field distribution near HTL/CE showing counter electrode work function value > 4.9 eV is required for the efficient extraction of holes from HTL. For bottom subcell, 24.1% efficient individually operated IBC-SiHJ solar cell is combined in mechanically stacked four terminal tandem configuration with 20.9% efficient perovskite top subcell. Passivation quality has been studied and SiC passivated IBC-SiHJ bottom subcell shows good photovoltaic parameters compared to ARC based IBC-SiHJ solar cell. The optical and electrical behavior of the devices has been obtained for both standalone as well as tandem configuration. The efforts resulted in PCEs of 29.5 % and 23.7% with 250 µm and 25 µm thick IBC-SiHJ bottom subcells, respectively. Moreover, rear contact devices reported in **Chapter 2**, **Chapter 3**, and **Chapter 4** contains Si as an active material, whose absorption coefficient is small at higher wavelengths; therefore, thick silicon wafers are required to obtained greater efficiencies in both standalone as well as tandem configuration as discussed in current **Chapter 3** and **Chapter 4**.

However, thicker silicon wafer eventually increases the module cost. Hence, modification in the bandgap (E_g< 1.1 eV) of the Si is required to increase the absorption of sunlight at higher wavelengths while keeping the thickness low, and $Si_{1-X}Ge_X$ alloy can be used for the same. Hence, **Chapter 5 and Chapter 6** has been dedicated to the analysis of rear contact SiGe solar cells for standalone and tandem configuration. In **Chapter 5**, initially, intrinsic wafer based rear contact SiGe solar cell has been designed with SiC, SiO_2, and Si_3N_4 based ARPLs. Photo reflectance is significantly reduced in the UV/visible spectral region due to the presence of SiC. Energy band analysis has been done to understand the movement of carriers. Moreover, the impact of material quality has also been discussed. In second approach, intrinsic wafer has been replaced with n-type SiGe, to obtain further high V_{OC}. Detailed analysis such as energy band, hole concentration, electric field, and recombination rates are achieved inside the device to understand the behavior of the device. Spectrum analysis resulted in EQE> 90% in the range of 400–650 nm wavelength. Also, at wavelengths equivalent to 300 nm, SiC passivated device shows EQE of 85%. The presence of SiC as a surface passivation layer shows enhanced surface characteristics in terms of reduced surface recombination and higher photon absorption rate. Moreover, optimization of diffusion depth of the device resulted in 15.4% PCE under standard AM1.5 illumination. Nevertheless, the proposed device has also been analyzed for CPV applications, resulting in 18.4% and 19.3% efficiencies at 1 W/cm^2 (10 suns, 27^OC) and 2 W/cm^2 (20 suns, 27^OC) respectively. The improved performance of the device in sub 10 µm thick regime is attributed to the superior absorption coefficient of SiGe compared to Si. Absorption at the higher wavelength is obtained without the need of thick wafer and complex texturing scheme. Evoking the concept of perovskite-based tandem devices, the perovskite top cell utilizes the lower wavelength photons, and to absorb the higher wavelength photons, thicker silicon cells are required. These issues have been resolved by using SiGe which is capable of absorbing higher wavelength photons in compact architecture. Therefore considering the discussed concept, **Chapter 6** proposes IBC-SiGeHJ bottom subcell based 4 terminal perovskite/SiGe tandem solar cells, to boost the efficiencies of tandem solar cell.

In **Chapter 6**, a novel 10 micron thick IBC-$Si_{1-x}Ge_x$HJ solar cell device has been designed and simulated for standalone and four-terminal mechanically stacked tandem applications. Optimization of i-a-SiGe: H thickness, width of n-a-SiGe: H region, width of p-a-SiGe: H region and pitch gap along with composition fraction led to 15.5% PCE in a standalone configuration, whereas, in combination with perovskite top subcell, further 25.7% PCE is demonstrated in four-terminal tandem configuration. In perovskite-based tandem devices, the spectrum till 800 nm wavelength will be absorbed by perovskite top subcell whereas wavelength greater than 800 nm will be available for bottom subcell. Therefore, the use of SiGe ensures higher absorption compared to Si-based IBC solar cell since the presence of Ge increases the optical absorption at higher wavelengths, which resulted in higher J_{SC}. The spectrum, as well as the electrical behavior of the devices, has been obtained to understand the device operation in both tandem as well as standalone conditions. Under tandem configuration, 4.8% PCE has been simulated in bottom subcell, which combines with 20.9% PCE of perovskite top subcell to give overall conversion efficiency of 25.7% (20.9% top subcell + 4.8% bottom subcell). 10µm thick IBC-$Si_{0.75}Ge_{0.25}$HJ solar cell has been used as bottom subcell in perovskite/SiGe tandem solar cell which is ~ 25-30 times thinner than conventional Si solar cell which is used as bottom subcell in perovskite/silicon tandem solar cell, and hence, significantly saves the material. The design principles reported in this thesis may open new doors for the energy efficient applications.

7.2: OUTLOOK

In the present thesis, several schemes are projected to enhance the performance of rear-contact solar cells and significant improvements have been obtained in both standalone and tandem applications. Remarkably low surface recombination and higher absorption is achieved in 10 micron thick device, along with UV stability. Efficient wavelength utilization has been obtained by using SiGe alloy. Additionally to minimize thermalization losses, mechanically stacked tandem devices have also been designed and simulated which requires only two transparent contacts. All the objectives are majorly accomplished with the help of simulation analysis and additional outlook of the work is reported as follows:

- Concentrator photovoltaic analysis of ZrO_2 textured SiC passivated device can be done with the help of temperature and irradiance variation.
- Analysis of SiC-based surface passivation quality can also be performed for p-type wafer based cells. Impact of doped SiC layer can also be obtained.
- Application of SiC layer at the metalized surface can also be analyzed to prevent the surface recombination at the back side of the device.
- Solar cells with textured SiC can be designed in future and angular analysis can be done for optimum angular efficiency.
- Experimental deposition of SiC is needed with the help of microwave and radio frequency plasma-enhanced chemical vapor deposition reactor and characterization of the SiC layer can be examined with quasi-steady-state photoconductance, microwave-detected photoconductance, and carrier density imaging techniques.
- Some of the experimental research work shows SiC is a good candidate for surface passivation, whereas some other researchers observed that addition of SiC reduces the lifetime of the carriers, which means SiC surface passivation is needed to be further researched, developed and improved.
- The tunnel junction can be formed for good device performance independent of the counter electrode work function.
- Perfect transparent electrode does not exist in reality and hence some other transparent contact can be used by comparing their transmittance of necessary photons.

- SiGe based devices simulated in this work does not exist practically; hence proper fabrication is required to verify the results obtained in the study.
- Comparisons with multiple layers antireflective coating, ARC can be performed in future work. Multi-stack ARC enables refection control over a broad range of wavelengths or near the infra-red range in the case of bottom cell in tandem.
- Cost of SiGe wafer is high compared to Si, and hence proper cost efficiency analysis is needed.

APPENDIX

SEMICONDUCTOR EQUATIONS AND MODELS USED DURING SIMULATIONS

This section of the thesis provides the semiconductor equations and models used during simulation. A detailed description of models and parameters are given in this section, which includes the following:

- The Poisson equation, along with electron and hole continuity equations.
- SRH, Auger, Radiative, concentration dependent SRH, and surface recombination model.

A.1: The Poisson equation (1) and electron and hole continuity equations (2) and (3)

$$\frac{d}{dx}\left(-\varepsilon(x)\frac{d\Psi}{dx}\right) = -q\begin{bmatrix} n(x) - p(x) + N_a^-(x) - N_d^+(x) + \\ n_t(x) - p_t(x) \end{bmatrix} \tag{1}$$

$$\frac{dn_p}{dt} = D_n \frac{d^2 n_p}{dx^2} + n_p \mu_n \frac{d\xi}{dx} + \mu_n \xi \frac{dn_p}{dx} + G_n - \frac{n_p - n_{p0}}{\tau_n} \tag{2}$$

$$\frac{dp_n}{dt} = D_p \frac{d^2 p_n}{dx^2} - p_n \mu_p \frac{d\xi}{dx} - \mu_p \xi \frac{dp_n}{dx} + G_p - \frac{p_n - p_{n0}}{\tau_p} \tag{3}$$

The q is electron charge, D the diffusion coefficient; ε is the permittivity and G the generation rate. The n_s, n_t, p_s and p_t are the free electron, trapped electron, free hole, and trapped hole, respectively. ψ is the electrostatic potential. N_a^- the ionized acceptor-like doping concentration and N_d^+ are the ionized donor-like doping concentration. ξ is the electric field and τ_n, τ_p are the carrier lifetimes. The last term in equations (2) and (3) known as recombination term R_n, R_p. Further, when models are enabled, the SRH, auger, and radiative recombination rate are included in the recombination terms in the carrier continuity equations.

A.2: Recombination models

1. SRH

The basic SRH model is modeled as:

$$R_{SRH} = \frac{pn - n_{ie}^2}{\tau_{n0}\left[p + n_{ie}\exp\left(\frac{E_i - E_t}{k_b T}\right)\right] + \tau_{p0}\left[n + n_{ie}\exp\left(\frac{E_t - E_i}{k_b T}\right)\right]} \tag{4}$$

The n_{ie} is the effective intrinsic carrier concentration and its value for perovskite, silicon and SiGe is $1.97\times10^{7}\,cm^{-3}$, $5.21\times10^{9}\,cm^{-3}$ $4.51\times10^{10}\,cm^{-3}$, respectively. K_b is Boltzmann's constant and E_i and E_t are the intrinsic Fermi level and trap energy level, respectively. T is the lattice temperature in degree Kelvin. n and p are the electron and hole concentrations. Basic for the SRH model are the assumptions of one trap level in the forbidden band i.e. $E_t = E_i$ and corresponds to the most efficient recombination center. τ_{n0} and τ_{p0} are the electron and hole bulk lifetimes, N is the doping concentration. Also, the constant carrier lifetimes that are used in the SRH recombination model above can be made a function of doping concentration and results in concentration dependent SRH (CONSRH) model where τ_{n0} and τ_{p0} will be replaced by τ_n and τ_p (Law et al., 1991, Atlas, 2017).

$$\tau_n = \frac{\tau_{n0}}{1 + \frac{N}{N_{SRHN}}}, \quad \tau_p = \frac{\tau_{p0}}{1 + \frac{N}{N_{SRHP}}} \tag{5}$$

N is the doping concentration $N_{SRHN} = N_{SRHP} = 5 \times 10^{16} cm^{-3}$.

2. AUGER

Capturing or emission of mobile charge carriers through three particle transition processes leads to Auger recombination, the underlying physics of such processes is still unclear, and normally qualitative understanding is sufficient as suggested by Selberherr et al. (Selberherr, 1984). Auger recombination has been modeled using the following expression:

$$R_{AUGER} = C_n\left(pn^2 - n_0 n_{ie}^2\right) + C_p\left(np^2 - p_0 n_{ie}^2\right) \tag{6}$$

The auger coefficients, $C_p = 9.9\text{x}10^{-32}$ cm^6.s^{-1} and $C_n = 2.8\text{x}10^{-31}$ cm^6.s^{-1} have been used for *p*-type and *n*-type Si (Dziewior and Schmid, 1977), whereas for SiGe these coefficient are $C_p = 8.3\text{x}10^{-32}$ cm^6.s^{-1} and $C_n = 1.8\text{x}10^{-31}$ cm^6.s^{-1}, respectively. Moreover, auger coefficient for the perovskite film has been obtained from experimental data (Yang et al., 2015, Wehrenfennig et al., 2014) and reported in thesis chapters. n_o, p_o is the concentration of electron and holes at equilibrium, respectively.

3. RADIATIVE

In radiative recombination, an electron loses energy on order of the band gap and moves from the conduction band to the valence band. This effect is necessary for narrow gap semiconductors and semiconductors whose specific band structure allows direct transitions. By assuming a capture rate C_c^{OPT} the partially involved process can be written as:

$$R_{np}^{OPT} = C_c^{OPT}\, np \,, \tag{7}$$

These rates must be equal in thermal equilibrium so that

$$C_{np}^{OPT} = C_c^{OPT} n_{ie}^2 \,, \tag{8}$$

The total band to band recombination is the difference of the partial rates i.e.

$$R_{np}^{OPT} = C_c^{OPT} (np - n_{ie}^2) \tag{9}$$

The radiative rate coefficient for perovskite film has been obtained from experimental data (Yang et al., 2015, Wehrenfennig et al., 2014) and reported in thesis chapters.

4. SURFACE RECOMBINATION

The standard method is to model interface recombination in a similar manner as the bulk generation-recombination rate. The recombination rate is an extension of the SRH model by introducing the surface recombination velocities for electrons and holes (S_{p0} and S_{n0}).

$$R_{surface} = \frac{pn - n_{ie}^2}{\tau_n^{eff}\left[p + n_{ie} \exp\left(\frac{E_i - E_t}{k_b T}\right) \right] + \tau_p^{eff}\left[n + n_{ie} \exp\left(\frac{E_t - E_i}{k_b T}\right) \right]} \tag{10}$$

$$\text{With } S_{p0} = \sigma_p v_{th} \mathrm{N}_{st} \text{ and } S_{n0} = \sigma_n v_{th} \mathrm{N}_{st} \tag{11}$$

$$\frac{1}{\tau_n^{eff}} = \frac{1}{\tau_n^i} + \frac{d_i}{A_i} S_{n0} \text{ and } \frac{1}{\tau_p^{eff}} = \frac{1}{\tau_p^i} + \frac{d_i}{A_i} S_{p0}$$

Where, A_i and d_i are the area and the length of the interface node i and τ_n^i is the bulk lifetime calculated at a node i along the interface. S_{p0}, S_{n0}, σ_p and σ_n are the surface recombination velocities (SRVs) parameters and capture cross-section for holes and electrons respectively. N_{st} is the surface states per unit area and ν_{th} is the thermal velocity of the charge carrier (~ 10^7 cm.s^{-1}). The surface recombination effect incorporated in the cell using interface statement in ATLAS software using surface recombination velocity parameters S_{p0} and S_{n0}.

Note: for further details about models that are not covered in Appendix, please refer ATLAS user manual (Atlas, 2017) .

A.3: REFERENCES

ATLAS 2017. ATLAS User ' s Manual. 567-1000.

DZIEWIOR, J. & SCHMID, W. 1977. Auger coefficients for highly doped and highly excited silicon. *Applied Physics Letters,* 31**,** 346-346.

LAW, M. E., SOLLEY, E., LIANG, M. & BURK, D. E. 1991. Self-consistent model of minority-carrier lifetime, diffusion length, and mobility. *IEEE Electron Device Letters,* 12**,** 401-403.

WEHRENFENNIG, C., EPERON, G. E., JOHNSTON, M. B., SNAITH, H. J. & HERZ, L. M. 2014. High Charge Carrier Mobilities and Lifetimes in Organolead Trihalide Perovskites. *Advanced Materials,* 26**,** 1584-1589.

YANG, Y., YANG, M., LI, Z., CRISP, R., ZHU, K. & BEARD, M. C. 2015. Comparison of Recombination Dynamics in CH3NH3PbBr3 and CH3NH3PbI3 Perovskite Films: Influence of Exciton Binding Energy. *Journal of Physical Chemistry Letters,* 6**,** 4688-4692.

Materials Research Bulletin 93 (2017) 282–289

Contents lists available at ScienceDirect

Materials Research Bulletin

journal homepage: www.elsevier.com/locate/matresbu

Numerical simulations of novel SiGe-based IBC-HJ solar cell for standalone and mechanically stacked tandem applications

Rahul Pandey, Rishu Chaujar*

Department of Engineering Physics, Delhi Technological University, Shahbad Daulatpur, Main Bawana Road, New Delhi, Delhi 110042, India

ARTICLE INFO

Article history:
Received 25 February 2017
Received in revised form 28 April 2017
Accepted 2 May 2017
Available online 6 May 2017

Keywords:
Perovskite
Solar cell
Tandem
IBC-SiGeHJ
Energy

ABSTRACT

In this study, a novel 10 μm thick interdigitated back contact silicon-germanium heterojunction (IBC-Si$_{1-x}$Ge$_x$HJ) solar cell device has been designed and simulated for standalone and four-terminal mechanically stacked tandem applications. Optimization of i-a-SiGe: H thickness, the width of n-a-SiGe: H region, p-a-SiGe: H region and gap along with composition fraction (x) lead to 15.5% power conversion efficiency (PCE) in a stand-alone configuration. Whereas in combination with perovskite top subcell we further demonstrate 25.7% PCE in four-terminal tandem configuration. In mechanical stacking, top and bottom subcells are fabricated individually and then assembled in a module, which avoids the need for current matching between subcells, thereby giving greater process and design flexibility. The proposed IBC-SiGeHJ solar cell is ~ (25–30) times thinner than conventional Si solar cells which are used as bottom subcell in perovskite/silicon tandem solar cell. The results reveal that the proposed 4-terminal mechanically stacked perovskite/IBC-SiGeHJ tandem device may open new doors for the energy efficient applications. All the simulations have been done using Silvaco technology computer aided design (TCAD) simulator.

1. Introduction

Sunlight is the major source of renewable energy, about 4.3×10^{20} J/h [1], is radiated because of a nuclear fusion reaction in the sun. Therefore, solar energy is one of the good renewable sources of energy substituting fossil fuels [2,3]. Photovoltaic (PV) devices are used for direct conversion of sunlight energy into electrical energy. The crystalline silicon (c-Si) solar cells have been dominating the PV market for several decades, with a current market share of 90% [4]. The efficiency of the crystalline silicon solar cell has only marginally improved during the last 15 years. The wafer size efficiency as high as 25.6% was obtained with amorphous silicon (a-Si)/c-Si heterojunction technology [5], and recently record of 26.3% has been achieved on 180 cm^2 crystalline silicon solar cell [6] which is close to the theoretical maximum efficiency of 29.4% [7].The increase in the PV market needs the new development and design to compete with conventional sources of energy fully. Hence, energy efficient modules are required. Further, to make PV system feasible at large scale, module cost should be <\$0.5/W [8]. Therefore, to obtain high efficiency at a lower cost, tandem approaches have been proposed, which combines small band-gap and large band-gap solar technologies. In tandem approach, to utilize the solar spectrum, the large bandgap solar cell has been used as top subcell, and small bandgap solar cells are used as bottom subcell, respectively. One of the most exciting top subcell candidates is perovskite solar cell. In a liquid based dye-sensitized solar cell (DSSC), optical absorption of methylammonium-lead-halide on nanocrystalline TiO$_2$ surface produces the PCE of 3–4%, as first discovered in 2009 [9]. The methylammonium-lead-halide, CH$_3$NH$_3$PbX$_3$ (X = Br, I) perovskite has a tunable bandgap, ranging from (1.6–2.3) eV depending on halide composition. In recent years, to obtain the higher efficiency at lower cost perovskite/silicon-based tandem approaches have been proposed, which combine a silicon cell with a low-cost cell with wide-bandgap (1.6–1.9 eV) absorber material to form a tandem cell [10,11]. Moreover, in perovskite/silicon tandem solar cell, the perovskite top cell utilize the lower wavelength photons. Whereas, to absorb the photons of higher wavelength i.e. >800, thickness more than 250 μm is required since the absorption coefficient (α) of silicon is small at a higher wavelength [12,13]. The requirement of large volume and high-quality silicon in tandem solar cell significantly increases the module cost. These issues can be fixed by using a different material which has higher optical absorption compared to silicon at higher wavelengths. The use of SiGe cell as a bottom cell is a possible solution to enhance the absorption at a

---

* Corresponding author.
E-mail address: Rishu.phy@dce.edu (R. Chaujar).

http://dx.doi.org/10.1016/j.materresbull.2017.05.006
0025-5408/

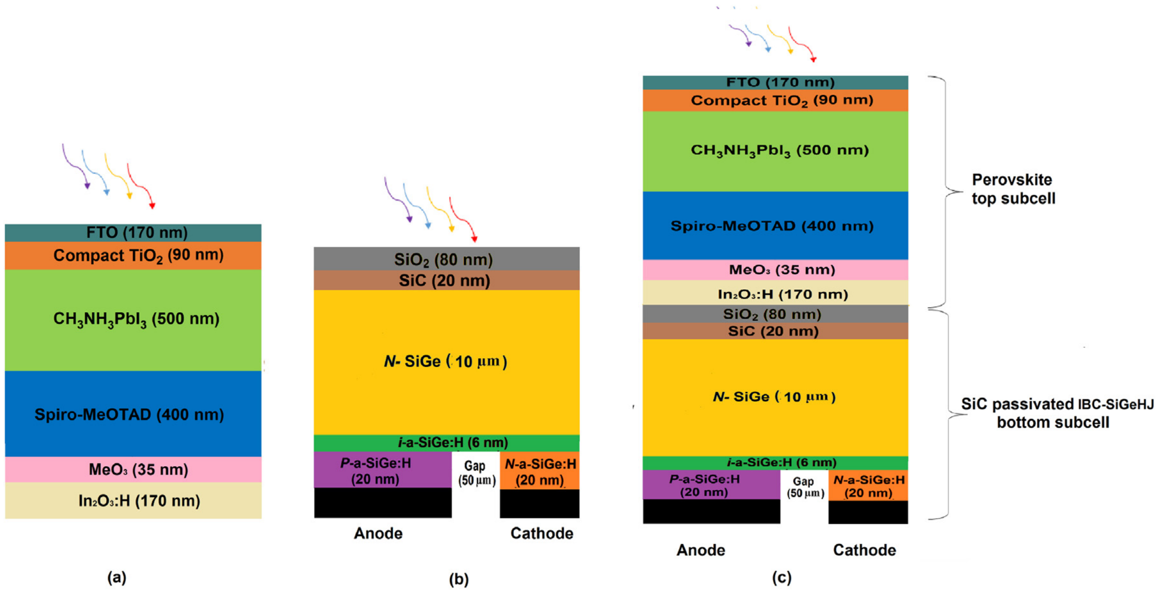

Fig. 1. Device structures used in simulations (a) semitransparent perovskite top subcell, with FTO and In_2O_2: H based front and rear contact (b) IBC-SiGeHJ bottom subcell, and (c) 4-terminal mechanically stacked tandem solar cell.

higher wavelength. The experimentally available data shows, the absorption coefficient (α) of SiGe is greater than Si in the higher wavelength region [14]. SiGe processing is simple since physical and electrical properties of silicon and germanium are similar [15]. The band gap of SiGe can be modified by changing the Ge content, and hence, the optical absorption [16,17]. Moreover, recent simulation work shows that the SiGe-based solar cell could be a good candidate to obtain higher PCE [18–20].

This work presents, a novel 4- terminal perovskite/SiGe-based tandem solar cell where the use of SiGe instead of Si is a possible solution to minimize the absorption loss at higher wavelengths. 10 µm thick SiGe solar cell has been used as bottom subcell, which is ~ (25–30) times thinner than conventional Si solar cell which is used as bottom subcell in perovskite/silicon tandem solar cell. This indicates that the proposed device significantly saves the material required for the fabrication. However, the cost of germanium doped wafer is higher compared to a silicon wafer, though present work shows a tandem device made using SiGe cell can be a good candidate for energy efficient applications. Moreover, future development of cost effective energy efficient methods may decrease the overall dollar per watt ($/W) of the device. The tandem architectures of perovskite are mainly divided into three categories: monolithically integrated, mechanically stacked, and spectrally split [21]. Mechanical stacking results in a 4-terminal tandem solar cell which mean that the top subcell and bottom subcell is fabricated independently, and then combined in the module. The 4-terminal perovskite/SiGe device simulated in this work is the mechanically stacked type. The overall work reported

Table 1
Equations and models used in simulations [23].

The Poisson equation, electron and hole continuity equation.	$\frac{d}{dx}\left(-\varepsilon(x)\frac{d\Psi}{dx}\right) = -q\begin{bmatrix} n(x) - p(x) + N_a^-(x) - N_d^+(x) + \\ n_t(x) - p_t(x) \end{bmatrix}$ $\frac{dn_p}{dt} = D_n\frac{d^2 n_p}{dx^2} + n_p\mu_n\frac{d\xi}{dx} + \mu_n\xi\frac{dn_p}{dx} + G_n - \frac{n_p - n_{p0}}{\tau_n}$ $\frac{dp_n}{dt} = D_p\frac{d^2 p_n}{dx^2} - p_n\mu_p\frac{d\xi}{dx} - \mu_p\xi\frac{dp_n}{dx} + G_p - \frac{p_n - p_{n0}}{\tau_p}$	Where q the electron charge, D the diffusion coefficient, ε is the permittivity and G the generation rate. The n_s, n_t, p_s and p_t are the free electron, trapped electron, free hole, and trapped hole, respectively. ψ is the electrostatic potential. N_a^- the ionized acceptor-like doping concentration and N_d^+ are the ionized donor-like doping concentration. ξ is the electric field and τ_n, τ_p are the carrier lifetimes.
Auger recombination	$R_{AUGER} = C_n(pn^2 - n_0 n_{ie}^2) + C_p(np^2 - p_0 n_{ie}^2)$	The auger coefficients, $C_p = 8.3 \times 10^{-32}\,cm^6\,s^{-1}$ and $C_n = 1.8 \times 10^{-31}\,cm^6\,s^{-1}$ have been used for p-type and n-type SiGe, respectively, at 300 K temperature. Whereas, auger coefficient for the perovskite film has been obtained from experimental data [25]. n_o, p_o are the concentration of electron and holes at equilibrium.
Shockley-Read-Hall (SRH) recombination.	$R_{SRH} = \frac{pn - n_{ie}^2}{\tau_{n0}\left[p + n_{ie}\exp\left(\frac{E_i - E_t}{k_b T}\right)\right] + \tau_{p0}\left[n + n_{ie}\exp\left(\frac{E_t - E_i}{k_b T}\right)\right]}$	The n_{ie} is the effective intrinsic carrier concentration and its value for perovskite and silicon are $1.97 \times 10^7\,cm^{-3}$an $4.51 \times 10^{10} cm^{-3}$, respectively. K_b is Boltzmann's constant and E_i and E_t are the intrinsic fermi level and trap energy level, respectively. T is the lattice temperature in degree Kalvin. n and p are the electron and hole concentrations. Basic for the SRH model are the assumptions of one trap level in the forbidden band i.e. $E_t = E_i$ and corresponds to the most efficient recombination center. τ_{nO} and τ_{pO} are the electron and hole bulk lifetimes, 2×10^{-5} has been used for SiGe. N is the doping concentration of SiGe
Radiative recombination	$R_{np}^{OPT} = C_c^{OPT}(np - n_{ie}^2)$	The radiative rate coefficient for perovskite film has been obtained from experimental data [25].
Surface recombination	$R_{surface} = \frac{pn - n_{ie}^2}{\tau_n^{eff}\left[p + n_{ie}\exp\left(\frac{E_i - E_t}{k_b T}\right)\right] + \tau_p^{eff}\left[n + n_{ie}\exp\left(\frac{E_t - E_i}{k_b T}\right)\right]}$ $\frac{1}{\tau_n^{eff}} = \frac{1}{\tau_n^i} + \frac{d_i}{A_i}S_{n0}$and $\frac{1}{\tau_p^{eff}} = \frac{1}{\tau_p^i} + \frac{d_i}{A_i}S_{p0}$ With $S_{pO} = \sigma_p \nu_{th} N_{st}$ and $S_{nO} = \sigma_n \nu_{th} N_{st}$	Where, A_i and d_i are the area and the length of the interface node i and τ_n^i is the bulk lifetime calculated at a node i along the interface. S_{pO}, S_{nO}, σ_p and σ_n are the surface recombination velocities parameters and capture cross section for holes and electrons respectively. N_{st} is the surface states per unit area and ν_{th} is the thermal velocity of the charge carrier (~$10^7\,cm\,s^{-1}$). The surface recombination effect incorporated in the bottom silicon solar cell using interface statement in ATLAS software and $S_{pO} = S_{nO} = 100\,cm\,s^{-1}$ have been used.

Table 2
Materials parameters used in the simulation [26,27].

Material		A	B	C	D	E	F	G	H	I
Dielectric Constant		100	30	3	12.9	11.9	11.9	11.9	9.72	
Band Gap (eV)		3.2	1.5	2.91	0.94	1.60	1.60	1.60	2.2	0.99
Electron Affinity (eV)		4	3.93	2.2	4.17	4.0	4.0	4.0	4.2	
Thickness (μm)		0.09	0.5	0.4	10	0.02	0.006	0.02	0.02	0.001
Electron, Hole mobility ($cm^2/V\,s$)		0.006, 0.006	50, 50	0.0001, 0.0001	1430, 480	20, 2	20, 2	20, 2	100, 50	
Effective conduction band (DOS) (cm^{-3})		1×10^{21}	2.5×10^{20}	2.5×10^{20}	2.36×10^{19}	2.5×10^{20}	2.5×10^{20}	2.5×10^{20}	6.4×10^{18}	
Effective valence band (DOS) (cm^{-3})		2×10^{20}	2.5×10^{20}	2.5×10^{20}	9.30×10^{18}	2.5×10^{20}	2.5×10^{20}	2.5×10^{20}	1.6×10^{18}	
Conduction tail states	$N^{c-tail}A$ (cm^{-3})	10^{14}	10^{14}	10^{14}	n/a	10^{21}	10^{18}	10^{21}	n/a	0
	$E^{c-tail}A$ (eV)	0.01	0.015	0.01	n/a	0.07	0.09	0.07	n/a	0.07
Valence tail states	$N^{v-tail}D$ (cm^{-3})	10^{14}	10^{14}	10^{14}	n/a	10^{21}	10^{18}	10^{21}	n/a	0
	$E^{v-tail}D$ (eV)	0.01	0.015	0.01	n/a	0.12	0.09	0.12	n/a	0.12
Acceptor-like (A) dangling bond states	$N^{db}A$ (cm^{-3})	10^{17}	10^{14}	10^{16}	n/a	10^{19}	10^{16}	10^{19}	n/a	2.4×10^{16}
	$E^{db}A$ (eV)	1.1	1.2	1.1	n/a	0.7	1.1	1.3	n/a	0.5
	$\sigma^{db}A$ (eV)	0.1	0.1	0.1	n/a	0.2	0.15	0.2	n/a	0.2
Donor-like (D) dangling bond states	$N^{db}D$ (cm^{-3})	10^{17}	10^{14}	10^{16}	n/a	10^{19}	10^{16}	10^{19}	n/a	2.4×10^{16}
	$E^{db}D$ (eV)	1.1	1.2	1.1	n/a	0.45	0.9	1.1	n/a	0.5
	$\boldsymbol{\sigma}^{db}$ D (eV)	0.1	0.1	0.1	n/a	0.2	0.15	0.2	n/a	0.2

A = Compact TiO_2, B = $CH_3NH_3PbI_3$, C = Spiro-MeOTAD, D = $Si_{0.85}Ge_{0.15}$, E = n- type a- $Si_{0.85}Ge_{0.15}$:H, F = Buffer a- $Si_{0.85}Ge_{0.15}$:H, G = p- type a- $Si_{0.85}Ge_{0.15}$:H, H = SiC, I = Interface defects.

in this work has been divided into two parts: first, designing and optimization of the 10 μm thick IBC-SiGeHJ standalone solar cell, and second, analyses of 4-terminal perovskite/IBC-SiGeHJ tandem solar cell. The IBC-SiGeHJ solar cell combines the advantages of the back contact that eliminates contact shading, leading to a higher short-circuit current (J_{SC}) and SiGe heterojunction solar cells with high open circuit voltage (V_{OC}) due to the better surface passivation with the help of the deposited i-a-SiGe: H layer. Further, to prevent the front surface recombination, SiC-based front surface passivation has been used as discussed in [22].

2. Device structures, models, and methods

The device simulation has been done using Silvaco ATLAS device simulator. The perovskite top subcell, IBC-SiGeHJ bottom subcell, and 4-terminal tandem cell have been shown in Fig. 1(a–c). The devices have been designed using ATHENA process simulator. The doping of *n-type* SiGe and *n-type* a-SiGe:H is $2.14 \times 10^{16}\,cm^{-3}$ and $4.8 \times 10^{18}\,cm^{-3}$, respectively and that of *p-type* a-SiGe:H is $2 \times 10^{19}\,cm^{-3}$. The gap width is 50 μm and width of *p-type* a-SiGe: H, *n-type* a-SiGe: H are 100 μm and 25 μm respectively. Moreover, for top subcell, fluorine-doped tin oxide (FTO) has been used as a top contact for perovskite solar cell. The Spiro-MeOTAD and $CH_3NH_3PbI_3$ are *p-type* with a doping density of $3 \times 10^{18}\,cm^{-3}$ and $2.14 \times 10^{17}\,cm^{-3}$ respectively, whereas compact TiO_2 is *n-type*, with a doping density of $5 \times 10^{19}\,cm^{-3}$. In the mechanically stacked tandem configuration, the top subcell requires two transparent contacts. Hence, indium oxide (In_2O_3: H) based transparent rear electrode has been used for perovskite top subcell as reported in [23]. The electron-hole continuity equation is solved along with Poisson equation to obtain the current density (J) – voltage (V) curve under AM1.5 illumination. Top subcell has been simulated based on the recombination dynamics in $CH_3NH_3PbI_3$ with the help of SRH, Auger, and radiative recombination models to account for the monomolecular, bimolecular and trimolecular recombinations in the perovskite top subcell [24]. The second and third order charge carrier decay constant $1.5 \times 10^{-10}\,cm^3\,s^{-1}$ and $3.4 \times 10^{-28}\,cm^6\,s^{-1}$ have been used for perovskite cell as suggested in [25]. In the bottom IBC-SiGeHJ cell, Fermi statistics is used for carriers and drift-diffusion combined with Bohm Quantum Potential to account for quantum correction. The concentration dependent SRH (CONSRH), concentration dependent mobility (CONMOB) and Auger recombinations are activated for bottom IBC-SiGeHJ solar cell [26]. The band to band recombination in SiGe is negligible since it is an indirect bandgap semiconductor and hence, radiative recombination model has been ignored for bottom subcell. The description of semiconductor equations and models has been shown in Table 1 whereas material parameters used in the simulation is shown in Table 2. The material parameters for perovskite cell have been obtained from [27].

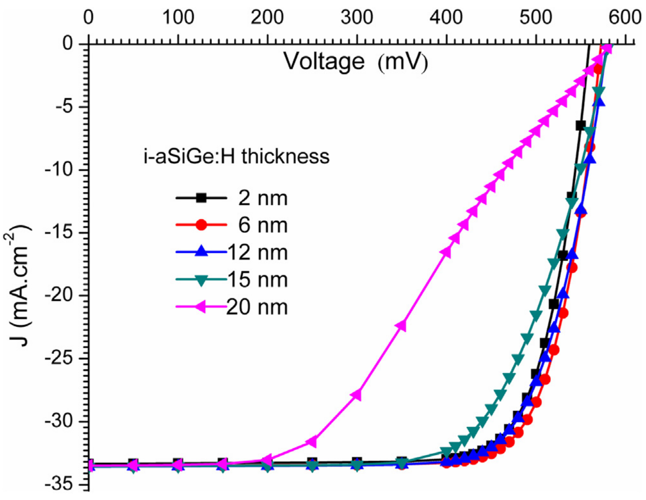

Fig. 2. Impact of i-a-SiGe: H thickness on the current density (J) – voltage (V) curve of IBC-SiGeHJ solar cell.

3. Results

3.1. Optimization of 10 μm thick IBC-SiGeHJ bottom subcell

This section deals with the optimization of IBC-SiGeHJ bottom subcell i.e. the thickness of i-a-SiGe: H, the width of n-type (BSF), the width of p-type (emitter), gap width, and composition fraction have been optimized for improved efficiency. The simulation of the IBC-SiGeHJ solar cell has been performed, and the current density-voltage (J-V) curve with different i-a-SiGe: H thicknesses has been reported in Fig. 2. Result shows, increasing the thickness of a-SiGe: H layer leads to decrease in the fill factor (FF). Intrinsic a-SiGe: H prevents the recombination at the a-SiGe/SiGe region. However, it also reduces the conduction of generated carriers and hence leads to low FF. This has been verified in Fig. 2 that increasing the thickness of i-a-SiGe: H leads to decrease in the FF. Results also show that at a thickness of 20 nm, "S" shaped J-V curve with low FF has been obtained, which is confirmed by the already available results of 200-μm thick silicon-based device with the same architecture as reported in [28]. The impact of i-a-SiGe: H thickness on the photovoltaic parameters are shown in Fig. 3a (i–iv).

Moreover, Fig. 3a (ii) shows a slight improvement in V_{OC} on increasing the thickness of i-a-SiGe: H, which is supported by comparing with the already published results [29]. However, an increase in V_{OC} is not sufficient to compensate the decrease in FF, and hence the overall PCE reduces by increasing the thickness of i-a-SiGe: H, as shown in Fig. 3a (iv). Moreover, the width of BSF (n-strip), the emitter (p-strip), and the gap was also optimized, and the results are shown in Fig. 3(b–d). The J_{SC} vs. n-strip width is reported in Fig. 3b (i), increasing n-strip width considerably reduces J_{SC}, to understand the effect of n- strip width, contour representation of recombination rate; and the vector representation of conduction current have also been obtained and shown in Fig. 4. To obtain the results, a very small region near the back side of the device is exaggerated as shown in Fig. 4(a–c). Increasing n-strip width will decrease the carrier collection probability of p-strip region. Since the minority carriers that are generated near or at n-strip region requires to travel not only vertical to the rear junction but also laterally to arrive at the collecting junction i.e. p-strip. Increasing n-width results in longer traveling distance for minority carrier, and hence the probability of carrier recombination is higher, as shown in Fig. 4(a–c). Higher the recombination rate, lower will be the conduction current density, and the direction of the conduction current density is shown in Fig. 4(a–c). The FF and V_{OC} remain almost unaffected due to good surface passivation quality. Further, the impact of gap width is studied in Fig. 3c. Increasing the gap width will increase the lateral distance and series resistance for minority carrier that is generated at or near the BSF region. Therefore, increasing the gap width will decrease J_{SC} and FF. Furthermore, at the end of the optimization process, the impact of p-strip width has also been obtained, and results show that the 100-μm thick p-strip is optimum to give a

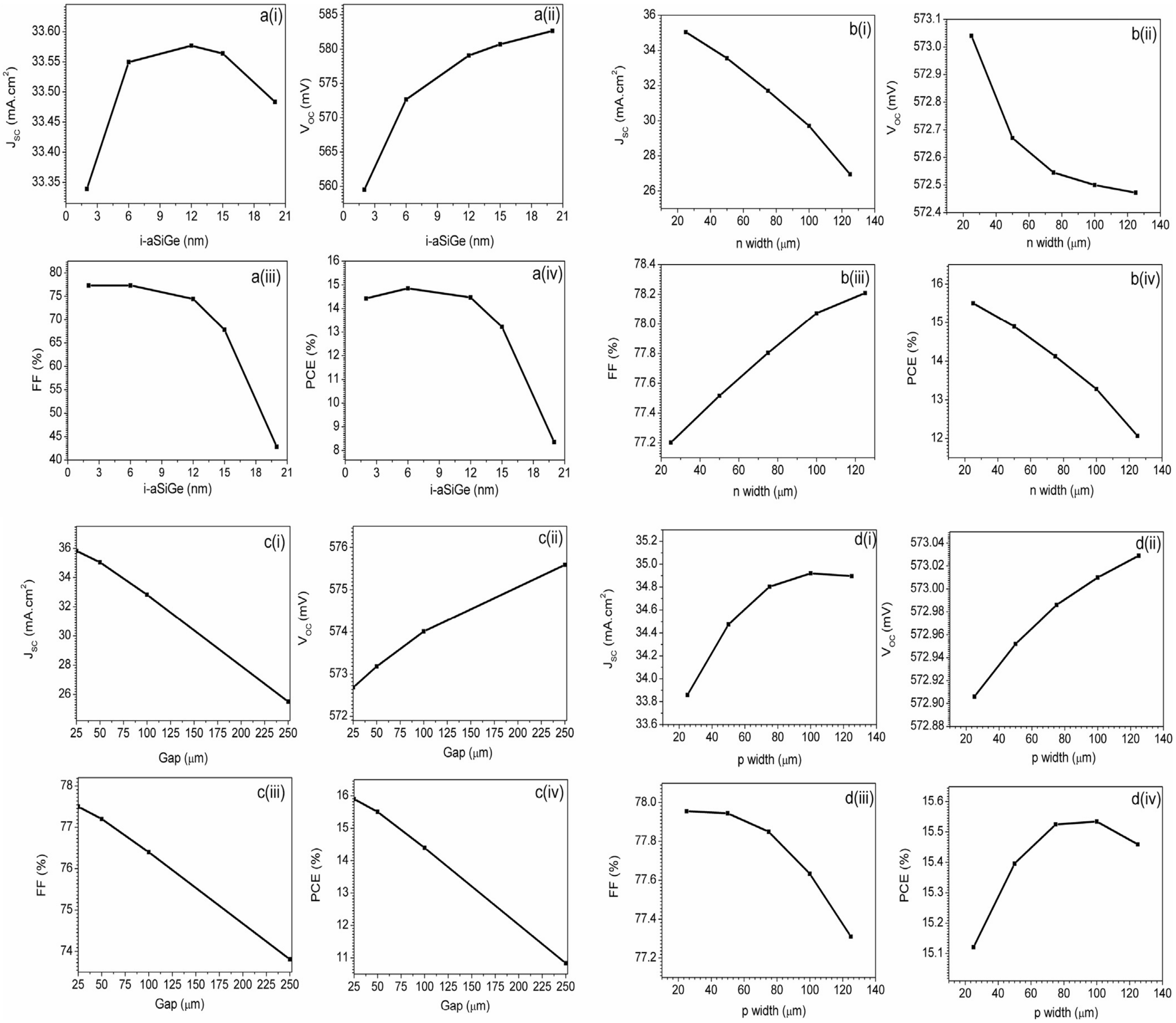

Fig. 3. Optimization of IBC-SiGeHJ solar cell (a) thickness of i-a-SiGe: H layer, (b) width of n- type region (BSF), (c) Gap width, and (d) width of p- type region (emitter).

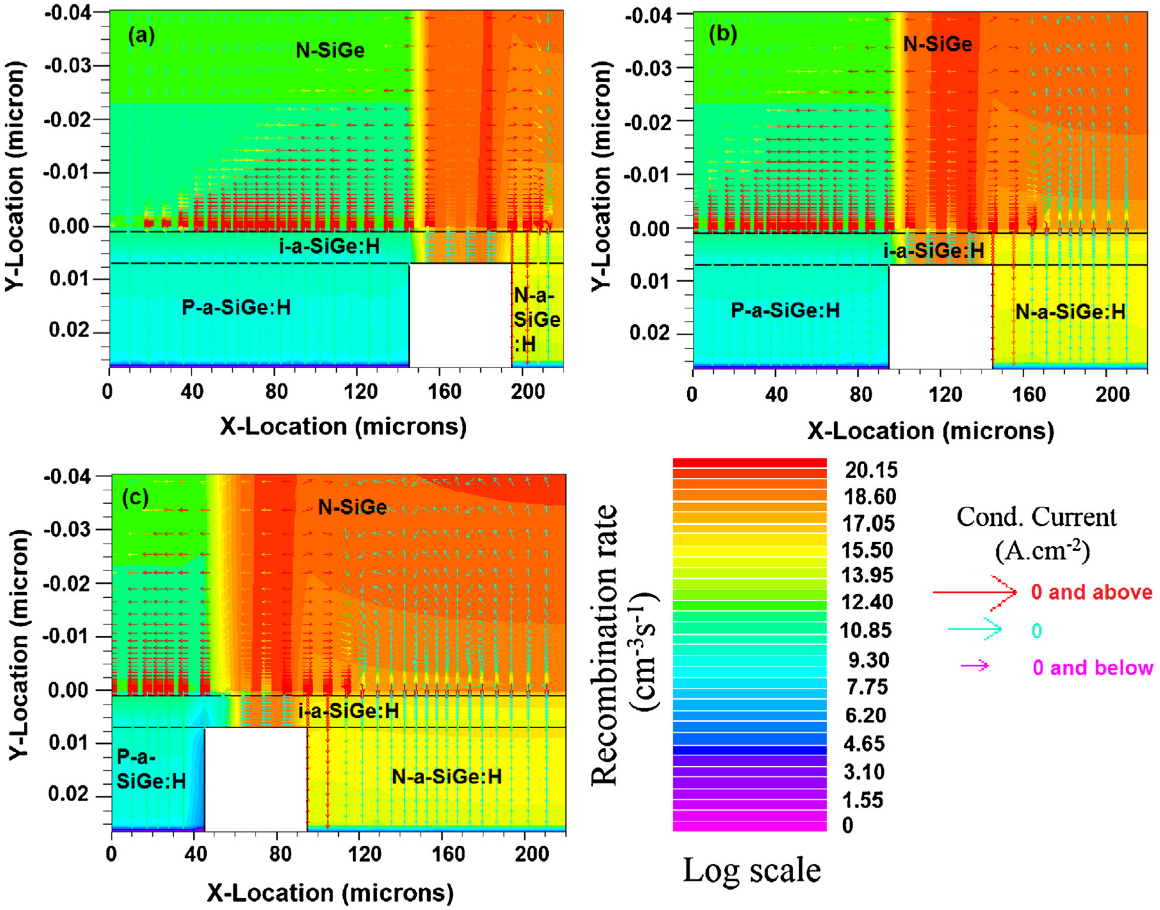

Fig. 4. Contour representation of recombination rate with different N-strip widths (a) 25 μm, (b) 75 μm, and (d) 125 μm.

good performance, as shown in Fig. 3d (iv). Concluding the section gives the optimized dimensions for 10 μm thick IBC-SiGeHJ solar cell i.e. width of BSF, gap, and emitter regions are 25 μm, 50 μm, and 100 μm respectively.

3.2. Analysis of semitransparent perovskite/IBC-SiGeHJ mechanically stacked tandem solar cell

In this section, the potential of semi-transparent perovskite/IBC-SiGeHJ mechanically stacked tandem solar cell, a novel photovoltaic device for ultra-high conversion efficiency has been simulated. The organic-inorganic halide semitransparent perovskite solar cells are potential candidates to be used as top subcell, due to its suitable bandgap. A 20.9% efficient perovskite top subcell as reported in [30] has been used as top subcell. Whereas 10-micon thick IBC-SiGeHJ solar cell has been used as bottom subcell. The optical properties of perovskite solar cell used in simulations are identical to the properties reported in [30]. Four-terminal device simulated in this work is shown in Fig. 1c. In mechanical stacking, the top and bottom subcell are fabricated independently and then organized in the module. Hence, top subcell has been simulated individually, whereas bottom subcell has been simulated by placing perovskite as a filter. All the materials used in perovskite solar cell has been placed as a filter over IBC-SiGeHJ solar cell when simulating IBC-SiGeHJ solar cell as bottom subcell. The addition of the PCE of perovskite top subcell and IBC-SiGeHJ bottom subcell in tandem configuration gives the overall PCE of the tandem device. In the previous section, the optimization of IBC-SiGeHJ solar cell for a standalone application, i.e. optimization has been done under the full AM1.5 spectrum. Moreover, in this section fresh optimization for IBC-SiGeHJ has been done under filtered spectrum by top subcell, and results are reported in Fig. 5 (a–d). Results show that the behavior of bottom subcell device is identical as obtained in standalone condition. However, the magnitude of photovoltaic parameters is lower, particularly J_{SC} as shown in Fig. 5a (i). This is due to reduced light intensity in the presence of perovskite top subcell. Results reported in Fig. 5 shows that optimized dimensions under filtered spectrum are same as obtained for the stand-alone case. This validates that optimized dimensions i.e. the width of BSF, gap, and emitter regions 25 μm, 50 μm, and 100 μm respectively, hold good for both standalone as well as bottom subcell conditions.

Further, the impact of composition fraction (x) on the performance of bottom IBC-$Si_{1-x}Ge_x$HJ solar cell has been studied for both standalone as well as tandem configuration. The performance of bottom subcell device has been obtained with three different composition fractions i.e. $x = 0$, 0.15, and 0.25. The optical properties i.e. complex reflective indices used in the simulation have been obtained from sopra database of ATLAS library [26] and reported in Fig. 6a. The J-V curves for different composition fraction are shown in Fig. 6b. Increasing the composition fraction results in higher optical absorption, and hence results in higher J_{SC} .However, bandgap also reduces which further results in lower V_{OC}. This has been verified in the J-V curve reported in Fig. 6b. Bottom subcell in standalone condition shows the J_{SC} values 26.4 mA cm^{-2}, 34.9 mA cm^{-2}, and 38.2 mA cm^{-2} with $x = 0$, 0.15, and 0.25 composition fractions, respectively. Whereas, the V_{OC} values 674 mV, 573 mV, and 524 mV, respectively has been obtained. This results in 14.4%, 15.5%, and 14.9% PCEs for composition values of 0, 0.15, and 0.25, respectively, in standalone configuration. This concludes that under the standalone condition

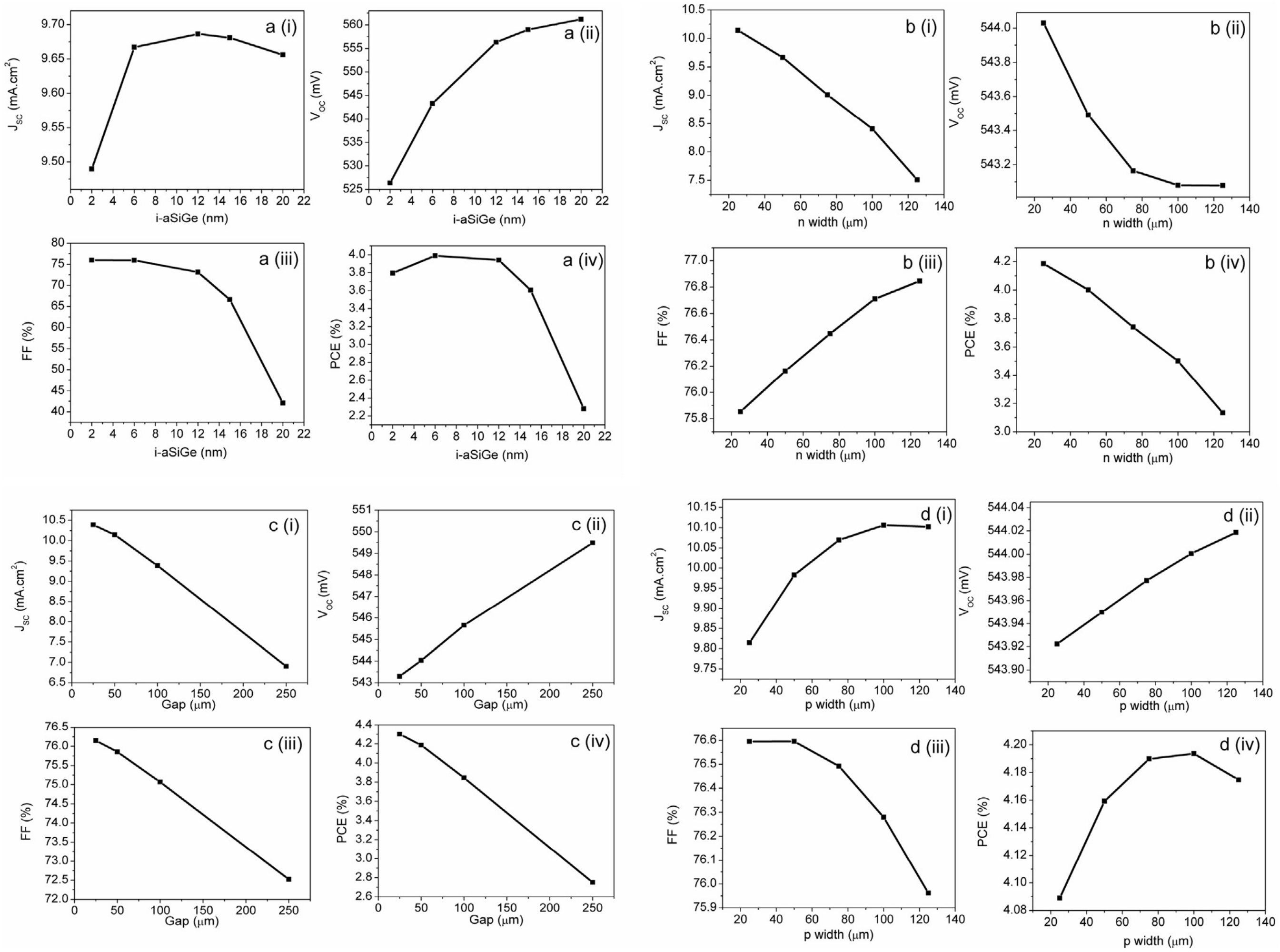

Fig. 5. Optimization of IBC-SiGeHJ solar cell under filtered spectrum (a) thickness of i-a-SiGe: H layer, (b) width of n- type region (BSF), (c) Gap width, and (d) width of p- type region (emitter).

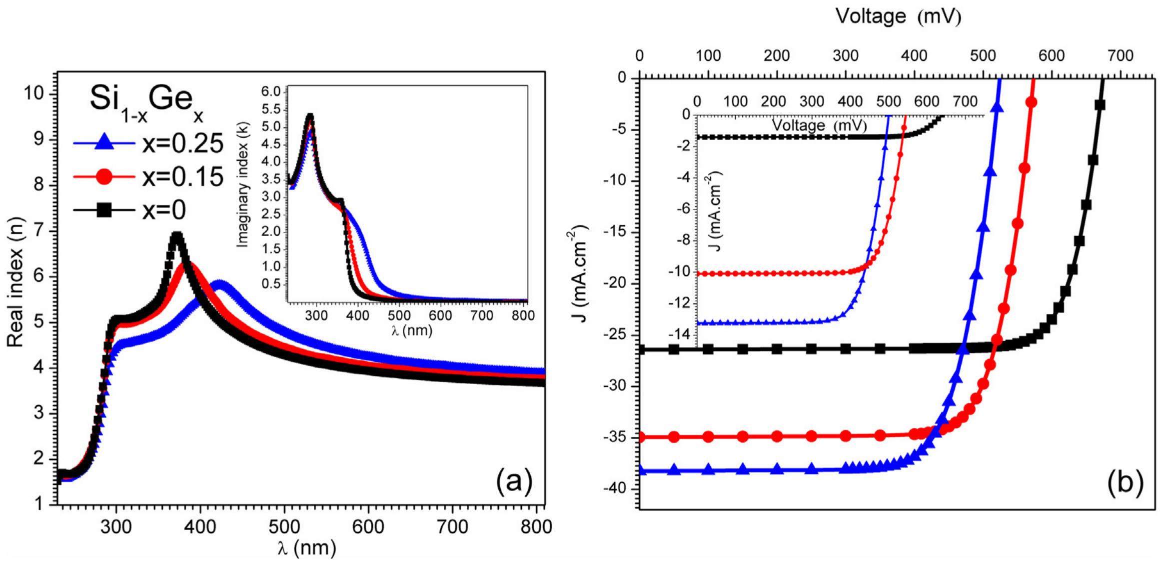

Fig. 6. (a) Optical properties i.e. real and imaginary indices of $Si_{1-x}Ge_x$ as a function composition fraction and (b) The standalone J-V curve under AM1.5 illumination: Insect shows the J-V curve under filtered spectrum by top sub cell.

Table 3
Photovoltaic parameters of IBC-SiGe bottom subcell with different composition fraction.

IBC-$Si_{1-x}Ge_x$HJ		J_{SC} (mA cm^{-2})	V_{OC} (mV)	FF (%)	PCE (%)
$x = 0$	standalone	26.4	674	81.1	14.4
	under tandem	1.4	640	79.6	0.7
$x = 0.15$	standalone	34.9	573	77.4	15.5
	under tandem	10.1	544	76.9	4.2
$x = 0.25$	standalone	38.2	524	74.5	14.9
	under tandem	13.2	498	73.2	**4.8**
Pervoskite top subcell		23.9	1121	77.8	**20.9**
Mechanically stacked perovskite/IBC-$Si_{1-x}Ge_x$HJ tandem solar cell					20.9 + 4.8 = 25.7

the optimum performance has been obtained for the composition fraction of 0.15. Moreover, under tandem configuration with $x = 0$, 0.15, and 0.25 the bottom subcell shows J_{SC} values of 1.4 mA cm^{-2}, 10.1 mA cm^{-2}, and 13.2 mA cm^{-2} and V_{OC} values of 640 mV, 544 mV, and 498 mV, respectively. Photovoltaic parameters of bottom subcell in standalone and bottom subcell operating conditions with different x values are reported in Table 3. Improved optical absorption at a higher wavelength in $Si_{0.75}Ge_{0.25}$ leads to higher J_{SC} under bottom subcell. In order to verify this contour representation of photon absorption rate has been obtained in the bottom subcell device under tandem configuration and reported in Fig. 7(a–b). Fig. 7(a–c) shows higher photon coupling in bottom subcell for x value of 0.25, due to superior optical absorption in $Si_{0.75}Ge_{0.25}$ compared to other two composition fraction values.

Simulation results show that IBC-$Si_{0.85}Ge_{0.15}$HJ solar cell shows optimum performance in standalone condition, whereas IBC-$Si_{0.75}Ge_{0.25}$HJ solar cell superior performance under tandem configuration. Further, simulation results are obtained for the final tandem device and reported in Fig. 8(a–b). The spectrum response i.e. EQE of the perovskite top subcell, IBC-$Si_{0.75}Ge_{0.25}$HJ standalone, and IBC-$Si_{0.75}Ge_{0.25}$HJ as a bottom subcell in the tandem configuration are shown in Fig. 8a. The perovskite top subcell shows the EQE up to 800 nm, which is in good agreement with already published experimental results [31–33]. Bottom subcell operated standalone shows EQE in the lower wavelength as well as higher wavelength region. However, when operated in tandem configuration as a bottom subcell, the EQE at lower wavelengths disappears, due to the presence of perovskite top subcell. Since, up to 800 nm, top subcell absorbs the solar spectrum. However, a wavelength greater than 800 nm will be available for bottom subcell, as shown in Fig. 6a. J-V curve of the final tandem device is shown in Fig. 8b and corresponding photovoltaic parameters are shown in Table 3.

4. Conclusion

This work investigates the efficiency potential of a novel semitransparent perovskite/IBC-SiGeHJ mechanically stacked tan-

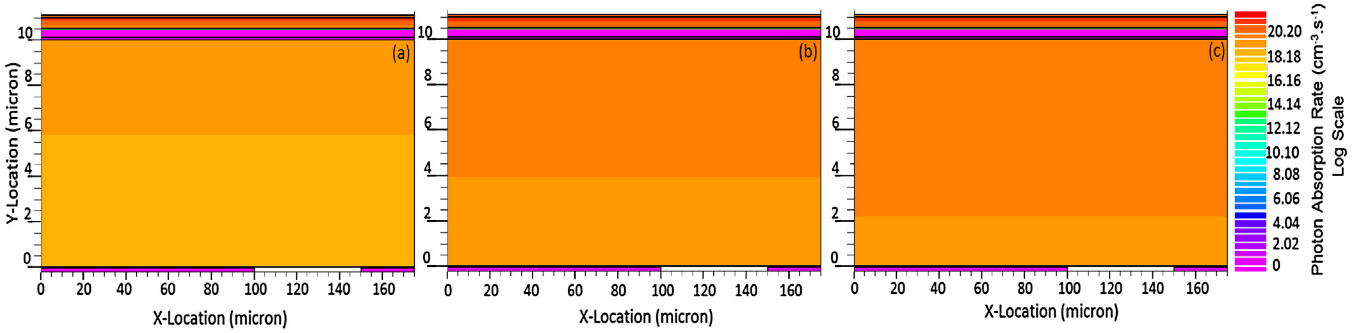

Fig. 7. Photon absorption rate ($cm^{-3}\,s^{-1}$) in bottom subcell under filtered spectrum by perovskite top subcell, with different x values. (a) x = 0, (b) x = 0.15, and (c) x = 0.25. Regions above 10 μm in Y-locations represents perovskite top filter, and below 10 μm represents bottom IBC-SiGeHJ solar cell.

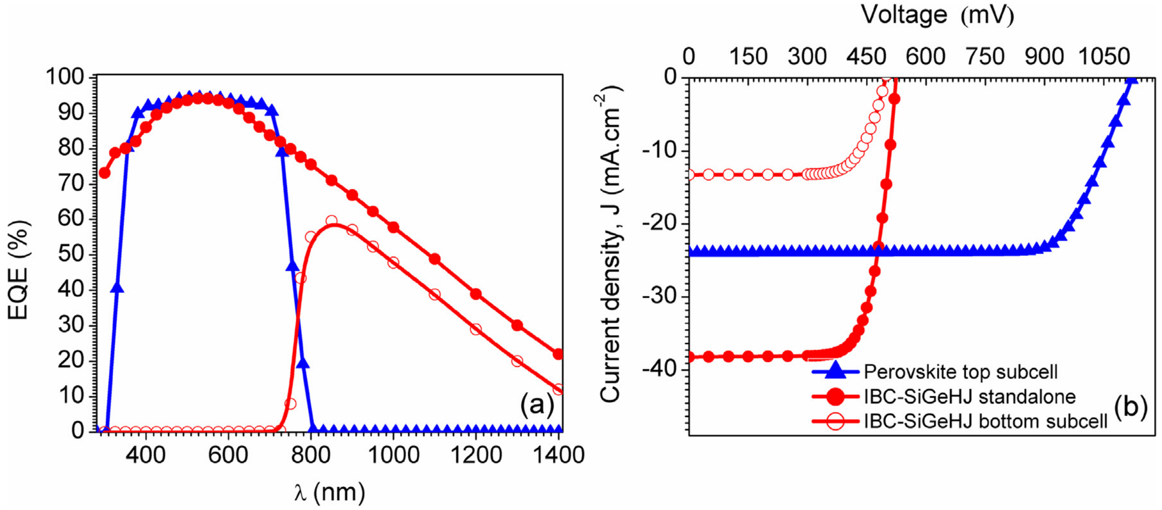

Fig. 8. (a) Spectrum response i.e. EQE of perovskite top subcell and IBC-$Si_{0.75}Ge_{0.25}$HJ bottom subcell in tandem and standalone configuration. (b) The J-V curve of top subcell and bottom subcell under illumination.

dem solar cell through numerical simulations. The first, optimization of IBC-SiGe solar cell has been performed for both standalone as well as bottom subcell operating conditions. Under tandem configuration, 4.8% PCE has been simulated in bottom subcell, which combines with 20.9% PCE of perovskite top subcell to gives overall conversion efficiency of 25.7% (20.9% top subcell + 4.8% bottom subcell). 10 μm thick SiGe solar cell has been used as bottom subcell in perovskite/SiGe tandem solar cell which is ~ (25–30) times thinner than conventional Si solar cell which is used as bottom subcell in perovskite/silicon tandem solar cell. This indicates that proposed design can significantly save the material requirements. Mechanical stacking discussed in this work avoids the need for current matching between the top and bottom subcell. In perovskite-based tandem devices, the spectrum till 800 nm wavelength will be absorbed by perovskite top subcell whereas wavelength greater than 800 nm will be available for bottom subcell. Therefore the use of SiGe ensures higher absorption compared to Si-based IBC solar cell since the presence of Ge increases the optical absorption at higher wavelengths, which results in higher J_{SC}. The spectrum, as well as the electrical behavior of the devices, has been obtained to understand the device operation in both tandem as well as standalone conditions. Results reveal that proposed design will be a good candidate for energy efficient application.

Acknowledgments

The authors would like to thank Microelectronics Research Laboratory at Delhi Technological University to carry out this work and University Grant Commission (UGC), Government of India, for providing research fellowship. Rahul Pandey acknowledges Dr. Rishu Chaujar for her continuous guidance during this research work.

References

[1] N.S. Lewis, Basic research needs for solar energy utilization, In Proceedings of the Basic Energy Sciences Workshop on Solar Energy Utilization Chair, California Institute of Technology, September 2005, 2005.
[2] M. Wang, X. Gu, P. Ma, W. Zhang, D. Yu, P. Chang, X. Chen, D. Li, Microstructured superhydrophobic anti-reflection films for performance improvement of photovoltaic devices, Mater. Res. Bull. 91 (2017) 208–213.
[3] Zhiyong Liu, Tielin Shi, Zirong Tang, Guanglan Liao, A large-area hole-conductor-free perovskite solar cell based on a low-temperature carbon counter electrode, Mater. Res. Bull. (2017), doi:http://dx.doi.org/10.1016/j.materresbull.2017.03.069.
[4] ITRPV, ITRPV Seventh Edition Vers 2. pdf, 2016.
[5] K. Masuko, M. Shigematsu, T. Hashiguchi, D. Fujishima, M. Kai, N. Yoshimura, et al., Achievement of more than 25% conversion efficiency with crystalline silicon heterojunction solar cell, IEEE J. Photovolt. 4 (2014) 1433–1435.
[6] Kaneka corporation. Available online. http://www.kaneka.co.jp/kanekae/images/topics/1473811995/1473811995_101.pdf
[7] A. Richter, M. Hermle, S.W. Glunz, Reassessment of the limiting efficiency for crystalline silicon solar cells, IEEE J. Photovolt. 3 (2013) 1184–1191.
[8] S. Jeong, M.D. McGehee, Y. Cui, All-back-contact ultra-thin silicon nanocone solar cells with 13.7% power conversion efficiency, Nat. Commun. 4 (2013) 2950.
[9] Rahul, B. Bhattacharya, Z.H. Khan, Effect of crystal and powder of CH3NH3I on the CH3NH3PbI3 based Perovskite sensitized solar cell, Mater. Res. Bull. 89 (2017) 292–296.
[10] J.P. Mailoa, C.D. Bailie, E.C. Johlin, E.T. Hoke, A.J. Akey, W.H. Nguyen, et al., A 2-terminal perovskite/silicon multijunction solar cell enabled by a silicon tunnel junction, Appl. Phys. Lett. 106 (2015).
[11] J. Werner, C.-H. Weng, A. Walter, L. Fesquet, J.P. Seif, S. De Wolf, et al., Efficient monolithic perovskite/silicon tandem solar cell with cell area >1 cm 2, J. Phys. Chem Lett. 7 (2015) p. acs.jpclett.5b02686.
[12] M.A. Green, M.J. Keevers, Optical properties of intrinsic silicon at 300 K, Prog. Photovolt. Res. Appl. 3 (1995) 189–192.
[13] M.A. Green, Self-consistent optical parameters of intrinsic silicon at 300 K including temperature coefficients, Sol. Energy Mater. Sol. Cells 92 (2008) 1305–1310.
[14] "NSM Archive - Silicon Germanium (SiGe) - Optical properties."
[15] "Springer Handbook of Electronic and Photonic Materials," 2007
[16] H. Povolny, P. Agarwal, S. Han, X. Deng, Comparison study of a-SiGe solar cells and materials deposited using different hydrogen dilution, MRS Proc. 609 (2011) p. A30.3.
[17] C.C. Wang, D.S. Wuu, S.Y. Lien, Y.S. Lin, C.Y. Liu, C.H. Hsu, et al., Characterization of nanocrystalline SiGe thin film solar cell with double graded-dead absorption layer, Int. J. Photoenergy 2012 (2012).
[18] R. Pandey, R. Chaujar, Rear contact SiGe solar cell with SiC passivated front surface for >90-percent external quantum efficiency and improved power conversion efficiency, Sol. Energy 135 (2016) 242–252.
[19] R. Pandey, R. Chaujar, Novel back-contact back-junction SiGe (BC-BJ SiGe) solar cell for improved power conversion efficiency, Microsyst. Technol. 22 (2016) 2673–2680.
[20] R. Pandey, A. Jain, R. Chaujar, Impact of minority carrier lifetime and temperature on SiC based rear contact sige solar cell for concentrator photovoltaic (cpv) applicationS, 32nd European Photovoltaic Solar Energy Conference and Exhibition (2016) p. 4.
[21] C.D. Bailie, M.D. McGehee, High-efficiency tandem perovskite solar cells, MRS Bull. 40 (2015) 681–686.
[22] R. Pandey, R. Chaujar, Numerical simulation of rear contact silicon solar cell with a novel front surface design for the suppression of interface recombination and improved absorption, Curr. Appl. Phys. 16 (2016) 1581–1587.
[23] F. Fu, T. Feurer, T. Jäger, E. Avancini, B. Bissig, S. Yoon, et al., Low-temperature-processed efficient semi-transparent planar perovskite solar cells for bifacial and tandem applications, Nat. Commun. 6 (2015) p. 8932.
[24] C. Wehrenfennig, G.E. Eperon, M.B. Johnston, H.J. Snaith, L.M. Herz, High charge carrier mobilities and lifetimes in organolead trihalide perovskites, Adv. Mater. 26 (2014) 1584–1589.
[25] Y. Yang, M. Yang, Z. Li, R. Crisp, K. Zhu, M.C. Beard, Comparison of recombination dynamics in CH3NH3PbBr3 and CH3NH3PbI3 perovskite films: influence of exciton binding energy, J. Phys. Chem. Lett. 6 (2015) 4688–4692.
[26] D.S. Software, ATLAS User ' s Manual, pp. 567–1000, 2013.
[27] F. Liu, J. Zhu, J. Wei, Y. Li, M. Lv, S. Yang, et al., Numerical simulation: toward the design of high-efficiency planar perovskite solar cells, Appl. Phys. Lett. 104 (2014) (253508).
[28] S.B. Meijun Lu, U. Das, R. Birkmire, A-Si/C-Si heterojunction for interdigitated back contact solar cell, Pro. 22nd European PVSEC vol. 22 (2007) p. 4.
[29] D. Thibaut, D.V. Sylvain, S. Florent, D. Djicknoum, M. Delfina, G.-F. Marie, et al., Development of interdigitated back contact silicon heterojunction (IBC Si-HJ) solar cells, Energy Procedia 8 (2011) 294–300 (2011/01/01).
[30] R. Pandey, R. Chaujar, Numerical simulations: toward the design of 27.6% efficient four-terminal semi-transparent perovskite/SiC passivated rear contact silicon tandem solar cell, Superlattices Microstruct. 100 (2016) 656–666.
[31] X. Yin, P. Chen, M. Que, Y. Xing, W. Que, C. Niu, et al., Highly efficient flexible perovskite solar cells using solution-derived NiOx hole contacts, ACS Nano 10 (2016) 3630–3636.
[32] Q. Lin, A. Armin, R.C.R. Nagiri, P.L. Burn, P. Meredith, Electro-optics of perovskite solar cells, Nat. Photon. 9 (2015) 106–112 02//print.
[33] W.S. Yang, J.H. Noh, N.J. Jeon, Y.C. Kim, S. Ryu, J. Seo, et al., High-performance photovoltaic perovskite layers fabricated through intramolecular exchange, Science (2015) p. science.aaa9272.

Journal of
Photonics for Energy

PhotonicsforEnergy.SPIEDigitalLibrary.org

Technology computer aided design of 29.5% efficient perovskite/interdigitated back contact silicon heterojunction mechanically stacked tandem solar cell for energy-efficient applications

Rahul Pandey
Rishu Chaujar

SPIE.

Rahul Pandey, Rishu Chaujar, "Technology computer aided design of 29.5% efficient perovskite/interdigitated back contact silicon heterojunction mechanically stacked tandem solar cell for energy-efficient applications," *J. Photon. Energy* **7**(2), 022503 (2017), doi: 10.1117/1.JPE.7.022503.

Technology computer aided design of 29.5% efficient perovskite/interdigitated back contact silicon heterojunction mechanically stacked tandem solar cell for energy-efficient applications

Rahul Pandey and Rishu Chaujar*
Delhi Technological University, Department of Engineering Physics, Shahbad Daulatpur,
New Delhi, India

Abstract. A 29.5% efficient perovskite/SiC passivated interdigitated back contact silicon heterojunction (IBC-SiHJ) mechanically stacked tandem solar cell device has been designed and simulated. This is a substantial improvement of 40% and 15%, respectively, compared to the transparent perovskite solar cell (21.1%) and Si solar cell (25.6%) operated individually. The perovskite solar cell has been used as a top subcell, whereas 250- and 25-μm-thick IBC-SiHJ solar cells have been used as bottom subcells. The realistic technology computer aided design analysis has been performed to understand the physical processes in the device and to make reliable predictions of the behavior. The performance of the top subcell has been obtained for different acceptor densities and hole mobility in Spiro-MeOTAD along with the impact of counter electrode work function. To incorporate the effect of material quality, the influence of carrier lifetimes has also been studied for perovskite top and IBC-SiHJ bottom subcells. The optical and electrical behavior of the devices has been obtained for both standalone as well as tandem configuration. Results reported in this study reveal that the proposed four-terminal tandem device may open a new door for cost-effective and energy-efficient applications. © *2017 Society of Photo-Optical Instrumentation Engineers (SPIE)* [DOI: 10.1117/1.JPE.7.022503]

Keywords: perovskite; interdigitated back contact silicon heterojunction; tandem; recombination; solar cell; SiC; atlas software.

Paper 16138SS received Dec. 26, 2016; accepted for publication Mar. 2, 2017; published online Apr. 7, 2017.

1 Introduction

Crystalline silicon (c-Si) solar cells have been dominating the photovoltaics (PVs) market for several decades, with a current market share of 90%.[1] The efficiency of the c-Si solar cell has only marginally improved during the last 15 years; the wafer size efficiency as high as 25.6% was obtained with amorphous silicon (a-Si)/c-Si heterojunction technology[2] which is close to the theoretical maximum efficiency of 29.4%.[3] Despite this, for a PV system fully competitive with the conventional energy source, a cost-effective energy-efficient module is required. Therefore, to obtain the ultrahigh conversion efficiency, i.e., efficiencies beyond the practical limit, Si-based tandem approaches have been projected, which combine a silicon cell with a low-cost cell with wide-bandgap (1.6 to 1.9 eV) absorber material to form a tandem cell. Commonly, III–V semiconductors have been used on top of silicon to make a tandem cell. However, their large area production is costly and difficult.[4] The emergence of an organic–inorganic halide perovskite solar cell drastically changes the situation. Perovskite is termed after the Russian mineralogist L. A. Perovski. The solar cell based on organometal halides represents an emerging PV technology. The methylammonium–lead–halide, $CH_3NH_3PbX_3$ ($X = Br, I$) perovskite solar cells are particularly interesting as the top cell in Si-based tandem device due to their suitable bandgap of 1.55 eV, a high absorption coefficient,[5] and sharp absorption edge

---

*Address all correspondence to: Rishu Chaujar, E-mail: rishu.phy@dce.edu

1947-7988/2017/$25.00

with little subbandgap absorption,[6] thus, making it an attractive candidate for high-efficiency tandem solar cells. Furthermore, the outstanding improvement in power conversion efficiency (PCE) of perovskite cells in the past few years suggests that it is a capable candidate for the next generation PV technology.[7] In 2015, the certified efficiency reached 20.1%.[8] Recently, record PCEs of 20.8% and 21.1% have been achieved in perovskite solar cells.[9,10] Moreover, 13.8% and 16.0% PCEs have been achieved using perovskite–perovskite-based two-terminal and four-terminal devices, respectively.[11] Despite the improvement in efficiency, perovskite-based devices suffer from thermal and environmental stability; however, these issues have been resolved by replacing the volatile methyl ammonium cation with cesium, reported by Bush et al.,[12] and using a solution-processed nanoparticle buffer layer along with a sputtered indium tin oxide (ITO) electrode, reported by Beal et al.[13] The IBC-SiHJ solar cell has been used as a bottom subcell, in IBC-SiHJ technology, a thin layer of a-Si: H deposited on c-Si at a low temperature. These cells combine the advantages of IBC which has Si heterojunction with higher open circuit voltage (V_{OC}) and higher short-circuit current density (J_{SC}), due to all the contacts being on the back side, thus eliminating the contact shading.[14] Moreover, in the perovskite/silicon tandem-based approach, tandem efficiencies greater than 30%, 35% are possible with a top subcell bandgap of $E_{\mathrm{g}} = 1.55$ eV and $E_{\mathrm{g}} = 1.7$ eV, respectively, with careful light management as suggested in Ref. 15. A 13.7% efficient two-terminal perovskite/silicon multijunction solar cell enabled by a silicon tunnel junction has been reported,[16] and an 18% efficient monolithic tandem cell formed by a silicon heterojunction bottom- and a perovskite top-cell has also been reported by Ref. 17. Moreover, 21.2% and 19.2% efficient monolithic perovskite/silicon tandem solar cells with a cell of 0.17 and 1.22 cm^2, respectively, have been proposed in the literature.[18] Recent work shows that conversion efficiency up to 31.8% is achievable for a perovskite/silicon two-terminal monolithic configuration using ITO as a transparent conductive electrode.[19] Also, one of the previous works shows numerical analysis of a four-terminal perovskite/SiC-based rear contact silicon solar cell to achieve 27.6% PCE under single AM1.5 illumination.[20,21] Previous research work shows a perovskite-based cell is a good candidate to be used in tandem configuration with a silicon cell to produce an efficient cell under illumination.

This work presents a design of a 29.5% efficient four-terminal mechanically stacked perovskite/SiC passivated IBC-SiHJ tandem device using numerical simulations. The four-terminal mechanically stacked devices are less complex compared to two-terminal tandem solar cells. In the four-terminal mechanically stacked tandem solar cells, top and bottom subcells are fabricated individually and then assembled in a module, which avoids the need for current matching between subcells, thereby giving greater process and design flexibility as reported by Bailie and McGehee.[4] The motivation to design a SiC-based IBC-SiHJ bottom subcell is to suppress the interface recombination and improve the thermal stability.[22,23]

2 Device Structure and Models

Physically based device simulation is very important. It predicts the electro-optical behavior of specified solar cell device structures and provides insight into the internal physical mechanisms associated with device operation that is difficult to measure. The carrier dynamics in a perovskite device can be quantitatively described by the following equation according to different recombination mechanisms:

$$\frac{\mathrm{d}n(t)}{\mathrm{d}t} = -Cn^3 - Bn^2 - An,$$

where $n(t)$ is the charge-carrier density and A, B, and C denote the monomolecular, bimolecular recombination rate (BRR), and trimolecular recombination rate (TRR) constants. Literature reports, monomolecular, bimolecular, and TRR constants as SRH recombination, radiative recombination, and auger recombination coefficients, respectively.[24] In this work, a Silvaco ATLAS technology computer aided design (TCAD) device simulator has been used to study the performance of perovskite top subcells. The parameters for each model have been calibrated according to experimentally available data.[24,25] Figures 1(a)–1(c) show the simulated device structure. Fluorine-doped tin oxide has been used as a front contact for the perovskite solar

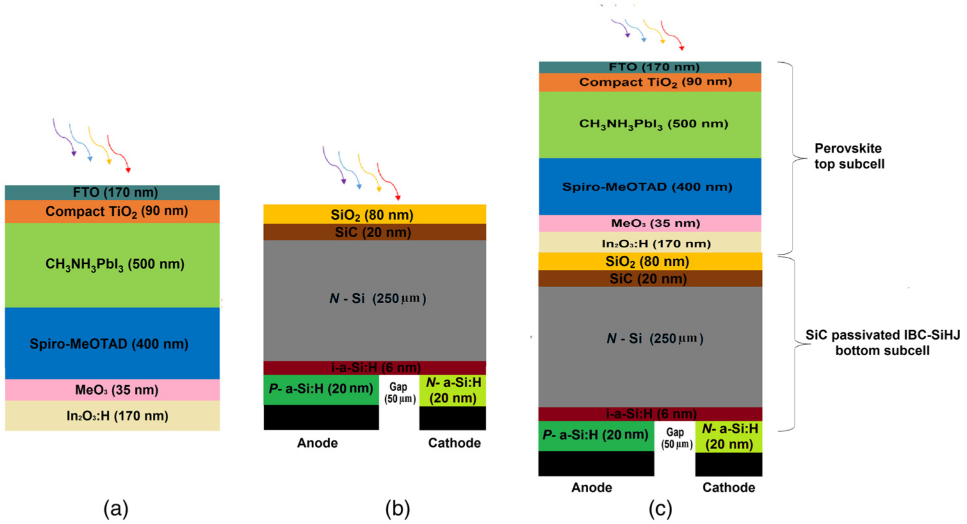

Fig. 1 Device structures used in simulation: (a) perovskite top subcell with indium oxide (In_2O_3: H) as a transparent rear electrode, (b) SiC-based IBC-SiHJ bottom subcell, and (c) mechanically stacked perovskite/IBC-SiHJ tandem cell.

cell. The P-type doping density of 2.14×10^{17} cm^{-3} and 3×10^{18} cm^{-3} has been used for perovskite and Spiro-MeOTAD, whereas compact TiO_2 is N-type with a doping density of 5×10^{19} cm^{-3}. In a four-terminal configuration, the perovskite top subcell requires two transparent contacts. Therefore, an indium oxide (In_2O_3: H)-based transparent rear electrode has been used for the perovskite top subcell as reported in Ref. 26. Moreover, for the bottom IBC-SiHJ subcell, the device structure has been designed using the ATHENA process simulator. The dimensions, doping, and material parameters are used as suggested by Ref. 27; the doping of N-type c-Si and N-type a-Si:H are 2.14×10^{16} cm^{-3} and 4.8×10^{18} cm^{-3}, respectively, and P-type a-Si:H is 2×10^{19} cm^{-3}. The width of N-type a-Si:H and P-type a-Si:H is 180 and 950 μm, respectively. The width of the gap region is 50 μm. After successfully reobtaining the results as reported by Ref. 27, the antireflective coating (ARC) is replaced with a 20-nm-thick SiC layer along with 80-nm-thick SiO_2-based encapsulation. The modified device is shown in Fig. 1(b). Furthermore, the Poisson equation is solved along with the electron and hole continuity equation to obtain the current density–voltage ($J - V$) curve under AM1.5 illumination. The perovskite cell is simulated, based on the recombination dynamics in $CH_3NH_3PbI_3$ with the help of SRH, Auger, and radiative recombination models to account for monomolecular, bimolecular, and trimolecular recombinations in the perovskite top subcell, whereas for the bottom IBC-SiHJ cell, Fermi statistics are used for carriers and drift-diffusion combined with Bohm quantum potential to account for quantum correction. The concentration-dependent SRH, concentration-dependent mobility, and Auger recombinations are activated for the bottom IBC-SiHJ solar cell.[28] The radiative recombination model is omitted for the IBC-SiHJ cell since silicon is an indirect bandgap semiconductor and band to band recombination is insignificant. The description of the material parameters used in the simulation is shown in Table 1. The material parameters for the perovskite cell have been obtained from Ref. 29, whereas model parameters are obtained from Refs. 24 and 25. The optical properties for a-Si: H, c-Si, SiC, SiO_2, TiO_2, and fullerene doped tin oxide have been used from the sopra database of the Silvaco ATLAS library, whereas the optical properties for $CH_3NH_3PbI_3$, Spiro-MeOTAD, MoO_3, and In_2O_3:H have been obtained from Refs. 30–33, respectively, and are identical to those reported in Ref. 21.

3 Results

3.1 *Analysis of Perovskite Top Subcell*

The perovskite cell as shown in Fig. 1(a) is simulated, and the $J - V$ curves are presented in Fig. 2. The circle and square symbol-based $J - V$ curves are obtained with the help of the

Table 1 Material parameters used during simulation.

Material		A	B	C	D	E	F	G	H	I
Dielectric constant		100	30	3	11.9	11.9	11.9	11.9	9.72	
Band gap (eV)		3.2	1.5	2.91	1.17	1.70	1.70	1.70	2.2	1.17
Electron affinity (eV)		4	3.93	2.2	4.05	3.9	3.9	3.9	4.2	
Thickness (μm)		0.09	0.5	0.4	25, 250	0.02	0.006	0.02	0.02	0.001
Electron, hole mobility ($\mathrm{cm^2/V \cdot s}$)		0.006, 0.006	50,50	0.0001, 0.0001	1417, 470	2.03	2.03	2.03	100,50	
Effective conduction band (DOS) ($\mathrm{cm^{-3}}$)		1×10^{21}	2.5×10^{20}	2.5×10^{20}	2.89×10^{19}	2.5×10^{20}	2.5×10^{20}	2.5×10^{20}	6.4×10^{18}	
Effective valence band (DOS) ($\mathrm{cm^{-3}}$)		2×10^{20}	2.5×10^{20}	2.5×10^{20}	3.14×10^{19}	2.5×10^{20}	2.5×10^{20}	2.5×10^{20}	1.6×10^{18}	
Conduction tail states	$N^{\text{c-tail}}A$ ($\mathrm{cm^{-3}}$)	10^{14}	10^{14}	10^{14}	n/a	10^{21}	10^{18}	10^{21}	n/a	0
	$E^{\text{c-tail}}A$ (eV)	0.01	0.015	0.01	n/a	0.12	0.09	0.07	n/a	0.07
Valence tail states	$N^{\text{v-tail}}D$ ($\mathrm{cm^{-3}}$)	10^{14}	10^{14}	10^{14}	n/a	10^{21}	10^{18}	10^{21}	n/a	0
	$E^{\text{v-tail}}D$ (eV)	0.01	0.015	0.01	n/a	0.12	0.09	0.12	n/a	0.12
Acceptor-like (A) dangling bond states	$N^{\text{db}}A$ ($\mathrm{cm^{-3}}$)	10^{17}	10^{14}	10^{16}	n/a	10^{19}	10^{16}	10^{19}	n/a	2.4×10^{16}
	$E^{\text{db}}A$ (eV)	1.1	1.2	1.1	n/a	0.7	1.1	1.3	n/a	0.5
	$\sigma^{\text{db}}A$ (eV)	0.1	0.1	0.1	n/a	0.2	0.15	0.2	n/a	0.2
Donor-like (D) dangling bond states	$N^{\text{db}}D$ ($\mathrm{cm^{-3}}$)	10^{17}	10^{14}	10^{16}	n/a	10^{19}	10^{16}	10^{19}	n/a	2.4×10^{16}
	$E^{\text{db}}D$ (eV)	1.1	1.2	1.1	n/a	0.45	0.9	1.1	n/a	0.5
	$\sigma^{\text{db}}D$ (eV)	0.1	0.1	0.1	n/a	0.2	0.15	0.2	n/a	0.2

A, compact TiO_2; *B*, $CH_3NH_3PbI_3$; *C*, Spiro-MeOTAD; *D*, c-Si; *E*, *n* type a-Si:H; *F*, buffer a-Si:H; *G*, *p* type a-Si:H; H, SiC; I, interface defects.

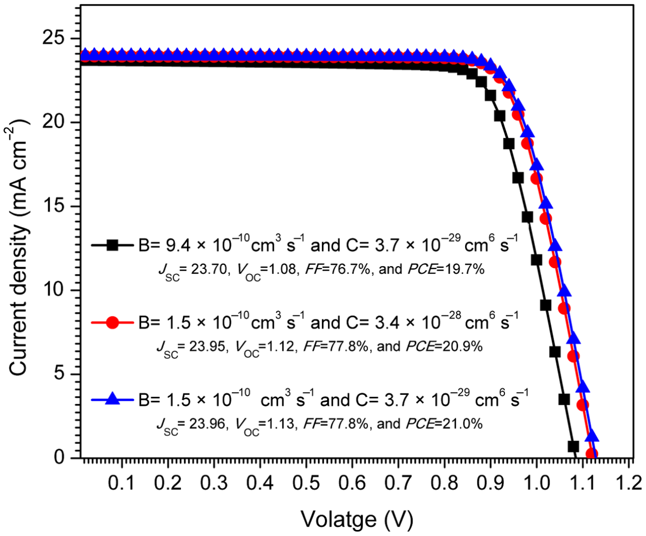

Fig. 2 $J - V$ curve of the perovskite top cell with different bimolecular and trimolecular carrier recombination coefficients as reported by Refs. 24 and 25, respectively. Monomolecular lifetime 10^{-6} s has been used.

bimolecular and TRR coefficients reported by Refs. 24 and 25, respectively. Monomolecular recombination lifetime 10^{-6} s has been used for the SRH recombination model. An additional $J - V$ curve, i.e., triangular symbol-based, is also obtained for optimum performance as shown in Fig. 2. The PCEs of 19.7%, 20.9%, and 21.0% have been obtained as shown in Fig. 2. The variation in the $J - V$ curve clearly shows that the impact of trimolecular recombination is lower as compared to bimolecular recombination since perovskite material has a direct bandgap. Therefore, Auger recombination is sufficiently suppressed, and this has been verified by experimental results.[34] The effect of trimolecular recombination, however, is not ignorable at high charge-carrier density.

Furthermore, the impact of material quality has also been obtained with the help of the SRH model. SRH recombination is defect-limited and proportional to the defect density. Literature reports a first-order recombination lifetime (τ) range from 10 to 10^3 ns.[35–37] Therefore, the perovskite cell has been simulated with three different carrier lifetimes i.e., (10^{-6} to 10^{-8}) s, and corresponding PV parameters are presented in Table 2. The result shows as the carrier lifetime changes from 10^{-6} to 10^{-7} s, the change in J_{SC}, V_{OC}, FF, and PCE are 23.95 to 23.67 mA cm^{-2}, 1121 to 1106 mV, 77.9% to 76.0%, and 20.95% to 19.91%, respectively. This results in 1.1%, 1.3%, 2.4%, and 4.9% decrease in J_{SC}, V_{OC}, FF, and PCE, respectively. However, as the lifetime of the carriers changes from 10^{-7} to 10^{-8} s, the decrease in J_{SC}, V_{OC}, FF, and PCE is 6.4%, 6.0%, 6.1%, and 17.4%, respectively, as shown in Table 2. This concludes that till 10^{-7} s, the PV parameters are less affected. However, as lifetime changes to 10^{-8} s, significant degradation has been obtained in PV parameters of the perovskite top subcell, due to the inadequate diffusion length of carriers.

The PV parameters of the 10^{-6} s lifetime-based perovskite device simulated in this work are almost equivalent to high-performance mixed cation perovskite solar cells with record power

Table 2 PV parameters of perovskite top subcell with different monomolecular recombination lifetimes.

τ (s)	J_{SC} (mA cm^{-2})	V_{OC} (mV)	FF (%)	PCE (%)
10^{-6}	23.95	1121	77.98	20.95
10^{-7}	23.67	1106	76.03	19.91
10^{-8}	22.15	1039	71.38	16.44

conversion efficiencies of 20.8% and 21.1% reported in Refs. 9 and 10. However, the performance of the low carrier lifetime-based perovskite device is also in close approximation with the experimentally available data.[38] Furthermore, for better understanding, contour representation of the monomolecular recombination rate in the $CH_3NH_3PbI_3$ layer has been obtained for three carrier lifetimes and presented in Figs. 3(a)–3(c), and the data plot is presented in Fig. 3(d). The recombination parameter is obtained under short-circuit (SC) condition with illumination. Figures 3(a)–3(d) clearly show that the higher recombination rate is observed when τ is equivalent to 10^{-8} s compared to 10^{-7} and 10^{-6} s lifetime-based devices. The monomolecular recombination is lower at the TiO_2 (ETL)/$CH_3NH_3PbI_3$ interface, increases in the bulk of the device and becomes maximum near the $CH_3NH_3PbI_3$/Spiro-MeOTAD (HTL) interface. The distribution is obtained under SC condition with illumination on. Therefore, under the SC condition, the associated electric field of the TiO_2 (ETL)/$CH_3NH_3PbI_3$ interface collects the generated minority carrier electrons from the electron–hole (e–h) pair, and the collection is complete in near interface (ETL/perovskite). However, the region outside the (ETL/perovskite) interface is neutral, and the collection will be by diffusion toward the field region, where they will be separated and collected. Therefore, the regions closer to the (ETL/perovskite) interface will have a lower recombination rate as shown in Figs. 3(a)–3(d). Furthermore, carrier concentration inside the device has been obtained and presented in Fig. 3(e); the carrier lifetime 10^{-6} has been used for further analysis in this paper. Near the ETL/perovskite interface electron concentration is less compared to the bulk region and perovskite/HTL interface, since outside the interface, the collection will be by diffusion of electrons toward the field region where it will be collected. The electrons that are generated in a region greater than the diffusion length are balanced by the recombination process. Hence, there is a lateral concentration gradient for electrons, showing the lateral flow of electrons to the collecting junction. This also validates the higher monomolecular recombination rate near the perovskite/HTL interface as shown in Figs. 3(a)–3(d). Moreover, the other two recombination dynamics, i.e., BRR and TRR have also been obtained in the perovskite layer and presented in Figs. 4(a)–4(d). Parameters obtained from Ref. 24 have a higher third-order recombination coefficient and lower second-order recombination coefficient compared to parameters reported in Ref. 25. Results show that the magnitude of TRR is lower compared to

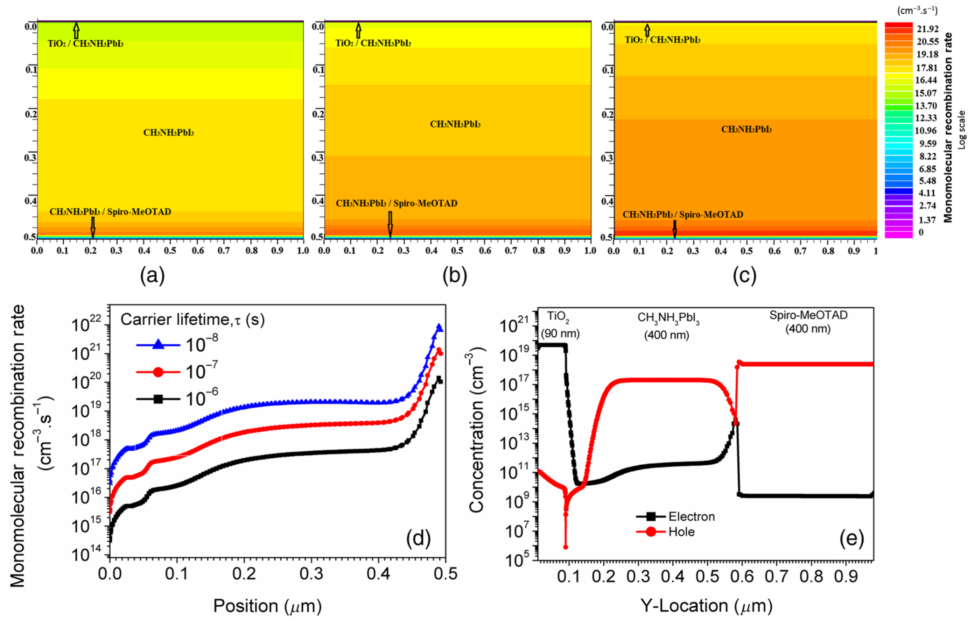

Fig. 3 (a)–(c) Contour representation of monomolecular recombination rate inside the perovskite region with varying values of first-order recombination lifetime, i.e., 10^{-6}, 10^{-7}, and 10^{-8} s, respectively, (d) $X - Y$ representation of monomolecular recombination rate, as shown in (a)–(c), the position in perovskite region is shown on X-axis and recombination rate is shown on Y-axis, and (e) the carrier concentration in perovskite top subcell device, lifetime 10^{-6} s has been used. All the data have been obtained under SC condition with illumination (on).

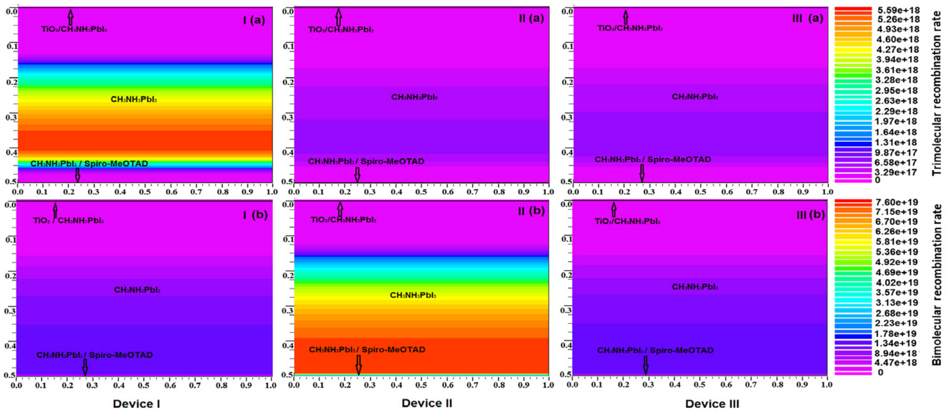

Fig. 4 The contour representation of trimolecular and BRR inside the perovskite layer. Device I is based on recombination coefficients 3.4×10^{-28} $cm^6\,s^{-1}$ and 1.5×10^{-10} $cm^3\,s^{-1}$, Device II is based on recombination coefficients 3.7×10^{-29} $cm^6\,s^{-1}$ and 9.4×10^{-10} $cm^3\,s^{-1}$, and Device C is based on recombination coefficients 3.7×10^{-29} $cm^6\,s^{-1}$ and 1.5×10^{-10} $cm^3\,s^{-1}$. TRR is higher in the device I compared to device II, since third-order recombination rate is 9.2 times higher, whereas BRR is lower compared to device II since second-order recombination rate is 6.3 times lower compared to device II.

BRR. This also validates the $J - V$ curves presented in Fig. 2. Here, we conclude that the major efficiency limiting factor is radiative recombination in the perovskite layer, and the statement is well supported by experimental results.[34] However, in the defected perovskite layer having a 10^{-8} s carrier lifetime, monomolecular recombination plays a significant role in the performance degradation as discussed earlier.

3.1.1 *Impact of acceptor density, hole mobility in Spiro-MeOTAD, and counter electrode work function on the perovskite top subcell device performance*

Here, through numerical simulations, the effect of doping and hole mobility in Spiro-MeOTAD (HTM) on device performance has been obtained and presented in Figs. 5(a) and 5(b). $J - V$ curve improves by improving the acceptor doping in HTM as shown in Fig. 5(a), since for low acceptor concentration the series resistance of HTM is high. Furthermore, the hole mobility of HTM has an appreciable effect on the performance of the device. The basic role of this layer is to extract the holes from the electron–hole pair reaching the (perovskite/HTM) interface. Therefore, HTM must be a good hole conductor, to perform its hole collecting function well. Also, it must not allow the stack up of the holes in it near the interface. However, if this occurs because of low hole mobility, the free holes will recombine with free electrons on both sides of the interface and thus lead to a decrease in collected current. Another effect also comes into the play. Having low

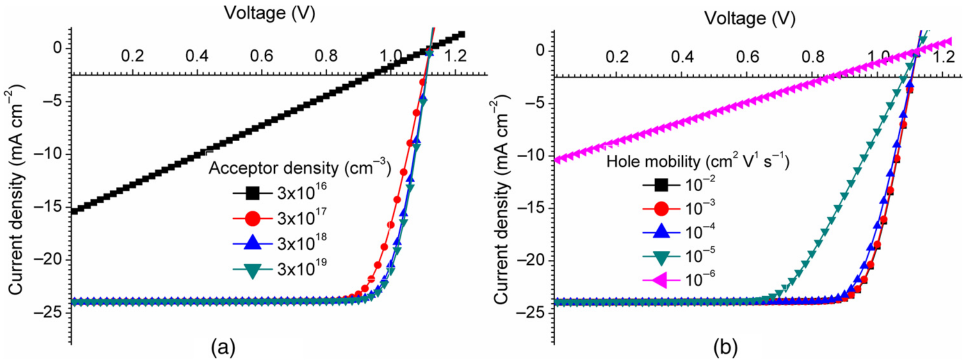

Fig. 5 The $J - V$ curves of the perovskite top cell (a) varying acceptor density in HTL layer with constant mobility of 10^{-4} $cm^2\,V\,s^{-1}$, (b) varying hole mobility in HTL layer with constant acceptor density of 3×10^{18} cm^{-3}.

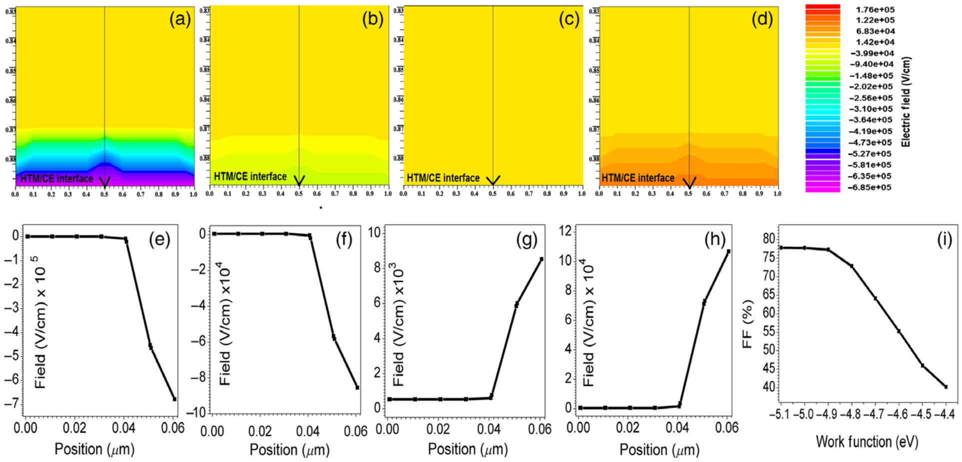

Fig. 6 The contour representation of electric field near HTL/CE interface with different CE work functions 4.3, 4.9, 5.0, and 5.1 eV, respectively, shown in (a)–(d), and the corresponding data have also been presented in (e)–(h), along with the cut line as shown in (a)–(d). The impact of CE metal work function on FF of the perovskite device has been shown in (i).

hole mobility results in increased resistance causing a larger voltage drop for the same cell current. Thus, increased series resistance of the cell leads to a decrease in the fill factor of the device. So the effect of hole mobility is twofold, i.e., decrease in both the collected current as well as FF of the device, as shown in Figs. 5(a) and 5(b). The effect of the CE work function has also been discussed. The performance of the device degrades by decreasing the work function. The distribution of the electric field examined in the HTL layer near the counter electrode (CE)/HTL interface is reported in Figs. 6(a)–6(h). Results reveal that direction of the field near HTM/CE interface becomes negative when the work function value is below 5.0 eV, which means the electric field direction is directed from CE to HTM, rendering it energetically unfavorable for hole transport to the electrode and hence increases the series resistance near the HTM/CE interface, which further results in decreased FF as shown in Fig. 6(i). The impact of acceptor density, hole mobility in HTM, and CE work function on the PV performance of the perovskite top cell shows identical behavior as reported in Ref. 29 using analysis of microelectronic and photonic structures (AMPS)-1-D device simulator.

3.2 *Analysis of SiC Passivated Interdigitated Back Contact Silicon Heterojunction Bottom Subcell*

In this section, initially, the performance of SiC-based IBC-SiHJ has been compared with conventional ARC-based IBC-SiHJ. The external quantum efficiency (EQE) and $J-V$ curves have been obtained for both the devices along with the effect of surface recombination velocity (SRV) on the performance of the devices. Figure 7(a) shows that EQE of the SiC passivated IBC-SiHJ device is higher as compared to the ARC-based device since the presence of SiC increases the optical coupling in the underlying substrate.[22,39] At a wavelength equivalent to 300 nm, the EQE of the SiC-based device is 79%, whereas in ARC-based, it is 69%. This results in 14.5% higher EQE in the SiC passivated device. Also, EQE of the SiC-based device is greater than 79% in the spectrum range of the (300 to 1040) nm wavelength, as shown in Fig. 7(a). The higher optical performance leads to higher J_{SC}; the J_{SC} values of 38.46 and 39.77 $\mathrm{mA\,cm}^2$ have been obtained in ARC and SiC-based devices, respectively, as shown in Fig. 7(b). The advantage of using the SiC-based IBC-SiHJ device is that it provides dual benefits in terms of increased optical behavior as well as enhanced front surface passivation quality. The presence of SiC at the front surface makes the interface insensitive to surface recombination by creating an electric field at the interface, hence preventing the minority carrier hole transport to the SiC/n-type c-Si interface.[22,40] In the surface recombination process, an electron recombines with a hole via defect level inside the bandgap. Therefore, decreasing the concentration of one type of carrier, i.e., electrons or holes, drastically reduces the recombination rate.[41]

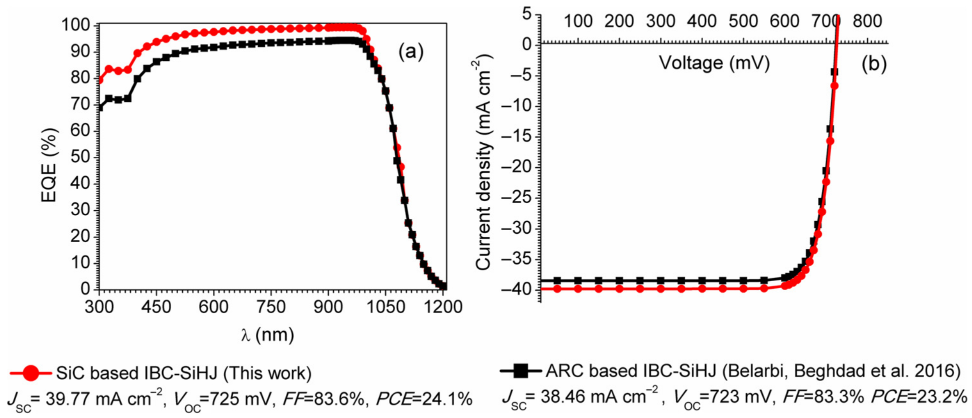

Fig. 7 Comparison of the optical and electrical behavior of SiC- and ARC-based IBC-SiHJ subcell in the standalone configuration: (a) EQE and (b) $J - V$ curve.

3.3 *Four-Terminal Perovskite/Interdigitated Back Contact Silicon Heterojunction Tandem Solar Cell*

In this section, a four-terminal perovskite/IBC-SiHJ-based mechanically stacked tandem device has been designed and analyzed using numerical simulation. Tandem devices reported in this work are based on perovskite as the top subcell, and SiC-based IBC-SiHJ as the bottom subcell, as shown in Fig. 1(c). In experimental approaches, both top and bottom subcells are separately handled and then assembled together to form a four-terminal mechanically stacked tandem device. Hence, both subcells are electrically independent. In this study, the performance of the IBC-SiHJ bottom cell is directly measured by placing the perovskite device as a filter under standard AM1.5 illumination, to simulate the condition when IBC-SiHJ is placed as the bottom subcell. For the bottom subcell, two types of the IBC-SiHJ solar cell have been used, one with the thickness of 250 μm and the second with the thickness of 25 μm. This results in two four-terminal tandem devices. All the dimensions of the 250-μm-thick device have been reduced 10 times except the gap width, to obtain a 25-μm-thick IBC-SiHJ solar cell. The carrier lifetime of 10^{-5} s is used for the 25-μm-thick device since lower diffusion length is required compared to a 250-μm-thick device. The 25-μm-thick device is thin compared to conventional 250-μm-thick silicon solar cells, and hence, the device can be fabricated with inexpensive, less pure material. The performance of IBC-SiHJ solar cells has been obtained for both standalone as well as bottom subcell conditions for the comparisons and presented in Figs. 8(a)–8(c).

Figure 8(a) shows the spectrum response of IBC-SiHJ solar cells. The result shows that the optical performance of the 25-μm-thick device is less compared to the 250-μm-thick device. The EQE starts to fall at a lower wavelength in the case of the 25-μm-thick device. This shows that the 25-μm-thick subcell device is not capable of absorbing high-energy photons compared to the 250-μm-thick device as shown in Figs. 8(a) and 8(b), since photon absorbance is directly related to the absorption coefficient and the thickness of the material used. This will lead to the superior PV performance of the 250-μm-thick bottom subcell-based tandem device. Moreover, Fig. 8(c) shows the performance of the bottom subcell with and without a perovskite filter. In a standalone configuration, the J_{SC} of 39.77 and 30.45 mA cm^{-2} have been obtained in 250- and 25-μm-thick bottom subcells, respectively, as shown in Fig. 8(c). After adding the perovskite top cell, the J_{SC} of the bottom subcells decreases to 14.74 and 5.42 mA cm^{-2} for 250- and 25-μm-thick devices, respectively, due to reduced light intensity. The decrease in V_{OC} is only marginal, resulting in 8.6% and 2.8% efficient bottom two subcells. Therefore, together with the 20.9% efficiency of the perovskite top subcell, this results in a 29.5% and 23.7% efficient tandem device with 250- and 25-μm-thick bottom subcells, respectively. This is a substantial improvement compared to a transparent perovskite solar cell and c-Si solar cell operated individually. The PV parameters of tandem devices are shown in Table 3.

Moreover, the impact of material quality has also been obtained on the performance of IBC-SiHJ solar cells. Therefore, the bottom subcell has been simulated with different carrier lifetimes

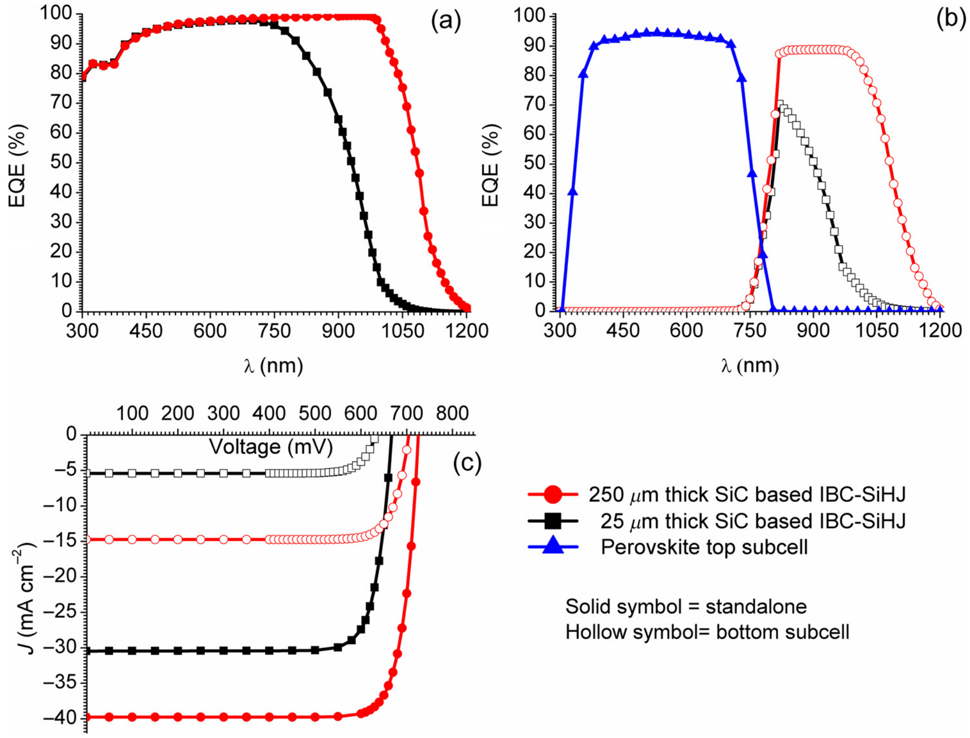

Fig. 8 (a) EQE of 250-and 25-μm-thick SiC passivated IBC-SiHJ solar cell under standalone conditions. (b) EQE of perovskite top subcell and IBC-SiHJ bottom subcell in a tandem configuration. (c) The $J-V$ curve of IBC-SiHJ cells in stand-alone and bottom subcell configuration.

Table 3 PV parameters of perovskite top subcell, IBC-SiHJ bottom subcell, and four-terminal tandem solar cell.

Solar cells	J_{SC} (mA cm^{-2})	V_{OC} (mV)	FF (%)	PCE (%)
Perovskite top subcell	23.95	1121	77.8	20.9
IBC-SiHJ cell 25 μm in stand-alone, subcell	30.45, 5.42	667, 632	82.3, 81.6	16.7, 2.8
IBC-SiHJ cell 250 μm in stand-alone, subcell	39.77, 14.74	725, 704	83.6, 82.7	24.1, 8.6
Four-terminal using 25-μm-thick bottom subcell				$20.9 + 2.8 = 23.7$
Four-terminal using 250-μm-thick bottom subcell				$20.9 + 8.6 = 29.5$

to obtain the impact of material (c-Si) quality. The charge carriers need to diffuse a shorter length in the thinner device. Therefore, the PV performance of a thinner device shows the negligible impact of material quality, whereas significant degradation has been observed in the thicker device. Results show that for lower carrier lifetime (2×10^{-5} s) the performance of a 250-μm-thick device is lower compared to a 25-μm-thick device, due to higher bulk recombination of the carrier in the thicker device, since lifetime is small. The V_{OC} values of the thinner device are higher compared to the thicker device as shown in Fig. 9(b). Since, the 25-μm-thick device has 10 times thinner substrate, the charge-carrier concentration in the 25-μm-thick device is higher than the 250-μm-thick device, which led to higher V_{OC}. The desired material quality and the device can be selected from Fig. 9, depending upon the application. Total efficiency in a tandem configuration can be obtained by adding the efficiencies of the bottom subcell and perovskite top cell.

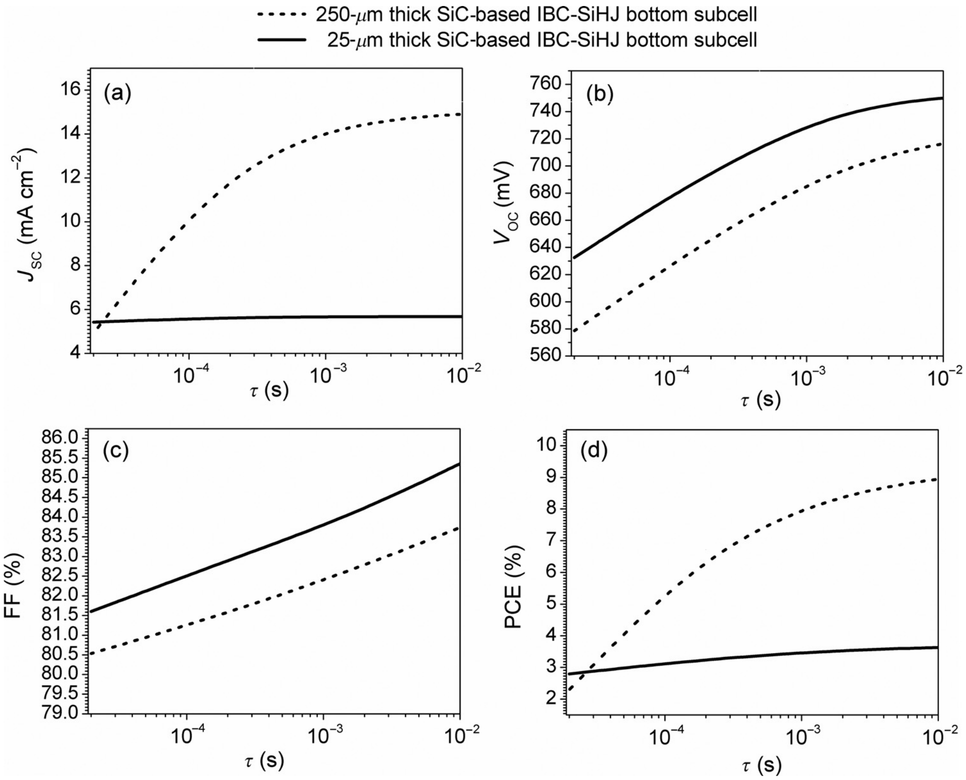

Fig. 9 The impact of carrier lifetime on the performance of IBC-SiHJ bottom subcells in a tandem configuration. (a) J_{SC}, (b) V_{OC}, (c) FF, and (d) PCE.

4 Conclusions

This work presents TCAD design of a 29.5% efficient mechanically stacked perovskite/IBC-SiHJ tandem device. Results show PCE of 29.5% and 23.7% with 250- and 25-μm-thick IBC-SiHJ bottom subcells, respectively. The performance of the top subcell has been obtained for different acceptor densities and hole mobility in HTM, along with the impact of the CE work function. Increasing the acceptor density and hole mobility in HTM beyond 3×10^{16} cm^{-3} and 10^{-5} cm^2 V^1 s^{-1} shows significant improvement in the performance of the perovskite top subcell. Electric field distribution near HTM/CE shows that a CE work function value >4.9 eV is required for the efficient extraction of holes from HTM. For the bottom subcell, a 24.1% efficient individually operated IBC-SiHJ solar cell is combined in a mechanically stacked four-terminal tandem configuration with a 20.9% efficient perovskite top subcell. The SiC passivated IBC-SiHJ bottom subcell shows less degradation on increasing the SRV, due to good surface passivation quality. The optical and electrical behavior of the devices has been obtained for both a standalone as well as tandem configuration. Results reveal that the discussed tandem device may open a new door for cost-effective and energy-efficient applications.

Acknowledgments

The authors would like to thank Microelectronics Research Laboratory at Delhi Technological University to carry out this work and University Grant Commission (UGC), Government of India, for providing research fellowship. Rahul Pandey acknowledges Dr. Rishu Chaujar for her continuous guidance during this research work.

References

1. ITRPV, "ITRPV seventh edition vers 2.pdf," (2016).
2. K. Masuko et al., "Achievement of more than 25% conversion efficiency with crystalline silicon heterojunction solar cell," *IEEE J. Photovoltaics* **4**, 1433–1435 (2014).

3. A. Richter, M. Hermle, and S. W. Glunz, "Reassessment of the limiting efficiency for crystalline silicon solar cells," *IEEE J. Photovoltaics* **3**, 1184–1191 (2013).
4. C. D. Bailie and M. D. McGehee, "High-efficiency tandem perovskite solar cells," *MRS Bull.* **40**, 681–686 (2015).
5. M. A. Leguy et al., "Reversible hydration of $CH_3NH_3PbI_3$ in films, single crystals, and solar cells," *Chem. Mater.* **27**, 3397–3407 (2015).
6. S. De Wolf et al., "Organometallic halide perovskites: sharp optical absorption edge and its relation to photovoltaic performance," *J. Phys. Chem. Lett.* **5**, 1035–1039 (2014).
7. N.-G. Park, "Perovskite solar cells: an emerging photovoltaic technology," *Mater. Today* **18**(2), 65–72 (2015).
8. W. S. Yang et al., "High-performance photovoltaic perovskite layers fabricated through intramolecular exchange," *Science* **348**, 1234–1237 (2015).
9. D. Bi et al., "Efficient luminescent solar cells based on tailored mixed-cation perovskites," *Sci. Adv.* **2**, e1501170 (2016).
10. M. Saliba et al., "Cesium-containing triple cation perovskite solar cells: improved stability, reproducibility and high efficiency," *Energy Environ. Sci.* **9**, 1989–1997 (2016).
11. G. E. Eperon et al., "Perovskite-perovskite tandem photovoltaics with optimized bandgaps," *Science* **354**(6314), 861–865 (2016).
12. K. A. Bush et al., "Thermal and environmental stability of semi-transparent perovskite solar cells for tandems enabled by a solution-processed nanoparticle buffer layer and sputtered ITO electrode," *Adv. Mater.* **28**(20), 3937–3943 (2016).
13. R. E. Beal et al., "Cesium lead halide perovskites with improved stability for tandem solar cells," *J. Phys. Chem.* **7**, 746–751 (2016).
14. M. D. Lammert and R. J. Schwartz, "The interdigitated back contact solar cell: a silicon solar cell for use in concentrated sunlight," *IEEE Trans. Electron Devices* **24**, 337–342 (1977).
15. N. N. Lal, T. P. White, and K. R. Catchpole, "Optics and light trapping for tandem solar cells on silicon," *IEEE J. Photovoltaics* **4**, 1380–1386 (2014).
16. J. P. Mailoa et al., "A 2-terminal perovskite/silicon multijunction solar cell enabled by a silicon tunnel junction," *Appl. Phys. Lett.* **106**, 121105 (2015).
17. S. Albrecht et al., "Monolithic perovskite/silicon-heterojunction tandem solar cells processed at low temperature," *Energy Environ. Sci.* **9**, 81–88 (2016).
18. J. R. M. Werner et al., "Efficient monolithic perovskite/silicon tandem solar cell with cell area >1 cm^2," *J. Phys. Chem. Lett.* **7**, 161–166 (2016).
19. Y. Jiang et al., "Optical analysis of perovskite/silicon tandem solar cells," *J. Mater. Chem. C* **4**, 5679–5689 (2016).
20. R. Pandey, A. Jain, and R. Chaujar, "Novel 4-terminal perovskite/SiC-based rear contact silicon tandem solar cell with 27.6% PCE," in *IEEE 43rd Photovoltaic Specialists Conf. (PVSC)*, pp. 1–4 (2016).
21. R. Pandey and R. Chaujar, "Numerical simulations: toward the design of 27.6% efficient four-terminal semi-transparent perovskite/SiC passivated rear contact silicon tandem solar cell," *Superlattices Microstruct.* **100**, 656–666 (2016).
22. R. Pandey and R. Chaujar, "Rear contact SiGe solar cell with SiC passivated front surface for >90-percent external quantum efficiency and improved power conversion efficiency," *Sol. Energy* **135**, 242–252 (2016).
23. M. Boccard and Z. C. Holman, "Amorphous silicon carbide passivating layers for crystalline-silicon-based heterojunction solar cells," *J. Appl. Phys.* **118**, 065704 (2015).
24. Y. Yang et al., "Comparison of recombination dynamics in $CH_3NH_3PbBr_3$ and $CH_3NH_3PbI_3$ perovskite films: influence of exciton binding energy," *J. Phys. Chem. Lett.* **6**(23), 4688–4692 (2015).
25. C. Wehrenfennig et al., "High charge carrier mobilities and lifetimes in organolead trihalide perovskites," *Adv. Mater.* **26**, 1584–1589 (2014).
26. F. Fu et al., "Low-temperature-processed efficient semi-transparent planar perovskite solar cells for bifacial and tandem applications," *Nat. Commun.* **6**, 8932 (2015).
27. M. Belarbi, M. Beghdad, and A. Mekemeche, "Simulation and optimization of n-type interdigitated back contact silicon heterojunction (IBC-SiHJ) solar cell structure using Silvaco TCAD Atlas," *Sol. Energy* **127**, 206–215 (2016).

28. D.S. Software, *ATLAS User's Manual*, pp. 567–1000, Santa Clara, California (2013).
29. F. Liu et al., "Numerical simulation: toward the design of high-efficiency planar perovskite solar cells," *Appl. Phys. Lett.* **104**, 253508 (2014).
30. A. M. A. Leguy et al., "Reversible hydration of $CH_3NH_3PbI_3$ in films, single crystals, and solar cells," *Chem. Mater.* **27**, 3397–3407 (2015).
31. M. Filipič et al., "$CH_3NH_3PbI_3$ perovskite / silicon tandem solar cells: characterization based optical simulations," *Opt. Express* **23**, A263–A278 (2015).
32. L. Lajaunie et al., "Strong anisotropic influence of local-field effects on the dielectric response of α-MoO_3," *Phys. Rev. B* **88**, 115141 (2013).
33. T. Koida, H. Sai, and M. Kondo, "$In_2O_3:H$ transparent conductive oxide films with high mobility and near infrared transparency for optoelectronic applications," *Surf. Eng.* **28**, 102–107 (2012).
34. G. Xing et al., "Low-temperature solution-processed wavelength-tunable perovskites for lasing," *Nat. Mater.* **13**, 476–480 (2014).
35. H. Zhu et al., "Lead halide perovskite nanowire lasers with low lasing thresholds and high quality factors," *Nat. Mater.* **14**, 636–642 (2015).
36. C. Wehrenfennig et al., "Homogeneous emission line broadening in the organo lead halide perovskite $CH_3NH_3PbI_{3-x}Cl_x$," *J. Phys. Chem. Lett.* **5**, 1300–1306 (2014).
37. D. Shi et al., "Low trap-state density and long carrier diffusion in organolead trihalide perovskite single crystals," *Science* **347**, 519–522 (2015).
38. M. Liu, M. B. Johnston, and H. J. Snaith, "Efficient planar heterojunction perovskite solar cells by vapour deposition," *Nature* **501**, 395–398 (2013).
39. S. Allen and Y. Awad, "Silicon carbide-based antireflective coating," US Patent App. 12/994, 973 (2009).
40. R. Pandey and R. Chaujar, "Numerical simulation of rear contact silicon solar cell with a novel front surface design for the suppression of interface recombination and improved absorption," *Curr. Appl Phys.* **16**, 1581–1587 (2016).
41. A. G. Aberle, "Surface passivation of crystalline silicon solar cells: a review," *Prog. Photovoltaics Res. Appl.* **8**, 473–487 (2000).

Rahul Pandey received his BSc (H) and MSc degrees in electronics from the University of Delhi, India, in 2011 and 2013, respectively. He is currently pursuing his PhD in design and simulation of silicon and SiGe solar cell at Microelectronics Research Laboratory, Engineering Physics Department, Delhi Technological University, New Delhi, India. He has authored 10 papers in international journals and conferences.

Rishu Chaujar received her BSc(H), MSc, and PhD degrees in electronics from the University of Delhi, India, in 2003, 2005, and 2009, respectively. She is currently working as an assistant professor in the Department of Engineering Physics at Delhi Technological University. Her doctoral research involves modeling, design, and simulation of solar cell devices. She is an executive member of various international and professional societies. She is a reviewer of various international journals and conferences.

Solar Energy 135 (2016) 242–252

Contents lists available at ScienceDirect

Solar Energy

journal homepage: www.elsevier.com/locate/solener

Rear contact SiGe solar cell with SiC passivated front surface for >90-percent external quantum efficiency and improved power conversion efficiency

Rahul Pandey, Rishu Chaujar *

Department of Engineering Physics, Delhi Technological University, Shahbad Daulatpur, Main Bawana Road, New Delhi, Delhi 110042, India

A R T I C L E I N F O

Article history:
Received 4 November 2015
Received in revised form 26 April 2016
Accepted 31 May 2016

Keywords:
ATLAS
Rear contact
Power conversion efficiency
Recombination
SiGe
Solar cell

A B S T R A C T

In this effort, 10 μm thick rear contact (RC) silicon–germanium (SiGe) based solar cell device has been discussed with SiC (20 nm)-based front surface passivation for the suppression of interface recombination as well as improvement of short circuit current density (J_{SC}) and open-circuit voltage (V_{OC}). The design principles presented here balance the electronic and photonic effects together and is a significant step to design highly efficient thin solar cells. Photo reflectance is significantly reduced in the UV/visible spectral region due to the presence of SiC. This results in external quantum efficiency (EQE) >90% in the spectrum range of 400–650 nm wavelength. Also, at wavelengths equivalent to 300 nm, SiC passivated device shows record EQE of 85%. The presence of SiC as a surface passivating layer shows enhanced surface characteristics in terms of reduced surface recombination and higher photon absorption rate. This results in 15.4% power conversion efficiency (PCE) under standard air mass 1.5 illuminations. Further, the proposed device has also been analyzed for concentrator photovoltaics (CPV) applications, resulting in 18.4% and 19.3% efficiencies at 1 W/cm^2 (10 suns, 27 °C) and 2 W/cm^2 (20 suns, 27 °C) respectively. Till date, the proposed design proves to be highly efficient in the sub 10 μm regime. All the simulations have been done using DEVEDIT and ATLAS device simulator

1. Introduction

Environment-friendly energy source has emerged as a great alternative for the grievous conventional energy source. Solar energy has been discovered to be the most eye-catching energy source because of its environment-friendly nature. In order to use this energy, it must be converted into the desired form of energy. Solar photovoltaic (PV) system is used to convert solar energy into electricity. The growing research topic in the field of PV is the development of low-cost and high-efficiency silicon solar cell. To maximize solar cell efficiency, it is necessary to optimize both the electrical characteristics and the optical absorption of the device (Green, 2003).

Systems based on silicon wafers are currently the dominant technology in PV market. Silicon is widely used material for PV due to its reliability, abundance, and mature fabrication process. In Silicon PV technology, to absorb the solar spectrum the thickness of conventional silicon cell typically more than 100 μm is required (Deinega et al., 2013). Since the absorption coefficient of silicon is small. The requirement of large volume and high-quality silicon significantly increases the module cost. Further, to make PV system feasible at large scale, it should be cost effective, with module cost to be <$0.5/W.

One promising high-efficiency solar cell concept is the back-contact back-junction (BC-BJ) solar cell, having both, junction and the electrodes are at the back side of the device. Now, since the junction and contacts are on the back side, front surface can be designed for optimum optical performance (Kerschaver and Beaucarne, 2006; Diouf et al., 2009). It has the advantages, such as prevention of optical shading losses at the front side and higher absorption and current density. The first 17% efficient under 50 sun condition BC-BJ solar cell was presented by Schwartz and Lammert (1975). It was designed as a cell for concentrator applications. The back diffusion, contact opening, and contacts were implemented using photolithography, about six lithography steps is required to produce the cell. This fabrication technique is not compatible with the cost-effective production of the solar cell. Further, a simplified processing of BC-BJ solar cell was introduced (Sinton and Swanson, 1990; Sinton et al., 1998). This was a major step toward the cost-effective BC-BJ solar cell and commercialized with Sunpower Corporation (Sinton et al., 1993). Today, Sunpower is the world leading

---

* Corresponding author.
E-mail address: Rishu.phy@dce.edu (R. Chaujar).

http://dx.doi.org/10.1016/j.solener.2016.05.056
0038-092X/

manufacturer of BC-BJ solar cell. Sunpower Corp. showed in 2007 that it is possible to achieve an average cell efficiency of 22% in the mass production of BC-BJ silicon solar cell (Ceuster et al., 2007). In year 2014, independently confirmed conversion efficiency of 23.0% for *N*-type RC cells has also been reported, at the end of the year, the interdigitated back contact (IBC) solar cells developed which resulted in an independently confirmed designated-area efficiency of 24.4%. The cell was fabricated on a 230 μm thick 1.5 Ω cm *N*-type CZ wafer (Feldmann et al., 2014; Franklin et al., 2014). The conventional RC solar cell has a large area which results in the higher material cost.

Further, nanostructuring has been projected as an appropriate method to make thin silicon an efficient absorber. However, these cells are not efficient due to Auger and surface recombination as the surface to volume ratio of the cells is large. However, a recent method to minimize the surface recombination for nanostructured based ~300 μm thick devices has been presented which results in 20% and 22% efficient cells (Ingenito et al., 2015; Savin et al., 2015). These cells have higher thickness, require high-quality materials, to have higher minority carrier lifetime: order of magnitude 10 ms. This kind of c-Si is very expensive, resulting in increased module cost. Conventional Si-based devices have 30 times higher thickness compared to the (15.4% efficient RC-SiGe) device proposed in this work. Some of the thin c-Si silicon-based solar cells are also available in the literature such as microsystem enabled 14 μm thick, 250 μm wide solar cell, with 14.9% efficiency is reported, and effort shows that the ultrathin wafer handling problem can be avoided by using low-cost microsystem techniques (Cruz-Campa et al., 2011). In the year 2013, an all-back-contact ultra-thin i.e. 10 μm thick silicon nanocone solar cell with 13.7% power conversion efficiency is reported (Jeong et al., 2013). A Si/Organic hybrid heterojunction solar cell has also been reported with PCE of 13.6% (He et al., 2015).

In our previous work, thin defect free SiC-based anti-reflection passivation layer has been designed for *N*-type wafer based RC Si and intrinsic wafer based SiGe solar cells (Pandey and Chaujar, 2015a,b). The SiC-based coaxial silicon nanowire solar cell has also been designed for optimal photovoltaic performance (Pandey and Chaujar, 2015c). Here, 10 μm thick SiC passivated *N*-type wafer based RC SiGe solar cell device has been designed and simulated which overcomes the critical problems associated with thin devices such as Auger, surface recombination and lower absorption at a higher wavelength. Present work shows superior EQE compared to Si cell, at higher wavelengths, since absorption coefficient of SiGe is higher as compared to Si in the higher wavelength regime. SiGe is used because the energy of the visible part of the spectrum used by the solar cell is less than 50% and to increase the absorption of sunlight, the low bandgap (<1.1 eV) material is required. Using low bandgap material in the solar cell makes the conversion efficiency of the cell effective. Nowadays, SiGe is used for high-frequency transistors as well as potential has been explored for solar cells also. In SiGe technology, the electrical properties of silicon are modified with germanium the number of free electrons in germanium is higher than silicon at a given temperature, which results in higher conductivity of Ge. SiGe processing is simple, the physical and electrical properties of silicon and germanium are similar (Ouellette, 2002; Kasap and Capper, 2007). Also, SiGe possesses higher mechanical strength and suppresses the high-intensity degradation of the solar cell under illumination (Yang et al., 2010). The band gap of SiGe can be modified by changing the Ge content, alternatively the optical absorption (Povolny et al., 2011; Wang et al., 2012). However, the cost of germanium doped wafer is higher compared to a silicon wafer, though present work shows it can be a good candidate for energy efficient applications. In future, development of novel cost effective energy efficient methode may reduce the overall dollar per watt ($/W) of the device. The discussed device shows superior EQE compared to silicon cell. Also, previous work shows that the photovoltaic parameters of 5 μm thick SiGe cell and 10 μm thick silicon cell are approximately same (Pandey and Chaujar, 2015d). This indicates that the proposed device significantly saves the material. In our previous work calibrated software program has been written in Silvaco ATLAS device simulator for 10 μm thick RC contact silicon cell (Pandey and Chaujar, 2015e). Therefore, 10 μm thick RC SiGe device has been simulated with the help of calibrated software program by changing the material parameters, since experimental results are not available for 10 μm thick RC SiGe solar cell.

2. Device structure and model description

Silvaco ATLAS has been used to simulate the device optoelectronic characteristics. In the simulation, we assume a two-dimensional structure i.e. RC SiGe solar cell as shown in Fig. 1(a). Also, the width is set so that the cell has an area of 1 cm^2. The $Si_{0.9}$ $Ge_{0.1}$ was used, with a very small Ge content. Since increasing the Ge content, decreases the band gap of SiGe, which further results in lower open circuit voltage. The bandgap 1.08 eV is used for SiGe. All the material parameters for SiGe including band gap have been obtained from experimentally available data (NSM Archive, 2016a), and the same has been used in the simulation. The substrate was *N*-type, with a doping density of 3×10^{15} cm^{-3}, whereas *N*+/*P*+ region has the doping density of 4×10^{20} cm^{-3}. The depth of *P*+ and *N*+ region was 3 μm and 2.5 μm, respectively, whereas the width was 45 μm and 30 μm, respectively and centre-to-centre distance (pitch) between the *N* + and *P*+ regions is 52 μm. In a standard solar cell, *P*-type wafer has been preferred, so hence the diffusion length of minority carrier (electrons) in *P*-type wafer is higher than the diffusion length of minority carrier (holes) in *N*-type wafer. However, in large-scale production, it is difficult to avoid chemical and mechanical imperfection to the wafer. Here, lies the big advantage of *N*-type wafer solar cells. The performance of *N*-type cell is less vulnerable by chemical and mechanical imperfections. The *N*-type cell have several advantages over *P*-type cells. They are not prone to light-induced degradation due to the splitting of boron-oxygen complexes (Glunz et al., 1999; Tjahjono and Cotter, 2005). Further, 70 nm thick Nitride (Si_3N_4) is used as anti-reflecting front surface passivation, and modeled as an optical layer. The oxide (SiO_2) is used for back surface passivation with a thickness of 50 nm. Also, as the contact interface between metal and semiconductor is highly doped both for the emitter and back surface field (BSF) i.e. ~10^{20} cm^{-3}, we have defined our contacts as ohmic. This is done to avoid Schottky barriers, and thus unnecessarily higher computation time. The contact width of 6 μm has been used for both *P*+ and *N*+ regions with the thickness of 700 nm as shown in Fig. 1(a).

Further, in the presence of heavy doping, (>10^{18} cm^{-3}), experimental work has shown that the *PN* product turns out to be doping dependent (Slotboom, 1977). As the doping level rises, a decrease in the bandgap occurs, where the valence band raises by an approximately same amount as the conduction band is lowered. Discussed structure has heavily doped *P* and *N* regions, and so bandgap narrowing effects are enabled. These effects can be described by an analytic expression relating the variation in the bandgap, ΔEg to the doping concentration, n (Slotboom and de Graaff, 1977). Furthermore, the solar cell is carrier recombination affected device. Therefore, Auger and Shockley–Read–Hall (SRH) recombination models are selected during the simulation. Phonon transitions occur in the presence of trap or defect within the forbidden gap of the semiconductor (Shockley and Read, 1952; Hall, 1952), and Auger recombination occurs through a three particle transition whereby a mobile carrier is either captured or emitted.

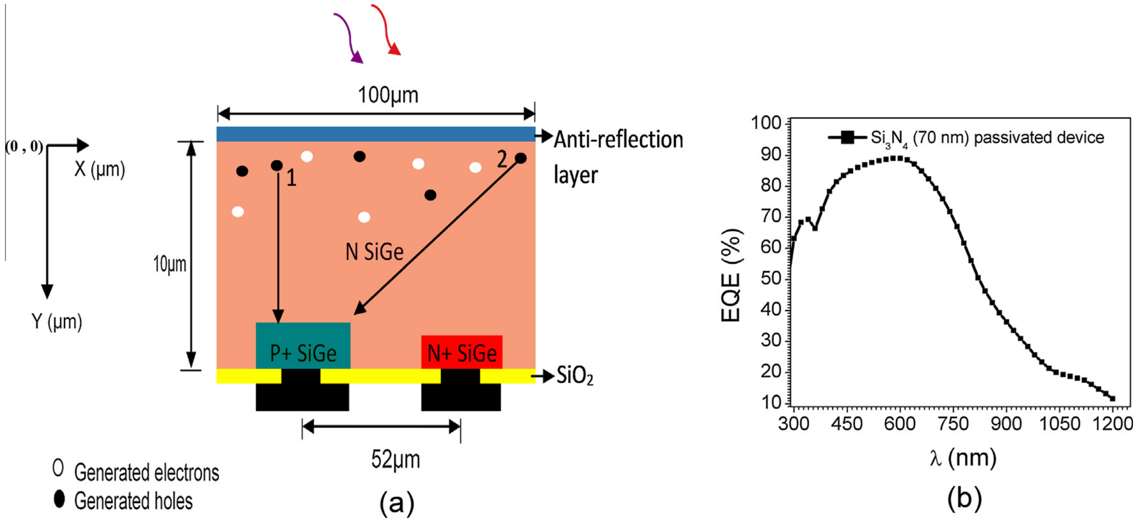

Fig. 1. (a) 10 µm RC-SiGe solar cell with 70 nm thick antireflection (AR) layer on top, 50 nm thick oxide layer has been used for back surface passivation. The region denoted by black color shows the ohmic contact to *N*+ and *P*+ regions. Pitch of the device is 52 µm, and (b) EQE of the device as shown in figure (a).

The underlying physics of such processes is unclear, and normally a more qualitative understanding is sufficient (Selberherr, 2012; Dziewior and Schmid, 1977). The concentration dependent mobility and field dependent mobility models have also been selected during simulation. The standard air mass 1.5G spectrum has been used for illumination and ray tracing algorithm is used to obtain the optical interaction. The complex reflective indices of all the materials as a function of wavelength and temperature have been obtained from sopra database (Atlas, 2014). Poisson's equation together with the continuity equation for electrons and holes are solved simultaneously by the software to obtain the current density–voltage (*J*–*V*) characteristics.

3. Results and discussions

3.1. Recombination rate and EQE of RC SiGe solar cell

In this section, 10 µm thick SiGe-based RC solar cell has been simulated as shown in Fig. 1(a). The EQE and recombination rate contour of proposed device have been presented in Figs. 1b and 2, respectively. In silicon-based cell, thickness more than 100 µm is required to absorb the solar spectrum (Deinega et al., 2013). Thinning the Si wafer, results in absorption loss, particularly at higher wavelengths, since the absorption coefficient (α) is small (Green and Keevers, 1995; Green, 2008). Therefore, use of SiGe instead of Si is a possible solution to minimize the absorption loss at higher wavelengths. The experimentally available data shows, the absorption coefficient (α) of SiGe is greater than Si in higher wavelength regime (NSM Archive, 2016b). The complex refractive index data of SiGe is obtained from software library and shown in Fig. 6(a) and (b), and the same have been used in the simulation. The proposed device shows superior EQE, and remarkably it achieved EQE > 76% in the spectrum range of 400–700 nm wavelength, shown in Fig. 1(b). At wavelength equivalent to 400 nm, proposed device shows EQE of the order of 78% that is at least 12% higher than of other Si nanostructured solar cells (Oh et al., 2012) and 18% greater than that of planar 10 µm thick Si cell with anti-reflection coating (Jeong et al., 2013).

Further, at the interface, the holes that are generated at point 1 need to travel the shorter diffusion length, to arrive at *N* – *P*+ junction compared to holes that are generated at point 2 shown in Fig. 1(a). This results in decreased collection probability in region II, therefore, higher recombination rate is observed in region II compared to the region I, as shown in Fig. 2(a) and (b). Region I and region II is defined in *N*-type region only, they do not includes the *P*+ and *N*+ regions. Further, the maximum recombination rate has been observed in *N*+ type and *P*+ type region due to heavy dop-

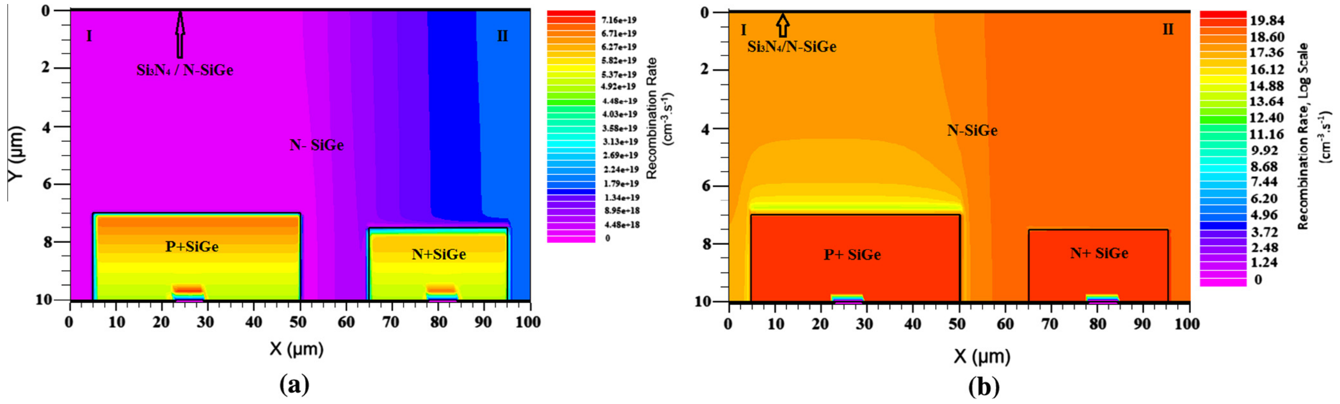

Fig. 2. Recombination rate contour ($cm^{-3}\ s^{-1}$) of illuminated, 10 µm thick RC SiGe solar cell under short circuit condition. Consisting 70 nm thick AR layer on top: (a) linear scale, and (b) log scale.

ing profile. Previous result shows, the recombination rate in region II of the 10 μm thick silicon-based RC solar cells is in the order of $\sim 10^{20}\ \mathrm{cm}^{-3}\ \mathrm{s}^{-1}$ (Pandey and Chaujar, 2015d), whereas in proposed device it is in the order of $\sim 10^{18}\ \mathrm{cm}^{-3}\ \mathrm{s}^{-1}$ shown in Fig. 2, suppressed minority carrier recombination has been observed in proposed device. In the case of back contact design, most of the carriers are generated near the front surface while the junction is far at the back surface. Lower recombination ensures higher carrier collection efficiency in proposed device.

3.2. Impact of front surface passivation on proposed device

In this section, different front surface passivation schemes have been discussed on proposed device i.e. 10 μm RC-RJ SiGe solar cell. The crystalline materials have the discontinuity of the crystal arrangement at the surface, which creates the dangling bond. Further, these dangling bonds at the interface create energy states within the forbidden energy band gap, which acts as a good recombination center. The recombination phenomena that arise from these states are known as Shockley–Read–Hall (SRH) recombination (Aberle et al., 1992). The front surface of most of the solar cell normally consists of well – passivated antireflective coating of thermal SiO_2 or Si_3N_4 layers (Diouf et al., 2010). In another technique, surface passivation is achieved by creating the front surface field using the high level of doping in low doped semiconductors of similar impurity. In this way, *P+*/*P* or *N+*/*N* regions are formed at the interface, which gives rise to an electric field at the junction. The electric field repels desired minority carriers from the interface and reduces the recombination at the surface. However, Auger recombination is increased due to the heavily doped region at the front surface.

Here, thin defect free SiC-based surface passivation scheme has been discussed with proposed device and results are compared with conventional insulators based passivation. The bandgap 2.2 eV has been used for SiC during simulation. Result shows, minority carrier concentration, is drastically reduced at the SiC/*N*-SiGe interface. This type of passivation prevents the minority carrier (holes) to reach the SiC/*N*-SiGe interface. The impact of three different front surface passivation (FSP) schemes has been obtained: single SiO_2 termed as FSP1, Si_3N_4 termed as FSP2, and SiC termed as FSP3.

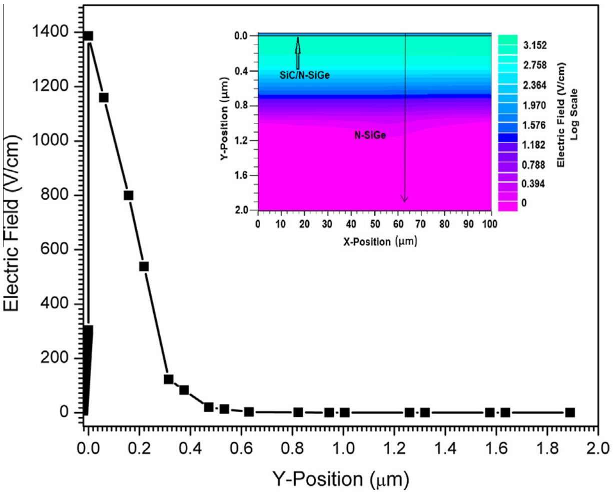

Fig. 3. The distribution of electric field near the (SiC/*N*-SiGe) interface. Inset shows the contour representation of electric field. Data is obtained under illumination with zero-bias voltage.

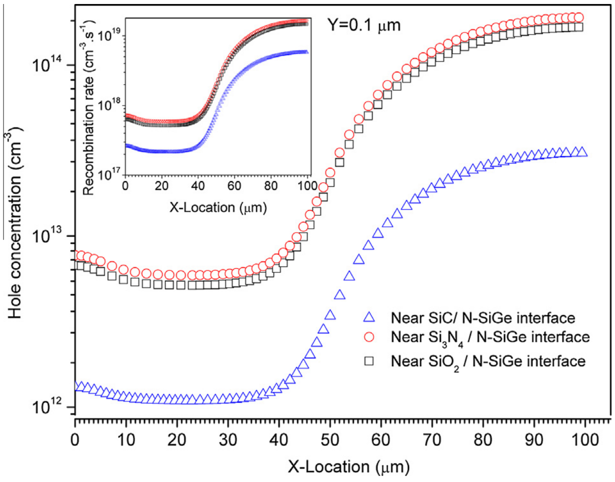

Fig. 4. Hole concentration near the interface of SiC, Si_3N_4 and SiO_2 passivated devices, respectively. Inset shows the recombination rate near the interface of SiC, Si_3N_4 and SiO_2 passivated devices, respectively. Data has been obtained from location (0, 0.1) to (100, 0.1) under illumination with short circuit condition.

Further, some useful parameters are plotted in Figs. 3 and 4, which shows that superior surface passivation has been achieved in the FSP3 layered device. The distribution of electric field near the passivating interface has been presented in Fig. 3. The electric field direction is directed from SiC to SiGe, rendering it energetically unfavourable for hole transport to SiC/*N*-SiGe interface, resulting in a low concentration of holes at the passivating interface. In surface recombination process, an electron from conduction band recombines with the hole in the valence band via a defect level within the bandgap. If the concentration of one comrade electrons or holes is drastically reduced, then recombination rate reduces strongly (Aberle, 2000). Therefore, higher the concentration difference between electron and hole, lower is the recombination. The concentration of electron in the *N*-SiGe region is $\sim 10^{15}\ \mathrm{cm}^{-3}$. Therefore, sinking the hole concertation at the interface will produce higher concentration difference between electrons and holes, and thus results in lower surface recombination rate, as shown in Fig. 4. Results shows, the concentration difference between electron and hole is higher in SiC passivated device compared to SiO_2 and Si_3N_4 devices. Thus, results in lower surface recombination rate, as shown in the inset of Fig. 4. In FSP3 layered device, ten times lower minority carrier concentration is obtained near the interface (SiC/*N*-SiGe), compared to minority carrier concentration in the bulk (*N*-SiGe) region of the device, this shows the presence of SiC reduces the concentration of minority carriers only at the interface. In region II, at the interface, the hole concentration of $\sim 10^{13}\ \mathrm{cm}^{-3}$ has been observed in FSP3 layer device, whereas the concentration of $\sim 10^{14}\ \mathrm{cm}^{-3}$ observed in FSP1 as well as FSP2 layer devices, shown in Fig. 4. The hole concentration as well as recombination rate is low in region I compared to region II, as shown in Figs. 2 and 4. It is a typical distribution in the case of a short-circuiting. Under short-circuit condition, a space charge region is formed around the junction having an associated electric field that collects the generated electron-hole pairs, and the collection is complete in near *P+* region. However, outside the *P+* region, the substrate is neutral, and the collection will be by diffusion of electrons and holes toward the field region where they will be collected and separated. So, the regions nearer to the junction will have lower hole concentration since its holes will diffuse to the collecting field regions. The electrons and holes generated in a region greater than the diffusion length will never reach the junction, and the recombination process will balance them. As there is a lateral hole concentration gradient showing lateral hole flow to the junction. This concentration gradient decreases with the distance from the *P+*—*N* junction region. Furthermore, Fig. 5 shows the contour plot of recombination rate in the devices. At the interface, the

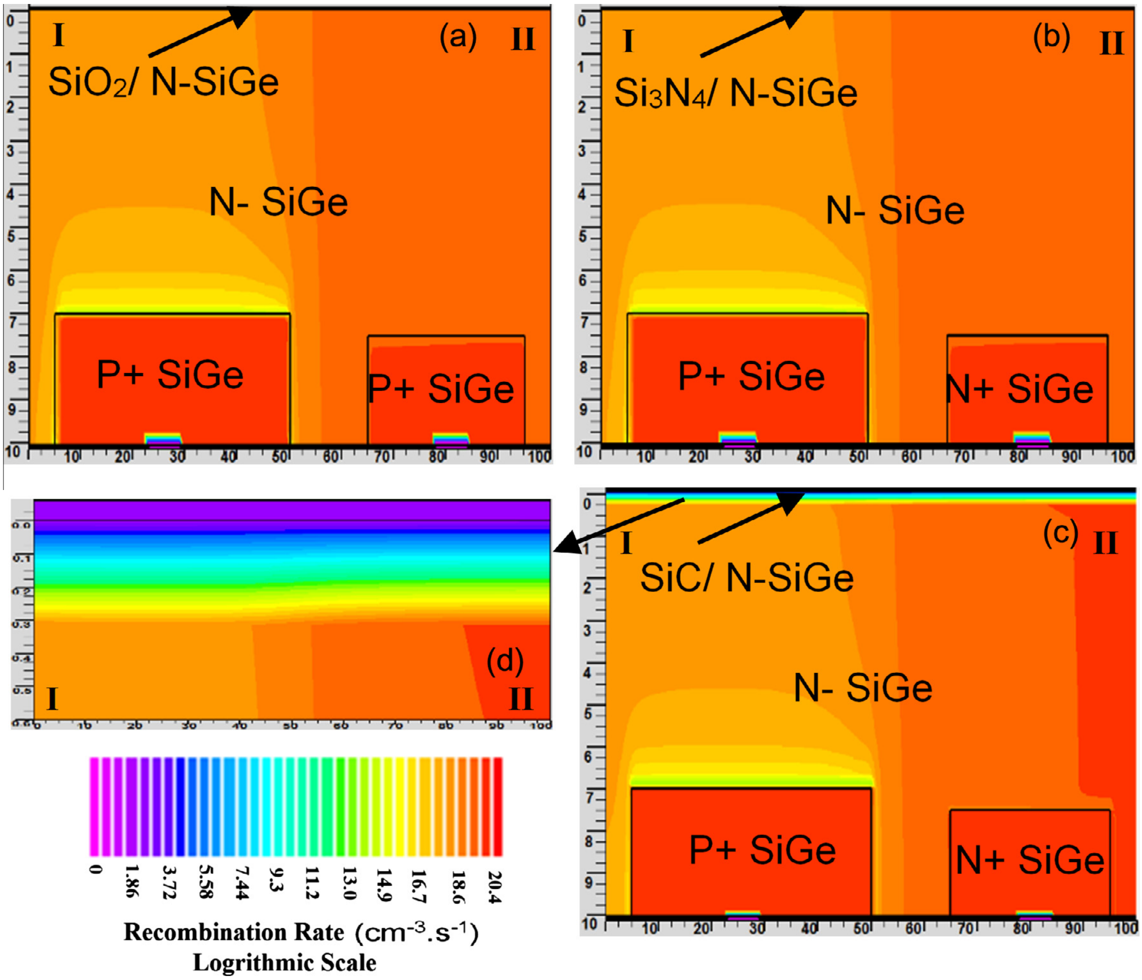

Fig. 5. Contour plot of recombination rate (cm^{-3} s^{-1}) in the log scale, (a) SiO_2 passivated RC-SiGe solar cell, (b) Si_3N_4 passivated RC-SiGe solar cell, (c) SiC passivated RC- SiGe solar cell and (d) Magnified view of (SiC/*N*-SiGe) interface in case of SiC passivated device. Data has been obtained under illumination with zero-bias voltage.

magnitude of recombination rate in the FSP3 layered device is of the order of 10^5–10^{14} cm^{-3} s^{-1} from the location ($Y = 0.05$ to $Y = 0.03$) shown in Fig. 5(c) and (d). Whereas in the FSP1 and FSP2 devices it is around 10^{18}–10^{19} cm^{-3} s^{-1}. This shows SiC layer is much better for surface passivation as compared to conventional SiO_2 or Si_3N_4 layers. Lower recombination ensures that generated carrier will contribute more in external current and recombination current density will be suppressed.

Moreover, the spectrum response has been obtained for SiO_2, Si_3N_4, and SiC passivated devices, respectively. The optical properties of material used in the simulation are shown in Fig. 6(a)–(c) and EQE with different front surface passivation layers are shown in Fig. 6(d). Normally, the blue response of solar cell is reduced due to front surface recombination, whereas the midway response is reduced due to lower diffusion length and the red response is reduced due to transmitted photons and the back surface recombination. Result shows, significant improvement in blue response, as well as midway response, in FSP3 layer device compared to FSP1 and FSP2 layer devices shown in Fig. 6(d). The SiC-based device achieved EQE > 80% in the wavelength range of 300–720 nm. At wavelength equivalent to 550 nm, it shows EQE of the order of 95% that is 25.5% and 10.2% higher than FSP1 and FSP2 layer devices, respectively as shown in Fig. 6(d). Moreover, at smaller wavelength (300 nm) the SiC-based device shows, 35%, and 70% higher EQE compared to Si_3N_4 and SiO_2 based devices, respectively, as shown in Fig. 6(d). The performance of a solar cell is directly related to the amount of light entering the cell. The optical properties i.e. refractive index (n) and extinction coefficient (k) required for an antireflection coating (ARC) of a solar cell depend on the refractive index of the underlying substrate and, if applicable on the encapsulated cover, as well as the operating wavelength of that solar cell, in addition to the absorption of the light in the ARC film for that solar cell. Therefore, to minimise the absorption of the useful light in the ARC, a material having low absorption of useful light is needed. A low k can be equated to a low absorption, α (e.g. a k of less than 0.01 corresponds to the absorption of less than 1%), since $\alpha = 4\pi k/\lambda$. Fig. 6(a) and (c) shows that SiC has n between 2.9 and 2.5 in the spectrum range of 300–1200 nm and k of less than 0.01 for the wavelengths greater than 430 nm. In addition, thin SiO_2 based encapsulation has been assumed at the front surface of the SiC-based device, to minimize the reflectivity (Pandey and Chaujar, 2015a). Also, as per the patented work of (Allen et al., 2009), SiC film having n between 2.7 and 2.3 and k of less than 0.01 at a wavelength of 630 nm is a good candidate for antireflective coating for solar cells. Further, wavelength dependent extinction coefficient and absorption coefficient reported in Fig. 6(c) shows that SiC has higher absorption coefficient at lower wavelengths, whereas it is desired that SiC should be transparent in the simulated spectrum. The absorbance in a material is directly related to the absorption coefficient and thickness of the material used. This suggests that to minimize the absorption and increase the transparency, thinner SiC layer should be used. This phenomenon sets the limit on the thickness of SiC. The SiC layer used in the simulation is only 20 nm thick whose absorbance is

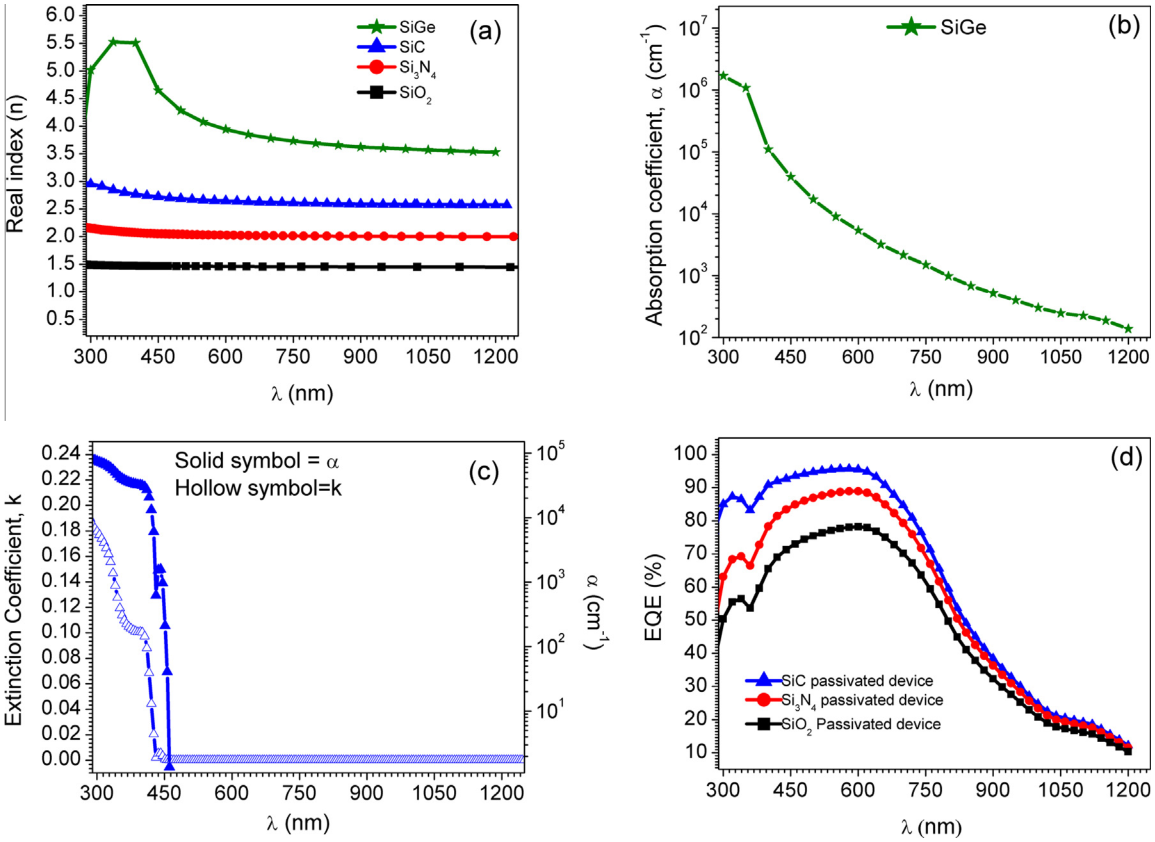

Fig. 6. Optical properties i.e. wavelength dependent (a) real index, n for the materials, (b) absorption coefficients of SiGe, (c) extinction and absorption coefficients of SiC, and (d) EQEs of SiC, Si_3N_4, and SiO_2 passivated RC-SiGe solar cells, respectively.

negligible. However, consequences of using thicker SiC layer has also been discussed. Four SiC-based *N*-type SiGe wafer has been designed with a different thickness of SiC i.e. 20 nm, 40 nm, 80 nm, and 160 nm respectively, and photon absorption rate has been obtained in underlying SiGe wafer as shown in Fig. 7(a)–(d). The contour representation shows that the photon coupling in underlying SiGe is higher for 20 nm thick SiC-based device. However, increasing the thickness results in absorbance in SiC and hence lower optical coupling in underlying SiGe. The 160 nm thick SiC-based SiGe wafer shows worst optical behavior compared to other wafers as shown in Fig. 7. Meanwhile, the photon absorption contour is also obtained for all the devices, and same has been presented in Fig. 8(a)–(f). Results reveal that higher photon absorption rate is achieved in FSP3 layer based device. FSP3 layer device

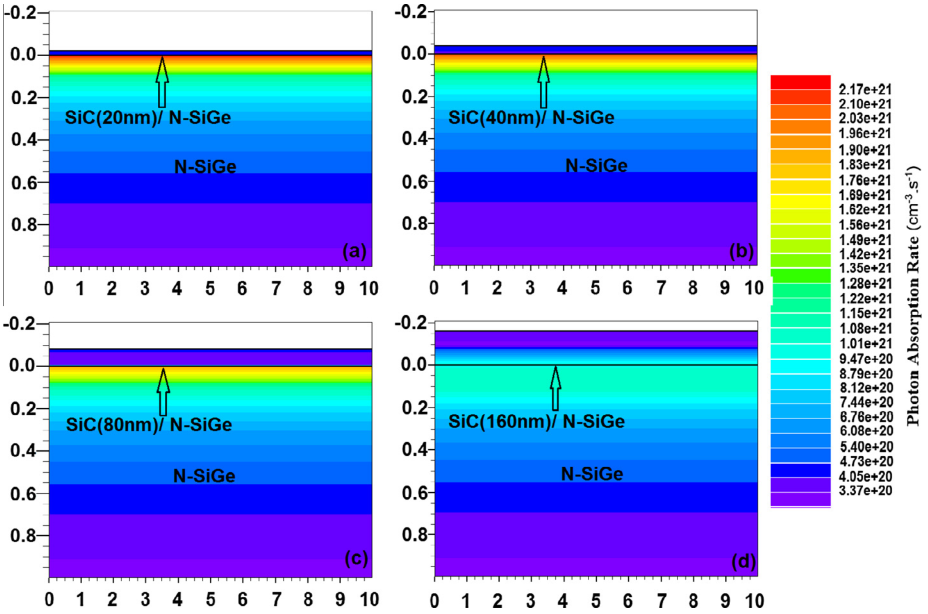

Fig. 7. The contour representation of photon absorption rate ($cm^{-3}\,s^{-1}$) in underlying SiGe with different SiC thicknesses: (a) 20 nm, (b) 40 nm, (c) 80 nm, and (d) 160 nm.

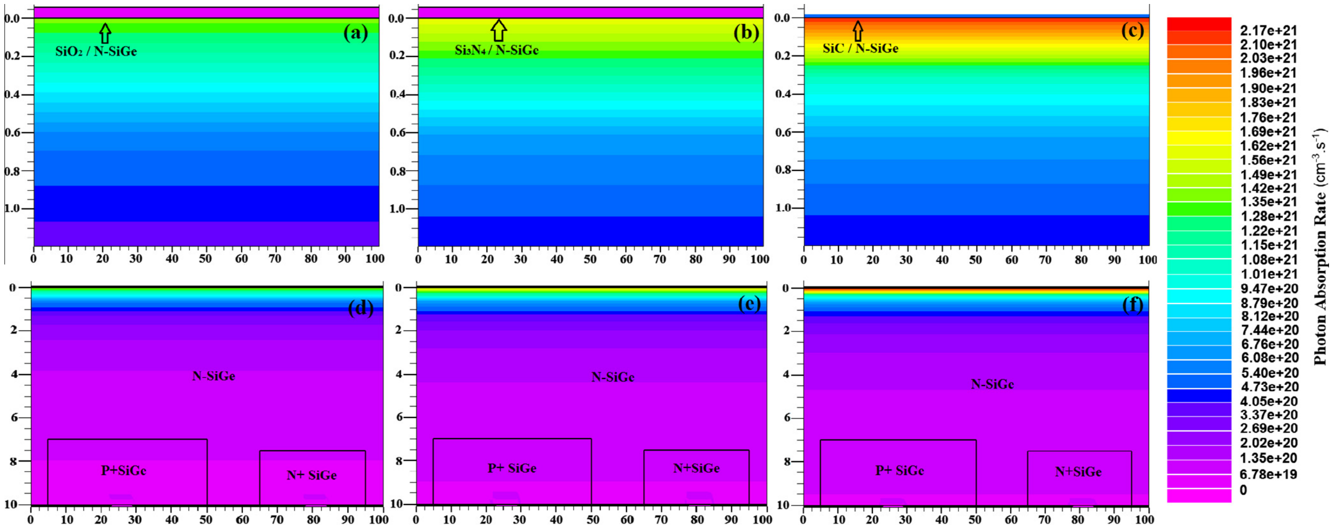

Fig. 8. The contour representation of photon absorption rate ($cm^{-3}\ s^{-1}$) in RC-SiGe solar cell: (a) magnified view near the (SiO_2/N-SiGe) interface in SiO_2 passivated device, (b) magnified view near the (Si_3N_4/N-SiGe) interface in Si_3N_4 passivated device, (c) magnified view near the (SiC/N-SiGe) interface in SiC passivated device, and figure (d–f) show the SiO_2, Si_3N_4, and SiC passivated device on full scale. Data has been obtained under illumination with zero-bias voltage.

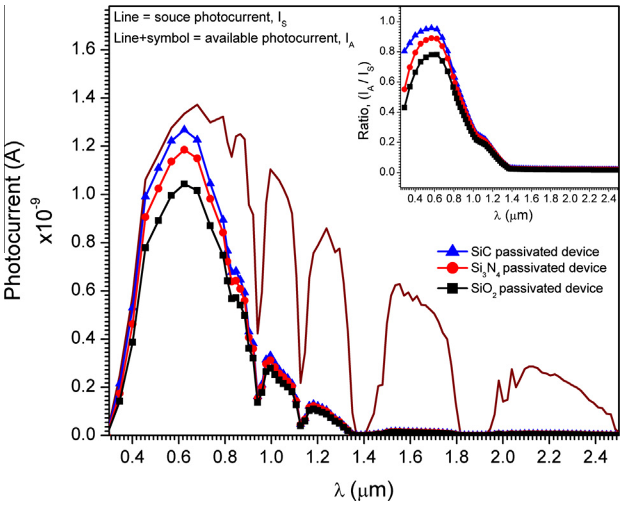

Fig. 9. Comparison of spectrum response under AM1.5 illumination for an RC-SiGe solar cell with SiC, Si_3N_4, and SiO_2 passivation layers, respectively. The inset shows the I_A/I_S ratio for all the three devices.

shows, the 12.5% and 5% higher photon absorption rate compared to FSP1 and FSP2 layer device, respectively as shown in Fig. 8(d)–(f). Also, magnified view of the interfaces shows higher photon absorption rate at the front surface, in SiC-based device, as shown in Fig. 8(a)–(c). This validates the higher optical coupling of photons with lower wavelengths. Further, Fig. 9 shows, the source photocurrent of AM1.5 spectrum, along with the ratio of available photocurrent (I_A) to the source photocurrent (I_S). The improved optical behavior of the SiC-based device results in higher available photocurrent, which further increases the I_A/I_S ratio. Result shows, >80% ratio with a maximum value of 95.7% in the spectrum range of 289–735 nm wavelengths. Thus, reflecting a superior spectrum response of SiC passivated device compared to SiO_2 and Si_3N_4 based devices. Improved optical coupling and better surface passivation, leads to superior EQE in the SiC-based device.

The most important part of the solar cell design is its current–voltage characteristics. Any design must have a higher short-circuit current density (J_{SC}) and a higher open circuit voltage (V_{OC}). The J–V characteristic of the device is simulated with ray tracing algorithm without reflection, under AM1.5 illumination with optical power 0.1 W/cm². Results are presented in Fig. 10 (a) and (b). In Fig. 10(a), the J_{SC} and V_{OC} in FSP3 layer device are 28 mA cm^{-2} and 668 mV, whereas J_{SC}, V_{OC} in FSP1 and FSP2 layer devices are 22.6 mA cm^{-2}, 662 mV and 25.8 mA cm^{-2}, 667 mV respectively. Thus, FSP3 layer device shows 24% and 8% higher J_{SC} compared to FSP1 and FSP2 layer devices, respectively. Also, the higher power density of 14.7 mW/cm² was obtained in FSP3 layer device compared to 11.7 mW/cm² and 13.5 mW/cm² in FSP1 and FSP2 layer devices, respectively. A detailed comparison of electrical parameters is shown in Table 1. Improved photovoltaic properties indicate proposed device with SiC passivation can be used in light-weight, low-cost installation of PV modules. Also, the device has RC architecture it is easier to interconnect and can be placed closer together in the modules, no need of space between cells. Also, Fig. 10(b) shows the comparison of illuminated and dark characteristics of the devices. In Fig. 10(b), the illuminated response shows sharp minima, taking intercept from this point to x-axis gives the V_{OC} of the respective devices.

3.3. Impact of surface recombination velocity (SRV) on the devices

Further, the impact of surface passivating layer is analyzed. The impact of surface recombination velocity on J_{SC} and PCE has been obtained which is presented Fig. 11. At, SRV equivalent to 10^2 cm s^{-1} the difference between available photocurrent and short circuit current is 2.2 mA cm^{-2} in FSP3 layered device whereas the difference of ~7 mA cm^{-2} has been observed in FSP1 and FSP2 layered devices. This shows, 7 mA cm^{-2} is lost because of the recombination and the parasitic absorption in FSP1 & FSP2 layered device, whereas only 2 mA cm^{-2} has been lost in FSP3 layered device. Also, when SRV changes from 10^1 to 10^7 cm s^{-1} the PCE and J_{SC} went down to 12.1% and 23.2 mA cm^{-2}, respectively in FSP3 device, whereas these values are 1.33% and 3.97 mA cm^{-2} and 1.5% and 4.49 mA cm^{-2} in FSP1 and FSP2 devices, respectively. Results reveal that characteristics of the FSP3 device are less affected by surface recombination velocity. Fig. 11 shows, enhanced surface characteristics has been obtained in the FSP3 layered device. Also, result reveals that new surface passivation

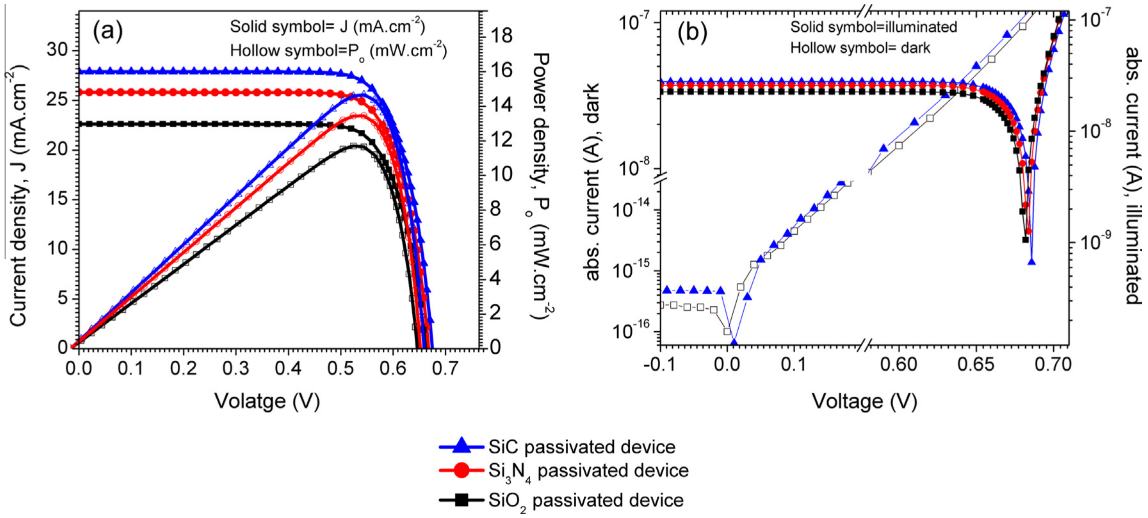

Fig. 10. Electrical characteristics i.e. current density–voltage (*J–V*) curve of RC-SiGe solar cell with different passivation layers. (a) *J–V* curve on primary axis and *P–V* curve on secondary axis, (b) *I–V* (dark and illuminated condition on primary and secondary axis, respectively).

Table 1
Comparisons of photovoltaic parameters of 10 µm thick RC-SiGe solar cell with SiO_2, Si_3N_4 and SiC based passivation layers, respectively.

Device	J_{SC} (mA cm^{-2})	V_{OC} (mV)	FF (%)	PCE (%)
FSP1 layered	22.6	662	78.2	11.7
FSP2 layered	25.8	667	78.0	13.5
FSP3 layered	28.0	668	78.6	14.7

scheme is useful when the surface to volume ratio of the device is a large i.e. thin device. Thin devices suffer from higher surface recombination.

3.4. Impact of diffusion depth of P+ and N+ regions

In this section, the impact of diffusion depth on device characteristics have been obtained. In Fig. 5, the Auger recombination rate in *P*+ and *N*+ region is higher because of the heavily doped region (~10^{20} cm^{-3}) and higher diffusion depth in *Y*-direction. Therefore, the diffusion depth of *P*+ and *N*+ region have been minimized to minimize the auger recombination rate in these regions. The PCE of 15.4% i.e. 4.7% higher than initial value (14.7%) is obtained by minimizing the diffusion depth of the regions. Fig. 12 shows the contour representation of recombination rate of the devices with different diffusion depth. Result reveals, carrier recombination, is reduced by reducing the diffusion depth of *P*+ and *N*+ regions. Further, the impact of depth on device characteristics is presented in Table 2.

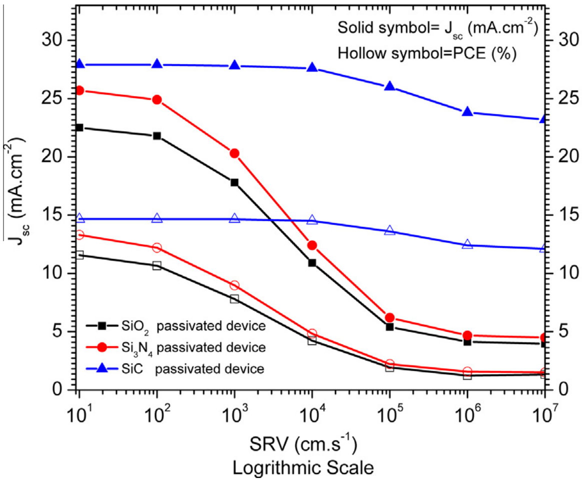

Fig. 11. Impact of surface recombination velocity on RC-SiGe solar cell with different passivation layers. J_{SC} and PCE are presented on primary and secondary axis, respectively.

3.5. Impact of Irradiance and temperature

In this section, we have discussed the application of RC SiGe solar cell for concentrator's photovoltaics (CPV) cell application. Altering the irradiance on a solar cell varies all solar cell parameters, including J_{SC}, V_{OC}, fill factor (FF), PCE, series and shunt resistances. The light intensity on a solar cell is called the number of suns, where one-sun corresponds to standard illumination at AM1.5, or 100 mW/cm^2. The PV module intended to work under one- sun is called a "flat plate" while those using more than one-sun or concentrated sunlight are called "concentrators." Further, concentrators have some advantages in terms of higher efficiency than a one-sun solar cell and the lower cost. The J_{SC} of a solar cell depends linearly on irradiance, this indicates, device operating under 10 Suns would have 10 times the J_{SC} as the same device under one sun operation. However, this will not result in increased PCE, since the incident power also increases linearly. The efficiency benefits arise from the open-circuit voltage, as V_{OC} increases logarithmically with light intensity (Würfe, 2008).

The impact of irradiance and temperature on different devices is obtained, and the results are presented in Fig. 13(a)–(c). The devices are simulated up to 20-suns (2 W/cm^2) condition at room temperature (300 K), since the temperature also increases as a function of input optical power per unit area. Further, cell operating at higher concentration levels requires complex cooling system, and overall cost of the PV module will be increased. Previously, the silicon-based concentrator solar cell with the efficiencies range of (15–27.5)% has been reported for the concentration level of (20–150) suns (Sinton et al., 1986; Cuevas et al., 1990; Lammert and Schwartz, 1977; Wenham and Green, 1995; Zhao et al., 1990). In silicon-based concentrator cells, thickness >100 µm is required to achieve high efficiency. This results in higher $/W. Further, V_{OCs} of 766 mV, 800 mV PCEs of, 18.37%, 19.32% at 10-sun and 20-sun conditions respectively have been

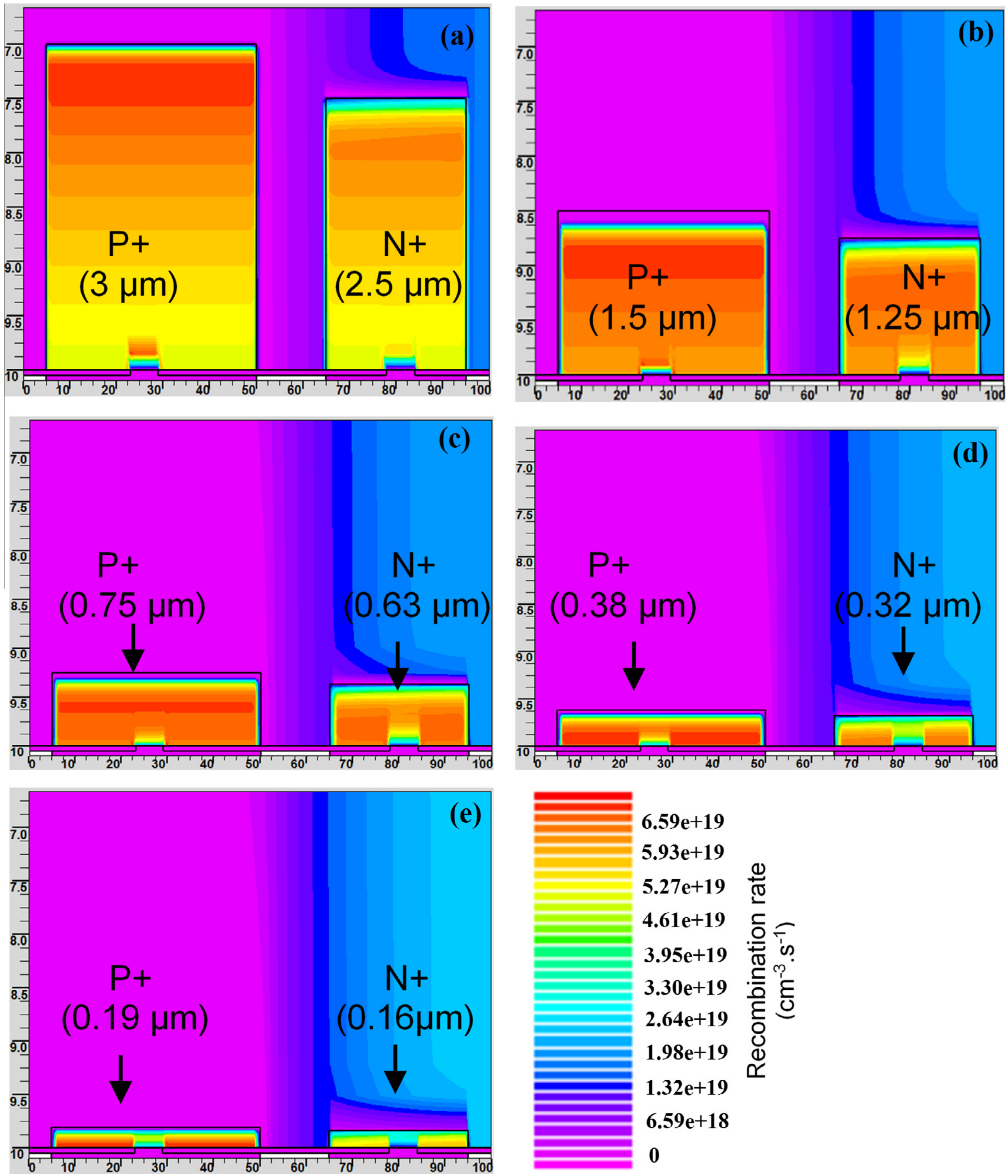

Fig. 12. Recombination rate ($cm^{-3}\,s^{-1}$) contour of SiC passivated RC-SiGe solar cell with different diffusion depth of *P*+ and *N*+ regions. Data has been obtained under illumination with zero-bias voltage.

Table 2
Impact of *N*+ and *P*+ regions diffusion depth on photovoltaic parameters of SiC passivated 10 µm thick RC-SiGe solar cell.

S. No.	Regions	Thickness (µm)	J_{SC} ($mA\,cm^{-2}$)	V_{OC} (mV)	FF (%)	PCE (%)
1	*P*+	3.0	28.0	668	78.6	14.70
	N+	2.5				
2	*P*+	1.5	28.9	666	78.6	15.13
	N+	1.25				
3	*P*+	0.75	29.3	666	78.3	15.30
	N+	0.63				
4	*P*+	0.38	29.5	666	78.3	15.37
	N+	0.32				
5	*P*+	0.19	29.6	667	78.2	15.41
	N+	0.16				

obtained as shown in Fig. 13(a). Also, results show 10.2% and 13.7% higher PCE at the concentration levels of 4, 6 suns compared to 1-sun condition. Further, the desired concentration level can be selected from Fig. 13(a) depending upon the applications. Furthermore, the impact of temperature on device parameters: V_{OC}, PCE and FF for three different conditions (1-sun, 10-suns, 20-suns) has been analyzed. Since, under concentrated light device temperature increases. Although, it can be avoided by using a suitable cooling system (Royne et al., 2005). Fig. 13(b) and (c), shows that device performance degrades as the temperature increases since intrinsic carrier concentrations increase at higher temperatures. Therefore, bandgap decreases, which further results in decrease V_{OC}, as shown in Fig. 13(b). The V_{OC} values 804 mV, 778 mV,

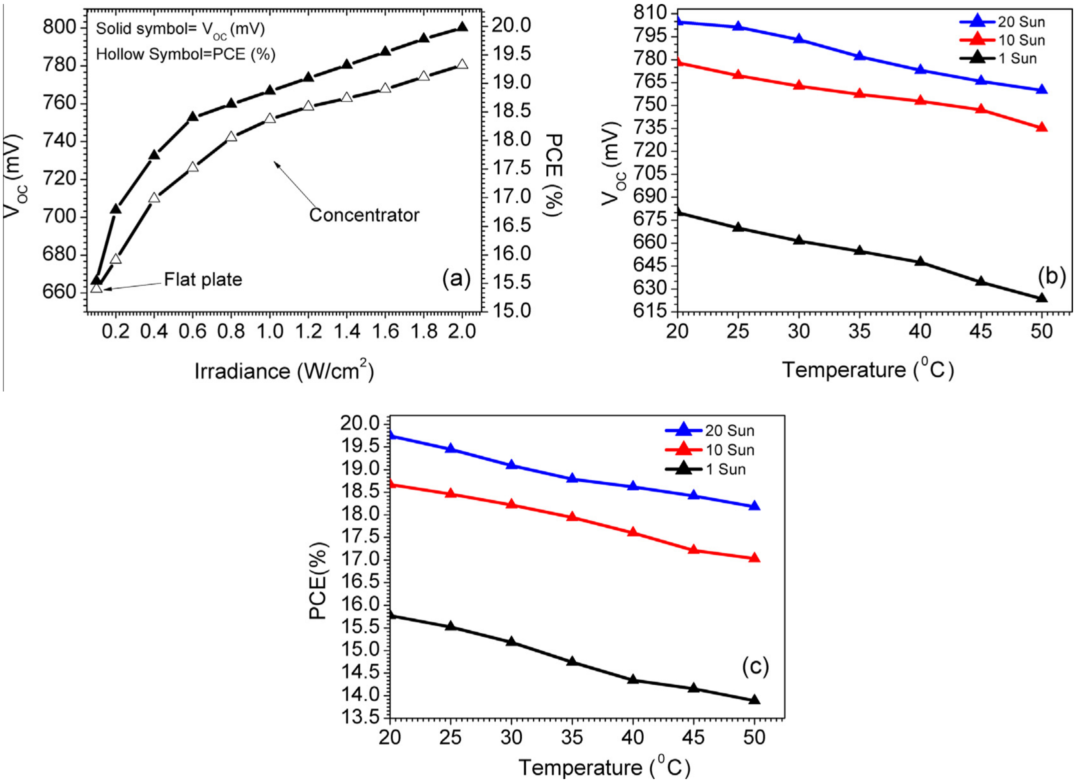

Fig. 13. Impact of irradiance and temperature on SiC passivated RC-SiGe solar cell: (a) effect of irradiance on V_{OC} and PCE, (b) effect of temperature on V_{OC} for 1 sun, 10 suns and 20 suns condition, respectively, (c) effect of temperature on PCE for 1 sun, 10 suns and 20 suns condition, respectively.

680 mV and PCE values of 19.75%, 18.67%, 15.77% is obtained at 20 °C for 20-sun, 10-sun and 1-sun conditions respectively, whereas V_{OC} values 760 mV, 735 mV, 623 mV and PCE values of 18.2%, 17%, 13.9% is obtained at 50 °C. Results show, as the temperature increases from 20 °C to 45 °C, 10.2% decrease in PCE is obtained for flat plate cell, whereas 7.8% and 6.7% decrease in PCE is obtained for the same cell operating at 10-suns and 20-suns, as shown in Fig. 13(c). Further, all the results of this section conclude that highest PCE of 19.3% is obtained at 20-suns in the sub 10 μm thick device with the cost effective material. This suggests that the proposed device can be a cost-effective candidate for the flat plate as well as low concentrator applications.

4. Conclusion

In the present work, RC SiGe solar cell with SiC-based front surface passivation has been proposed, which shows enhanced photovoltaic properties. EQE > 90% in the wavelength range of 400–650 nm has been achieved. Also, at wavelengths equivalent to 300 nm, SiC passivated device shows record EQE of 85%. The presence of SiC as a surface passivating layer shows enhanced surface characteristics. At the (SiC/*N*-SiGe) interface, the barrier height of 1.1 eV has been achieved for minority carrier (Holes) in SiC passivated device this suppresses the surface recombination. The power conversion efficiency (PCE) of 15.4% has been achieved, and the device is less affected by SRV. Further, discussed device has RC architecture it is useful in high current cells such as CPV or large areas. Therefore, device performance for concentrator application has also been discussed. We obtained 19.3% PCE at 2 W/cm^2 (20 suns, 27 °C) in 10 μm regime. This suggests, proposed device can be an energy efficient candidate for the flat plate as well as low concentrator applications. The simulation work achieved here shows that if fabricated experimentally it can prove to be a cost-effective solution for energy efficient applications. In future, thin defect free SiC-based passivation scheme can be used in nanostructured based thin devices. This can tackle the problem like auger and surface recombination by stacking a thin layer of SiC between nanostructures and the front surface of the cell.

Acknowledgements

The authors would like to thank Microelectronics Research Lab, Department of Engineering Physics, Delhi Technological University to carry out this work. Rahul Pandey (JRF) acknowledge UGC, Govt. of India for providing fellowship.

References

Aberle, A.G., Glunz, S., Warta, W., 1992. Impact of illumination level and oxide parameters on Shockley–Read–Hall recombination at the Si–SiO$_2$ interface. J. Appl. Phys. 71 (9), 4422 (accessed October 15, 2015) <http://scitation.aip.org/content/aip/journal/jap/71/9/10.1063/1.350782>.

Aberle, A.G., 2000. Surface passivation of crystalline silicon solar cells: a review. Prog. Photovoltaics Res. Appl. 8 (5), 473–487. http://dx.doi.org/10.1002/1099-159X(200009/10)8:5<473::AID-PIP337>3.0.CO;2-D.

Allen, S., Awad, Y., Gaumond, A., & Davies, M., 2009. U.S. Patent Application No. 12/994,973.

Atlas user manual, 2014. Silvaco, Inc. Santa Clara. pp. 481.

Ceuster, D.D., Cousins, P., Rose, D., Vicente, D., Tipones, P., Mulligam, W., 2007. Low cost, high volume production of >22% efficiency silicon solar cells. In: Proceedings of the 22nd European Photovoltaic Solar Energy Conference, pp. 816–819.

Cruz-Campa, J.L. et al., 2011. Microsystems enabled photovoltaics: 14.9% efficient 14 μm thick crystalline silicon solar cell. Sol. Energy Mater. Sol. Cells 95 (2), 551–558. http://dx.doi.org/10.1016/j.solmat.2010.09.015.

Cuevas, A. et al., 1990. 26-percent efficient point-junction concentrator solar cells with a front metal grid. IEEE Electron Device Lett. 11 (1), 6–8, <http://ieeexplore.ieee.org/lpdocs/epic03/wrapper.htm?arnumber=46913> (accessed October 15, 2015).

Deinega, A., Eyderman, S., John, S., 2013. Coupled optical and electrical modeling of solar cell based on conical pore silicon photonic crystals. J. Appl. Phys. 113 (22), 224501 (accessed October 15, 2015) <http://scitation.aip.org/content/aip/journal/jap/113/22/10.1063/1.4809982>.

Diouf, D. et al., 2009. Study of interdigitated back contact silicon heterojunctions solar cells by two-dimensional numerical simulations. Mater. Sci. Eng. B: Solid-State Mater. Adv. Technol. 159–160 (C), 291–294.

Diouf, D. et al., 2010. Effects of the front surface field in *n*-type interdigitated back contact silicon heterojunctions solar cells. Energy Procedia 2 (1), 59–64. http://dx.doi.org/10.1016/j.egypro.2010.07.011.

Dziewior, J., Schmid, W., 1977. Auger coefficients for highly doped and highly excited silicon. Appl. Phys. Lett. 31 (5), 346 (accessed October 15, 2015) <http://scitation.aip.org/content/aip/journal/apl/31/5/10.1063/1.89694>.

Feldmann, F. et al., 2014. Passivated rear contacts for high-efficiency *n*-type Si solar cells providing high interface passivation quality and excellent transport characteristics. Sol. Energy Mater. Sol. Cells 120 (PART A), 270–274.

Franklin, E. et al., 2014. Design, fabrication and characterisation of a 24.4% efficient interdigitated back contact solar cell. Progr. Photovolt.: Res. Appl. http://dx.doi.org/10.1002/pip.2556, pp. n/a–n/a. (accessed October 10, 2015).

Green, M.A., Keevers, M.J., 1995. Optical properties of intrinsic silicon at 300 K. Prog. Photovoltaics Res. Appl. 3 (3), 189–192. http://dx.doi.org/10.1002/pip.4670030303 (accessed December 7, 2015).

Green, M.A., 2003. Third Generation Photovoltaics – Advanced Solar Energy. Springer. <http://www.springer.com/jp/book/9783540401377> (accessed March 2, 2016).

Green, M.A., 2008. Self-consistent optical parameters of intrinsic silicon at 300 K including temperature coefficients. Sol. Energy Mater. Sol. Cells 92 (11), 1305–1310 (accessed December 19, 2015) <http://www.sciencedirect.com/science/article/pii/S0927024808002158>.

Glunz, S.W. et al., 1999. Comparison of boron- and gallium-doped *p*-type Czochralski silicon for photovoltaic application. Prog. Photovoltaics Res. Appl. 7 (6), 463–469. http://dx.doi.org/10.1002/%28SICI%291099-159X%28199911/12%297%3A6%3C463%3A%3AAID-PIP293%3E3.0.CO%3B2-H (accessed October 15, 2015).

Hall, R., 1952. Electron-hole recombination in Germanium. Phys. Rev. 87 (2), 387. http://dx.doi.org/10.1103/PhysRev.87.387 (accessed December 28, 2014).

He, J. et al., 2015. Realization of 13.6% efficiency on 20 μm Thick Si/Organic hybrid heterojunction solar cells via advanced nanotexturing and surface recombination suppression. ACS Nano 9 (6), 6522–6531. http://dx.doi.org/10.1021/acsnano.5b02432 (accessed February 25, 2016).

Ingenito, A., Isabella, O., Zeman, M., 2015. Nano-cones on micro-pyramids: modulated surface textures for maximal spectral response and high-efficiency solar cells. Prog. Photovoltaics Res. Appl. 20 (1), 6. http://dx.doi.org/10.1002/pip.1160, http://dx.doi.org/10.1002/pip.2606.

Jeong, S., McGehee, M.D., Cui, Y., 2013. All-back-contact ultra-thin silicon nanocone solar cells with 13.7% power conversion efficiency. Nature Commun. 4 (May), 2950 <http://www.ncbi.nlm.nih.gov/pubmed/24335845>.

Kasap, S., Capper, P. (Eds.), 2007. Springer Handbook of Electronic and Photonic Materials. Springer US, Boston, MA, pp. 481–498 (accessed February 26, 2016) <http://www.springerlink.com/index/10.1007/978-0-387-29185-7>.

Kerschaver, E.Van., Beaucarne, G., 2006. Back-contact solar cells: a review. Prog. Photovoltaics Res. Appl. 14 (2), 107–123. http://dx.doi.org/10.1002/pip.657 (accessed October 14, 2015).

Lammert, M.D., Schwartz, R.J., 1977. The interdigitated back contact solar cell: a silicon solar cell for use in concentrated sunlight. IEEE Trans. Electron Dev. 24 (4), 337–342, <http://ieeexplore.ieee.org/lpdocs/epic03/wrapper.htm?arnumber=1478930> (accessed October 15, 2015).

NSM Archive – Silicon Germanium (SiGe), 2016a. <http://www.ioffe.rssi.ru/SVA/NSM/Semicond/SiGe/> (accessed February 26, 2016).

NSM Archive – Silicon Germanium (SiGe) – Optical Properties, 2016b. <http://www.ioffe.ru/SVA/NSM/Semicond/SiGe/optic.html> (accessed February 26, 2016).

Oh, J., Yuan, H.-C., Branz, H.M., 2012. An 18.2%-efficient black-silicon solar cell achieved through control of carrier recombination in nanostructures. Nat. Nanotechnol. 7 (11), 743–748. http://dx.doi.org/10.1038/nnano.2012.166 (accessed February 26, 2016).

Ouellette, J., 2002. Silicon-germanium gives semiconductors the edge. Indust. Phys. 8 (3), 22–25.

Pandey, R., Chaujar, R., 2015a. Novel back-contact back-junction SiGe (BC-BJ SiGe) solar cell for improved power conversion efficiency. Microsyst. Technol., 1–8 http://dx.doi.org/10.1007/s00542-015-2552-1 [accessed October 15, 2015) <http://www.researchgate.net/publication/275660629_Novel_back-contact_back-junction_SiGe_(BC-BJ_SiGe)_solar_cell_for_improved_power_conversion_efficiency>.

Pandey, R., Chaujar, R., 2015b. Front Surface Passivation Scheme for Back-Contact Back-Junction (BC-BJ) Silicon Solar Cell. Adv. Sci. Lett., in press.

Pandey, R., Chaujar, R., 2015c. Novel SiC encapsulated coaxial silicon nanowire solar cell for optimal photovoltaic performance. In: 2015 IEEE 42nd Photovoltaic Specialist Conference (PVSC). IEEE, pp. 1–5, <http://ieeexplore.ieee.org/lpdocs/epic03/wrapper.htm?arnumber=7355933> (accessed January 6, 2016).

Pandey, R., Chaujar, R., 2015d. TCAD Analysis of Silicon-Germanium (SiGe) based Back-Contact Back-Junction (BC-BJ) solar cell as an alternative for silicon based cells. In: TechConnectWorld Innovation Conference and Expo, June 14–17, 2015 Washington, DC, USA, pp. 199–202. http://dx.doi.org/10.13140/RG.2.1.1008.6246.

Pandey, R., Chaujar, R., 2015e. Rear contact solar cell with ZrO_2 nano structured front surface for efficient light trapping and enhanced surface passivation. In: 2015 IEEE 42nd Photovoltaic Specialist Conference (PVSC). IEEE, pp. 1–5 (accessed February 4, 2016) <http://ieeexplore.ieee.org/lpdocs/epic03/wrapper.htm?arnumber=7356322>.

Povolny, H. et al., 2011. Comparison study of a-SiGe solar cells and materials deposited using different hydrogen dilution. MRS Proceed. 609, A30.3 (accessed October 15, 2015) <http://journals.cambridge.org/abstract_S1946427400605596>.

Royne, A., Dey, C., Mills, D., 2005. Cooling of photovoltaic cells under concentrated illumination: a critical review. Sol. Energy Mater. Sol. Cells 86 (4), 451–483 (accessed January 12, 2015) <http://www.researchgate.net/publication/223267048_Cooling_of_photovoltaic_cells_under_concentrated_illumination_A_critical_review>.

Savin, H. et al., 2015. Black silicon solar cells with interdigitated back-contacts achieve 22.1% efficiency. Nat. Nanotechnol. 10 (May), 1–6 <http://www.ncbi.nlm.nih.gov/pubmed/25984832>.

Schwartz, R.J., Lammert, M.D., 1975. Silicon solar cells for high concentration applications. In: 1975 International Electron Devices Meeting. IRE, pp. 350–352, <http://ieeexplore.ieee.org/lpdocs/epic03/wrapper.htm?arnumber=1478257> (accessed October 15, 2015).

Selberherr, S., 2012. Analysis and Simulation of Semiconductor Devices. Springer Science & Business Media.

Sinton, R.A. et al., 1986. 27.5-Percent Silicon Concentrator Solar Cells. IEEE Electron Device Lett. 7 (10), 567–569.

Sinton et al., 1998. Development efforts in silicon backside-contact solar cells. In: Eighth E.C. Photovoltaic Solar Energy Conference, vol. 2, pp. 1472–1476.

Sinton, R.A., Swanson, R.M., 1990. Simplified backside-contact solar cells. IEEE Trans. Electron Dev. 37 (2), 348–352, <http://ieeexplore.ieee.org/lpdocs/epic03/wrapper.htm?arnumber=46364> (accessed October 15, 2015).

Sinton, R.A. et al., 1993. Large-area 21% efficient Si solar cells. In: Conference Record of the Twenty Third IEEE Photovoltaic Specialists Conference - 1993 (Cat. No. 93CH3283-9). IEEE, pp. 157–161, <http://ieeexplore.ieee.org/lpdocs/epic03/wrapper.htm?arnumber=347061> (accessed October 15, 2015).

Shockley, W., Read, W., 1952. Statistics of the recombinations of holes and electrons. Phys. Rev. 87 (5), 835–842. http://dx.doi.org/10.1103/PhysRev.87.835 (accessed July 9, 2014).

Slotboom, J.W., 1977. The pn-product in silicon. Solid-State Electron. 20 (4), 279–283 (accessed August 31, 2015) <http://www.sciencedirect.com/science/article/pii/0038110177901083>.

Slotboom, J.W., de Graaff, H.C., 1977. Bandgap narrowing in silicon bipolar transistors. IEEE Trans. Electron Dev. 24 (8), 1123–1125, <http://ieeexplore.ieee.org/lpdocs/epic03/wrapper.htm?arnumber=1479081> (accessed October 15, 2015).

Tjahjono, B.S., Cotter, J.E., 2005. 19.2% efficiency *n*-type laser-grooved silicon solar cells. In: Conference Record of the Thirty-first IEEE Photovoltaic Specialists Conference, 2005. IEEE, pp. 983–986, <http://ieeexplore.ieee.org/lpdocs/epic03/wrapper.htm?arnumber=1488297> (accessed October 15, 2015).

Wang, C.C. et al., 2012. Characterization of nanocrystalline SiGe thin film solar cell with double graded-dead absorption layer. Int. J. Photoen. 2012 (1).

Wenham, S., Green, M.A., 1995. Large area, concentrator buried contact solar cells. IEEE Trans. Electron Dev. 42 (1), 144–149, <http://ieeexplore.ieee.org/lpdocs/epic03/wrapper.htm?arnumber=370024> (accessed October 15, 2015).

Würfe, 2008. Physics of Solar Cells: From Principles to New Concepts - Wiley Online Library <http://onlinelibrary.wiley.com/book/10.1002/9783527618545> (accessed February 26, 2016).

Yang, D. et al., 2010. Germanium-doped crystal silicon for solar cells. In: 2010 10th IEEE International Conference on Solid-State and Integrated Circuit Technology. IEEE, p. 1994, <http://ieeexplore.ieee.org/lpdocs/epic03/wrapper.htm?arnumber=5667855> (accessed October 15, 2015).

Zhao, J., Wang, A., Green, M.A., 1990. 24% efficient PERL structure silicon solar cells. In: IEEE Conference on Photovoltaic Specialists. IEEE, pp. 333–335, <http://ieeexplore.ieee.org/lpdocs/epic03/wrapper.htm?arnumber=111642> (accessed October 15, 2015).

Superlattices and Microstructures 100 (2016) 656–666

Contents lists available at ScienceDirect

Superlattices and Microstructures

journal homepage: www.elsevier.com/locate/superlattices

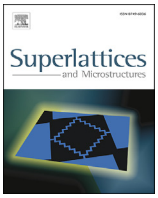

Numerical simulations: Toward the design of 27.6% efficient four-terminal semi-transparent perovskite/SiC passivated rear contact silicon tandem solar cell

Rahul Pandey, Rishu Chaujar*

Department of Engineering Physics, Delhi Technological University, Shahbad Daulatpur, Main Bawana Road, New Delhi, 110042, India

ARTICLE INFO

Article history:
Received 6 October 2016
Accepted 12 October 2016
Available online 14 October 2016

Keywords:
Perovskite
Organic-inorganic halide
Silicon
Simulation
Solar cell
Tandem

ABSTRACT

In this work, a novel four-terminal perovskite/SiC-based rear contact silicon tandem solar cell device has been proposed and simulated to achieve 27.6% power conversion efficiency (PCE) under single AM1.5 illumination. 20.9% efficient semitransparent perovskite top subcell has been used for perovskite/silicon tandem architecture. The tandem structure of perovskite-silicon solar cells is a promising method to achieve efficient solar energy conversion at low cost. In the four-terminal tandem configuration, the cells are connected independently and hence avoids the need for current matching between top and bottom subcell, thus giving greater design flexibility. The simulation analysis shows, PCE of 27.6% and 22.4% with 300 μm and 10 μm thick rear contact Si bottom subcell, respectively. This is a substantial improvement comparing to transparent perovskite solar cell and c-Si solar cell operated individually. The impact of perovskite layer thickness, monomolecular, bimolecular, and trimolecular recombination have also been obtained on the performance of perovskite top subcell. Reported PCEs of 27.6% and 22.4% are 1.25 times and 1.42 times higher as compared to experimentally available efficiencies of 22.1% and 15.7% in 300 μm and 10 μm thick stand-alone silicon solar cell devices, respectively. The presence of SiC significantly suppressed the interface recombination in bottom silicon subcell. Detailed realistic technology computer aided design (TCAD) analysis has been performed to predict the behaviour of the device.

1. Introduction

Refining the performance of the photovoltaic (PV) device is crucial to surge their competitiveness with a conventional source of electricity. Crystalline silicon solar cell have dominated the PV market for decades, with 90% current market share. The efficiency of the crystalline silicon solar cell has only marginally improved during the last 15 years, wafer size efficiency as high as 25.6% has been reported, which is close to the theoretical maximum efficiency of 29.4% [1,2]. However, to make photovoltaic fully competitive with the conventional energy source, further cost effective energy efficient module is required. Therefore, to obtain the higher efficiency at lower cost Si-based tandem approaches have been proposed, which combine a silicon cell with a low-cost cell with wide-bandgap (1.6–1.9 eV) absorber material to form a tandem cell. Commonly, III-V

---

* Corresponding author.
E-mail address: Rishu.phy@dce.edu (R. Chaujar).

http://dx.doi.org/10.1016/j.spmi.2016.10.033
0749-6036/

semiconductors have been used on the top of silicon to make a tandem cell; however, their large area production is costly and challenging [3]. The emergence of organic-inorganic halide perovskite solar cell drastically changes the situation. The methylammonium-lead-halide, $CH_3NH_3PbX_3$ (X = Br, I) perovskite has a tunable band gap, ranging from 1.6 to 2.3 eV depending on halide composition. The solar cell based on organometal halides represents an emerging photovoltaic (PV) technology. Optical absorption of methylammonium-lead-halide on nanocrystalline TiO_2 surface produces the power conversion efficiency of 3–4%, in a liquid based dye-sensitized solar cell (DSSC), as first discovered in 2009. Further by optimizing the perovskite coating condition the PCE has been doubled after 2 years. However, owing to stability issue liquid based perovskite receives little attention. In 2012, a long-term stable perovskite solar cell was developed with PCE of 10%, by substituting the solid hole conductor with liquid electrolytes. The outstanding improvement in PCE achieved in the past few years suggest that it is a capable candidate for the next-generation PV technology [4]. In the year 2015, the certified efficiency has reached 20.1% [5]. Recently, record PCEs of 20.8% and 21.1% have been achieved in perovskite solar cells [6,7]. Further, in tandem based approach, 13.7% efficient 2-terminal perovskite/silicon multijunction solar cell enabled by a silicon tunnel junction has been reported [8]. Moreover, 21.2% and 19.2% efficient monolithic perovskite/silicon tandem solar cell with a cell of 0.17 cm^2 and 1.22 cm^2 respectively, have been proposed in the literature [9] and previous research work shows perovskite-based cell is a good candidate to be used in tandem configuration with silicon cell to produce an efficient cell under illumination. Moreover, this work proposes a new 4-terminal perovskite/silicon-based tandem device for energy efficient applications. The $CH_3NH_3PbI_3$ based perovskite solar cell has been used for the top subcell, and SiC passivated all back contact Si solar cell has been used for the bottom subcell. The SiC has been used to prevent the interface recombination in silicon-based bottom subcell. Tandem device investigated in this work achieves PCE of 27.6% with 300 μm thick Si subcell and PCE of 22.4% with 10 μm thick Si subcell which is 1.25 times and 1.42 times higher as compared to experimentally available efficiencies of 22.1% and 15.7% in 300 μm and 10 μm thick stand-alone silicon solar cell devices, respectively [10,11].

2. Device structure, models, and methods

The carrier dynamics in perovskite device can be quantitatively described by the following equation according to different recombination mechanisms:

$$\frac{dn(t)}{dt} = -Cn^3 - Bn^2 - An \tag{1}$$

Where n (t) is the charge carrier density and A, B and C denotes the monomolecular, bimolecular and trimolecular recombination rate constants. Literature reports, monomolecular, bimolecular, and trimolecular recombination rate constant as SRH recombination, radiative recombination, and auger recombination coefficients, respectively [12]. With the rapid progress in perovskite-based solar cell device performance, critical studies i.e. device simulation considering the impact of the various recombination mechanisms on photovoltaic device parameters are lagging. In present work, technological computer aided design (TCAD) analysis has been done with the help of Silvaco ATLAS device simulator to study the performance of $CH_3NH_3PbI_3$ based perovskite solar cell. The parameters for each model have been calibrated according to experimentally

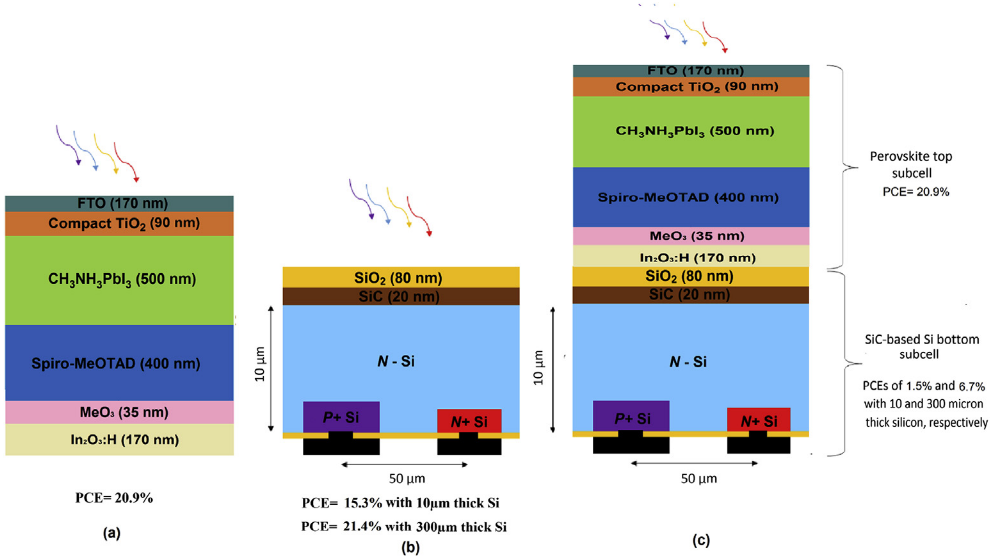

Fig. 1. The device structures used in simulation: (a) perovskite top subcell with indium oxide (In_2O_3: H) as transparent rear electrode, (b) SiC-based silicon bottom subcell and (c) mechanically stacked perovskite/silicon tandem cell.

available data as reported in Refs. [12,13]. This results in 20.9% efficient perovskite solar cell. Fig. 1(a–c) shows the simulated device structure. Fluorine doped tin oxide has been used as a front contact for perovskite solar cell. The Compact TiO_2 is *N*-type, with doping density of 5×10^{19} cm^{-3}, whereas $CH_3NH_3PbI_3$ and Spiro-MeOTAD are *P*-type with doping density of 2.14×10^{17} cm^{-3} and 3×10^{18} cm^{-3} respectively. In a four-terminal configuration, the perovskite top subcell requires two transparent contacts. Therefore, hydrogenated indium oxide (In_2O_3: H) based rear transparent electrode has been used for perovskite solar cell as reported in Ref. [14]. For bottom silicon subcell, dimensions (46 μm-wide *P*+, and 30-μm-wide *N*+) was used. The substrate was *N*-type, with doping density (3×10^{15} cm^{-3}). *P*+ region was doped with boron (4×10^{20} cm^{-3}, depth of 300 nm). *N*+ region was doped with phosphorous (1×10^{20} cm^{-3}, depth of 100 nm). The Poisson equation (2) is solved along with electron and hole continuity equations (3) and (4) to obtain the current density-voltage (J-V) curve. The last term in equations (3) and (4) known as recombination term R_n, R_p

$$\frac{d}{dx}\left(-\varepsilon(x)\frac{d\Psi}{dx}\right) = -q\begin{bmatrix} n(x)-p(x)+N_a^-(x)-N_d^+(x)+ \\ n_t(x)-p_t(x) \end{bmatrix} \tag{2}$$

$$\frac{dn_p}{dt} = D_n\frac{d^2n_p}{dx^2} + n_p\mu_n\frac{d\xi}{dx} + \mu_n\xi\frac{dn_p}{dx} + G_n - \frac{n_p-n_{p0}}{\tau_n} \tag{3}$$

$$\frac{dp_n}{dt} = D_p\frac{d^2p_n}{dx^2} - p_n\mu_p\frac{d\xi}{dx} - \mu_p\xi\frac{dp_n}{dx} + G_p - \frac{p_n-p_{n0}}{\tau_p} \tag{4}$$

Where q the electron charge, D the diffusion coefficient, ε is the permittivity and G the generation rate. The n_s, n_tp_s andp_t are the free electron, trapped electron, free hole, and trapped hole, respectively. ψ is the electrostatic potential. N_a^- the ionized acceptor-like doping concentration and N_d^+ are the ionized donor-like doping concentration. ξ is the electric field and τ_n, τ_p are the carrier lifetimes. Further, when models are enabled, the SRH, auger, and radiative recombination rate are included in the recombination terms in the carrier continuity equations (3) and (4). Perovskite cell is simulated, based on the recombination dynamics in $CH_3NH_3PbI_3$ with the help of SRH, Auger, and radiative recombination models to account monomolecular, bimolecular and trimolecular recombinations in the perovskite top subcell. Whereas concentration dependent SRH, Auger, concentration dependent mobility, and bandgap narrowing models have been used for the bottom silicon solar cell [15]. The radiative recombination model is omitted for silicon solar cell since it is an indirect bandgap semiconductor. The input parameters for perovskite cell used in simulation has been obtained from already published results [16] and shown in Table 1. The optical properties of all the materials used in the simulation are shown in Fig. 2(a–f).

2.1. Recombination models

2.1.1. Shockley-Read-Hall (SRH) recombination

The basic SRH recombination is modeled as follows:

$$R_{SRH} = \frac{pn - n_{ie}^2}{\tau_{n0}\left[p + n_{ie}\exp\left(\frac{E_i-E_t}{k_bT}\right)\right] + \tau_{p0}\left[n + n_{ie}\exp\left(\frac{E_t-E_i}{k_bT}\right)\right]} \tag{5}$$

Table 1
Material parameters used in simulation.

Material		Compact TiO_2	$CH_3NH_3PbI_3$	Spiro-MeOTAD	Silicon	SiC
Dielectric Constant		100	30	3	11.8	9.72
Band Gap (eV)		3.2	1.5	2.91	1.12	2.2
Electron Affinity (eV)		4	3.93	2.2	4.17	4.2
Thickness (μm)		0.09	0.5	0.4	10, 300	0.02
Electron, Hole mobility (cm2/V·s)		0.006, 0.006	50, 50	0.0001, 0.0001	1417, 470	1000, 50
Effective conduction band (DOS) (cm^{-3})		1×10^{21}	2.5×10^{20}	2.5×10^{20}	2.76×10^{19}	6.49×10^{18}
Effective valence band (DOS) (cm^{-3})		2×10^{20}	2.5×10^{20}	2.5×10^{20}	1.02×10^{19}	1.66×10^{18}
Conduction tail states	$N^{c\text{-}tail}A$ (cm^{-3})	10^{14}	10^{14}	10^{14}	n/a	n/a
	$E^{c\text{-}tail}A$ (eV)	0.01	0.015	0.01	n/a	n/a
Valence tail states	$N^{v\text{-}tail}D$ (cm^{-3})	10^{14}	10^{14}	10^{14}	n/a	n/a
	$E^{v\text{-}tail}D$ (eV)	0.01	0.015	0.01	n/a	n/a
Acceptor-like (A) dangling bond states	$N^{db}A$ (cm^{-3})	10^{17}	10^{14}	10^{16}	n/a	n/a
	$E^{db}A$ (eV)	1.1	1.2	1.1	n/a	n/a
	$\sigma^{db}A$ (eV)	0.1	0.1	0.1	n/a	n/a
Donor-like (D) dangling bond states	$N^{db}D$ (cm^{-3})	10^{17}	10^{14}	10^{16}	n/a	n/a
	$E^{db}D$ (eV)	1.1	1.2	1.1	n/a	n/a
	$\sigma^{db}D$ (eV)	0.1	0.1	0.1	n/a	n/a

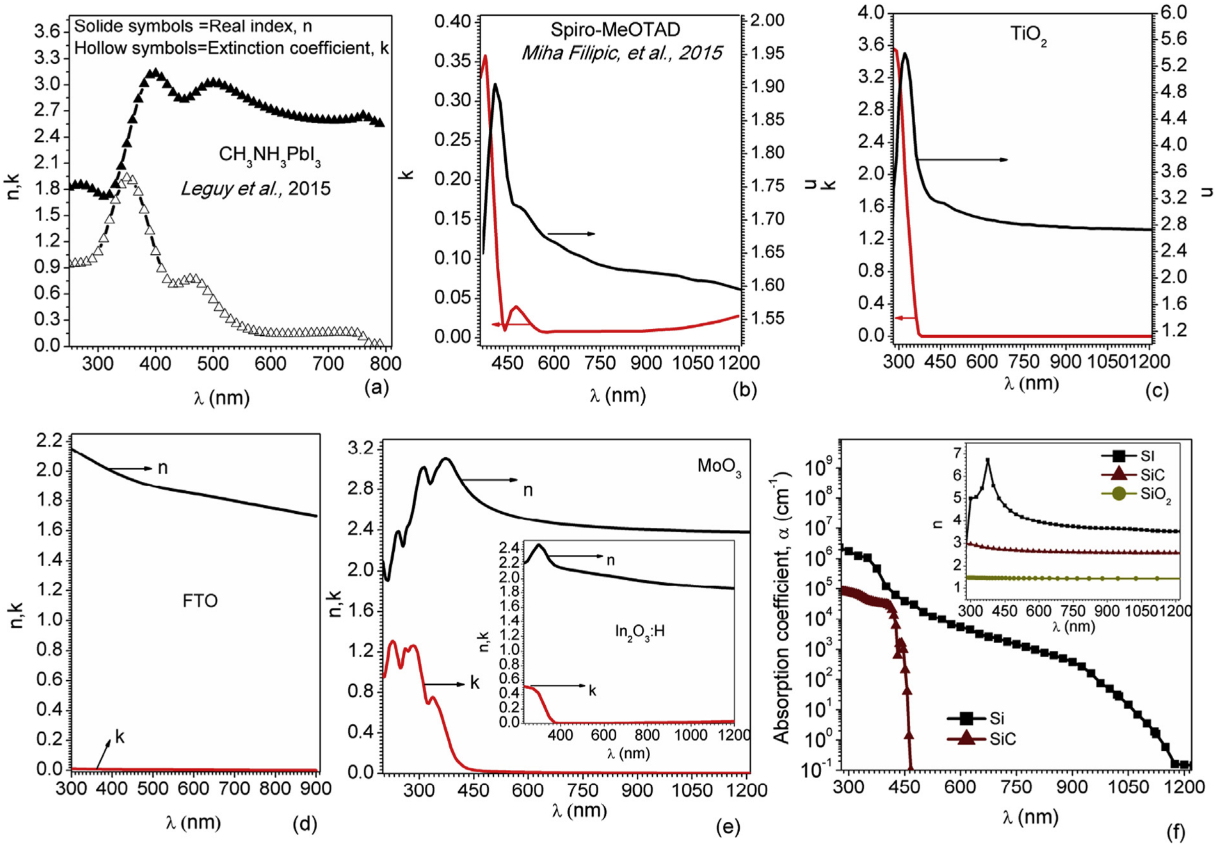

Fig. 2. The optical properties used in simulation: (a) n, k of $CH_3NH_3PbI_3$ obtained from *Leguy* et al., *2015* [32], (b) n, k of Spiro-MeOTAD obtained from *Filipic* et al., *2015* [33], (c) n,k of TiO_2, (d) n,k of FTO, (e) n,k of MoO_3. Inset shows the n,k of In_2O_3:H and (f) absorption coefficient of silicon and SiC. Inset shows real index of Si, SiC, and SiO_2 respectively.

The n_{ie} is the effective intrinsic carrier concentration and its value for perovskite and silicon are $1.97\times10^7\ cm^{-3}$ an$5.21\times10^9\ cm^{-3}$, respectively. K_b is Boltzmann's constant and E_i and E_t are the intrinsic fermi level and trap energy level, respectively. T is the lattice temperature in degree Kalvin. n and p are the electron and hole concentrations. Basic for the SRH model are the assumptions of one trap level in the forbidden band i.e. $E_t = E_i$ and corresponds to the most efficient recombination center. τ_{n0} and τ_{p0} are the electron and holes lifetimes. Also, the constant carrier lifetimes that are used in the SRH recombination model above can be made a function of doping concentration and results in concentration dependent SRH model where τ_{n0} and τ_{p0} will be replaced by τ_n and τ_p [17].

$$\tau_n = \frac{\tau_{n0}}{1 + N/N_{SRHN}},\ \tau_p = \frac{\tau_{p0}}{1 + N/N_{SRHN}} \tag{6}$$

N is the doping concentration in silicon and $N_{SRHN} = N_{SRHP} = 5\times10^{16}\ cm^{-3}$. The bulk lifetime 10^{-3} s and 10^{-5} s has been used for 300 μm and 10 μm thick bottom silicon cell respectively, whereas 10^{-6} s has been used for perovskite film and the impact of a lifetime has also been obtained in the result section.

2.1.2. Auger recombination

Auger recombination occurs through a three particle transition whereby a mobile carrier is either captured or emitted. The underlying physics of such processes is unclear, and normally a more qualitative understanding is sufficient. Auger recombination has been modeled using the following expression:

$$R_{AUGER} = C_n\left(pn^2 - n_0 n_{ie}^2\right) + C_p\left(np^2 - p_0 n_{ie}^2\right) \tag{7}$$

The auger coefficients, $C_p = 9.9 \times 10^{-32}$ cm^6 s^{-1} and $C_n = 2.8 \times 10^{-31}$ cm^6 s^{-1} have been used for p-type and n-type silicon, respectively, at 300 K temperature [18]. Whereas, auger coefficient for the perovskite film has been obtained from experimental data [12,13] and shown in Table 2 n_o, p_o are the concentration of electron and holes at equilibrium.

Table 2
Photovoltaic parameters of perovskite solar cell: charge carrier decay constant has been obtained from experimentally available data from [12, 13].

Charge carrier decay constants		Photovoltaic parameters			
2nd order, B ($cm^3\ s^{-1}$)	3rd order, C ($cm^6\ s^{-1}$)	J_{SC} ($mA\ cm^{-2}$)	V_{OC} (V)	FF (%)	PCE (%)
9.4×10^{-10}	3.7×10^{-29}	23.70	1.08	76.7	19.7
1.5×10^{-10}	3.4×10^{-28}	23.95	1.12	77.8	20.9
1.5×10^{-10}	3.7×10^{-29}	23.96	1.13	77.8	21.0

2.1.3. *Radiative recombination*

In radiative recombination, an electron loses energy on order of the band gap and moves from the conduction band to the valence band. This effect is necessary for narrow gap semiconductors and semiconductors whose specific band structure allows direct transitions. By assuming a capture rate C_c^{OPT} the partially involved process can be written as:

$$R_{np}^{OPT} = C_c^{OPT} np, \tag{8}$$

These rates must be equal in thermal equilibrium so that

$$C_{np}^{OPT} = C_c^{OPT} n_{ie}^2 \tag{9}$$

The total band to band recombination is the difference of the partial rates i.e.

$$R_{np}^{OPT} = C_c^{OPT}\left(np - n_{ie}^2\right) \tag{10}$$

The radiative rate coefficient for perovskite film has been obtained from experimental data [12,13] and shown in Table 2.

2.1.4. *Surface recombination*

The standard method is to model interface recombination in a similar manner as the bulk generation-recombination rate. The recombination rate is an extension of the SRH model by introducing the surface recombination velocities for electrons and holes (S_{n0} or S_{p0}).

$$R_{surface} = \frac{pn - n_{ie}^2}{\tau_n^{eff}\left[p + n_{ie}\exp\left(\frac{E_i - E_t}{k_b T}\right)\right] + \tau_p^{eff}\left[n + n_{ie}\exp\left(\frac{E_t - E_i}{k_b T}\right)\right]} \tag{11}$$

Here:

$$\frac{1}{\tau_n^{eff}} = \frac{1}{\tau_n^i} + \frac{d_i}{A_i} S_{n0} \text{ and } \frac{1}{\tau_p^{eff}} = \frac{1}{\tau_p^i} + \frac{d_i}{A_i} S_{p0} \tag{12}$$

With

$$S_{p0} = \sigma_p v_{th} N_{st} \text{ and } S_{n0} = \sigma_n v_{th} N_{st} \tag{13}$$

Where, A_i and d_i are the area and the length of the interface node i and τ_n^i is the bulk lifetime calculated at a node$i$ along the interface. $S_{p0} S_{n0}$,σ_p and σ_n are the surface recombination velocities parameters and capture cross section for holes and electrons respectively. N_{st} is the surface states per unit area and v_{th} is the thermal velocity of the charge carrier (~10^7 cm s^{-1} in Si at 300 K). The surface recombination effect incorporated in the bottom silicon solar cell using interface statement in ATLAS software and $S_{p0} = S_{n0} = 100$ cm s^{-1} have been used.

3. Results

3.1. *Analysis of perovskite top subcell*

In this section, the analysis of perovskite top subcell has been performed, where the impact of $CH_3NH_3PbI_3$ thickness on photovoltaic parameters has been obtained. The spectrum response i.e. external quantum efficiency (EQE) of the device is presented in Fig. 3 and the J-V curve is shown in Fig. 3b, respectively. The result shows that the performance of the device increases with increasing the thickness of perovskite layer. Perovskite layers with <400 nm thickness are not proficient to absorb the photons of visible spectrum region efficiently as shown in Fig. 3a. Significant improvement is observed in the thickness range of 50–400 nm. Therefore, substantial improvement in current density is also observed as shown in Fig. 3b,

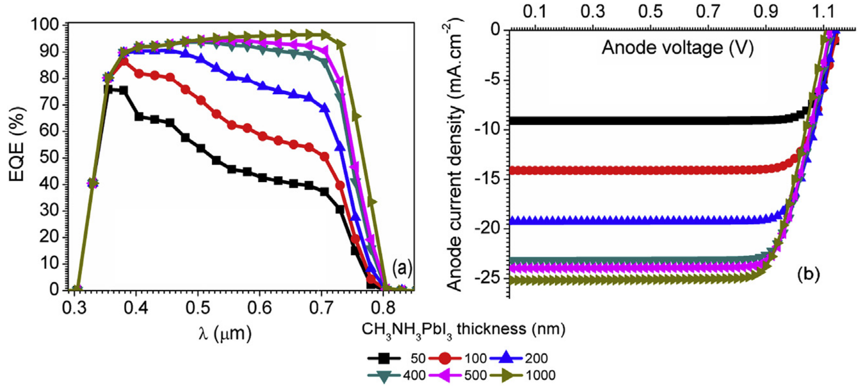

Fig. 3. . Impact of perovskite layer thickness on perovskite top subcell: (a) EQE, and (b) J-V curve.

however, the open circuit voltage (V_{OC}) decreases slightly. Indicating increased carrier recombination in a thicker film. Further, increasing the thickness from 400 to 1000 nm does not provide any substantial improvement. The simulation results are in agreement with the fact that increasing the thickness of perovskite, results in higher PCE [19–21].

The efficiency limit for $CH_3NH_3PbI_3$ solar cell having a perfect mirror at the rear side has been predicted by a detailed balance model, which shows short circuit current density (J_{SC}), V_{OC}, fill factor (FF), and PCE of 25.97 mA cm^{-2}, 1.315 V, 91%, and 30.0%, respectively in 500 nm thick perovskite solar cell [22]. Whereas the device (which do not include perfect mirror at rear side) simulated in this work, shows J_{SC}, V_{OC}, FF, and PCE of 24.1 mA cm^{-2}, 1.3 V, 82%, and 25.9%, respectively, as shown in Fig. 4a. The J-V curve presented in Fig. 4a has been obtained by eliminating the recombination models such as Auger, and radiative recombination. This has been done to perceive the impact of these recombination dynamics on the performance of perovskite solar cell. Further, recombination dynamics has been included in the simulation and three J-V curves are obtained with different second and third order recombination rate constants i.e. *B* and *C*. The constants *B* and *C* have been obtained from recent experimental data as reported by (*Yang* et al., 2015 and *Wehrenfennig* et al., 2014) [12,13]. The carrier lifetime 10^{-6}s has been used for SRH recombination model. Fig. 4b shows significant degradation when recombination dynamics is incorporated in the $CH_3NH_3PbI_3$ layer. The square and circle symbol based J-V curve are based on the constants reported by (*Wehrenfennig* et al., 2014) and (*yang* et al., 2015), respectively. Triangular symbol based J-V curve is also obtained for optimum performance by selecting the smaller values of the constants as shown in Fig. 4b. The PCEs of 19.7%, 20.9%, and 21.0% have been obtained, and the same has been reported in Table 2.

Moreover, the use of SRH model gives the freedom to obtain the impact of material quality on the performance of the device. SRH recombination is defect-limited and proportional to the defect density. Literature reports, first order recombination lifetime range from 10 to 10^3 ns [23–25]. Therefore, the impact of material quality on photovoltaic parameters has been obtained by changing the carrier lifetime from 10 to 5×10^3 ns and presented in Fig. 5(a–d). Fig. 5 shows as the carrier lifetime changes from 5×10^{-6} s to 5×10^{-8} s the change in J_{SC}, V_{OC}, FF, and PCE are 23.98 to 23.40 mA cm^{-2}, 1.12 to 1.09 V, 78.2% to 74.8%, and 21.0% to 19.1%, respectively. This results in 2.4%, 2.6%, 4.3%, and 9.0% decrease in J_{SC}, V_{OC}, FF, and PCE, respectively. However as the lifetime of the carriers changes from 5×10^{-8} s to 10^{-8} s, the decrease in J_{SC}, V_{OC}, FF, and PCE is 5.3%, 4.6%, 4.6%, and 14.1%, respectively as shown in Fig. 5 a–d. The photovoltaic parameters of 10^{-6} s lifetime based perovskite device simulated in this work is almost equivalent to high performance mixed cation perovskite solar cells with record power conversion efficiencies of 20.8% and 21.1% reported in Refs. [6,7], whereas, the performance of low carrier

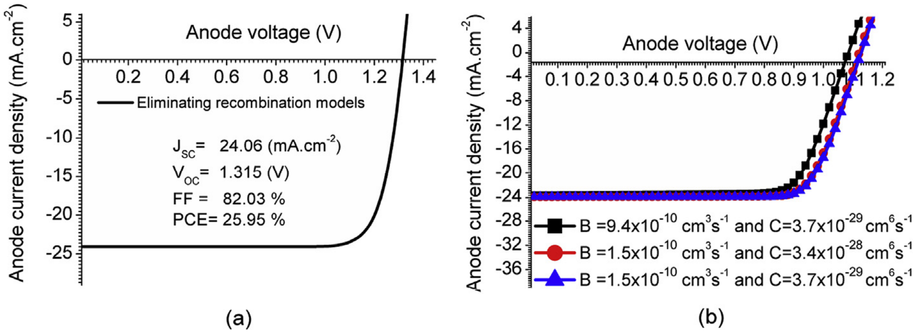

Fig. 4. (a) The J-V curve of the perovskite top subcell, by eliminating the recombination models and (d) J-V curve of the perovskite top cell with different bimolecular and trimolecular carrier recombination coefficient as reported in [12, 13].

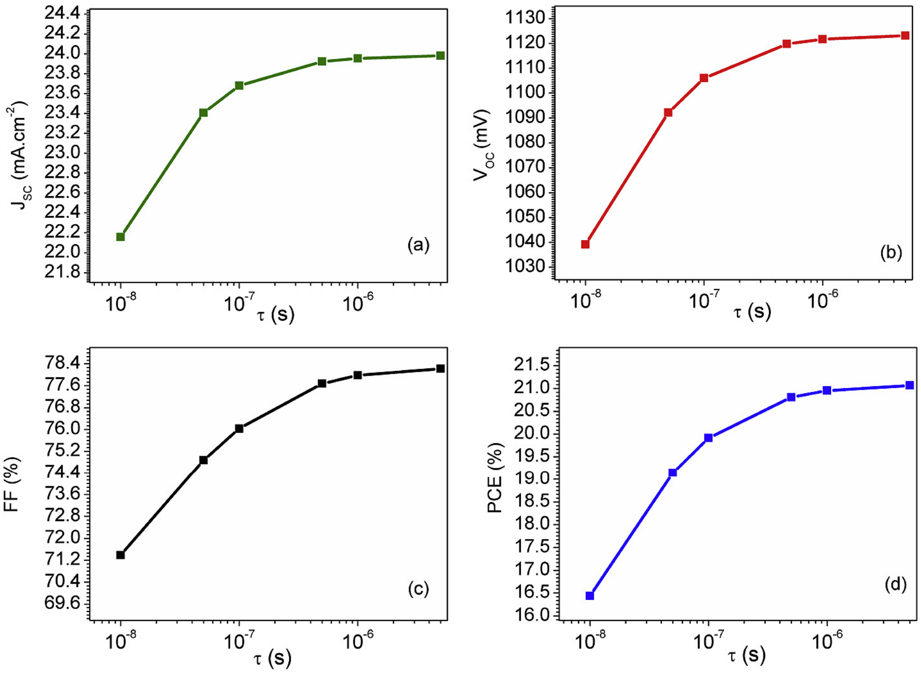

Fig. 5. The impact of first order recombination lifetime on the device photovoltaic parameters for perovskite top subcell: (a) J_{SC}, (b) V_{OC}, (c) FF, and (d) PCE.

lifetime based perovskite device is also in close approximation with the experimentally available data [26]. Furthermore, fundamental recombination dynamics inside the perovskite region has also been obtained and shown in Fig. 6(a–d). Fig. 4b and Fig. 6 shows that the impact of trimolecular recombination is lower compared to bimolecular recombination, on the

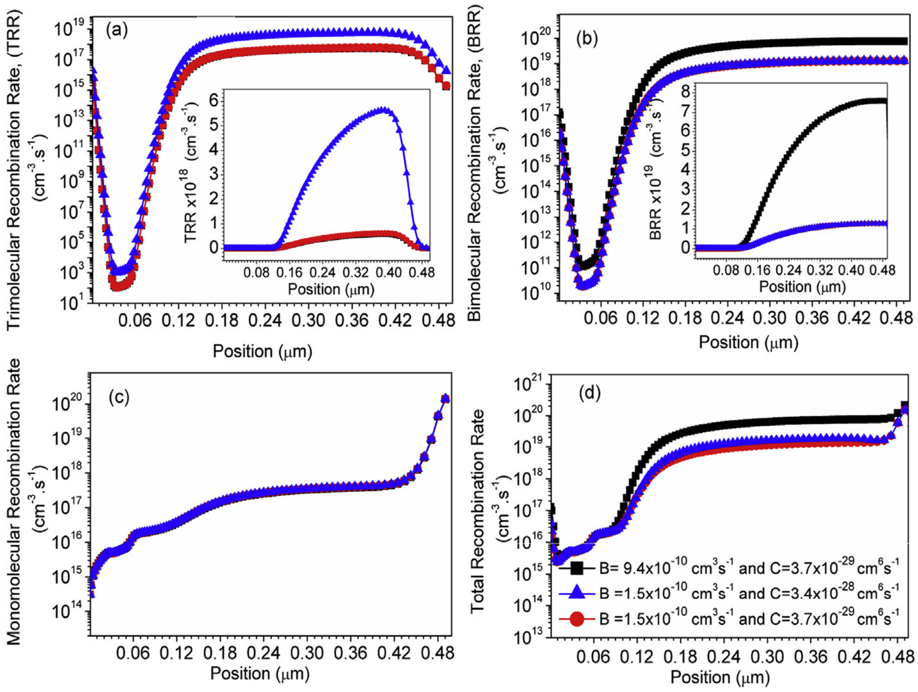

Fig. 6. The carrier recombination rate inside the perovskite region with different bimolecular and trimolecular carrier recombination coefficient as reported in [9,10]. Inset shows the recombination rate on linear scale. Analysis has been done under short circuit condition with standard AM1.5 illumination. Also, fixed first order recombination lifetime 10^{-6} s has been used during simulation.

photovoltaic parameters, since perovskite material has a direct bandgap. Therefore, Auger recombination is sufficiently suppressed, and this has been verified by experimental results [27]. The effect of trimolecular recombination, however, is not ignorable at high charge carrier density.

3.2. Analysis of SiC-based silicon bottom subcell and 4-terminal perovskite/SiC-based silicon tandem solar cell

This section demonstrates four-terminal stacked tandem device based on perovskite as top cell and SiC-based silicon cell as bottom subcell, as schematically shown in Fig. 1c. The efficiency of each subcell is evaluated, and the sum of the two gives the overall efficiency in a tandem configuration. Two different thickness i.e. 10 and 300-μm thick silicon wafer-based devices have been used for bottom subcell silicon solar cell. The performance of bottom silicon subcell is measured with perovskite device (Fig. 1a) as a filter under standard AM1.5 illumination. The motivation to design SiC-based silicon cell is to suppress the interface recombination and improvement of V_{OC}, in rear contact architecture-based silicon solar cell. Initially, we have analyzed the SiC-based rear contact silicon solar cell. The contour representation of recombination rate has been shown in Fig. 7 a-b, the analysis reveals that recombination rate near the SiC/*N*-Si interface is small compared to the bulk region (*N*-Si) of the device. The presence of SiC creates a positive electric field at the interface and direction are directed from SiC to Si, rendering it energetically unfavorable for hole transport to SiC/*N*-Si interface, resulting in a low concentration of holes at the passivating interface [28–30]. In surface recombination process, an electron from conduction band recombines with the hole in the valence band via a defect level within the bandgap. If the concentration of one comrade electrons or holes is drastically reduced, then recombination rate reduces strongly [31]. Therefore, sinking the hole concentration at the interface will produce higher concentration difference between electrons and holes, and thus results in lower surface recombination rate, as shown in Fig. 7(a-b). EQEs of perovskite top subcell and silicon bottom subcell in the tandem configuration are shown in Fig. 8a. The result shows the 10 μm thick Si-based bottom subcell device is not capable of absorbing high energy photon compared to 300-μm thick device. Since photon absorbance is directly related to the absorption coefficient and the thickness of the material used. This leads to superior photovoltaic performance of 300 μm thick Si bottom subcell based tandem device, as shown in Table 3. Further, the performance of Si cell without perovskite filter has also been presented in Fig. 8b, for comparison. In a stand-alone configuration, the J_{SC} of 28.08 mA cm^{-2} and 37.64 mA cm^{-2} have been obtained in 10 μm and 300-μm thick wafer based rear contact solar cells, respectively as shown in Fig. 8b. After adding the perovskite top cell, the J_{SC} of bottom Si cell decreases to 3.06 mA cm^{-2} and 12.61 mA cm^{-2} for 10 and 300 μm thick devices respectively due to reduced light intensity. The decrease in FF and V_{OC} are only marginally, resulting in 1.5% and 6.7% efficient two Si-based bottom subcell, shown in Table 3. Therefore, together with the 20.9% efficiency of perovskite top subcell, this results in 22.4% and 27.6% efficient tandem devices with 10 and 300-μm thick silicon-based bottom subcells, respectively. This is a substantial improvement comparing to transparent perovskite solar cell and c-Si solar cell operated individually.

Moreover, the impact of carrier lifetime has been studied to obtain the effect of material quality on the performance of bottom subcell, and the results are presented in Fig. 9 a-d. The 10 μm thick device is thin compared to conventional ~300 μm thick silicon solar cells and hence, the device can be fabricated with inexpensive, less pure material. Also, the charge carriers need to diffuse shorter length whereas, in 300 μm thick device, a long carrier lifetime is required to collect the carrier. Therefore, the photovoltaic performance of thinner device shows the negligible impact of material quality, whereas significant degradation has been observed in the thicker device. Results shows for lower carrier lifetime (10^{-5} s) the performance of 300 μm thick is lower compared to 10-μm thick device, due to higher bulk recombination of the carrier in the thicker device, since lifetime is small. The desired material quality and the device can be selected from Fig. 9 depending upon the application. Total efficiency in tandem configuration can be obtained by adding the efficiencies of bottom subcell and perovskite top cell.

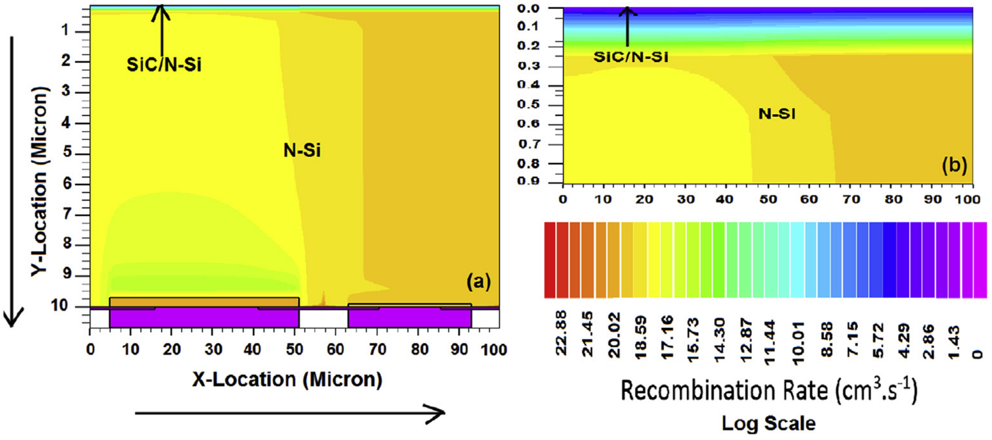

Fig. 7. (a) The contour representation of recombination rate in SiC-based bottom silicon subcell, (b) magnified view near SiC/n-Si interface.

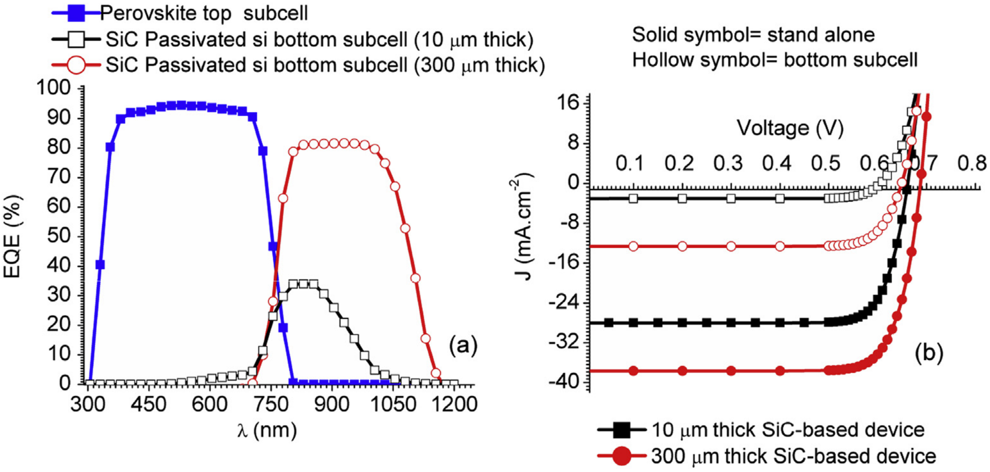

Fig. 8. (a) EQE of perovskite top subcell and SiC based silicon bottom subcell in tandem configuration, and (b) J-V curve of silicon cell in stand-alone and bottom subcell configuration.

Table 3
Photovoltaic parameters of the 4 terminal perovskite/SiC-based silicon tandem solar cell.

Solar cells	J_{SC} (mA cm^{-2})	V_{OC} (mV)	FF (%)	PCE (%)
Perovskite top subcell	23.95	1121	77.8	20.9
Si bottom cell 10 μm in stand-alone, subcell	28.08, 3.06	662, 606	82.3, 81.8	15.3, 1.5
Si bottom cell 300 μm in stand-alone, subcell	37.64, 12.61	688, 649	82.9, 82.3	21.4, 6.7
4-terminal using 10 μm thick Si bottom subcell				20.9 + 1.5 = 22.4
4-terminal using 300 μm thick Si bottom subcell				20.9 + 6.7 = 27.6

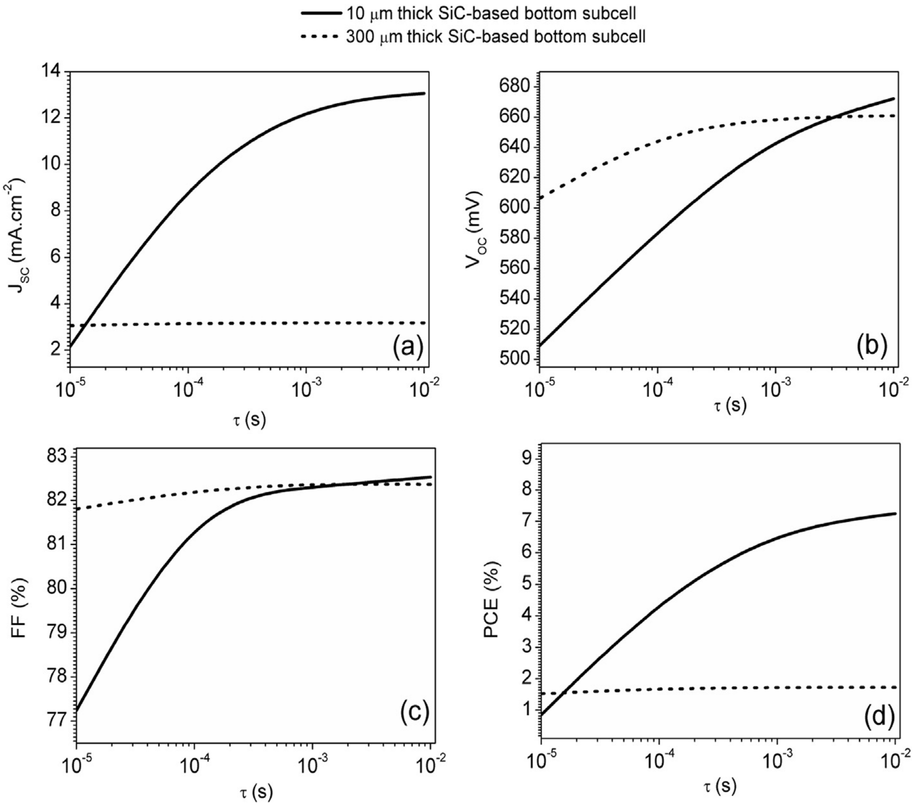

Fig. 9. Impact of carrier lifetime on the performance of bottom silicon subcell under tandem configuration: (a) J_{SC}, (b) V_{OC}, (c) FF, and (d) PCE.

4. Conclusions

This work presents TCAD analysis of 27.6% efficient 4-terminal perovskite/SiC-based silicon tandem solar cell for energy efficient applications. This is a substantial improvement comparing to transparent perovskite solar cell and c-Si solar cell operated individually. The motivation to design SiC-based silicon bottom subcell is to suppress the interface recombination by preventing the minority carrier to reach the passivating interface. The 21.4% efficient individually operated SiC-based rear contact silicon solar cell is combined in four terminal tandem configuration with 20.9% efficient perovskite cell. The perovskite device has been used as top subcell whereas silicon rear contact device has been used as bottom subcell. The efficiency of bottom si subcell went down 6.7% compared to 21.4% when operated stand-alone due to reduced light intensity. The influence of silicon material quality on the performance of bottom silicon subcell has also been obtained. Detailed analysis of perovskite top subcell has been done. The impact of perovskite layer thickness, perovskite material quality has been obtained on the performance of perovskite top subcell. The nature of all fundamental recombination i.e. monomolecular, bimolecular, and trimolecular recombination have been obtained inside the perovskite region, to understand the device physics of perovskite top subcell.

Acknowledgement

The authors would like to thank Microelectronics Research Lab, Department of Engineering Physics, Delhi Technological University to carry out this work. Rahul Pandey (JRF) acknowledge UGC, Govt. of India for providing fellowship.

References

[1] P. Loper, B. Niesen, S.J. Moon, S. Martin De Nicolas, J. Holovsky, Z. Remes, M. Ledinsky, F.J. Haug, J.H. Yum, S. De Wolf, C. Ballif, Organic-inorganic halide perovskites: perspectives for silicon-based tandem solar cells, IEEE J. Photovoltaics 4 (2014) 1545–1551.

[2] A. Richter, M. Hermle, S.W. Glunz, Reassessment of the limiting efficiency for crystalline silicon solar cells, IEEE J. Photovoltaics 3 (2013) 1184–1191.

[3] C.D. Bailie, M.D. McGehee, High-efficiency tandem perovskite solar cells, MRS Bull. 40 (2015) 681–686.

[4] N.-G. Park, Perovskite solar cells: an emerging photovoltaic technology, Mater. Today 18 (2) (2015) 65–72.

[5] W.S. Yang, J.H. Noh, N.J. Jeon, Y.C. Kim, S. Ryu, J. Seo, S.I. Seok, High-performance photovoltaic perovskite layers fabricated through intramolecular exchange, Science. 348 (6240) (2015) 1234–1237.

[6] D. Bi, W. Tress, M.I. Dar, P. Gao, J. Luo, C. Renevier, K. Schenk, A. Abate, F. Giordano, J.-P. Correa Baena, J.-D. Decoppet, S.M. Zakeeruddin, M.K. Nazeeruddin, M. Grätzel, A. Hagfeldt, Efficient Luminescent solar Cells Based on Tailored Mixed-cation Perovskites, (2016).

[7] M. Saliba, et al., Cesium-containing triple cation perovskite solar cells: improved stability, reproducibility and high efficiency, Energy Environ. Sci. 9 (2016) 1989–1997.

[8] J.P. Mailoa, C.D. Bailie, E.C. Johlin, E.T. Hoke, A.J. Akey, W.H. Nguyen, M.D. McGehee, T. Buonassisi, A 2-terminal perovskite/silicon multijunction solar cell enabled by a silicon tunnel junction, Appl. Phys. Lett. 106 (2015).

[9] J. Werner, C.-H. Weng, A. Walter, L. Fesquet, J.P. Seif, S. De Wolf, B. Niesen, C. Ballif, Efficient monolithic perovskite/silicon tandem solar cell with cell area > 1 cm 2, J. Phys. Chem. Lett. 7 (2015) acs.jpclett.5b02686.

[10] M.S. Branham, W.-C. Hsu, S. Yerci, J. Loomis, S.V. Boriskina, B.R. Hoard, S.E. Han, G. Chen, 15.7% efficient 10-μm-Thick crystalline silicon solar cells using periodic nanostructures, Adv. Mater. Deerf. Beach, Fla.) (2015) 2182–2188.

[11] H. Savin, P. Repo, G. von Gastrow, P. Ortega, E. Calle, M. Garín, R. Alcubilla, Black silicon solar cells with interdigitated back-contacts achieve 22.1% efficiency, Nat. Nanotechnol. 10 (2015) 1–6.

[12] Y. Yang, M. Yang, Z. Li, R. Crisp, K. Zhu, M.C. Beard, Comparison of recombination dynamics in CH_3NH_3 $PbBr_3$ and $CH_3NH_3PbI_3$ perovskite films: influence of exciton binding energy, J. Phys. Chem. Lett. 6 (2015) acs.jpclett.5b02290.

[13] C. Wehrenfennig, G.E. Eperon, M.B. Johnston, H.J. Snaith, L.M. Herz, High charge carrier mobilities and lifetimes in organolead trihalide perovskites, Adv. Mater. 26 (2014) 1584–1589.

[14] F. Fu, T. Feurer, T. Jäger, E. Avancini, B. Bissig, S. Yoon, S. Buecheler, A.N. Tiwari, Low-temperature-processed efficient semi-transparent planar perovskite solar cells for bifacial and tandem applications, Nat. Commun. 6 (2015) 8932.

[15] D.S. Software, ATLAS User ' s Manual, 2013, pp. 567–1000.

[16] F. Liu, J. Zhu, J. Wei, Y. Li, M. Lv, S. Yang, B. Zhang, J. Yao, S. Dai, Numerical simulation: toward the design of high-efficiency planar perovskite solar cells, Appl. Phys. Lett. 104 (2014) 253508.

[17] M.E. Law, E. Solley, M. Liang, D.E. Burk, Self-consistent model of minority-carrier lifetime, diffusion length, and mobility, IEEE Electron Device Lett. 12 (1991) 401–403.

[18] J. Dziewior, W. Schmid, Auger coefficients for highly doped and highly excited silicon, Appl. Phys. Lett. 31 (1977) 346.

[19] W.A. Laban, L. Etgar, Depleted hole conductor-free lead halide iodide heterojunction solar cells, Energy & Environ. Sci. 6 (2013) 3249.

[20] L. Etgar, P. Gao, Z. Xue, Q. Peng, A.K. Chandiran, B. Liu, M.K. Nazeeruddin, M. Grätzel, Mesoscopic $CH_3NH_3PbI_3/TiO_2$ heterojunction solar cells, J. Am. Chem. Soc. 134 (2012) 17396–17399.

[21] S. Sun, T. Salim, N. Mathews, M. Duchamp, C. Boothroyd, G. Xing, T.C. Sum, Y.M. Lam, The origin of high efficiency in low-temperature solution-processable bilayer organometal halide hybrid solar cells, Energy & Environ. Sci. 7 (2014) 399.

[22] W.E.I. Sha, X. Ren, L. Chen, W.C.H. Choy, The efficiency limit of $CH_3NH_3PbI_3$ perovskite solar cells, Appl. Phys. Lett. 106 (2015) 221104.

[23] H. Zhu, Y. Fu, F. Meng, X. Wu, Z. Gong, Q. Ding, M.V. Gustafsson, M.T. Trinh, S. Jin, X.-Y. Zhu, Lead halide perovskite nanowire lasers with low lasing thresholds and high quality factors, Nat. Mater. 14 (2015) 636–642.

[24] C. Wehrenfennig, M. Liu, H.J. Snaith, M.B. Johnston, L.M. Herz, Homogeneous emission line broadening in the organo lead halide perovskite $CH_3NH_3PbI_{3-x}Cl_x$, J. Phys. Chem. Lett. 5 (2014) 1300–1306.

[25] D. Shi, V. Adinolfi, R. Comin, M. Yuan, E. Alarousu, A. Buin, Y. Chen, S. Hoogland, A. Rothenberger, K. Katsiev, Y. Losovyj, X. Zhang, P.A. Dowben, O.F. Mohammed, E.H. Sargent, O.M. Bakr, Low trap-state density and long carrier diffusion in organolead trihalide perovskite single crystals, Science 347 (2015) 519–522.

[26] M. Liu, M.B. Johnston, H.J. Snaith, Efficient planar heterojunction perovskite solar cells by vapour deposition, Nature 501 (2013) 395–398.

[27] G. Xing, N. Mathews, S.S. Lim, N. Yantara, X. Liu, D. Sabba, M. Grätzel, S. Mhaisalkar, T.C. Sum, Low-temperature solution-processed wavelength-tunable perovskites for lasing, Nat. Mater. 13 (2014) 476–480.

[28] R. Pandey, R. Chaujar, Rear contact SiGe solar cell with SiC passivated front surface for >90-percent external quantum efficiency and improved power conversion efficiency, Sol. Energy 135 (2016) 242–252.

[29] R. Pandey, R. Chaujar, Numerical simulation of rear contact silicon solar cell with a novel front surface design for the suppression of interface recombination and improved absorption, Curr. Appl. Phys. (2016), http://dx.doi.org/10.1016/j.cap.2016.09.002.

[30] R. Pandey, R. Chaujar, Front surface passivation scheme for back-contact back-junction (BC-BJ) silicon solar cell, Adv. Sci. Lett. 22 (2016) 815–820.
[31] A.G. Aberle, Surface passivation of crystalline silicon solar cells: a review, Prog. Photovoltaics Res. Appl. 8 (2000) 473–487.
[32] M.A. Leguy, Y. Hu, M. Campoy-quiles, M.I. Alonso, O.J. Weber, P. Azarhoosh, M.V. Schilfgaarde, M.T. Weller, T. Bein, J. Nelson, P. Docampo, P.R.F. Barnes, Reversible Hydration of CH3NH3PbI3 in Films, Single Crystals, and Solar Cells, 2015.
[33] M. Filipič, P. Löper, B. Niesen, S. De Wolf, J. Krč, C. Ballif, M. Topič, $CH_3NH_3PbI_3$ perovskite/silicon tandem solar cells: characterization based optical simulations, Opt. Express 23 (2015) A263–A278.

Current Applied Physics 16 (2016) 1581–1587

Contents lists available at ScienceDirect

Current Applied Physics

journal homepage: www.elsevier.com/locate/cap

Numerical simulation of rear contact silicon solar cell with a novel front surface design for the suppression of interface recombination and improved absorption

Rahul Pandey, Rishu Chaujar*

Microelectronics Research Laboratory, Department of Engineering Physics, Delhi Technological University, New Delhi 110042, India

ARTICLE INFO

Article history:
Received 29 June 2016
Received in revised form
19 August 2016
Accepted 2 September 2016
Available online 22 September 2016

Keywords:
Absorption
Recombination
Solar cell
Silicon carbide (SiC)
ZrO_2

ABSTRACT

Nanostructuring has been projected as an appropriate technique to make thin silicon an efficient absorber. Although nano-textured surfaces have shown an anti-reflective effect, their surface passivation properties are found to be generally worse compared to standard micro-textured surfaces. Here, a novel front surface design has been proposed and simulated to balance the photonic and electronic effects together. ZrO_2 based texturing has been used along with SiC-based front surface passivation for the suppression of interface recombination and improvement of open-circuit voltage (V_{OC}). The device under investigation shows record V_{OC} of 662 mV in the sub-10 μm-thick rear contact silicon solar cell. The presence of ZrO_2 and SiC significantly improves the optical as well as the electrical behavior of the device. The device exhibits external quantum efficiency (EQE) > 81% in the spectrum range of 320–720 nm wavelength spectrum with a maximum of 95.6% at wavelength 560 nm. These improvements lead to 15.7% efficient rear contact silicon solar cell, in the sub-10 μm-thick regime. In second approach power conversion efficiency (PCE) of 21.6% has been achieved, by introducing the same front surface design to a 300 μm thick device. All the simulations have been done using calibrated software program in ATLAS device simulation.

1. Introduction

Photovoltaic (PV) is a simple and elegant method of coupling the sun's energy. Solar cells are exceptional in that they directly convert the incident solar radiation into electricity, with no pollution and noise, making them robust, reliable and long lasting. Solar cells are attractive candidates for clean and renewable power [1]. Silicon (Si) is the most extensively used material for solar cell production due to its abundance, reliability, nontoxicity, and mature fabrication techniques. Further, solar cell technology is a function of efficiency, cost, and a lifetime of the cell. Hence, large-scale implementation is not economically feasible. To absorb the solar spectrum, the thickness of the planar cell is typically more than 100 μm [2]. This requirement results in higher cost. Also, in order to increase the collection of the generated carriers, the dimension of the device should be comparable to the carrier diffusion length. Thinner silicon solar cells with high efficiency are fruitful for cost-effective energy solution [3,4]. Further, to maximize solar cell efficiency, it is necessary to optimize both, the device electrical characteristics and the optical absorption of thin devices [5,6]. Nanostructuring has been projected as an appropriate method to make thin silicon an efficient absorber. However, these cells are not efficient due to Auger and surface recombination as the surface to volume ratio of the cells is large. However, recently, methods to minimize the surface recombination for nanostructured based ~300 μm thick devices have been presented which results in 20% and 22% efficient cells [7,8]. The PCE of nanostructured Si solar cell remains below 22.2% for thick devices [7,8] and below 11% for thin devices [9], except 13.7% and 15.7% reported in Refs. [9,10] for the 10 μm thick devices. In previous work, a 14.3% efficient ZrO_2 textured rear contact solar cell has been proposed. The work shows efficient photon absorption in the sub-10-μm-thick device [11]. ZrO_2 is a material of great technology due to its outstanding mechanical and electrical properties and high dielectric constant. Large band gap (E_g ~ 6eV) and dielectric properties (ε ~ 25) suggested its potential to replace SiO_2 in the advance semiconductor device and optical applications [12]. Also, it has an excellent thermal stability. This work further extends the study of ZrO_2 textured front surface based

---

* Corresponding author.
E-mail address: Rishu.phy@dce.edu (R. Chaujar).

http://dx.doi.org/10.1016/j.cap.2016.09.002
1567-1739/

rear contact silicon solar cell having thin defect free SiC layer at the ZrO_2/Si interface. The presence of thin SiC layer minimizes the reflectivity [13,14]. Previous work shows, embedding 3C-SiC nanoparticles significantly reduces the photo reflectivity in UV/visible spectrum region [15]. The SiC is an indirect ($E_g = 2.2$ eV) semiconductor with wide energy band gap, high thermal conductivity, large breakdown field, and high saturation velocity make this material an ideal choice for high temperature, high power, high voltage electron devices. Its high melting point, chemical inertness, high wear resistance, and extreme hardness, make it possible to fabricate sensors and actuators capable of performing in harsh environments [16]. The SiC film formation has been done for Si solar cell passivation. The film was deposited on silicon (100) and glass substrates by an RF magnetron co-sputtering system [17]. Recently, SiC passivated SiGe wafer based rear contact solar cells have been proposed for ultra-high efficiency in sub 10 μm thick devices; work shows improved optical absorption without the need of complex texturing [18,19].

Moreover, this work shows that the presence of SiC improves the photovoltaic parameters of ZrO_2 based rear contact solar cell. The discussed device shows J_{SC} and V_{OC} of 29.3 mA cm^{-2}, 662 mV respectively. This results, in 15.7% PCE in sub 10-μm thick solar cell, which is equivalent to the experimentally achieved record PCE of 15.7% using periodic nanostructure [10]. However, present work shows superior V_{OC}, which shows that the surface recombination issue has truly been solved and SiC passivation based nanostructured silicon solar cell have real potential for industrial production. The rear contact silicon solar cell has been selected because it is a promising high-efficiency solar cell having both, junction and the electrodes at the back side of the device. Now, since the junction and contacts are on the back side, front surface can be designed for optimum optical performance [20].

2. Device structure and simulation

In this section, the calibrated software program is written in Silvaco ATLAS device simulator as per the results reported by (*sangmoo jeong* et al., *2013*) for 10 μm thick rear contact solar cell with antireflection (AR) coating [9]. The dimensions and the doping density of the planar device were identical to the referenced cell and named as Device A as shown in Fig. 1. The device geometry in the simulation was (50-μm-wide pitch, 46 μm-wide *P*+, and 30-μm-wide *N*+). The substrate was *N-type*, with doping density (3×10^{15} cm^{-3}). *P*+ region was doped with boron (4×10^{20} cm^{-3}, depth of 300 nm). *N*+ region was doped with phosphorous (1×10^{20} cm^{-3}, depth of 100 nm).

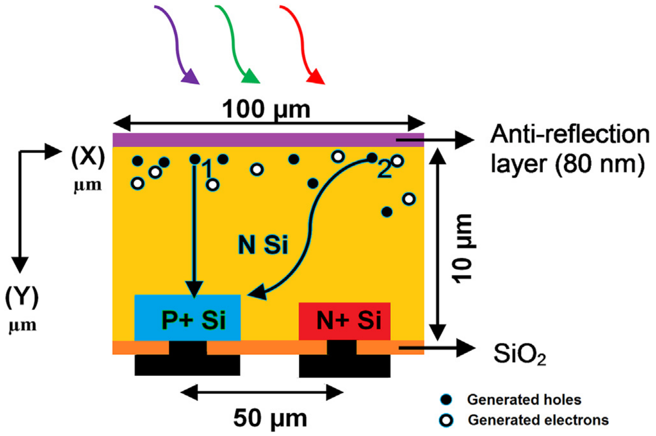

Fig. 1. The simulated device structure i.e. 10 μm thick rear-contact silicon solar cell with the anti-reflective (AR) coating.

Further, in the presence of heavy doping, (>10^{18} cm^{-3}), experimental work has shown that the *PN* product in silicon turns out to be doping dependent [21]. As the doping level rises, a decrease in the bandgap occurs, where the valence band raises by the approximately same amount as the conduction band is lowered. Discussed structure has heavily doped *P* and *N* regions, and so bandgap narrowing effects are enabled. These effects can be described by an analytic expression relating the variation in the bandgap, ΔEg to the doping concentration, N [22]. Furthermore, the solar cells are the carrier recombination affected devices. Therefore, Auger and Shockley- Read- Hall (SRH) recombination models are selected during the simulation. Phonon transitions occur in the presence of a trap or defect within the forbidden gap of the semiconductor [23,24]. Basic for the SRH model are the assumptions of one trap level in the forbidden band and drift-diffusion assumption for the transport of electrons and holes, and the assumption that the dynamics of the trapped carrier is quasi-stationary [25]. Auger recombination occurs through a three particle transition whereby a mobile carrier is either captured or emitted. The underlying physics of such processes is unclear, and normally a more qualitative understanding is sufficient [26]. The auger coefficients, $C_p = 9.9 \times 10^{-32}$ cm^6 s^{-1} and $C_n = 2.8 \times 10^{-31}$ cm^6 s^{-1} have been used for *P*-type and *N*-type silicon, respectively, at 300 K temperature [27]. The concentration dependent mobility and field dependent mobility models have also been selected during simulation. The consistent set of models and parameters for the simulation of Si solar cell have been used as suggested in already published article [28].

To obtain the current density (J)- voltage (V) curve under illumination, the standard AM1.5 solar spectrum has been used. Also, as the contact interface between metal and semiconductor is highly doped both for the *P*+ and *N*+ region i.e. ~10^{20} cm^{-3}, therefore, the ohmic contacts are used in this work. This has been done to avoid Schottky barriers, and thus unnecessarily higher computation time. Result reveals, the software program, is well calibrated within the acceptable range shown in Table 1.

3. Results

The result section is divided into two parts, first, designing a ZrO_2 textured and thin SiC-based ZrO_2 textured 10 × 10 μm thick *N-type* silicon wafer for optimal spectrum response and second, the designed ZrO_2 pattern with and without SiC has been introduced to Device A, by removing anti-reflective coating (ARC) layer. ZrO_2 textured 10 μm thick rear contact silicon solar cell is called as Device B, and ZrO_2 textured device with SiC layer at the ZrO_2/*N*-Si interface is termed as Device C.

3.1. Spectrum response of ZrO_2 textured SiC-based silicon wafer

In this section, a 10 × 10 μm thick *N*-type Si wafer without ARC, with ARC, textured ZrO_2 and textured ZrO_2 having SiC (20 nm) layer at ZrO_2/*N*-Si interface have been designed and simulated to obtain the spectrum response. The entire front surface is covered with repeated ZrO_2 facet structures and optimized height, 175 nm, and width, 250 nm is used for texturing. The smaller and larger width size than 250 nm will show lower optical coupling and lower conversion efficiency, as suggested in Ref. [29]. In the real cell, the nanopatterns can be fabricated via inexpensive and scalable imprinting technique. The complex refractive index of various materials has been obtained from Sopra database [30] and presented in Fig. 2 (a–b). Fig. 2a shows, as wavelength changes from 300 to 1200 nm, the reflective index, n of ZrO_2 changes from 2.45 to 2.17. the n values of ZrO_2 are close to the n values of nitride, which is

Table 1
Photovoltaic parameters of 10 μm thick devices: Device A, Device B, and Device C corresponds to Si_3N_4 coated, ZrO_2 textured, and SiC-based ZrO_2 textured devices, respectively.

Device	J_{SC} (mA cm^{-2})	V_{OC} (mV)	FF (%)	PCE (%)
Reference cell [9]	22.2	615	80.2	10.9
Device A	22.2	616	80.8	11.0
Device B	28.6	623	80.9	14.4
Device C	29.3	662	80.9	15.7
Periodic nanostructure based silicon solar cell [10]	33.9	589	78.5	15.7

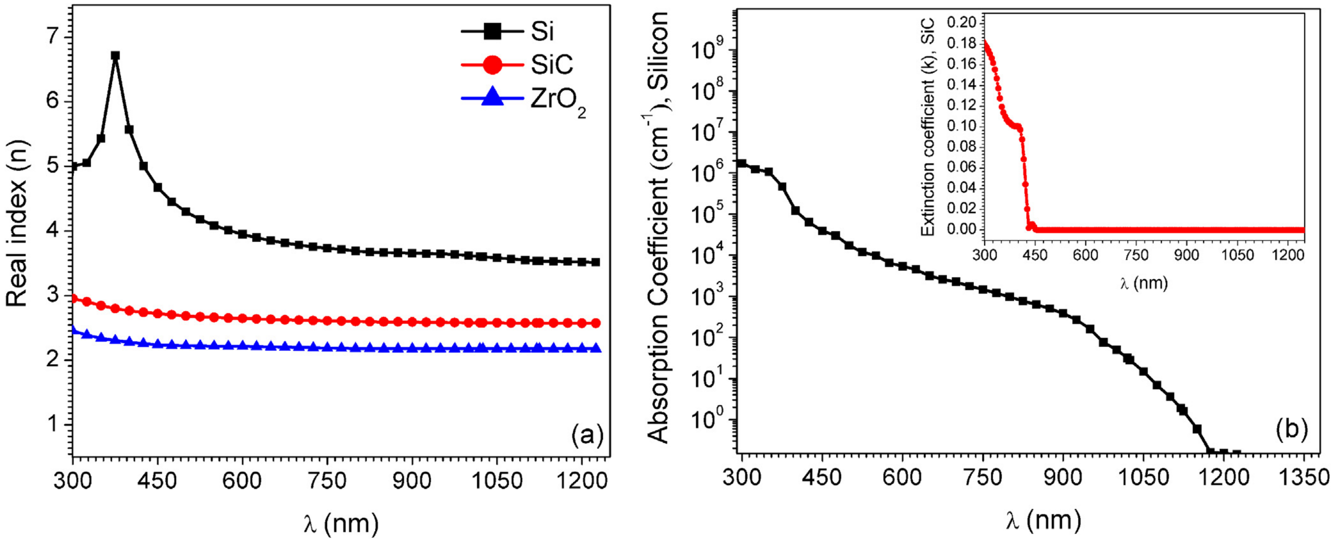

Fig. 2. Wavelength-dependent optical properties of the materials used in simulation: (a) Real index, and (b) Absorption coefficient of silicon. Inset shows the extinction coefficient of SiC.

usually used as AR coating for silicon solar cell [31–33].

Further, the spectral response of Si wafers is presented in Fig. 3 (a–b). Result shows, planar silicon wafer without coating is highly reflective i.e. absorption is small in the range of 300–1000 nm wavelength spectrum. Also, ARC coating based Si wafer shows >96% absorption in the spectrum range of 500–625 nm wavelength. Lower and higher wavelength response is however not remarkable. The ZrO_2 textured wafer shows improved optical behavior compared to ARC coating based wafer due to anti-reflection and light scattering. This concludes that higher absorption is achieved in the ZrO_2 textured wafer, which further results in higher available photocurrent shown in Fig. 3b. Results also indicate that throughout the spectrum range (300–1000 nm), ZrO_2 textured wafer shows enhanced absorption as compared to ARC

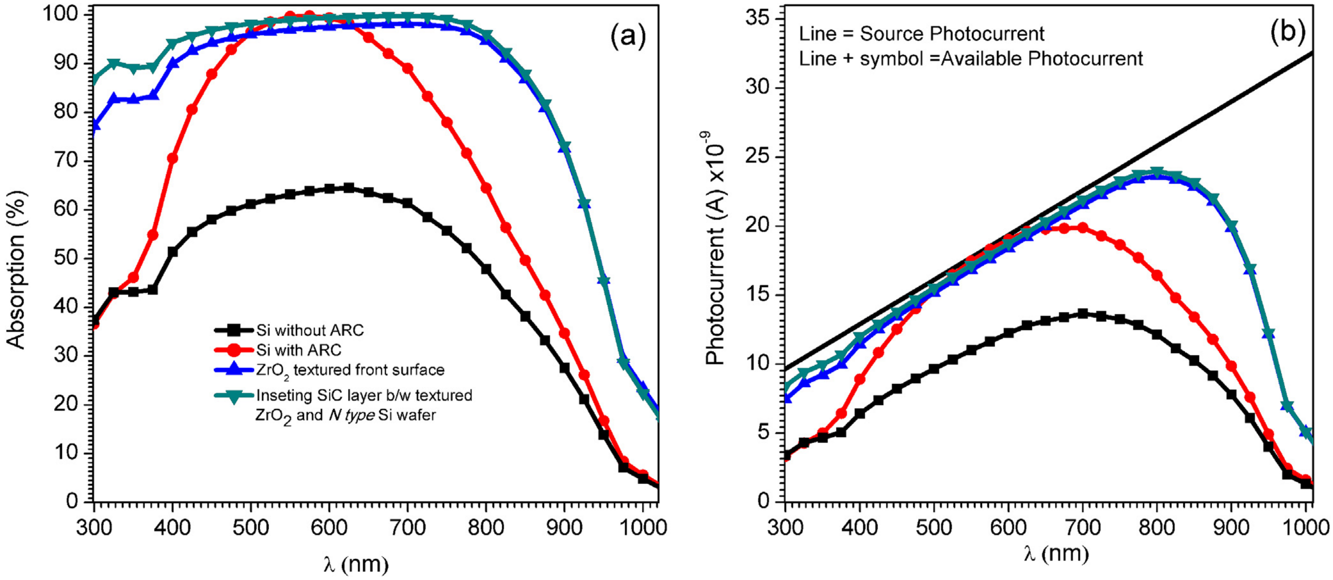

Fig. 3. Spectral response of (10 μm × 10 μm) thick Si wafer with the different type of front surface. (a) Absorption, and (b) Source and available photocurrent. Si_3N_4 was used with the thickness of 80 nm for anti-reflection (AR) layer.

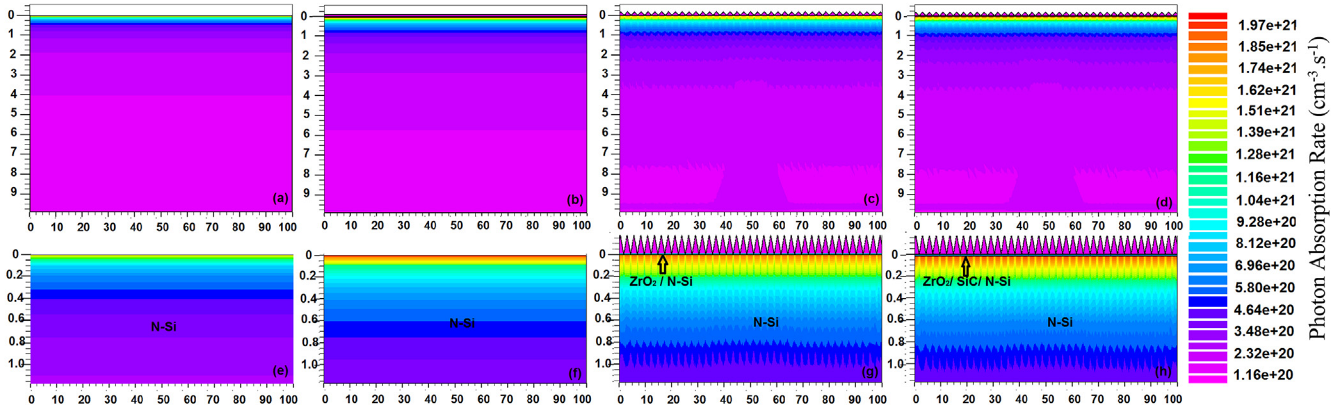

Fig. 4. Photon absorption rate (cm^{-3} s^{-1}) in the silicon wafer with the different type of front surface: (a) Without ARC, (b) with ARC, (c) ZrO_2 textured, and (d) SiC-based ZrO_2 textured. Fig. 4 (e–h) shows the magnified view near the interface for uncoated, ARC based, ZrO_2 textured, and SiC based ZrO_2 textured wafers, respectively.

coated wafer. At a wavelength equivalent to 300 nm, 77% absorption is achieved in the silicon wafer. Also, photon absorption >82% has been achieved in the spectrum range of 325–850 nm wavelength with a maximum of 98.2%. This shows spectrum response has been improved due to ZrO_2 textured front surface. Further, optical behavior of SiC-based ZrO_2 textured wafer has also been obtained. The efficiency of a solar cell is directly related to the amount of light entering the cell. Antireflection coating is used to reduce the reflection of the useful light while not absorbing it. Our previous work shows that the photon coupling in underlying substrate is higher for 20 nm thick SiC-based device. Whereas, increasing the SiC thickness results in parasitic absorbance in SiC, and lower photon coupling in underlying substrate. Since, absorbance directly depends on the thickness of the material. This further results in lower short circuit current density and power conversion efficiency [18]. Therefore, the thickness of SiC used in the simulation is only 20 nm whose absorption is negligible hence, optical coupling in underlying silicon is higher. Also, the optical properties i.e. refractive index (n) and extinction coefficient (k) required for an AR coating depends on the refractive index of the underlying substrate, encapsulated cover, and the operating wavelengths. The material having low absorption of useful light is needed, to reduce the absorption of useful light in ARC. Therefore, low k values are required, k value of 0.01 corresponds to less than 1% absorption, since $\alpha = 4\pi k/\lambda$. Fig. 2a and b shows that SiC has n between 2.9 and 2.5 in the spectrum range of 300–1200 nm and k of less than 0.01 for the wavelengths greater than 430 nm. Also, according to the patented work of *Allen* et al. [34] SiC film having n between 2.7 and 2.3 and k of less than 0.01 at a wavelength of 630 nm is a good candidate for antireflective coating for solar cells. This confirms that presence of SiC will not degrade the optical behaviors of ZrO_2 based wafer. Furthermore, a contour plot of photons absorption rate in the wafers is also shown in Fig. 4(a–d). Higher photon coupling has been observed in both ZrO_2 based and SiC- based ZrO_2 textured wafer. This results in higher absorption rate as well as higher absorption depth compared to ARC based device, as shown in Fig. 4c and d and Fig. 4g and h.

3.2. *Rear-contact solar cell with ZrO_2 textured front surface*

Spectral results as discussed shows that the optical performance of Si wafer is significantly improved in the case of ZrO_2 textured front surface. Therefore, ARC coating of Device A is replaced with ZrO_2 textured front surface with rest of the device parameters being the same. In this section, the performance of two ZrO_2 textured solar cells has been obtained, one with 20 nm thick SiC layer at the interface (Device B) and another without SiC layer at the interface (Device C). Also, the results of the devices are compared with planar rear contact device as shown in Fig. 1.

Here, Device B and Device C have been simulated with the help of calibrated program written for device A. Results of previous section shows, an amalgamation of thin SiC layer does not degrade

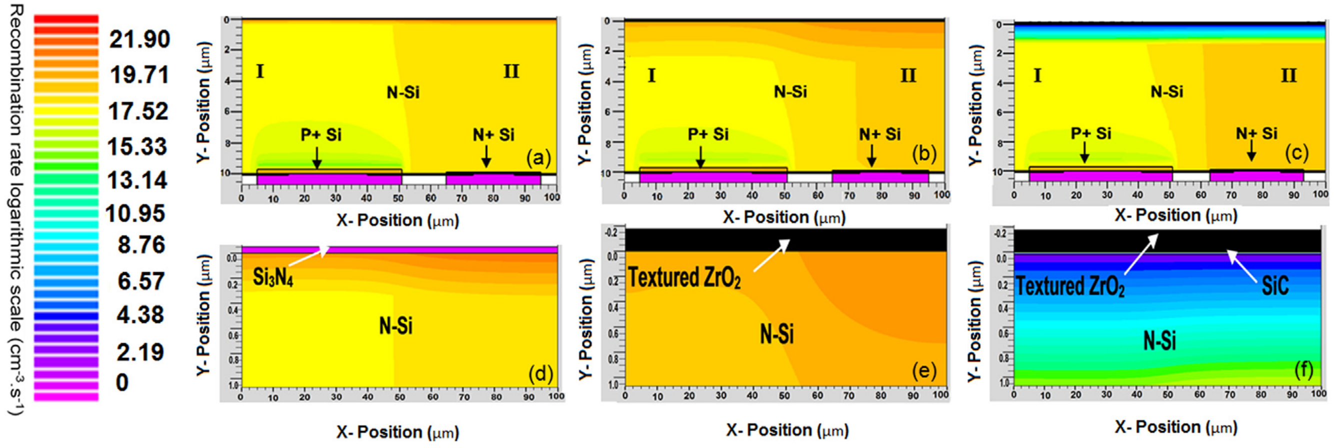

Fig. 5. Contour representation of Recombination rate (cm^{-3} s^{-1}): (a) Si_3N_4 coated device, (b) ZrO_2 textured device, and (c) SiC-based ZrO_2 textured device. Fig. 5 (d–f) shows the magnified view of Si_3N_4/N-Si, ZrO_2/N-Si, and ZrO_2/SiC/N-Si interfaces, respectively.

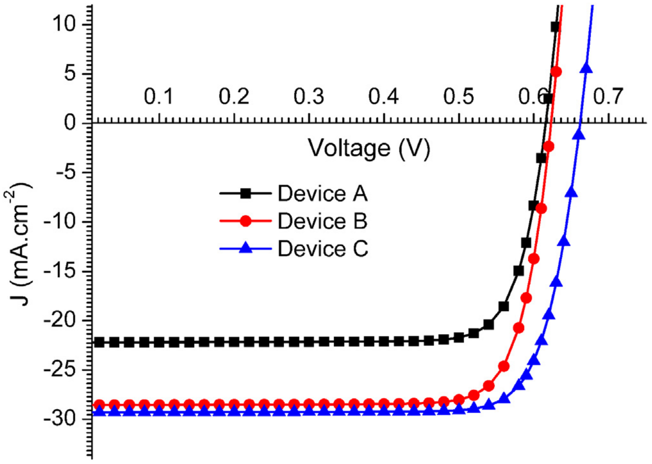

Fig. 6. Current density – voltage (J-V) curve under illumination for different devices: Si_3N_4 coated, ZrO_2 textured, and SiC-based ZrO_2 textured devices respectively.

the optical behavior of the wafer. Hence, both the devices i.e. device B and device C shows significant improvement in device photovoltaic parameters: in terms of short circuit current density (J_{SC}), V_{OC}, fill factor (FF), and PCE compared to device A. Fig. 5(a–f), shows the contour plot of recombination rate in Device A, Device B, and Device C, respectively. The device architecture is such that the holes generated at point 1, in Fig. 1 need to travel shorter to arrive at $N - P+$ interface, whereas the holes generated at point 2, needs to travel a greater lateral distance. Under short-circuit condition, a space charge region is formed around the junction having an associated electric field that collects the generated electron-hole pairs, and the collection is complete near $P+$ region. However, outside the $P+$ region, the substrate is neutral, and the collection will be by diffusion of electrons and holes towards the field region where they will be collected and separated. The electrons and holes generated in a region greater than the diffusion length will never reach the junction, and the recombination process will balance out. This results in higher recombination rate in region II compared to the region I, shown in Fig. 5. Further, Fig. 5c and f shows that significant improvement in surface recombination has been obtained in Device C compared to Device A and Device B. The analysis reveals that recombination rate near the SiC/N-Si interface is small compared to the bulk region (N-Si) of the device. The presence of SiC creates an electric field at the interface and is directed from SiC to Si, rendering it energetically unfavorable for holes transport to SiC/N-Si interface, resulting in a low concentration of holes at the passivating interface [18,35]. Thus, sinking the holes concentration at the interface will produce higher concentration difference between electrons and holes, and results in lower surface recombination rate [36].

Results conclude that presence of ZrO_2 textured front surface increases the optical response and presence of SiC at the ZrO_2/N-Si interface minimizes the surface recombination. Therefore, the dual advantage has been obtained with the help of SiC and ZrO_2. Further, the J-V curve is presented in Fig. 6, for Device A, Device B, and Device C, respectively. Also, the photovoltaic parameters are concluded in Table 1. The J-V curve of Device A is identical to the J-V curve of the planar 10-μm-thick solar cell with anti-reflection (AR) layer, presented by (*sangmoo jeong* et al., *2013*) [9]. This also validates the calibration of the software program. Moreover, lower recombination and higher Photogeneration lead to improved J_{SC} and V_{OC} in Device B and Device C compared to Device A. The J_{SC}, V_{OC} of 28.6 mA cm^{-2}, 623 mV, and 29.3 mA cm^{-2}, 662 mV have been

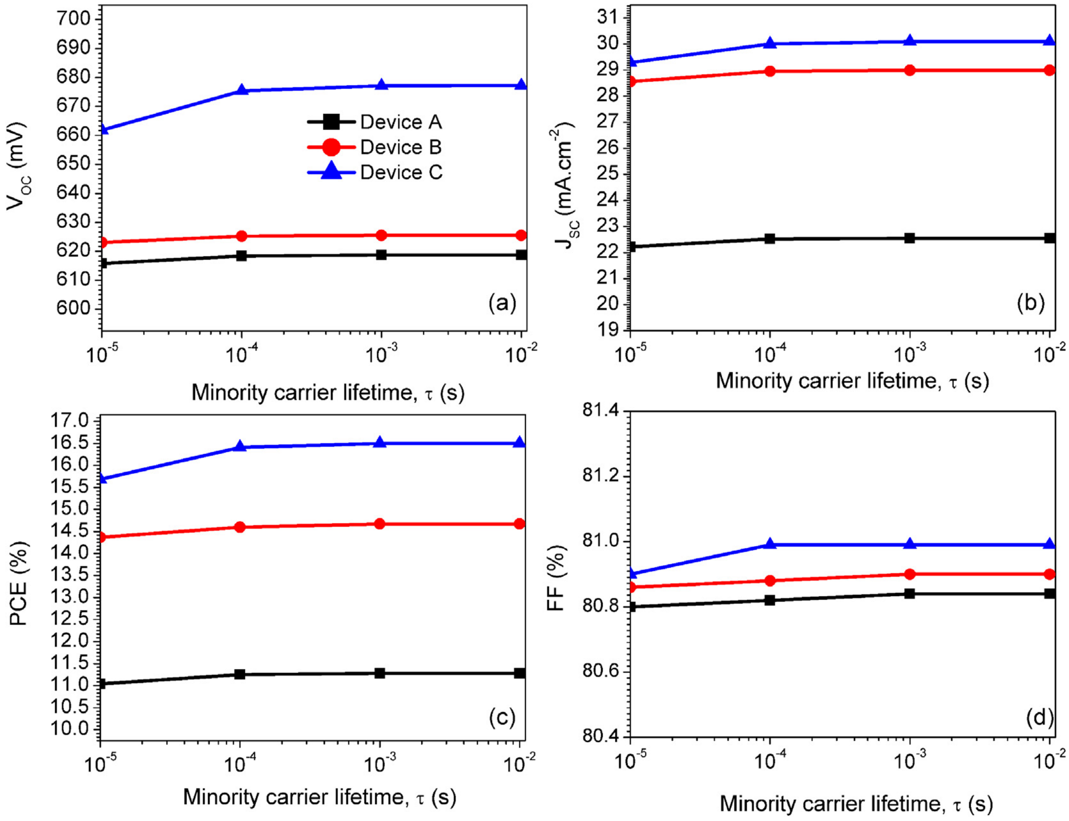

Fig. 7. Impact of minority carrier lifetime on photovoltaic parameters of Si_3N_4 coated, ZrO_2 textured, and SiC-based ZrO_2 textured devices: (a) V_{OC}, (b) J_{SC}, (c) PCE and (d) FF.

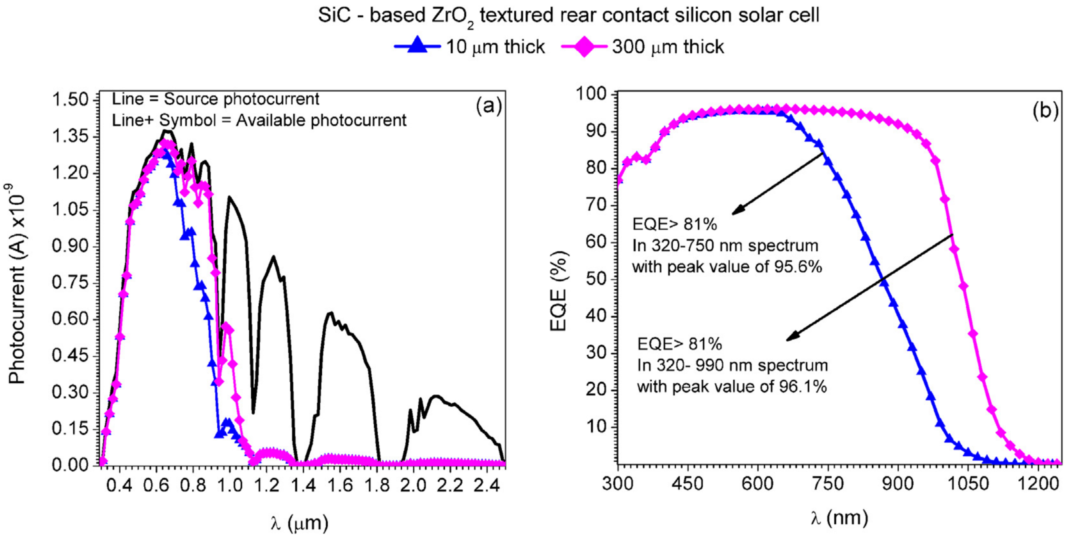

Fig. 8. (a) Available photocurrent in the 10 μm and 300 μm thick SiC-based ZrO_2 textured devices, respectively under AM1.5 illumination, and (b) EQE of the 10 μm and 300 μm thick SiC-based ZrO_2 textured devices, respectively.

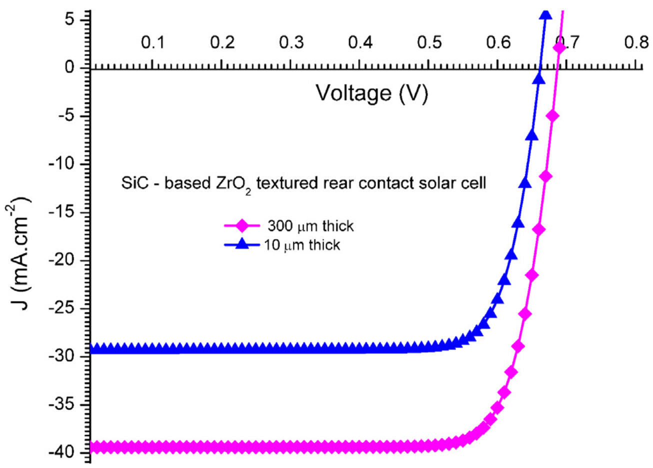

Fig. 9. The J-V curve of the 10 μm and 300 μm thick SiC-based ZrO_2 textured devices, respectively.

obtained in Device B and Device C, respectively, as shown in Fig. 6. Hence, 32% higher J_{SC} and 7% higher V_{OC} has been obtained in Device C compared to Device A. Also, the V_{OC} of the Device C is 6% higher compared to Device B which shows that the presence of SiC in ZrO_2 textured rear contact device significantly boost the photovoltaic performance of the device by suppressing the surface recombination. The overall PCE of the Device C is 42% and 11% higher compared to Device A and Device B respectively.

Moreover, the impact of minority carrier lifetime has been studied to obtain the effect of material quality on photovoltaic parameters, and the results are presented in Fig. 7 (a–d). The discussed device is thin compared to conventional silicon solar cells and hence, the device can be fabricated with inexpensive, less pure material. Also, the charge carriers in discussed device need to diffuse shorter length whereas, in conventional rear contact device, a long carrier lifetime is required to collect the carrier because the thickness is usually >150 μm. This results in, increased module cost since high-purity material is required. Results show that the impact of minority carrier lifetime is negligible on all the three devices. However, the overall photovoltaic parameters of the Device C are superior compared to Device A and Device B. At τ equivalent to 10^{-2} s, the PCE of 11.3%, 14.7%, and 16.5% have been obtained in Device A, Device B, and Device C respectively, whereas, for τ equivalent to 10^{-5} s, the values are 11.0%, 14.4%, and 15.7%, respectively. This shows only 4% change in PCE is observed for Device C, as carrier lifetime changes from 10^{-2} s to 10^{-5} s. All the photovoltaic parameters of Device C are good compared to Device A and Device B as shown in Fig. 7 (a–d).

3.3. SiC- based ZrO_2 textured 300 μm thick rear contact solar cell

The results of the previous section show that the performance of silicon solar cell is improved with the help of SiC- based ZrO_2 texturing, however, optical absorption falls to lower values in the wavelength range of 900–100 nm, whereas simulated spectrum goes up to 1200 nm. The absorption coefficient of silicon is small at higher wavelength [37,38] and hence to increase the absorption up to 1200 nm, thicker silicon is required. Therefore, a 300 μm thick SiC-based ZrO_2 textured rear contact solar cell has also been designed and its optical, as well as electrical parameters, are compared with 10 μm thick device as discussed in previous sections. Fig. 8 show the optical behavior of the devices i.e. 10 μm and 300 μm thick devices, respectively. The available photocurrent is shown in Fig. 8a along with source photocurrent of the spectrum. Improved available photocurrent has also been obtained in 300 μm thick device in higher wavelength regime. The EQEs of the two devices have also been obtained and presented in Fig. 8b. Results

Table 2
Photovoltaic parameters of 300 μm thick SiC-based rear contact silicon solar cell along with already published experimental results.

Device	Thickness (μm)	J_{SC} (mA cm^{-2})	V_{OC} (mV)	FF (%)	PCE (%)
SiC based ZrO_2 textured	300	39.4	687	80.0	21.6
MST based device [7]	285 ± 25	40.5	635	77.0	19.8

show, significant improvement in the higher wavelength region. The EQE fall to lower values at higher wavelength compared to 10-μm thick device, as shown in Fig. 8b. Further, J-V curve of the devices is shown in Fig. 9. Results indicate that improved optical response of 300 μm thick device leads to significant improvement in J_{SC}. The minority carrier lifetime of 1 ms has been selected for the thicker device to prevent the bulk recombination of generated carriers. The J_{SC} (39.40 mA cm^{-2}), V_{OC} (687 mV), FF (80%), and PCE (21.6%) have been obtained. In experimental work, modulated surface textured (MST) based rear contact device shows J_{SC}, V_{OC}, FF, and PCE values of 40.5 mA cm^{-2}, 635 mV, 77%, and 19.8%, respectively [7]. This shows that simulated results are in good agreement with experimental results. The V_{OC} value of the experimental device is lower compared to the device under investigation. This concludes that the optimum surface passivation has been achieved in this work compared to experimental results due to the presence of SiC. This shows that the amalgamation of SiC in experimental devices can significantly suppress the carrier recombination at the interface and lead to higher open circuit voltage. The photovoltaic parameters of the devices are shown in Table 2 along with already available experimental results.

4. Conclusions

This work presents an efficient optical absorption and improved surface passivation in sub-10 μm-thick Si solar cell device. ZrO_2 and SiC based front surface are designed for the silicon wafer, and spectrum response is obtained. The wafer shows absorption (87%) at short wavelengths (300 nm). Results show that throughout the wavelength spectrum 300–1000 nm i.e. (UV–Visible–Infrared), ZrO_2 textured wafer having thin SiC at the interface (ZrO_2/N-Si) shows significant improvement in optical absorption. Hence, ZrO_2 textured SiC-based rear contact solar cell has been designed and simulated to achieve lower interface recombination and improved open-circuit voltage (V_{OC}). This results in enhanced photovoltaic parameters compared to the conventional rear contact solar cell with AR coating. The J_{SC} and V_{OC} of 29.3 mA cm^{-2}, 661 mV have been obtained. This results in 15.7% PCE in the sub-10 μm-thick rear contact silicon solar cell. Further, a 21.6% efficient 300 μm thick device has also been designed and simulated. Results show that if fabricated experimentally it can prove to be a cost-effective solution for energy efficient applications.

Acknowledgment

The authors would like to thank Microelectronics Research Lab, Department of Engineering Physics, Delhi Technological University to carry out this work. Rahul Pandey (JRF) acknowledge UGC, Govt. of India for providing fellowship.

References

[1] B. Tian, X. Zheng, T.J. Kempa, Y. Fang, N. Yu, G. Yu, J. Huang, C.M. Lieber, Coaxial silicon nanowires as solar cells and nanoelectronic power sources, Nature 449 (2007) 885–889.

[2] A. Deinega, S. Eyderman, S. John, Coupled optical and electrical modeling of solar cell based on conical pore silicon photonic crystals, J. Appl. Phys. 113 (2013) 1–9.

[3] R. Pandey, R. Chaujar, TCAD Analysis of Silicon-Germanium (SiGe) based Back-Contact Back-Junction (BC-BJ) solar cell as an alternative for silicon based cells, TechConnectWorld Innov. Conf. Expo (June 14-17, 2015) 199–202, http://dx.doi.org/10.13140/RG.2.1.1008.6246. Washington DC, USA.

[4] C.V. Lare, F. Lenzmann, M. Verschuuren, A. Polman, Dielectric scattering patterns for efficient light trapping in thin-film solar cells, Nano Lett. 24 (June 2015), http://dx.doi.org/10.1021/nl5045583.

[5] N. Dwivedi, S. Kumar, A. Bisht, K. Patel, S. Sudhakar, Simulation approach for optimization of device structure and thickness of HIT solar cells to achieve~27% efficiency, Sol. energy 88 (2013) 31–41.

[6] E. Garnett, P. Yang, Light trapping in silicon nanowire solar cells, Nano Lett. 10 (2010) 1082–1087.

[7] A. Ingenito, O. Isabella, M. Zeman, Nano-cones on micro-pyramids: modulated surface textures for maximal spectral response and high-efficiency solar cells, Prog. Photovolt. Res. Appl. 20 (1) (2015) 6.

[8] H. Savin, P. Repo, G. von Gastrow, P. Ortega, E. Calle, M. Garín, R. Alcubilla, Black silicon solar cells with interdigitated back-contacts achieve 22.1% efficiency, Nat. Nanotechnol. 10 (2015) 1–6 no. May.

[9] S. Jeong, M.D. McGehee, Y. Cui, All-back-contact ultra-thin silicon nanocone solar cells with 13.7% power conversion efficiency, Nat. Commun. 4 (2013) 1–7, 2950.

[10] M.S. Branham, W.-C. Hsu, S. Yerci, J. Loomis, S. V Boriskina, B.R. Hoard, et al., 15.7% efficient 10-μm-Thick crystalline silicon solar cells using periodic nanostructures, Adv. Mater. (2015) 2182–2188, http://dx.doi.org/10.1002/adma.201405511.

[11] R. Pandey and R. Chaujar, "Rear contact solar cell with ZrO_2 Nano structured front surface for efficient light trapping and enhanced surface passivation" IEEE PVSC 42nd, Jun 14-19, 2015, New Orleans, USA.

[12] J.C. Garcia, L.M.R. Scolfaro, Structural, electronics, and optical properties of ZrO_2 from ab initio calculation, J. Appl. Phys. 100 (2006) 1–9.

[13] R. Pandey, R. Chaujar, Novel back-contact back-junction SiGe (BC-BJ SiGe) solar cell for improved power conversion efficiency, Microsyst. Technol. (2015), http://dx.doi.org/10.1007/s00542-015-2552-1. Available, http://link.springer.com/article/10.1007%2Fs00542-015-2552-1#page-1.

[14] R. Pandey and R. Chaujar, "Novel SiC encapsulated coaxial silicon nanowire solar cell for optimal photovoltaic performance" IEEE PVSC 42nd, June 14-19, New Orleans, USA.

[15] B. Parida, J. Choi, G. Lim, K. Kim, Enhanced visible light absorption by 3C-SiC nanoparticles embedded in Si solar cells by plasma-enhanced chemical vapor deposition, J. Nanomater 2013 (2013) 1–10, http://dx.doi.org/10.1155/2013/953790.

[16] G.S. Chung, K.S. Kim, F. Yakuphanoglu, Electrical characterization of Au/3C-SiC/n-Si/Al Schottky junction, J. Alloys Compd. 507 (2) (2010) 508–512.

[17] Y.-H. Joung, H. Kang, J. Kim, H.-S. Lee, J. Lee, W. Choi, SiC formation for a solar cell passivation layer using an RF magnetron co-sputtering system, Nanoscale Res. Lett. 7 (1) (2012) 22.

[18] R. Pandey, R. Chaujar, Rear contact SiGe solar cell with SiC passivated front surface for > 90-percent external quantum efficiency and improved power conversion efficiency, Sol. Energy 135 (2016) 242–252, http://dx.doi.org/10.1016/j.solener.2016.05.056.

[19] R. Pandey, A. Jain, A. Kumar, R. Chaujar, Impact of minority carrier lifetime and temperature on SiC based rear contact SiGe solar cell for concentrator photovoltaic (CPV) applications, in: 32nd Eur. Photovolt. Sol. Energy Conf. Exhib, 2016, pp. 270–273, http://dx.doi.org/10.4229/EUPVSEC20162016-1BV.6.45.

[20] E.V. Kerschaver, G. Beaucarne, Back-contact solar cells: a review, Prog. Photovolt. Res. Appl. 14 (2006) 107–123.

[21] J.W. Slotboom, The pn-product in silicon, Solid. State. Electron. 20 (4) (Apr. 1977) 279–283.

[22] J.W. Slotboom, H.C. De Graaf, Measurements of bandgap narrowing in silicon bipolar transistors, Solid State Electron. 19 (1976) 857–862.

[23] W. Shockley, W.T. Read, Statistics of the recombinations of holes and electrons, Phys. Rev. 87 (1952) 835–842.

[24] R.N. Hall, Electron hole recombination in germanium, Phys. Rev. 87 (1952) 835–842.

[25] T. Goudon, V. Miljanović, C. Schmeiser, On the shockley–read–hall model: generation-recombination in semiconductors, SIAM J. Appl. Math. 67 (4) (2007) 1183–1201.

[26] S. Selberherr, Analysis and Simulation of Semiconductor Devices, Springer-Verlag, Wien, New York, 1984.

[27] J. Dziewior, W. Schmid, Auger coefficient for highly doped and highly excited silicon, Appl. Phys. Lett. 31 (1977) 346–348.

[28] P.P. Altermatt, Models for numerical device simulations of crystalline silicon solar cells—a review, J. Comput. Electron 10 (2011) 314–330, http://dx.doi.org/10.1007/s10825-011-0367-6.

[29] S. Yoshinaga, Y. Ishikawa, S. Araki, Y. Uraoka, Light trapping effect of nanoimprinted-textured crystalline silicon solar cells, in: 2013 IEEE 39th Photovolt. Spec. Conf., IEEE, 2013, pp. 1310–1313, http://dx.doi.org/10.1109/PVSC.2013.6744383.

[30] Atlas User Manual, Silvaco, Inc, Santa Clara, 2014, pp. 1565–1574.

[31] H.R. Philipp, Optical properties of silicon nitride, J. Electrochem. Soc. 120 (2) (Feb. 1973) 295.

[32] T. Bååk, Silicon oxynitride; a material for GRIN optics, Appl. Opt. 21 (6) (Mar. 1982) 1069–1072.

[33] http://refractiveindex.info/?shelf=main&book=Si3N4.

[34] Allen, S., Awad, Y., Gaumond, A. and Davies, M., 2009. Silicon carbide-based antireflective coating. U.S. Patent Application 12/994,973.

[35] R. Pandey, R. Chaujar, Front surface passivation scheme for back-contact back-junction (BC-BJ) silicon solar cell, Adv. Sci. Lett. 22 (2016) 815–820.

[36] A.G. Aberle, Surface passivation of crystalline silicon solar cells: a review, Prog. Photovolt. Res. Appl. 8 (2000) 473–487, http://dx.doi.org/10.1002/1099-159X(200009/10)8:5<473::AID-PIP337>3.0.CO;2-D.

[37] M.A. Green, M.J. Keevers, "Optical properties of intrinsic silicon at 300 K, Prog. Photovolt. Res. Appl. 3 (3) (1995) 189–192.

[38] M.A. Green, Self-consistent optical parameters of intrinsic silicon at 300K including temperature coefficients, Sol. Energy Mater. Sol. Cells 92 (11) (Nov. 2008) 1305–1310.

Microsyst Technol (2016) 22:2673–2680
DOI 10.1007/s00542-015-2552-1

TECHNICAL PAPER

Novel back-contact back-junction SiGe (BC-BJ SiGe) solar cell for improved power conversion efficiency

Rahul Pandey[1] · **Rishu Chaujar**[1]

Received: 2 November 2014 / Accepted: 18 April 2015 / Published online: 1 May 2015

Abstract In this paper, a SiGe based Back-Contact Back-Junction (BC-BJ) device structure called BC-BJ SiGe solar cell has been proposed. Photo reflection is significantly reduced in UV/Visible spectrum region in case of SiC/Si_3N_4/SiO_2 passivated BC-BJ SiGe solar cell. Result, indicates that presence of SiC play an important role in photoelectric conversion. Ray tracing and finite difference time domain (FDTD) algorithms are used to simulate optoelectronics characteristics of the device. Simulation achieves the barrier height of 0.8 eV for holes at the interface which results in a higher field. The lower interface recombination rate of the order of 10^{17} cm^{-3} s^{-1} has been obtained. The device shows improved photovoltaic parameters. External quantum efficiency >84 % in the spectrum range of 450–700 nm wavelength and more than 80 % in the range of 350–700 nm wavelength is obtained. Further, we obtained the fill-factor (FF) and power conversion efficiency (PCE), 79 %, 17.8 % and 79 %, 14.8 %, using FDTD and ray tracing methods, respectively. All the simulations have been done using atlas and devedit device simulator.

1 Introduction

Over the last 53 years, commercial silicon photovoltaics (PV) have been developed to convert sunlight into electricity and provide the most feasible carbon–neutral route to displacing terawatts(TW) of nonrenewable power consumed worldwide (Garnett and Yang 2010). Since solar cell technology is not an individual function of efficiency but also depends on the cost, hence large scale implementation is not economically feasible. In order to maximise solar cell efficiency, it is necessary to optimize both the electrical device characteristics and the optical absorption of the device (Deceglie et al. 2012; Deinega et al. 2013; Tian et al. 2007). Power conversion efficiency of Si-solar cell remains below 10.5 % for thin devices (Green et al. 2014). However, it has been observed that reducing the thickness of the photovoltaic cell to sub 10 μm can potentially have considerable impact on cost reduction.

One promising high-efficiency solar cell concept is the back-contact back- junction solar cell (Kerschaver and Beaucarne 2006) having both, junction and the electrodes at back side of the device. The first 17 % efficient under 50 sun condition BC-BJ solar cell presented by (Schwartz and Lammert 1975). The conventional BC-BJ solar cell have large area which result in higher material cost. Microsystem enabled 14 μm thick, 250 μm wide rear contact solar cell, with 14.9 % efficiency are presented by (Cruz-Campa et al. 2011), work shows that the ultrathin wafer handling problem can be avoided by using low cost microsystem techniques. Further, an all back-contact ultra-thin i.e., 10 μm thick silicon nanocone solar cell with 13.7 % power conversion efficiency is reported (Jeong et al. 2013). Further, back-contacted silicon heterojunction solar cells with 9 cm^2 active cell area were fabricated on 250-μm-thick, n-type, 4-in float-zone (FZ) wafers, with a nominal resistivity of 3 Ω cm, resulting in 21.5 % PCE (Tomasi et al. 2014). Also, independently confirmed conversion efficiency of 23.0 % for n-type rear contact cells has been reported (Feldmann et al. 2014) and at

---

✉ Rahul Pandey
rahulpandey@dtu.ac.in; rahulp.electronics@gmail.com

Rishu Chaujar
rishu.phy@dce.edu

[1] Microelectronics Research Lab, Department of Engineering Physics, Delhi Technological University, Bawana Road, Delhi 110042, India

the end of the year, the interdigitated back contact (IBC) solar cells developed which resulted in an independently confirmed designated-area efficiency of 24.4 %, The cell was fabricated on a 230 µm thick 1.5 Ω cm n-type CZ wafer (Franklin et al. 2014). These cells have higher thickness they require high quality materials, in order to have higher minority carrier lifetime: order of magnitude 10 ms. These kind of c-Si are very expensive, resulting in increased module cost.

Here, we propose a 10 µm thin novel BC-BJ SiGe solar cell with a 14.8 % power conversion efficiency that will overcome the problems associated with thin devices such as auger and surface recombination. Here, SiGe is used because the energy of the visible part of the spectrum used by solar cell is less than 50 % and in order to increase the absorption of sunlight, low bandgap (<1.1 eV) material is required. Using low bandgap material in solar cell makes the conversion efficiency of the cell effective. Nowadays, SiGe is used for high frequency transistors as well as potential has been explored for solar cells also. SiGe has higher carrier lifetime and higher mobility as compared to silicon. In SiGe technology, the electrical properties of silicon are modified with germanium. SiGe processing is simple because the physical and electrical properties of silicon and germanium are similar (Ouellete 2002). Also SiGe possesses higher mechanical strength, and suppresses the high intensity degradation of solar cell under illumination (Yang et al. 2010). The band gap of SiGe can be modified to vary by changing the Ge ratio (Wang et al. 2012; Povolny et al. 2000) and alternatively by varying the optical absorption, absorption is directly related to band gap of semiconductor

2 Device structure: parameters and simulation models

The simulation device structure i.e., BC-BJ SiGe solar is shown in Fig. 1. Device contains intrinsic SiGe wafer having length in y-direction equal to 10 µm and in x-direction equals to 100 µm, without optical absorber coating on top. The $Si_{0.9}$ $Ge_{0.1}$ was used during the simulation, very small fraction of germanium is used. Because, if we increase the germanium content the bandgap of SiGe decreases (Atlas user manual 2014), which further results in lower open circuit voltage. The width of *N* +/*P* + regions are 30 and 45 µm respectively, in X direction whereas the depth is 100 and 300 nm in Y direction. The pitch of the device is 52 µm. The device consists of ohmic contacts and the doping concentration of *N* +/*P* + regions are 4×10^{20} cm^{-3}. All simulations have been performed using atlas and devedit device simulator. The complex refractive index of various materials as a function of temperature and composition has been obtained from sopra database. SiGe parameters are obtained from Silvaco library and shown in Table 1.

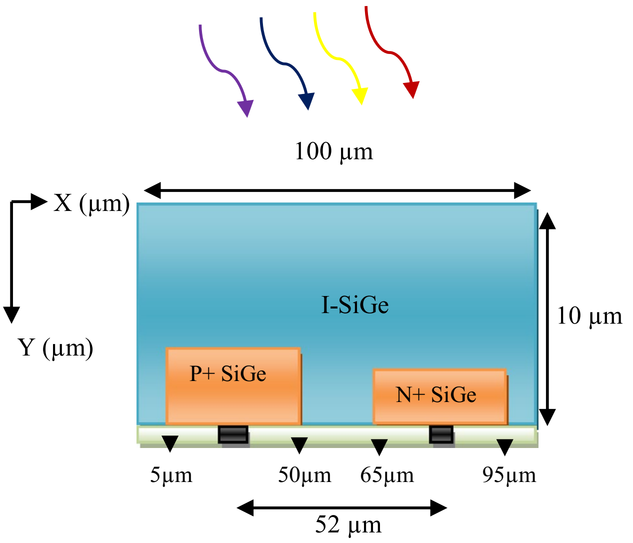

Fig. 1 Proposed SiGe based device: BC-BJ SiGe solar cell

Table 1 Parameters of SiGe used in simulation

Energy band gap (Eg)	1.08 eV
Band density (Nc)	2.8×10^{19} (cm^{-3})
Band density (Nv)	1.04×10^{19} (cm^{-3})
Intrinsic carrier conv (Ni)	1.45×10^{10} (cm^{-3})
Minority carrier lifetime for electron	3×10^{-5} s
Minority carrier lifetime for holes	1×10^{-5} s
Electron mobility (μ_n)	1430 cm^2/Vs
Hole mobility (μ_p)	480 cm^2/Vs

The energy band diagrams from *P*+–*I*–*N*+ regions are examined under dark and illuminated conditions, respectively. It is clearly observed that electron quasi Fermi level lies within the valence band and conduction band at *P*+ region and *N*+ region, respectively shown in Fig. 2a. This helps in analyzing the motion of the carriers i.e., if an electron is generated in the I region, then it finds build-in potential at *P*+ side and hence, will not travel towards *P*+ side but as there is no barrier in *N*+ side, it can easily move toward *N*+ region. In Fig. 2b, under illumination, the electron quasi Fermi level and band diagram is changed because of the light generated carriers. In intrinsic SiGe region, as the number of free carriers are increased during illumination, Fermi level moves closer to the bottom of the conduction band. The *N*+ , *P*+ region acts as a back surface field (BSF) for holes and electrons, respectively. Thereby reflecting, the hole

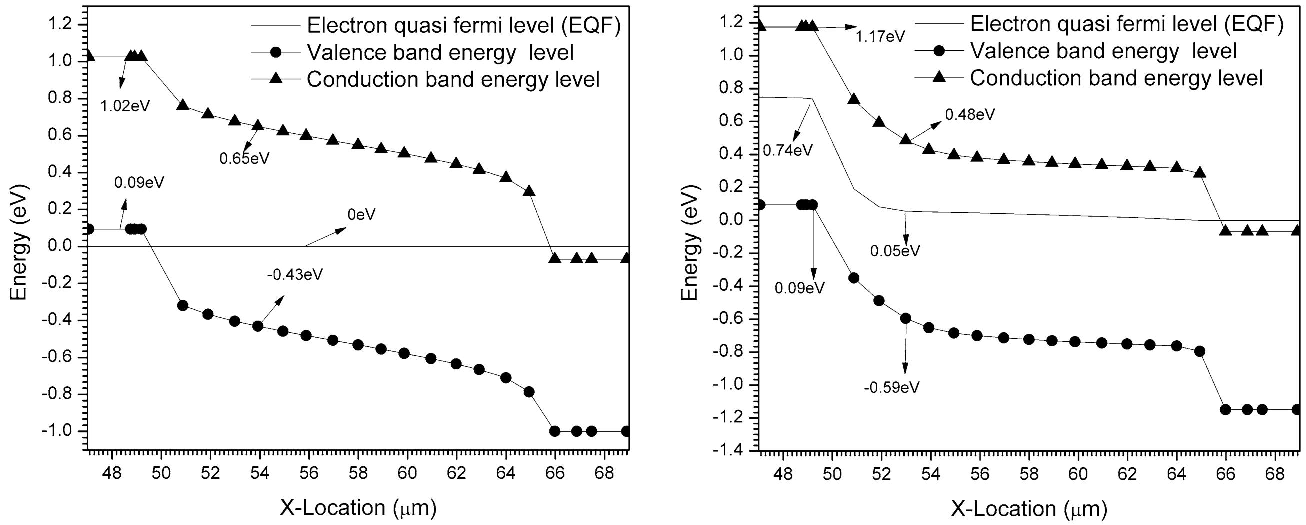

(a) **(b)**

Fig. 2 The energy band diagrams from *P*+–*I*–*N*+ regions with Electron Quasi Fermi Level at zero bias V = 0. **a** Under dark and **b** With Illumination Pin = 0.1 W/cm^2

moving towards *N*+ region and electron moving towards *P*+ region by the barrier at *I*-*N*+ region and *I*-*P*+ region, respectively.

Further, in the presence of heavy doping (>10^{18} cm^{-3}), experimental work has shown that the pn product in silicon turn out to be doping dependent (Slotboom 1977). As the doping level rises, a decrease in the bandgap occurs, where the valence band raises by approximately same amount as the conduction band is lowered. Proposed device has heavily doped *P*+ and *N*+ regions and so bandgap narrowing effects are enabled. These effects may be described by an analytic expression relating the variation in bandgap (Eg) to the doping concentration, N. The expression used in simulation is from Slotboom and de Graaf (Slotboom and de Graaff 1976). Furthermore, Auger and Shockley- Read- Hall (SRH) recombination models are selected during the simulations. Auger recombination occurs through a three particle transition whereby a mobile carrier is either captured or emitted. The underlying physics for such processes is unclear and normally a more qualitative understanding is sufficient (Dziewior and Schmid 1977; Selberherr 1984). In SRH, Phonon transitions occur in the presence of a trap or defect within the forbidden gap of the semiconductor (Shockley and Read 1952; Hall 1952). The Poisson equation together with the continuity equation for electrons and holes are solved simultaneously by the software to obtain the current density- voltage (J-V) characteristics. The standard air mass 1.5 (AM1.5) spectrum is used.

3 Simulation results

3.1 Designing of highly absorbing surface passivation layer (HAPL) using carbide, oxide and nitride

In this section, we have designed and discussed the HAPL layer for rear contact SiGe solar cell, using carbide, and oxide and nitride layers. We have simulated a (10 × 10) μm thick intrinsic SiGe wafer and with different absorbing layers. Spectrum response i.e., reflectivity and available photo current as a function of wavelength is presented in Fig. 3a, b with different absorbing layers for intrinsic SiGe wafer. Results, indicate significant decrease in photo reflectivity in UV region due to presence of SiC. However, results also indicate SiC is highly reflective in visible region, therefore only SiC layered device shows lower available photocurrent in visible spectrum shown in Fig. 3b. So, in order to avoid this problem, oxide and nitride coated layers has been placed on SiC. Result shows, SiO_2 coated SiC provide better absorption compared to Si_3N_4 coated SiC shown in Fig. 3a, b. Result also indicates SiGe wafer without absorbing layer is highly reflective. Further, highest absorption is achieved in $SiC/Si_3N_4/SiO_2$ coated SiGe compared to other layers. Furthermore, results also indicate that SiC/SiO_2 coated SiGe wafer shows approximately same response as $SiC/Si_3N_4/SiO_2$ coated SiGe. This indicates SiC/SiO_2 coated SiGe can be used instead of $SiC/Si_3N_4/SiO_2$ coated SiGe in order to avoid complexity.

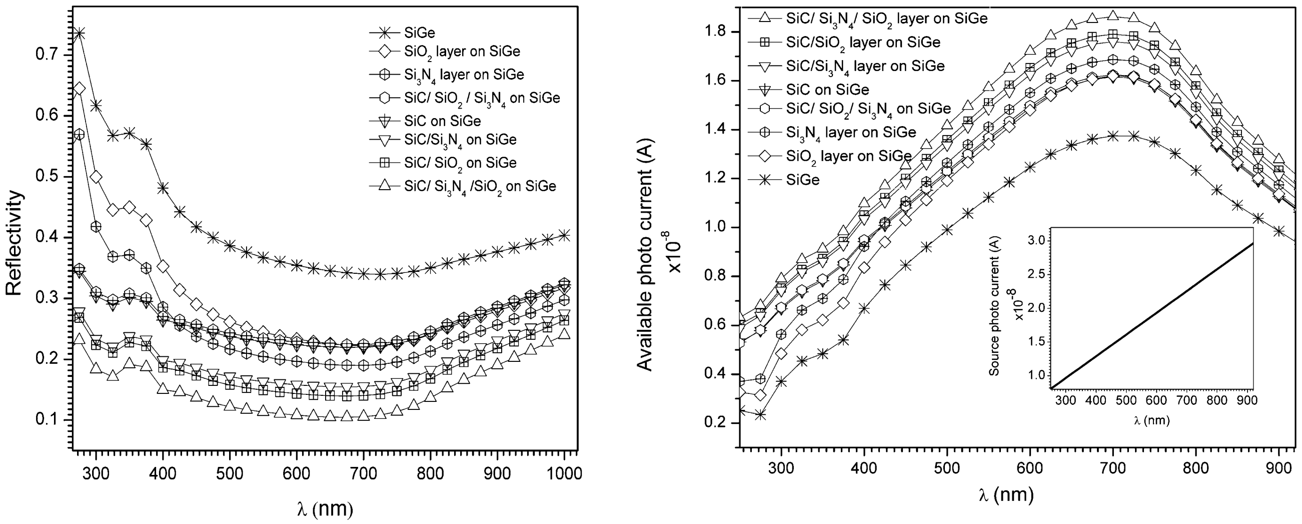

(a) **(b)**

Fig. 3 Spectrum response of (10 × 10) µm thick *I-SiGe* wafer with different absorbing layers. **a** Reflectivity plot, **b** available photocurrent. *Inset* shows source photocurrent

3.2 Optical analysis of SiC/Si_3N_4/SiO_2 coated SiGe solar cell

In previous section, result shows that SiC/Si_3N_4/SiO_2 coated *I-SiGe* wafer shows superior spectrum response compared to other layers. In this section, we have performed SiC/Si_3N_4/SiO_2 coating on proposed device discussed earlier in device section. Thickness of SiC/Si_3N_4/SiO_2 layers are 0.05/0.05/0.1 µm respectively, simulated modified structure is shown in Fig. 4. The spectrum response of (BC-BJ) SiGe solar cell with conventional Si_3N_4 and SiC/Si_3N_4/SiO_2 layers on top is obtained and presented in Fig. 5a, b. From Fig. 5a, it is clear that an optical absorption >85 % is achieved in the spectrum range of 400–700 nm wavelength which higher than the conventional Si_3N_4 passivated SiGe cells. Result shows, significant improvement in absorption as well as EQE of SiC/Si_3N_4/SiO_2 passivated solar cell. Significant improvement has been observed in UV/Visible spectrum in SiC/Si_3N_4/SiO_2 passivated SiGe solar cell compared to conventional Si_3N_4 passivated cell, thereby increasing the photon absorption of proposed device. Higher absorption results in higher EQE shown in Fig. 4b. The device achieved EQE >80 % in the wavelength range of 400–700 nm. At wavelength equivalent to 600 nm it shows EQE of the order of 87.6 %. Also, in UV region, at wavelength equivalent to 250 nm SiC/Si_3N_4/SiO_2 passivated device shows 77 % EQE, whereas Si_3N_4 passivated device shows 43 % EQE. This results in 79 % higher EQE in SiC/Si_3N_4/SiO_2 passivated device compared to Si_3N_4 cell, at 250 nm wavelength.

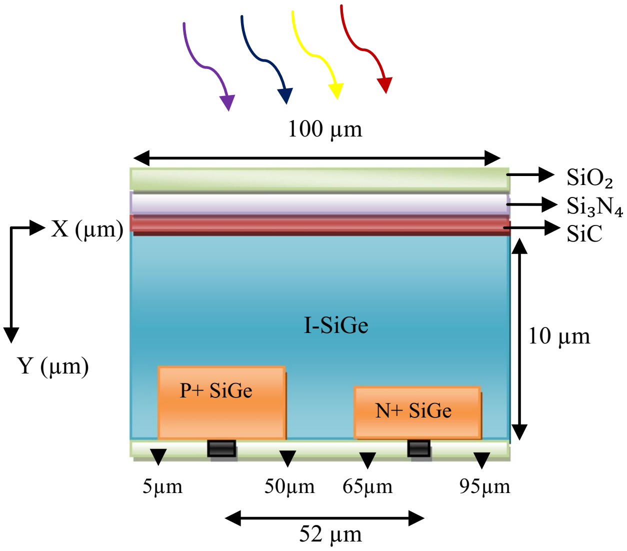

Fig. 4 Proposed SiGe based device: BC-BJ SiGe solar cell with SiC/Si_3N_4/SiO_2 coating on top

3.3 Analysis of SiC/Si_3N_4/SiO_2 coated SiGe solar cell parameters: surface recombination rate and carrier concentrations

Further, in solar cell technology an absorbing layer should also provide good surface passivation, which prevents the recombination of the carriers at the interface. Our previous work shows that the presence of SiC as front surface passivation layer for rear contact silicon solar cell results in improved photovoltaic parameters compared to

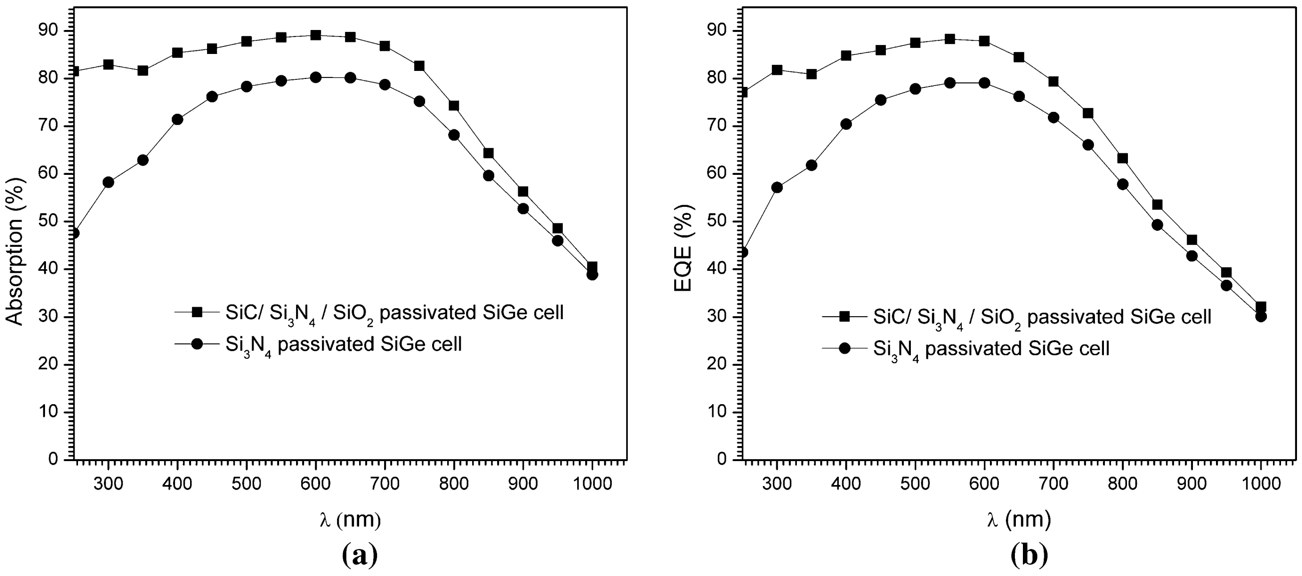

Fig. 5 Comparison of optical parameters of SiC/Si_3N_4/SiO_2 and Si_3N_4 passivated device: **a** absorption spectrum of BC-BJ SiGe Solar Cell. **b** External quantum efficiency of BC-BJ SiGe Solar Cell

conventional front surface passivation scheme (Pandey and Chaujar 2014a, b). Here, we have studied the SiC/Si_3N_4/SiO_2 based front surface passivation on BC-BJ SiGe solar cell. We have obtained the holes quasi Fermi energy level near the *SiC/I-SiGe* interface. Results are compared with BC-BJ SiGe solar cell having only Si_3N_4 as a front surface passivation. The obtained results are plotted in Fig. 6a–c. Result shows, in the proposed device higher field at the interface is achieved. We obtained the barrier height of ~0.8 eV for holes, in proposed device with SiC/Si_3N_4/SiO_2 based front surface passivation. Higher field will assist the holes to move towards the junction, resulting in low concentration of carriers (holes) at the interface shown in Fig. 6c. After illumination, at the interface, the carrier concentration of 2.15×10^9 cm^{-3} and 7.4×10^8 cm^{-3} for electron and holes, respectively has been observed in the device, whereas the bulk concentration of the carrier is ~10^{15} cm^{-3}. Further, Fig. 6b shows the comparison of interface recombination rate. In surface recombination process, an electron from conduction band recombines with the hole in the valance band via a defect level within the bandgap (Aberle 2010). If the concentration of the carriers is drastically reduced, then recombination rate reduces strongly. Further, Results reveal that the magnitude of interface recombination rate is less in the proposed device. The magnitude of interface recombination rate of order of 10^{17} cm^3 s^{-1} has been achieved in proposed device shown in primary axis in Fig. 6b. This section concludes, presence of SiC provides good surface passivation. The Ray tracing and Finite-difference time-domain method is used for the computation of the optoelectronics properties. Also, total current density from *P+–I–N+* region is presented in Fig. 7. Higher current density is observed in case of FDTD simulation compared to ray tracing method. This is because the ray tracing algorithm does not includes the diffraction and coherence effects, whereas FDTD algorithm accounts both diffraction and coherence effect. This algorithm solves the electric and magnetic field propagation directly from the fundamental wave equations. FDTD simulation results in a higher carrier generation inside the device. The light generated current is directly proportional to the light generated carriers.

3.4 Electrical characteristic i.e., J-V characteristics of SiC/Si_3N_4/SiO_2 passivated BC-BJ SiGe solar cell

The most important part of the solar cell design is its current voltage characteristics. Any design must have a higher short circuit current density (J_{sc}) and a higher open circuit voltage (V_{oc}). The current density–voltage (J-V) characteristic of the device is measured under AM1.5 illumination with optical power (0.1 W/cm^2) and is presented in Fig. 8 along with power density- voltage (P_o-V) curve. Ray tracing and FDTD simulation has been done to obtained the J-V curve. FDTD simulation has been done in order to obtain the maximum possible efficiency from the device. In case of FDTD, zero optical lose is considered. This shows, in future, further enhancement in absorption of device will lead to ~18 % PCE. In FDTD, We obtained the short circuit current density (J_{sc}) of 37.86 mA·cm^{-2} and open circuit voltage (V_{oc}) of 593 mV, whereas in ray tracing J_{sc} and V_{oc} are 28.93 mA·cm^{-2} and 585 mV, respectively. FDTD

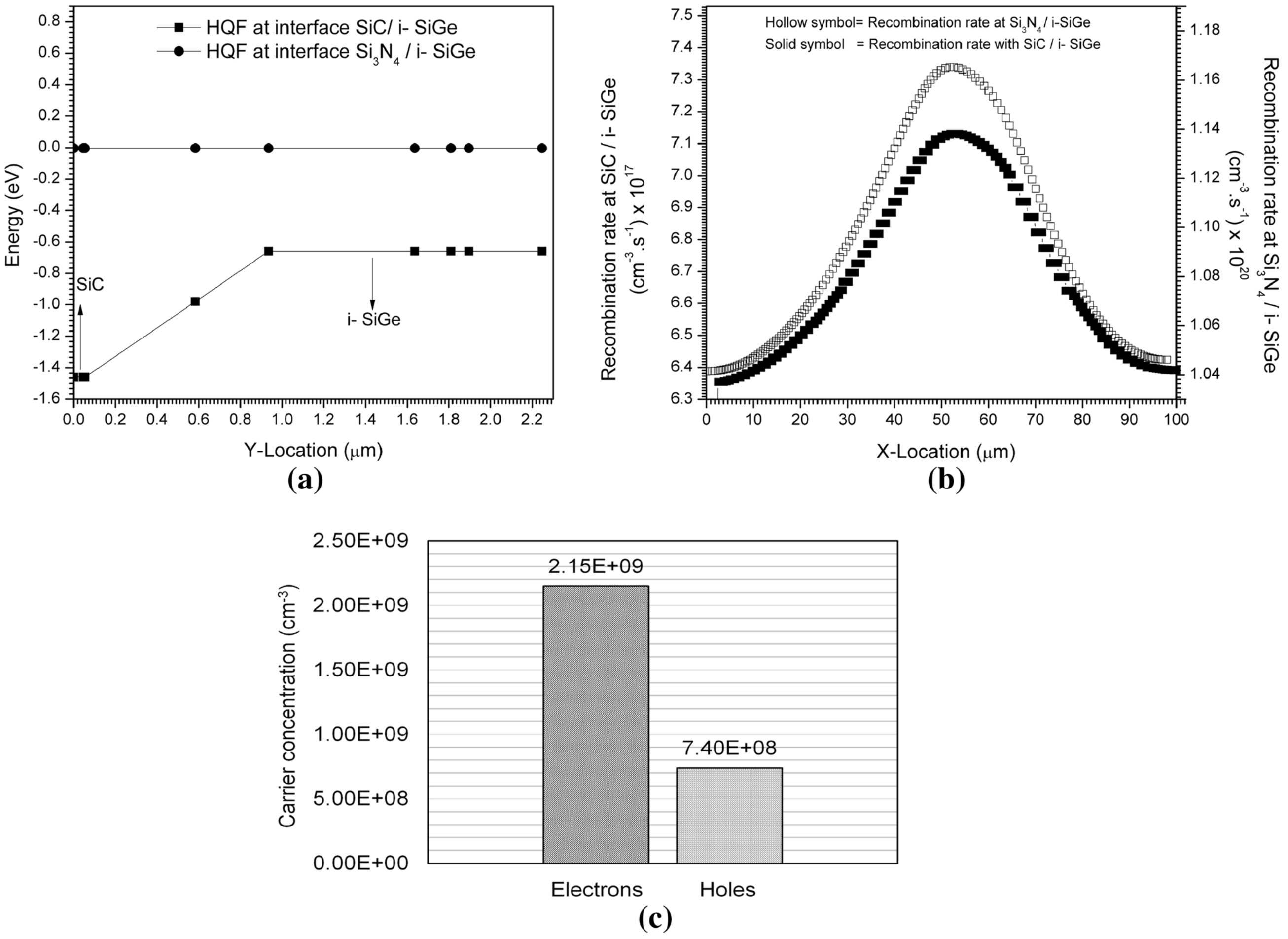

Fig. 6 Advantageous parameters at the interface. **a** Comparison of hole quasi Fermi (HQF) energy levels. **b** Recombination rate near *SiC/I-SiGe* interface, primary axis and recombination rate near *Si_3N_4/I-SiGe* interface, secondary axis. **c** Electrons and holes concentrations near *SiC/I-SiGe* interface

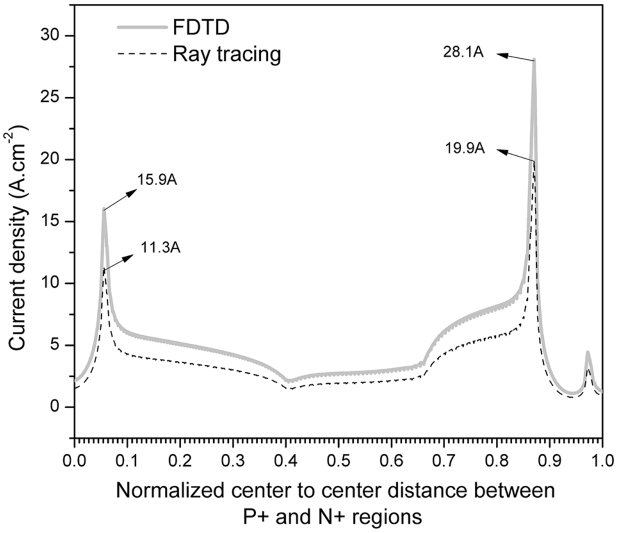

Fig. 7 Comparison of light generated current density of BC-BJ SiGe solar cell using ray tracing and FDTD method

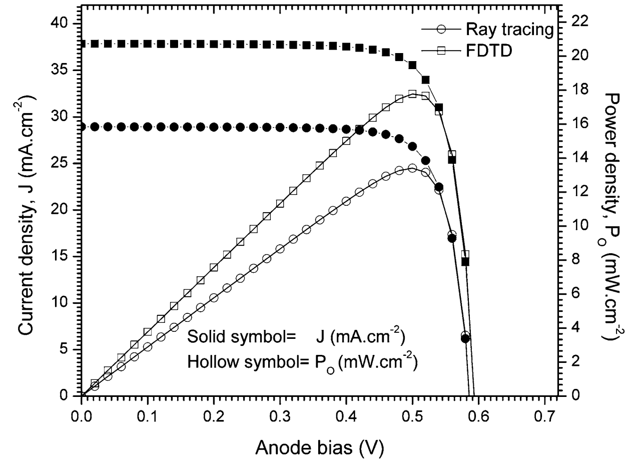

Fig. 8 Electrical parameters of $SiC/Si_3N_4/SiO_2$ passivated BC-BJ SiGe Solar Cell: J-V curve-primary axis and P_o-V curve-secondary axis

Table 2 Photovoltaic properties of ultra-thin BC-BJ SiGe Solar cell

	J_{sc} (mA·cm^{-2})	V_{oc} (V)	FF (%)	PCE (%)
FDTD	37.8	0.593	79.1	17.8
Ray tracing	28.9	0.585	79.1	14.8

FF fill factor, *PCE* power conversion efficiency

simulation shows 30.8 and 1.4 % increment in J_{sc} and V_{oc}, respectively compared to ray tracing simulation. The FDTD simulation results in higher absorption and higher carrier concentration which further results in higher Jsc and variation in the V_{oc} is negligible. Some of the important parameters of the design have been summarized in Table 2.

4 Conclusion

In this work, we proposed a novel, thin BC-BJ SiGe Solar cell design as a cost-effective solution for energy efficient applications. Results, indicates that presence of SiC play an important role in photoelectric conversion, photo reflection is significantly reduced in UV/Visible spectrum region in case of $SiC/Si_3N_4/SiO_2$ passivated BC-BJ SiGe solar cell. The work analyses the band diagrams, internal current density, and surface recombination of the proposed design. The ray tracing and FDTD method is used to simulate the device optoelectronics characteristics. TCAD analysis results in a higher EQE >82 % throughout the spectrum range of 450–700 nm wavelength and a significantly improved power conversion efficiency of 14.8 %. The carrier concentration at the interface is lower than the bulk, therefore reduced recombination rate of ~10^{17} cm^{-3} s^{-1} has been obtained at the interface. We have achieved the concentration of ~10^{9} cm^{-3} and ~10^{8} cm^{-3} for electron and hole, respectively at the interface. This ensures the enhanced surface passivation. In addition, enhanced photovoltaic properties: J_{sc} (28.9 mA), V_{oc} (0.585 V), FF (79.1 %) are also observed for the proposed design. Improved photovoltaic properties indicates proposed device with SiC passivation can be used in lightweight, low cost installation of PV modules. Also, device has rear contact architecture it is easier to interconnect and can be placed closer together in the modules, no need of space between cells. Therefore, it can support lightweight, low cost installation of PV modules. Also, rear contact architecture supports its application in concentrator photovoltaics (CPV) system. Result concludes, proposed device can be a cost effective candidate for PV applications.

Acknowledgments The authors would like to thank Microelectronics Research Lab, Department of Engineering Physics, Delhi Technological University to carry out this work. Rahul Pandey (JRF) acknowledges UGC, Govt. of India for providing fellowship.

References

Aberle AG (2010) Surface passivation of crystalline silicon solar cell a review. Prog Photovolt Res Appl 8(5):487–473. http://onlinelibrary.wiley.com/doi/10.1002/1099-159X(200009/10)8:5%3C473::AID-PIP337%3E3.0.CO;2-D/pdf. Accessed 14 May 2015

Franklin E et al (2014) Design, fabrication and characterisation of a 24.4 % efficient interdigitated back contact solar cell. Prog Photovolt Res Appl. doi:10.1002/pip.2556

Atlas user manual (2014) Silvaco, Inc. 4701 Patrick Henry Drive, Bldg. Santa Clara, CA 95054

Cruz-Campa et al (2011) Microsystems enabled photovoltaics: 14.9 % efficient 14 µm thick crystalline silicon solar cell. Sol Energy Mater Sol Cells 95(2):551–558. doi:10.1016/j.solmat.2010.09.015

Deceglie MG, Ferry VE, Alivisatos AP, Atwater HA (2012) Design of nanostructured solar cells using coupled optical and electrical modeling. Nano Lett 12(6):2894–2900. doi:10.1021/nl300483y

Deinega A, Eyderman S, John S (2013) Coupled optical and electrical modeling of solar cell based on conical pore silicon photonic crystals. J Appl Phys 113:224501

Dziewior J, Schmid W (1977) Auger coefficient for highly doped and highly excited silicon. Appl Phys Lett 31(5):346–348

Feldmann F, Bivour M, Reichel C, Hermle M, Glunz SW (2014) Passivated rear contacts for high-efficiency n-type Si solar cells providing high interface passivation quality and excellent transport characteristics. Sol Energy Mater Solar Cells 120:270–274. doi:10.1016/j.solmat.2013.09.017

Garnett E, Yang P (2010) Light trapping in silicon nanowire solar cells. Nano Lett 10:1082–1108. doi:10.1021/nl100161z

Green MA, Emery K, Hishikawa Y, Warta W, Dunlop ED (2014) Solar cell efficiency tables 43. Prog Photovolt Res Appl. doi:10.1002/pip.2452

Hall RN (1952) Electron-hole recombination in germanium. Phys Rev 87(2):387. doi:10.1103/PhysRev.87.387

Jeong S, McGehee MD, Cui Y (2013) All-back-contact ultra-thin silicon nanocone solar cells with 13.7 % power conversion efficiency. Nature Communications 4. Article number 2950:1–7. doi:10.1038/ncomms3950

Kerschaver EV, Beaucarne G (2006) Back-contact solar cells: a review. Prog Photovolts 14(2):107–123. doi:10.1002/pip.657

Ouellete J (2002) Silicon-Germanium Gives Semiconductor the Edge. Am Inst Phys pp 22–25. https://prezi.com/odedrjji90jc/will-hambleton-silicon-germanium-gives-semiconductors-the-edge/

Pandey R, Chaujar R (2014) Enhanced Back-Contact Back-Junction Crystalline Silicon Solar Cell Performance With A Silicon-Carbide (SiC) Based Front Surface Passivation. Int J Adv Technol Eng Sci 2(01):626–630. http://www.ijates.com/images/short_pdf/1412233437_151.pdf. Accessed 14 May 2015

Pandey R, Chaujar R (2014) Front Surface Passivation Scheme for Back-Contact Back-Junction (BC-BJ) Silicon Solar Cell. International Conference on Nanotechnology, Nanocon 014, Pune, India

Povolny H, Agarwal P, Han S, Deng X (2000) Comparison study of a-SiGe solar cells and materials deposited Using different hydrogen dilution. Mat Res Soc Symp Proc 609:6. doi:10.1557/PROC-609-A30.3

Schwartz RJ, Lammert MD (1975) Silicon solar cells for high concentration applications. IEEE International Electron Devices Meeting, pp 350–352. doi:10.1109/IEDM.1975.188896

Selberherr S (1984) Analysis and simulation of semiconductor devices. Springer, Vienna, New York. doi:10.1007/978-3-7091-8752-4

Shockley W, Read WT (1952) Statistics of the recombinations of holes and electrons. Phys Rev 87(5):835–842. doi:10.1103/PhysRev.87.835

Slotboom JW (1977) The pn-product in silicon. Solid State Electron 20(4):279–283. doi:10.1016/0038-1101(77)90108-3

Slotboom JW, de Graaff HC (1976) Measurements of bandgap narrowing in Si bipolar transistors. Solid State Electron 19(10):857–862. doi:10.1016/0038-1101(76)90043-5

Tian B et al (2007) Coaxial silicon nanowires as solar cells and nanoelectronic power sources. Nature 449:885–889. doi:10.1038/nature06181

Tomasi A et al (2014) Back-Contacted Silicon Heterojunction Solar Cells With Efficiency >21%. IEEE J Photovolt 4(4):1046–1054. doi:10.1109/JPHOTOV.2014.2320586

Wang CC et al (2012) Characterization of nanocrystalline SiGe thin film solar cell with double graded-dead absorption layer. Int J Photoenergy. doi:10.1155/2012/890284

Yang D, Yu X, Li X, Wang P, Wang L (2010) Germanium-doped crystal silicon for solar cells. Solid-State and Integrated Circuit Technology (ICSICT), 10th IEEE International Conference. doi:10.1109/ICSICT.2010.5667855